Star formation, quenching and chemical enrichment in local galaxies from integral field spectroscopy

Francesco M. C. Belfiore

University of Cambridge,
St John's College,
Cavendish Laboratory Astrophysics Group
& Kavli Institute for Cosmology

A thesis submitted for the degree of Doctor of Philosophy
June 2017

Star formation, quenching and chemical enrichment in local galaxies from integral field spectroscopy

Francesco Belfiore

Summary

Within the currently well-established ΛCDM cosmological framework we still lack a satisfactory understanding of the processes that trigger, regulate and eventually quench star formation on galactic scales. Gas flows (including inflows from the cosmic web and supernovae-driven outflows) are considered to act as self-regulatory mechanisms, generating the scaling relations between stellar mass, star formation rate and metallicity observed in the local Universe by large spectroscopic surveys. These surveys, however, have so far been limited by the availability of only one spectrum per galaxy. The aim of this dissertation is to expand the study of star formation and chemical abundances to resolved scales within galaxies by using integral field spectroscopy (IFS) data, mostly from the ongoing SDSS-IV MaNGA survey.

In the first part of this thesis I demonstrate the ubiquitous presence of extended low ionisation emission-line regions (LIERs) in both late- and early-type galaxies. By studying the Hα equivalent width and diagnostic line ratios radial profiles, together with tracers of the underlying stellar population, I show that LIERs are not due to a central point source but to hot evolved (post-asymptotic giant branch) stars. In light of this, I suggest a new classification scheme for galaxies based on their line emission. By analysing the colours, star formation rates, morphologies, gas and stellar kinematics and environmental properties of galaxies with substantial LIER emission, I identify two distinct populations. Galaxies where the central regions are LIER-like, but show star formation at larger radii are late types in which star formation is slowly quenched inside-out. This transformation is associated with massive bulges. Galaxies dominated by LIER emission at all radii, on the other hand, are red-sequence galaxies harbouring a residual cold gas component, acquired mostly via external accretion. Quiescent galaxies devoid of line emission reside in denser environments, which suggests environmental effects as a likely cause for the existence of line-less galaxies on the red sequence.

In the second part of this dissertation I focus on the study of resolved chemical abundances by characterising the gas phase oxygen and nitrogen abundance gradients in a large sample of star forming galaxies. I analyse the deviations from an exponential profile at small and large radii and the dependence of the gradients on stellar mass. These findings are interpreted in the context of the inside-out paradigm of disc growth. I then demonstrate the necessity of gas flows, which are responsible for the observed flattening of the metallicity and N/O ratio gradients at large radii. Finally, I present a case study based on one nearby galaxy (NGC 628), in which I combine IFS and cold gas data to derive a spatially resolved metal budget and estimate the mass of metals lost by the galaxy throughout its lifetime. By using simple physically-motivated models of chemical evolution I infer the average outflow loading factor to be of order unity.

Declaration

I hereby declare that this dissertation is not substantially the same as any that I have submitted for a degree or diploma or other qualification at any other University. I further state that no part of my thesis has already been, or is being concurrently submitted, for any such degree, diploma or other qualification.

This dissertation is the result of my own work and includes nothing which is the outcome of work done in collaboration except as specified in the text. In particular, this dissertation is based on material published in:

- *P-MaNGA Galaxies: emission-lines properties - gas ionization and chemical abundances from prototype observations*, F. Belfiore, R. Maiolino, K. Bundy, D.Thomas, C. Maraston, D. Wilkinson, S. F. Sanchez, M. Bershady, G. A. Blanc, M. Bothwell, S. L. Cales, L. Coccato, N. Drory, E. Emsellem, H. Fu, J. Gelfand, D. Law, K. Masters, J. Parejko, C. Tremonti, D. Wake, A. Weijmans, R. Yan, T. Xiao, K. Zhang, T. Zheng, D. Bizyaev, K. Kinemuchi, D. Oravetz, A. Simmons, 2015, MNRAS, 449, 867.

- *SDSS IV MaNGA - Spatially resolved diagnostic diagrams: A proof that many galaxies are LIERs*, F. Belfiore, R. Maiolino, C. Maraston, E. Emsellem, M. Bershady, K. L. Masters, R. Yan, D. Bizyaev, M. Boquien, J. R. Brownstein, K. Bundy, N. Drory, T. M. Heckman, D. R. Law, A. Roman-Lopes, K. Pan, L. Stanghellini, D. Thomas, A. Weijmans and K. B. Westfall, 2016, MNRAS, 461, 3111.

- *SDSS IV MaNGA - The spatially resolved transition from star formation to quiescence*, F. Belfiore, R. Maiolino, C. Maraston, E. Emsellem, M. Bershady, K. L. Masters, D. Bizyaev, M. Boquien, J. R. Brownstein, K. Bundy, A. M. Diamond-Stanic N. Drory, T. M. Heckman, D. R. Law, O. Malanushenko, A. Oravetz, K. Pan, A. Roman-Lopes, D. Thomas, A. Weijmans, K. B. Westfall, R. Yan, 2017, MNRAS, 446, 2570.

- *SDSS IV MaNGA - The shape of the gas metallicity and nitrogen abundance gradients in the local Universe*, F. Belfiore, R. Maiolino, C. Tremonti, S. F. Sánchez, K. Bundy, M. Bershady, K. Westfall, L. Lin, N. Drory, M. Boquien, D. Thomas and J. Brinkmann, 2017, MNRAS, 469, 151.

- *Galaxy gas flows inferred from a detailed, spatially resolved metal budget*, F. Belfiore, R. Maiolino & M. Bothwell, 2016, MNRAS, 455, 1218.

Work based on these papers was conducted in collaboration with the listed co-authors.
This thesis does not exceed the word limit set by the relevant Degree Committee.

Contents

Declaration **i**

1 Star formation, feedback and chemical enrichment in galaxy evolution **1**
1.1 Galaxy formation in the cosmological context . . . 2
1.1.1 Cosmological framework and initial conditions . . . 2
1.1.2 Cosmological accretion . . . 3
1.1.3 Stars and black holes: feedback in action . . . 4
1.2 Star formation (and its suppression) in galaxies . . . 5
1.2.1 Star formation on galactic scales . . . 5
1.2.2 Galaxy bimodality . . . 9
1.2.3 The quenching of star formation . . . 11
1.3 Chemical evolution and gas regulation in galaxies . . . 13
1.3.1 The nucleosynthetic yield . . . 13
1.3.2 The fundamental equations of chemical evolution . . . 15
1.3.3 Gas regulation in galaxies . . . 17
1.3.4 The chemical evolution of nitrogen . . . 19
1.4 Probing the ISM of galaxies via optical spectroscopy . . . 21
1.4.1 HII region models . . . 21
1.4.2 The determination of chemical abundances . . . 24
1.4.3 The classical star formation-AGN division . . . 27
1.4.4 Dust and extinction . . . 29
1.5 Integral field spectroscopy of nearby galaxies . . . 30
1.5.1 Thesis aims . . . 31

2 The MaNGA survey **33**
2.1 An overview of the MaNGA instrument and data . . . 33
2.1.1 The MaNGA instrument . . . 34
2.1.2 Observing strategy . . . 36
2.1.3 Sample selection . . . 37
2.1.4 Data reduction and calibration . . . 38
2.2 Spectral fitting . . . 40
2.2.1 The choice of binning scheme . . . 40

2.2.2 The fitting algorithm . . . 42
2.3 The MaNGA prototype instrument and data . . . 45

3 Emission lines diagnostic ratios: why some galaxies are LIERs 49
3.1 Emission line diagnostic diagrams and the role of LI(N)ER excitation . . . 51
3.1.1 Hot evolved stars as sources for LI(N)ER emission . . . 51
3.1.2 LI(N)ERs host old stellar populations . . . 52
3.1.3 The role of diffuse ionised gas (DIG) . . . 53
3.1.4 From LINER to LIER . . . 53
3.2 Excitation morphologies of emission line galaxies . . . 55
3.2.1 The BPT diagram on kpc scales . . . 55
3.2.2 A new classification scheme based on spatially resolved line emission . . . 56
3.2.3 Summary of galaxy classes . . . 60
3.3 Hα emission profiles . . . 61
3.3.1 Hα surface brightness and equivalent width distributions . . . 61
3.3.2 Hα radial gradients . . . 64
3.3.3 Are galaxies really line-less? . . . 65
3.4 Line ratio gradients . . . 66
3.5 Discussion . . . 69
3.5.1 Energetics: powering the observed line emission in LIER galaxies . . . 69
3.5.2 Local ionisation conditions and the state of the LIER gas . . . 70
3.5.3 The case for shock excitation in interacting/merging galaxies . . . 71

4 The spatially resolved transition from star formation to quiescence 73
4.1 From nebular lines to stellar indices: tracing star formation and quiescence . . . 74
4.1.1 Age-sensitive indices . . . 74
4.1.2 Age radial gradients . . . 76
4.1.3 The $D_N(4000)$ - Hδ_A plane . . . 76
4.2 LIER galaxies within the bimodal galaxy population . . . 77
4.2.1 Integrated colours and star formation rates . . . 77
4.2.2 Morphological type . . . 82
4.2.3 The importance of the bulge . . . 83
4.3 Kinematic misalignment . . . 83
4.4 The effect of environment . . . 85
4.5 Discussion . . . 88
4.5.1 Inside-out quenching and the nature of cLIER galaxies . . . 88
4.5.2 Ionised gas on the red sequence and the nature of eLIER galaxies . . . 90
4.6 Additional material . . . 92

5 Metallicity gradients in the local Universe 95
5.1 The MaNGA galaxy sample . . . 96
5.2 Deriving the abundance gradient . . . 97
5.2.1 Identifying star forming regions . . . 97
5.2.2 The effect of spatial resolution . . . 99

5.2.3 The determination of disc inclination . . . 101
5.2.4 Measuring the gradient . . . 102
5.3 The shape of the oxygen and nitrogen abundance gradients . . . 102
5.3.1 The mass dependence of the metallicity gradient . . . 102
5.3.2 Dependence of the metallicity gradient on secondary parameters . . . 106
5.3.3 The mass dependence of the N/O abundance ratio . . . 107
5.3.4 The behaviour at small and large radii . . . 107
5.3.5 The relation between oxygen and nitrogen abundance . . . 110
5.4 Sources of systematic error . . . 111
5.4.1 The choice of radial scale length . . . 111
5.4.2 The effect of spatial resolution . . . 113
5.4.3 The contamination from DIG . . . 114
5.5 Comparisons to previous work . . . 115
5.5.1 The metallicity gradient in nearby galaxies . . . 115
5.5.2 Abundance gradients in the Milky Way . . . 116
5.6 Discussion . . . 117
5.6.1 Chemical evolution models and 'inside-out' growth . . . 117
5.6.2 Interpreting the shape of the metallicity gradient . . . 118
5.6.3 The N/O ratio gradient . . . 119

6 Where are the metals? - A galaxy-wide metal budget 121
6.1 Overview of the data . . . 122
6.1.1 Integral field spectroscopy . . . 122
6.1.2 HI 21 cm observations . . . 124
6.1.3 CO(2 -1) observations . . . 124
6.1.4 Multi-wavelength photometric data . . . 125
6.1.5 Stellar mass surface density . . . 125
6.1.6 Stellar metallicity . . . 126
6.1.7 Gas mass surface density . . . 127
6.1.8 Radial gradients . . . 128
6.2 The chemical evolution model . . . 129
6.2.1 Analytical solution for constant inflow models . . . 130
6.2.2 Metal mass budget . . . 131
6.3 Applying the chemical evolution model to NGC 628 . . . 132
6.3.1 Accounting for the missing metals . . . 132
6.3.2 Inferred net outflow loading factor . . . 134
6.3.3 Modelling the gas metallicity . . . 135
6.4 Discussion . . . 136
6.4.1 Gas flows and disc-halo interaction . . . 136
6.4.2 Towards larger galactocentric distances . . . 139
6.4.3 The effect of the IMF and the nucleosynthetic yield . . . 139
6.4.4 The oxygen deficit in context . . . 140
6.4.5 A link between outflows and baryon fraction . . . 141

6.5 Additional material 141
6.5.1 A comparison with the SFR $\propto$ inflow rate model 141

7 Conclusions **145**
7.1 Summary 146
7.2 Future work 150

Bibliography **155**

Appendix **171**

Chapter 1

Star formation, feedback and chemical enrichment in galaxy evolution

In the first publication making use of the telescope for astronomical observations, the *Nuncius Sidereus*, published in 1610, Galileo Galilei conclusively settled the ancient question regarding the nature of the Milky Way by resolving our Galaxy into stars. In the subsequent century, inspired by the increasing understanding of the Milky Way as a flattened disc of stars, thinkers and philosophers like René Descartes and Immanuel Kant developed new speculative cosmologies. These theories aimed, for the first time, to place galaxies in a wider cosmological framework. In his prescient work *Universal Natural History and Theories of the Heavens*[1] Kant put forward the idea that spiral nebulae could actually be external galaxies, or 'island universes', much like our own Milky Way. It was not until 1925 that Edwin Hubble demonstrated the extragalactic nature of Andromeda and M33 (Hubble, 1925, 1926a) by calculating their distances based on observation of Cepheid variables and exploiting the period-luminosity relation previously calibrated by Henrietta Leavitt (Leavitt & Pickering, 1912).

Making use of the high-quality photographic images from the Mount Wilson 100-inch telescope, Hubble further put forth the basic framework for the classification of galaxies, in the form of his popular 'tuning fork' diagram (Hubble 1926b, 1936, Fig. 1.1). This classification scheme, based entirely on morphological appearance, arranges galaxies in a continuous sequence from *elliptical* (or early types) to *spiral* (late types). Elliptical galaxies are mildly-flattened spheroidal systems, supported by the random motion of their stars. Spiral galaxies, on the other hand, are composed of a disc, supported by rotation, and a central spheroidal component, called the bulge. The two sequences merge in the middle, where we find the S0, or lenticular, galaxies. Further refinements to this classification have included irregular galaxies, exemplified by our closest galactic neighbours, the Magellanic Clouds.

This simple classification into two main galaxy classes, which Hubble intended to be purely *'descriptive and entirely independent of any theory'* (Hubble, 1926b), was found to be deeply insightful, as further studies have demonstrated that galaxies are bimodal in several other physical parameters, including the age of their stellar populations, their chemical abundances and their content of cold gas. It was not until the end of the 1960s, however, that the first theories were put forward to realistically describe the evolutionary processes responsible for the make-up of the Hubble sequence.

In this chapter I provide a brief overview of the many processes that shape the formation and

[1] *Allgemeine Naturgeschichte und Theorie des Himmels* in the original German.

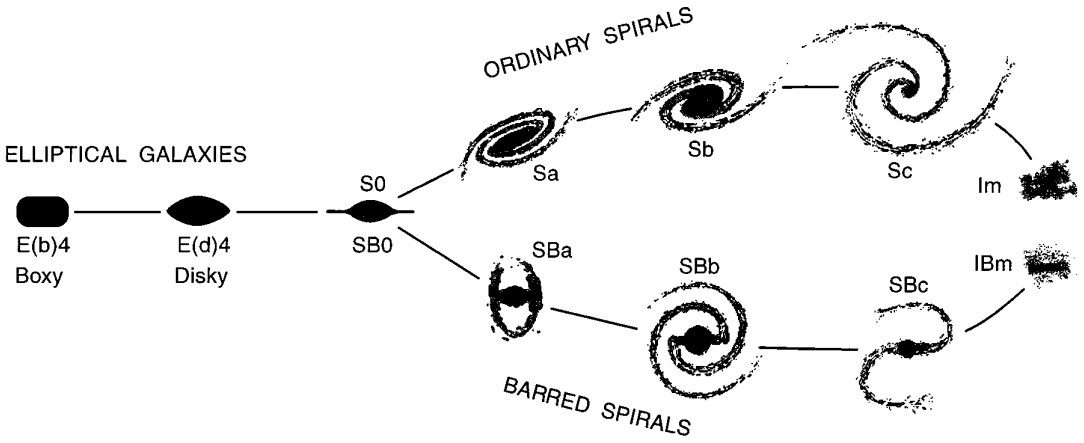

Figure 1.1: A revision of Hubble's original tuning fork diagram (Hubble, 1936) according to Kormendy & Bender (1996). On the left-hand side elliptical galaxies (E) are divided into boxy and discy depending on their isophote shapes (while the original Hubble classification sub-divides ellipticals into classes depending on their observed ellipticity on the plane of the sky). S0 (or lenticular galaxies) are shown as intermediate bulge+disc systems. On the right-hand side, spiral galaxies are subdivided into barred (SBa, SBb, SBc) and non-barred (Sa, Sb, Sc), with later types having smaller bulges and more flocculent arms. At the extreme end of the diagram Magellanic irregular (Im) and barred irregular galaxies (IBm) have been added. Figure from Kormendy & Bender (1996).

evolution of galaxies and observational probes thereof, with special emphasis on the two key concepts further discussed in this dissertation: the regulation of star formation and chemical evolution in galaxies. In detail, in Sec. 1.1 I present a brief introduction to galaxy formation in the cosmological framework, including cosmological gas accretion and feedback. In Sec. 1.2 I discuss the main processes responsible for the regulation of star formation and quenching in galaxies. Sec. 1.3 focusses on chemical evolution in the context of equilibrium models, aiming to highlight how chemical abundances can be used to constrain gas flows in galaxies. Finally in Sec. 1.4 I discuss the observational probes used in this dissertation, focussing on the role of optical emission lines used to investigate the distribution of star formation and chemical abundances within galaxies.

1.1 Galaxy formation in the cosmological context

1.1.1 Cosmological framework and initial conditions

The formation of structure in the Universe is driven by the inexorable attractive force of gravity. Einstein's theory of general relativity, which specifies the geometry of space-time in the presence of matter, and the cosmological principle, positing that the Universe is homogeneous and isotropic on large enough scales, are the corner stones of the modern cosmological paradigm.

The dynamical evolution of such a model Universe is therefore completely specified by its geometrical curvature and its mass and energy content. Detailed observations of the cosmic microwave background (CMB, Hinshaw et al. 2013; Planck Collaboration et al. 2016), combined with inference based on Type Ia supernovae (Riess et al., 1998; Perlmutter et al., 1999), have greatly improved the precision in our determinations of these parameters and have led to the establishment of a 'standard model' for cosmology, referred to as ΛCDM (Λ cold dark matter). In this paradigm, the energy density of the Universe consists of three main components: baryons, cold dark matter and dark energy. In astronomical parlance, baryons refer to all 'visible' matter contemplated by the standard model of

particle physics, including leptons. The nature of the other two components, accounting together for more $\sim 95\%$ of the energy density of the Universe, remains elusive. Dark matter constitutes the main mass component in the Universe, and its existence is strongly supported by a wide range of independent lines of evidence, including the dynamics of disc galaxies and clusters and inferences from Big Bang nucleosynthesis. Dark energy, on the other hand, is responsible for the observed acceleration in the expansion of the Universe, an effect analogous to that of a cosmological constant (Λ).

The process of galaxy formation is driven by the effect of gravity acting on inhomogeneities in the matter distribution in an otherwise homogeneous and isotropic Universe. Unfortunately the standard model of ΛCDM cosmology does not provide a natural explanation for the origin of these perturbations. This is not altogether surprising, as any model for the Universe based on general relativity ought to break down at sufficiently early times, when quantum effects become important. Several theories of the early Universe, including the popular family of inflationary theories (Guth, 1981), may account for the quantum origin of primeval perturbations.

As originally demonstrated in Jeans (1902), the stability of a perturbation depends on the relative ratio between gravity and pressure support. If the size of a perturbation exceeds the Jeans' length, $\lambda_{\rm J} = {\rm c_s}/({\rm G}\,\rho_0/\pi)^{1/2}$, then the overdensity is subject to gravitational instability, and will collapse. In a static Universe the growth of perturbations is an exponential process. In the case of an expanding Universe perturbations grow algebraically with time, following $\Delta\rho/\rho \sim t^{\alpha}$, where $\alpha > 0$ depends on the cosmological parameters. When the perturbation reaches $\Delta\rho/\rho \sim 1$, it decouples from the underlying expansion of the Universe and forms a gravitationally bound virialised structure (Gunn & Gott, 1972), known as a *dark matter halo*.

Haloes keep growing after collapse by accreting mass from nearby regions and by smaller haloes merging into larger ones (a process known as hierarchical growth). In this way the large scale structure in the Universe acquires its 'Swiss cheese' topology, characterised by large overdensities, sheets and filaments: the cosmic web.

1.1.2 Cosmological accretion

Baryons distinguish themselves from dark matter by their striking ability to be luminous. While dark matter is collisionless, baryons are capable of emitting radiation via a variety of physical processes. The formation of baryonic structures in a ΛCDM model was first discussed in the seminal paper of White & Rees (1978). In this model, the baryonic gas, embedded in the collapsing dark matter halo, shocks and heats to the halo's virial temperature. The ability of gas to cool, which depends primarily on the halo's virial temperature, has long been recognised as a key requirement for galaxy formation (Silk, 1977; Rees & Ostriker, 1977; Binney, 1977).

If cooling is inefficient, the gas may form a quasi-equilibrium hot atmosphere in the halo and then slowly cool over time (hot mode accretion). Cold gas from the intergalactic medium may directly accrete onto the galaxy if the cooling time is short enough (cold mode accretion). This mode, which dominates in case of accretion onto small haloes and at high-redshift, proceeds via cold, dense filaments, which can now be studied by means of high-resolution hydrodynamical simulations (Birnboim & Dekel, 2003; Kereš et al., 2005; Van de Voort et al., 2012).

The accretion rate onto haloes is predicted to decrease with time, going from tens of $\rm M_\odot\ yr^{-1}$ at $z \sim 2$ to a few $\rm M_\odot\ yr^{-1}$ at $z \sim 0$ for a Milky Way size halo (Dekel et al., 2013). Unfortunately, despite

its obvious importance in understanding the growth of galaxies, studies of accretion remain limited to the theoretical Universe, modelled in large-scale numerical hydrodynamical simulations, with little direct observational evidence available regarding even the most basic properties of the accreting gas (for a review of accretion from an observational perspective see Sancisi et al. 2008; Sánchez Almeida et al. 2014). Indirect evidence, based on the star formation and chemical abundances *inside* galaxies, still provides the best handle to infer the properties of the accreting gas (Sec. 1.3.3).

1.1.3 Stars and black holes: feedback in action

The first stars and black holes

As gas cools onto dark matter haloes, its density increases to the point where the gas becomes self-gravitating. In the presence of dust, atomic hydrogen can become molecular, leading to the formation of cold, dense clouds, within which star formation may occur. Despite its key role in astrophysics, the physics of star formation has proved to be a particularly hard problem from the theoretical perspective, and represents a very active area of research, both theoretically and observationally (Kennicutt, 1998; Evans, 1999; McKee & Ostriker, 2007; Kennicutt & Evans, 2012). Further discussion of the physics of star formation on galactic scales is presented in Sec. 1.2.1.

In the early Universe the first black holes may have been formed from the death of first generation, metal-free stars (population III stars, Bromm & Larson 2004). Because of the total absence of heavy elements, these stars are predicted to have unusually high masses ($\sim$ 100 $M_\odot$) and very different properties from stars of subsequent generations. Black holes grow by further accretion of matter and release large amounts of energy in the process, which makes them shine as quasars (Lynden-Bell, 1969; Rees, 1984) or active galactic nuclei (AGN). Despite this basic theoretical picture, the details of the seeding and growth of black holes at very early epochs are mostly unconstrained by observations, with a number of competing theories aiming to link black hole seeds to the emergence of the first quasars (see review in Volonteri 2010), observed at redshifts $z \sim 6 - 7$ (Fan et al., 2001; Mortlock et al., 2011).

Since the first models of galaxy formation in the ΛCDM framework were worked out in detail, it became apparent that the baryonic gas tends to cool and form stars at high redshift, when the gas is dense and cooling times are short. This expected early period of intense star formation, however, is incompatible with the observed evolution of the cosmic star formation rate (SFR) and the current stellar mass function of galaxies (White & Frenk, 1991; Springel & Hernquist, 2003; Kereš et al., 2009). In order to solve the overcooling problem subsequent studies have therefore concluded that stars and black holes must be *active* agents in shaping the growth of galaxies.

Supernovae feedback

One or more mechanisms are required to inject energy and momentum into the gas at both small and large scales. It was soon realised that supernovae, caused by the death of massive stars and known to release a substantial amount of energy into the interstellar medium (ISM), may be a key ingredient in order to heat and eventually expel the gas from galaxies (White & Rees, 1978; Dekel & Silk, 1986; White & Frenk, 1991). Signatures of supernovae-driven outflows, with mass outflow rates likely of the same order as the SFR, are ubiquitously observed in star-forming galaxies (Heckman et al., 2000; Veilleux et al., 2005). Outflows are also necessary to explain why the baryon fraction within haloes is

much smaller than the universal value (Behroozi et al., 2010; Moster et al., 2010), and have a key role in regulating the galaxies' content of heavy metals (as discussed in Sec. 1.3.3). More careful studies of feedback due to star formation have also recognised that a wide range of other processes associated with massive stars (e.g., radiation pressure, photoionisation heating and stellar winds, see Hopkins et al. 2012) need to be invoked in order to solve the overcooling problem.

The stellar mass function

A commonly adopted way of testing the validity of the assumed feedback model is to compare the number of galaxies of different stellar masses obtained in the model with the observed stellar mass function of galaxies. The observed luminosity function of galaxies (in several photometric bands) is well fitted by a Schechter function (Schechter, 1976) of the form

$$\phi(L)dL = \phi_0 \left(\frac{L}{L^*}\right)^{\alpha} \exp\left(-\frac{L}{L^*}\right)\frac{dL}{L^*}, \tag{1.1}$$

where $\phi(L)$ is the number of galaxies per unit luminosity, L^* is the characteristic luminosity at the 'knee' of the LF, where the form changes from power law to exponential, and α is the *faint end slope* , which is typically observed to be in the range $-1.5 < \alpha < -1.0$ (de Jong & Lacey, 2000; Bell et al., 2003; Blanton et al., 2003a). In order to obtain the stellar mass function one needs to compute the mass-to-light ratio for the relevant band. In practice, in recent work stellar masses are computed by fitting the observed fluxes in several photometric bands to stellar population models with varying star formation histories, age, metallicity and dust attenuation (Fig. 1.2, left).

It has been recognised for some time that the halo mass function predicted by ΛCDM and the observed stellar mass function have divergent behaviours at both the high- and low-mass ends (Fig. 1.2, right). For low stellar masses, the general consensus requires star formation to be regulated by supernova feedback, since supernovae are most efficient at removing gas from galaxies with a shallow gravitational potential well. At even lower masses, photoionisation heating from the intergalactic ultraviolet (UV) background causes star formation to become increasingly inefficient for $M_\star < 10^{10}$ $M_\odot$ (Gnedin, 2000; Benson et al., 2002).

For massive haloes the situation is more complicated, since the energy released by supernovae or injected by stellar photoionisation is not sufficient to overcome the dark matter gravitational potential. Most recent models claim that the energy released by accretion onto supermassive black holes (AGN feedback) is capable of offsetting cooling and of leading to the shut-down ('quenching') of star formation in massive haloes. I will return to a discussion of the quenching process in Sec. 1.2.3

1.2 Star formation (and its suppression) in galaxies

1.2.1 Star formation on galactic scales

The multiphase ISM

While most of the mass in galaxies in the nearby Universe lies in their dark matter haloes and their stellar components, the processes driving the baryon cycle take place in the diffuse gas and dust between the stars (i.e. the ISM). The ISM is a multiphase medium, where gas phases at different temperatures, densities and ionisation states can coexist in approximate pressure equilibrium. The interplay between

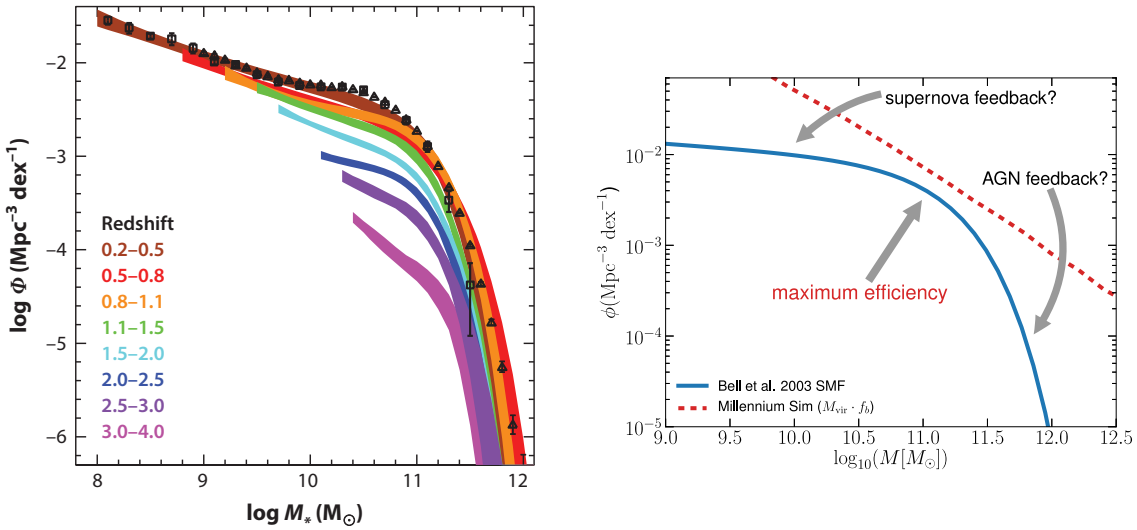

Figure 1.2: *Left*: The stellar mass function at different redshifts. From Madau & Dickinson (2014), adapted from Ilbert et al. (2013). *Right*: A comparison between the halo mass function predicted by a dark-matter only numerical simulation of the ΛCDM Universe (Millennium simulation, Springel et al. 2005) multiplied by the cosmic baryon fraction (f_b) and the stellar mass function at redshift $z \sim 0.1$ derived observationally by Bell et al. (2003). From Mutch et al. (2013).

the different phases is complex, and is driven by the balance of radiative cooling with heating by supernovae and cosmic rays. In the Milky Way much of the volume ($\sim 50\%$) is occupied by hot diffuse gas (T $\sim 10^{5.5-6}$K), which is maintained at this high temperature by continuous heating due to supernovae. Ionised gas at temperatures around 10^4 K is found around the sites of formation of massive stars. These photoionised nebulae (*HII regions*) emit strongly in optical emission lines and are the subject of Sec. 1.4.1. The neutral ISM segregates into warm (T $\sim 10^{3.7}$ K) and cold (T $\sim$ 100 K) components due to thermal instability (Field et al., 1969; McKee & Ostriker, 1977; Cox, 2005). When the cold neutral medium is sufficiently shielded by the interstellar UV radiation field, it may become molecular and form giant molecular clouds (GMCs), which have temperatures of $\sim$ 10-30 K, typical masses of order of $10^5 - 10^6$ M$_\odot$ and are tens of pc in size. Star formation is only found to occur in the densest parts of molecular clouds, known as cores and clumps.

The formation of GMCs and star formation thresholds

The question of whether the ISM can form gravitationally bound molecular structures is often cast in terms of a star formation rate *threshold* (Kennicutt et al., 1989; Leroy et al., 2008). In this context, a critical gas surface density is defined, which is a function of local conditions, like pressure, metallicity or kinematics of the gas. When the gas density lies below this threshold, star formation is assumed to be strongly suppressed. The detailed physics driving this threshold is a matter of current research and may be associated with thermal instability (which drives the segregation of warm and cold neutral gas, Schaye 2004), gravitational instability (Toomre, 1964; Kennicutt, 1998; Martin & Kennicutt, 2001), galactic shear (Hunter et al., 1998) or ISM pressure (Elmegreen, 1993).

Observationally, the existence of a star formation threshold is supported by the fact that the SFR radial profiles decline much more steeply than the cold gas surface density in the outer regions of nearby spirals (Kennicutt, 1998; Bigiel et al., 2010). Systematic observations of atomic and molecular gas in nearby galaxies (e.g. THINGS, Walter et al. 2008, and HERACLES, Leroy et al. 2009, surveys)

have demonstrated that the HI surface density varies remarkably little over the optical disk of typical nearby star forming galaxies. Moreover, the scale length of the HI disc is larger than that of the stellar light, molecular gas or SFR (Leroy et al. 2008, see also the radial profiles of different ISM components, SFR and stellar mass presented for a typical nearby star forming galaxy, NGC 628, discussed in detail in Sec. 6.1.8). The idea that cold gas may be prevented from forming stars by lying below some local star formation threshold is therefore invoked in explaining the low star formation efficiency in outer discs (Sec. 5.6.2 and Sec. 6.4.2) and potentially the lower star formation efficiency observed in bulges and ellipticals (Sec. 1.2.3 and Sec. 4.5.1).

The star formation law

A fundamental theoretical problem with star formation is its inefficiency. In the absence of feedback, molecular clouds are generally predicted to experience runaway collapse and eventually turn nearly all their gas into stars. This contrasts with observations which demonstrate that the efficiency of star formation (the fraction of gas eventually converted into stars) is closer to a few percent (Zuckerman & Palmer, 1974; Evans, 1999; Bigiel et al., 2008; Leroy et al., 2013). Interestingly, the problem of inefficiency of star formation can be thought of as another instance of the overcooling problem, already discussed in the context of galaxies as a whole (Sec. 1.1.3). To tackle this problem, modern theories of star formation invoke a combination of magnetic fields, turbulence and feedback, although the relative roles of these mechanisms remains the matter of much speculation.

Neglecting the physical processes which sets the star formation efficiency on small scales, we may parametrise the star formation process via an empirical relation of the form

$$\rho_{SFR} = \frac{\epsilon_\star}{t_\star}\rho_g, \tag{1.2}$$

where $\rho_{\rm SFR}$ is the SFR volume density, $\epsilon_\star$ is the star formation efficiency set by the microphysics, $t_\star$ is a relevant timescale and $\rho_{\rm g}$ is the cold gas volume density. This parametrisation of the star formation law needs to be coupled with an appropriate definition of the timescale $t_\star$. Possible proposals for this timescale include the free-fall timescale, the orbital timescale or the characteristic timescale for cloud-cloud collisions (Madore, 1977; Silk, 1997; Tan, 2000). These different possibilities lead to considerable differences in the derived star formation laws. For example, if one considers the free-fall time[2] ($t_{\rm ff} \propto \rho_{\rm gas}^{-0.5}$) to be the relevant timescale, then one obtains a star formation law with a scaling $\rho_{\rm SFR} \propto \rho_{\rm g}^{1.5}$, remarkably close to the observed one.

Observationally, it is customary to parametrise the star formation relation via a power law relationship between the SFR surface density ($\Sigma_{\rm SFR}$) and the cold gas surface density ($\Sigma_{\rm g}$) of the form $\Sigma_{\rm SFR} \propto \Sigma_{\rm g}^{\rm N}$ (the Schmidt-Kennicutt law, Schmidt 1959; Kennicutt 1998). Observations demonstrate a strong correlation between $\Sigma_{\rm SFR}$ and $\Sigma_{\rm g}$ with a non-linear slope ~ 1.4 (Kennicutt, 1998; Leroy et al., 2008; Blanc et al., 2009; Liu et al., 2011). Moreover the data broadly support the existence of (at least) two regimes: a low-density regime, where the ISM is mostly atomic and $\Sigma_{\rm SFR}$ is not strongly correlated with $\Sigma_{\rm g}$ (typical of galaxy outskirts and possibly low-mass galaxies), and a higher-density regime (typical of the central regions of normal spirals) where $\Sigma_{\rm SFR}$ and $\Sigma_{\rm g}$ are more strongly correlated (see Fig. 1.3).

[2] The free-fall time is defined as the time required for a uniform, pressure-free sphere of gas to collapse to a point, and is given by $t_{\rm ff} = (3\,\pi/32\,{\rm G}\,\rho)^{1/2}$, where ρ is the gas density.

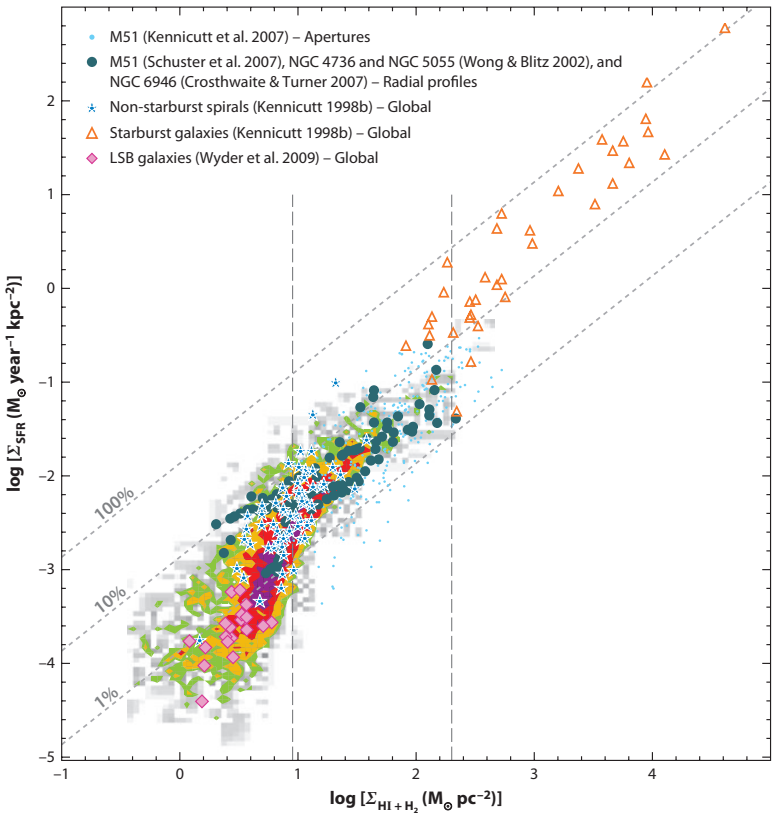

Figure 1.3: The relation between the SFR surface density and the cold gas (atomic + molecular) surface density from various sets of measurements. The coloured contours represent the kpc-scale data from the SINGS sample of nearby galaxies (Bigiel et al., 2008). The other data points are colour-coded as detailed in the legend. The grey dotted lines represent the star formation law obtained with a constant SFE. The vertical dashed lines divide the plot into a low-density regime (where the ISM is dominated by atomic gas and star formation is inefficient), an intermediate regime (typical of the central regions of normal spiral galaxies) and a high-density regime (characteristic of starburst galaxies). From Kennicutt & Evans (2012).

The initial mass function

Since the evolution of a star is driven almost entirely by its mass at birth (and, to second order, by its chemical composition), a fundamental question regarding the process of star formation is the mass distribution of new stars (the *initial mass function*, or IMF). While it should be possible to derive the IMF from first principles, so far a theoretical justification for the observed IMF remains elusive. Parametrisations of the IMF are thus derived either from stellar counts in specific regions of the Milky Way, or (in the extragalactic context) by assuming a functional form and testing model predictions against particular sets of observations.

Based on stellar counts in the solar neighbourhood, Salpeter (1955) suggested the IMF to be a power law of the form

$$dN/dM = \phi_{IMF}(M) \propto M^{-\alpha} \tag{1.3}$$

where dN/dM indicates the number of stars formed per unit mass and $\alpha = 2.35$. The Salpeter (1955) analysis was limited to stars of masses > 0.4 $M_\odot$. More recent determinations of the Milky Way IMF, which include a wider range of stellar masses, indicate a clear flattening at lower masses, either as broken power laws (Kroupa et al., 1993) or a lognormal distribution (Chabrier, 2003) (see Fig. 1.6, left panel, for a comparison of different IMFs). Moreover studies of extragalactic objects have

questioned the universality of the IMF (van Dokkum & Conroy, 2010; Cappellari et al., 2013). The uncertainty caused by our limited knowledge of the IMF severely affects several predictions based on models of stellar populations, including the conversion of light to mass, the computation of the nucleosynthetic yield per stellar generation (see Sec. 1.3.1), or the conversion factor between the SFR and the number of ionising photons (see Sec. 1.4.4).

1.2.2 Galaxy bimodality

Before the spectroscopic revolution enabled by the large galaxy surveys of the early 2000s, typical properties of galaxies were derived via careful observations of small samples of bright, nearby objects (de Vaucouleurs, 1948; van den Bergh, 1976; de Vaucouleurs et al., 1991; Roberts & Haynes, 1994). These studies have further refined Hubble's original morphological classification and confirmed that a number of physical properties of galaxies, including their mass, colour[3], neutral hydrogen content and number of HII regions change systematically over the Hubble sequence. Moreover, they have provided the basis for a quantitative study of the structural properties of galaxies, as encoded in their light profiles. A convenient general model for the light distribution of elliptical and spiral galaxies is provided by the Sérsic (1963) profile,

$$\log\left[\frac{I(r)}{I(R_e)}\right] = -b_n\left[\left(\frac{r}{R_e}\right)^{1/n} - 1\right], \tag{1.4}$$

where I(r) is the galaxy surface brightness in a specific photometric band, R_e (the half-light or *effective* radius) is the radius within which half of the light is emitted, b_n is a numerical factor which depends only on n, and n (the Sérsic index) reflects the concentration of the galaxy's light profile. Elliptical galaxies and bulges are generally well-fitted by a de Vaucouleurs profile (n=4, de Vaucouleurs 1948), while the light distribution of the disc component is well-represented by an exponential profile (n=1). Bulge + disc systems are generally fitted by two components: an exponential disc and a higher Sérsic index bulge.

The blue cloud and red sequence

In the early 2000s a new generation of large galaxy surveys, such as the Sloan Digital Sky Survey (SDSS, York et al. 2000) and the 2 Degree Field Galaxy Survey (Colless et al., 2001), have revolutionised the quality and quantity of data available to study the physical and structural properties of galaxies in the nearby Universe. As an example, SDSS has now observed more than a quarter of the sky in five broad optical bands (u, g, r, i, z, Fukugita et al. 1996) and obtained optical fibre spectra for $\sim 10^6$ galaxies.

These unprecedented statistics have revealed that the distribution of galaxies in the colour-absolute magnitude (or colour-stellar mass) plane is strongly bimodal (Strateva et al., 2001; Blanton et al., 2003b; Baldry et al., 2004). Two sequences are generally identified in this plane, known as the *red sequence* and the *blue cloud* (Fig. 1.4, left). Only few galaxies are found lying at intermediate colours (in the so-called *green valley*). At the low-mass end, blue galaxies dominate the population, while at

[3] A colour index in optical astronomy is defined as the difference between the magnitudes in two photometric bands. Massive stars, which are short-lived, emit a larger fraction of their light in the blue and UV. Hence a colour index including a blue/UV band and an redder optical band encodes information about the galaxy's recent star formation history.

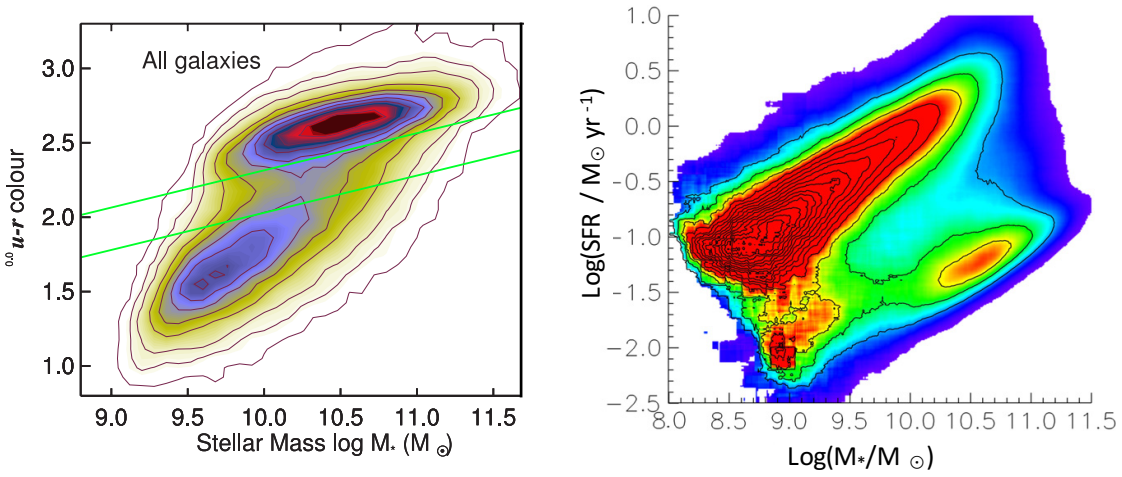

Figure 1.4: *Left*: The distribution of galaxies in the $u - r$ colour-stellar mass plane for a roughly mass-limited sample of galaxies from SDSS. Observed colours have been corrected to account for the finite redshift of the sources (k-correction, see Blanton & Roweis 2007), although the effect of the correction is negligible. The green lines delimit the green valley, between the red sequence (on the top) and the blue cloud (on the bottom). From Schawinski et al. (2014). *Right*: The star formation 'main sequence', i.e. the relation between SFR and stellar mass. The density of galaxies, represented by the change in colour-coding, has been corrected for volume incompleteness. The SFR and stellar masses are taken from the analysis performed by the MPA-JHU group (Brinchmann et al., 2004) on SDSS data. From Renzini & Peng (2015).

the high-mass end the majority of galaxies are red, with a transition mass at $\sim 10^{10.5}$ $M_\odot$ (Kauffmann et al., 2003a).

Red galaxies are generally early-type, have little recent star formation, and their colour is weakly related to mean stellar age and metallicity, both of which increase with mass. Blue galaxies, on the other hand, are mostly spirals and irregulars. Their optical colour is mostly related to the recent history of star formation and to dust extinction. The use optical-UV colours, which have become widely available with the launch of the *GALEX* mission (Martin, 2005), makes the observed bimodality even stronger, as the UV is a very sensitive tracer of recent star formation (see Sec. 4.2.1)

Bimodality is also present in the structural properties of galaxies: blue galaxies have lower Sérsic indices than red galaxies, although more massive galaxies, both red and blue, tend to be more concentrated (i.e. have higher Sérsic indices, Blanton & Moustakas 2009, see also Sec. 4.2.3).

The star formation main sequence

Several observational tracers have been developed to measure a galaxy's SFR. The most widely used include: near-UV emission, tracing directly the emission of young stars: Hα emission (from photoionised HII regions, see Sec. 1.4.4); and far-infrared (far IR) emission, tracing the radiation absorbed and reprocessed by dust (see Kennicutt 1998; Kennicutt & Evans 2012 for comprehensive reviews of multi-wavelength tracers of the SFR).

In the local Universe Hα measurements from SDSS (combined with UV photometry from *GALEX* to better overcome the aperture effects caused by the small size of the SDSS spectroscopic fibre) have demonstrated that blue, star forming galaxies lie on a tight relation between SFR and stellar mass (Brinchmann et al., 2004; Renzini & Peng, 2015) of the form

$$SFR = \alpha \, M_\star^\beta, \tag{1.5}$$

where α is a normalisation factor and β lies in the approximate range 0.7 - 0.9 (Fig. 1.4, right). This relation is generally referred to as the star formation 'main sequence'[4] and only applies to star-forming galaxies, which are widely separated in SFR from quiescent, red-sequence galaxies.[5]

Works extending the study of star formation to the higher-redshift Universe (Bell et al., 2005; Noeske et al., 2007; Daddi et al., 2007) have demonstrated that the normalisation of the main sequence evolves with redshift, reaching a maximum at $z \sim 2$ (Lilly et al., 1996; Madau & Shull, 1996), possibly declining again at even higher redshifts. This evolution of the cosmic SFR is such that between $z \sim 2$ and $z = 0$ the SFR (at fixed stellar mass) has decreased at a steady rate by a factor of ~ 30 (Daddi et al., 2007).

The existence of the star formation main sequence and its redshift evolution suggest that star formation in the Universe is driven primarily by the smooth process of gas accretion. Indeed simulations suggest that direct accretion from the cosmic web dominates relative to mergers by about an order of magnitude (Wang et al., 2011; van de Voort et al., 2011). There is thus broad consensus that the elevated levels of star formation observed at high redshift can be explained by the higher accretion rate and cold gas content of galaxies in the early Universe (Bouché et al., 2010).

1.2.3 The quenching of star formation

The existence of a well-defined bimodality in the galaxy population suggests the need for a process, or set of processes, that cause the eventual shutdown of star formation on galactic scales (here generally referred to as *quenching*). This idea is confirmed by studies of galaxy colours at higher redshifts, which have revealed that the number of red galaxies has at least doubled since $z \sim 1$, while the number of blue galaxies has remained relatively constant (Bell et al., 2004; Bundy et al., 2006; Faber et al., 2007; Ilbert et al., 2010).

The physics that drives quenching is currently hotly debated, although it seems likely that the overall quenching rate can be subdivided into two broad categories of processes: a set of processes that is directly related to the large scale environment in which a galaxy is embedded (*environmental quenching*) and an independent set of processes related to the galaxy's stellar mass (*mass or internal quenching*). This nomenclature has been put forward by Peng et al. (2010) in a study based on SDSS and higher-redshift spectroscopic data. By using this large dataset Peng et al. (2010) empirically demonstrated that the fraction of galaxies on the red sequence can be written as a product of two independent factors, correlated respectively with environment and mass (Fig. 1.5, left). Below I discuss the physical processes that may be responsible for these two quenching channels.

Environmental quenching

As predicted by the ΛCDM cosmological framework, galaxies are found in a wide range of large scale environments, from pairs to groups to clusters. Rich clusters, which may contain hundreds of galaxies, host large amounts of hot gas due to their high virial temperatures, and can thus be observed via their bright emission in the X-ray band.

In the context of galaxy evolution, it has been known since the seminal work of Dressler (1980) that the properties of galaxies differ remarkably depending on the large scale environment they live

[4] Rather confusingly, since it does not have any relation to the main sequence of *stellar evolution*.

[5] For red sequence galaxies Hα-based SFRs generally provide only upper limits, sometimes misinterpreted as measurements in the literature.

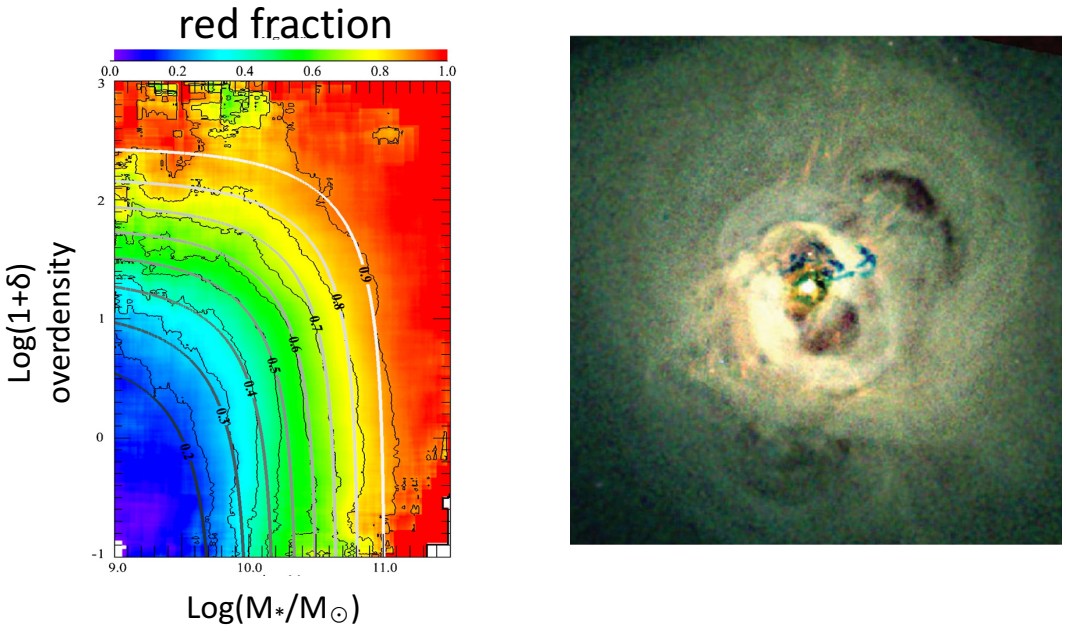

Figure 1.5: *Left*: The fraction of red sequence galaxies as a function of mass and environment (quantified via the overdensity parameter δ). The passive fraction increases as a function of both mass and environment, two processes that have independent and separable effects. From Peng et al. (2010). *Right*: The hot gas in the Perseus cluster core traced by X-ray emission, as observed by the *CHANDRA* satellite. Note the bubbles and shocks blown by the energy input from the central black hole. The energy flux in the sound waves is comparable to that required to offset cooling. From Fabian (2012).

in. In particular, spirals become rarer in higher density environments, while ellipticals become more common. With the advent of large spectroscopic surveys, it was confirmed that large-scale environment correlates well with morphology (e.g Bamford et al., 2009), but importantly also colour (Blanton et al., 2005b; Baldry et al., 2006; Peng et al., 2010) and gas content (Cortese et al., 2011; Boselli et al., 2014). This means that galaxies found in denser environments are more concentrated, redder and less gas rich.

Theoretically, when a satellite galaxy orbits a dark matter halo, it experiences tidal forces due to the combined potential of the central galaxy in the halo, other satellites and the halo itself. These tidal interactions can remove gas and stars from the galaxy, and potentially also alter its structure. Moreover, if the halo contains a hot gas component, the ISM in the infalling satellite galaxy will experience a drag force. If this force exceeds the satellite's gravitational pull, the ISM of the satellite can be lost to the hot halo in a process known as ram-pressure stripping (Gunn & Gott, 1972). The effects of this process in action can be observed as trails of HI (Chung et al., 2009) and ionised gas (Fumagalli et al., 2014; Poggianti et al., 2016).

Mass (or internal) quenching

Regarding the mass quenching regime, the observational picture is more complex. Several studies agree on the fact that the presence of a massive bulge is the single best observational parameter correlating with the probability of a galaxy to be passive (Pasquali et al., 2012; Cheung et al., 2012; Wake et al., 2012; Bluck et al., 2014). Since black hole mass is correlated to the bulge mass (Marconi & Hunt, 2003; Häring & Rix, 2004; McConnell & Ma, 2013), it can be expected that galaxies with more massive bulges experience a larger amount of energetic feedback from their black holes.

The details of the coupling between the black hole and its host galaxy are, however, not currently understood. As recently reviewed by Heckman & Best (2014), AGN appear as a bimodal population, which can be broadly divided into *radiative-mode* (including Seyfert galaxies and quasars) and *radio-mode* AGN. In the low redshift Universe, no direct correlation is observed between radiative-mode AGN and the shutdown of star formation, as radiative-mode AGN are often associated with the presence of star formation in the central regions of galaxies (inner few kpc). Radiative-mode AGN are observed to power large scale outflows (Maiolino et al., 2012; Cicone et al., 2014; Carniani et al., 2015) in both ionised and molecular gas, often at rates sufficient to starve the galaxy of cold gas on very short timescales. Theoretically, however, there is still considerable uncertainty on whether radiative-mode AGN feedback is capable of suppressing cooling on long timescales (Gabor & Davé, 2012; Choi et al., 2014; Somerville & Davé, 2015). Radio mode AGN, on the other hand, are observed to inflate large bubbles of hot gas in massive haloes (Fig. 1.5, right) and may thus play an important contribution in offsetting the cooling of the gas in the haloes of massive galaxies (McNamara & Nulsen, 2007; Fabian, 2012).

1.3 Chemical evolution and gas regulation in galaxies

Nuclear reactions during the first three minutes after the Big Bang resulted in a Universe which is composed primarily of hydrogen (~75%) and helium (~25%), with small amounts of lithium. All other heavier elements (*metals* in astronomical parlance) are produced by nuclear reactions in stars and are released into the ISM via stellar winds or supernova explosions. The *metallicity* (the mass fraction of metals) of a galaxy can in principle be calculated, provided sufficient knowledge of stellar nucleosynthesis, and assuming a history of star formation and gas flow (including inflows and outflows). In general, the aim of chemical evolution models is to solve the complex 'inverse' problem, and derive constraints on the star formation and gas flow history of galaxies from the measured chemical abundances.

1.3.1 The nucleosynthetic yield

Stellar nucleosynthesis

Perhaps the most fundamental ingredient in chemical evolution modelling is represented by the amount of mass of a given chemical element produced by a star of a certain mass and metallicity, the so-called stellar *yield*. Stellar yields are computed theoretically by following the thermodynamics and nuclear reactions in stellar interiors (see review by Nomoto et al. 2013). Despite several systematic uncertainties in these computations (often associated with the complex modelling of the late stages of stellar evolution), there is a general agreement between different authors on the mechanisms and the associated stellar mass ranges responsible for the production of different elements.[6] The case of nitrogen, however, represents a well-known exception, as its production mechanism is still a matter of current research (Sec. 1.3.4).

[6] A short review of the role of stars of different masses to the nucleosynthesis of different chemical elements can be found in Matteucci (2008). For detailed calculations of the stellar yields see Renzini & Voli (1981); van Den Hoek & Groenewegen (1997); Karakas (2010); Ventura et al. (2013) for low- and intermediate-mass stars ($0.8 < M_\star/M_\odot < 8$) and Woosley & Weaver (1995); Meynet & Maeder (2002); Kobayashi et al. (2006) for massive stars ($M_\star/M_\odot > 8$).

For the purposes of chemical evolution modelling, stars are assumed to enrich the ISM with metals at the moment of their death (even though some amount of metals may be lost during earlier phases of stellar evolution via stellar winds). Since stellar lifetimes depend strongly on the initial mass of the star, elements produced by stars in different mass ranges are released into the ISM on different timescales. Oxygen, for example, the most common metal, is primarily produced by high-mass stars dying as Type II supernovae, and is thus the classical example of a chemical element released into the ISM on short timescales. Given its abundance and its strong nebular lines in the optical wavelength range, oxygen has been long been the element of choice for studies of the chemical enrichment of the ISM in external galaxies.

The instantaneous recycling approximation

Tinsley (1980) proposed that the chemical evolution of elements that are readily released into the ISM, like oxygen, may be computed with great simplicity by adopting the so called 'instantaneous recycling approximation'. In this simplified framework one assumes that all stars more massive than $M_{long-lived}$ (generally assumed to be 1.0 $M_{\odot}$) die instantaneously, and those of lower masses live forever. One generally also assumes that the metals produced by the previous generation of stars are immediately and uniformly mixed with the pre-existing ISM.

If we denote the stellar yield[7] of oxygen as a function of mass as $\Pi(M)$, the mass of the stellar remnant generated by a star of mass M by M_r and the IMF (as defined in Eq. 1.3) as ϕ_{IMF} we may define two important quantities, the *return fraction* (R),

$$R = \int_{M_{long-lived}}^{M_{up}} dm\ (m - M_r)\ \phi_{IMF}(m), \tag{1.6}$$

and the *yield per stellar generation* (or average yield, y)

$$y = \frac{1}{1-R} \int_{M_{long-lived}}^{M_{up}} dm\ \Pi(m)\ m\ \phi_{IMF}(m), \tag{1.7}$$

where the IMF is normalised in mass, so that $\int_{M_{low}}^{M_{up}} dm\ \phi_{IMF}(m) = 1$. According to the above definitions, the return fraction is the fraction of mass promptly returned to the ISM by a stellar generation, while the yield per stellar generation is the ratio of the mass of oxygen newly produced and restored to the ISM by a simple stellar population to the amount of mass locked up in long-lived stars (as originally defined by Searle & Sargent 1972). One may define the yield per stellar generation also by normalising to the total mass of gas taking part in star formation, which we denote as p and is trivially related to y by $y = p/(1-R)$.

Both the average yield and the return fraction are a function of the IMF and, in general, also depend on metallicity and time. In the context of modelling the chemical evolution of oxygen, the metallicity dependences of R and y are generally neglected, since the oxygen yield is shown to be approximately independent of metallicity and the effect of stellar lifetimes on the return fraction can be considered negligible for most purposes (Thomas et al., 1998; Kobayashi et al., 2006; Zahid et al., 2012; Vincenzo et al., 2016b).

The dependence of the yield per stellar generation on the IMF, on the other hand, is found to be significant (Henry et al., 2000). In Vincenzo et al. (2016b), for example, we find that the yield per

[7] The stellar yield is defined as the amount of *new* oxygen formed by the star of mass M.

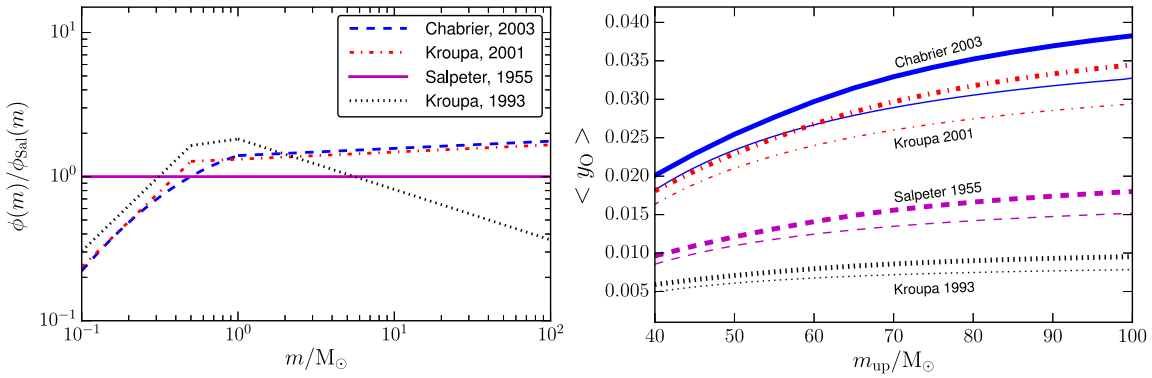

Figure 1.6: *Left*: The relative number of stars of different masses, with respect to the Salpeter (1955) IMF ($\phi_{\rm IMF}/\phi_{\rm IMF,Salpeter}$). The Kroupa et al. (1993) IMF contains less massive stars than Salpeter, while both Kroupa (2001) and Chabrier (2003) contain more. *Right*: The change in the oxygen yield per stellar generation ($< {\rm y_O} >$) as a function of the upper-mass IMF cutoff ($\rm M_{up}$). The thick lines corresponds to the stellar yields of Romano et al. (2010) while the thin lines represent the Nomoto et al. (2013) yields. From Vincenzo et al. (2016b).

stellar generation can vary by a factor larger than three for the same choice of stellar yields, if the IMF is changed from Kroupa et al. (1993) to Chabrier (2003). The large variation is due to the fact that the Chabrier IMF assumes a larger fraction of massive stars than Salpeter or Kroupa 1993. For the same reason, a change to the upper-mass cutoff of the IMF ($\rm M_{up}$) also has an effect on the average oxygen yield. The effect is more pronounced for the IMFs which put a larger fraction of mass in massive stars, like Chabrier (see Fig. 1.6, right).

1.3.2 The fundamental equations of chemical evolution

Within the instantaneous recycling approximation, denoting the oxygen fraction (by mass) in the ISM as $\rm Z_g$, the gas mass as $\rm M_g$, the star formation rate as SFR, the stellar mass as $\rm M_\star$, the total mass in oxygen in the galaxy as $\rm M_Z$, the mass of oxygen in the ISM as $\rm M_{Zg}$, the outflow rate as Ψ and the inflow rate as Φ, the galaxy's chemical evolution is described by the following set of constitutive equations

$$\frac{{\rm dM_g}}{{\rm dt}} = \Phi - (1 - {\rm R})\ {\rm SFR} - \Psi, \tag{1.8}$$

$$\frac{{\rm dM_\star}}{{\rm dt}} = (1 - {\rm R})\ {\rm SFR}, \tag{1.9}$$

$$\frac{{\rm dM_{Zg}}}{{\rm dt}} = \frac{{\rm d(M_g\ Z_g)}}{{\rm dt}} = {\rm p\ SFR} - \Psi {\rm Z_g} - (1 - {\rm R})\ {\rm Z_g\ SFR}, \tag{1.10}$$

and

$$\frac{{\rm dM_Z}}{{\rm dt}} = {\rm p\ SFR} - \Psi {\rm Z_g}. \tag{1.11}$$

By combining Eq. 1.10 with 1.9 we obtain a general relation for the time evolution of metallicity

$$\frac{{\rm dZ_g}}{{\rm dt}} = \frac{1}{\rm M_g}({\rm p\ SFR} - {\rm Z_g}\ \Phi). \tag{1.12}$$

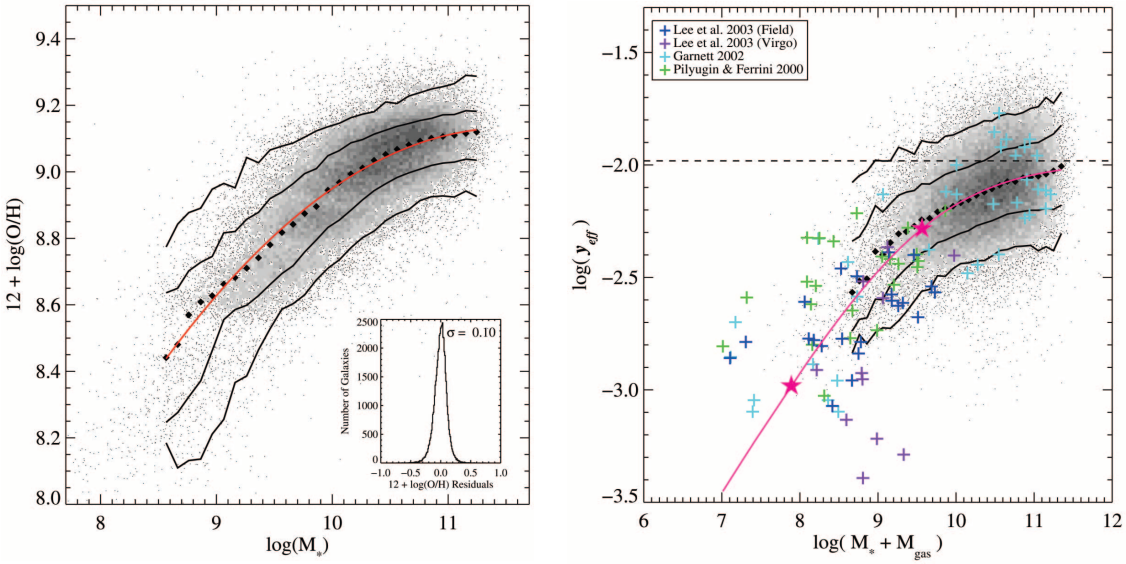

Figure 1.7: *Left*: The relation between stellar mass and gas phase metallicity for ∼ 50000 star-forming galaxies in SDSS. The large diamonds represent the median metallicity in 0.1 dex mass bins. The solid lines enclose 68% and 95% of the data, while the red line is a polynomial fit to the median relation. The inset shows the fit residuals. *Right*: Effective yield (as defined in Eq. 1.14) as a function of the total baryonic mass (stars + gas) for the same sample of SDSS galaxies. The gas masses are obtained by inverting the Schmidt-Kennicutt law, with SFR estimated from Hα. Diamonds and solid lines are defined in the same way as in the left panel. Coloured symbols are taken from the literature as detailed in the legend. The dashed line represents the theoretical yield, while the pink stars represent the position of galaxies that have lost 50% and 90% of their metals respectively. From Tremonti et al. (2004).

The closed-box model

By combining Eq. 1.8 and 1.12 it can be trivially shown that, in the case of 'closed box' evolution, i.e. no inflow and no outflow ($\Phi = 0$ and $\Psi = 0$), the gas metallicity is given by

$$Z_g = \frac{p}{1-R} \ln\left(f_{gas}^{-1}\right) = y \ln\left(f_{gas}^{-1}\right), \tag{1.13}$$

where $f_{gas} \equiv M_g/(M_g + M_\star)$ is the gas fraction. Some authors find it convenient to define the so-called 'effective yield' as

$$y_{eff} \equiv \frac{Z_g}{\ln\left(f_{gas}^{-1}\right)}. \tag{1.14}$$

This definition is advantageous because the effective yield is an observable quantity which can be directly compared with the theoretical yield. Moreover it has been demonstrated (Edmunds, 1990) that the presence of outflows and pristine gas inflows causes a decrease in the effective yield. Hence an observed offset between the theoretical and the effective yield points to the importance of gas flows in galaxies.

The first unambiguous evidence against the closed-box model came from observations of the metallicity distribution of stars in the Milky Way: the classical G-dwarf problem (Schmidt, 1963; Lynden-Bell, 1975). In short, there is a deficit of sub-solar metallicity G-dwarf stars in the solar neighbourhood with respect to the prediction from a closed-box model. This problem can be solved assuming a continuous inflow of metal-poor gas. In the next section I will explore the evidence for deviations from the closed-box model in the overall galaxy population.

1.3.3 Gas regulation in galaxies

Observations of abundances in external galaxies demonstrate the existence of a tight relation between luminosity or stellar mass and metallicity (the mass-metallicity relation, Lequeux et al. 1979; Tremonti et al. 2004). The effective yield measured in galaxies or inferred from this scaling relation is found to be lower than the theoretical yield (Matteucci & Chiosi, 1983; Edmunds, 1990; Vila-Costas & Edmunds, 1992; Garnett, 2002; Tremonti et al., 2004), especially for low-mass, high gas fraction systems (Fig. 1.7).

More recently Mannucci et al. (2010) and Lara-López et al. (2010) have argued in favour of the existence of a secondary dependence of the mass-metallicity relation on SFR. The observed correlation goes in the sense that galaxies of a fixed stellar mass have lower metallicity when they have higher SFR, or gas mass (Hughes et al., 2013; Bothwell et al., 2013).

These observations have motivated the development of a set of simple analytical models generally referred to as 'gas regulatory' or 'bathtub' models (Bouché et al., 2010; Finlator & Davé, 2008; Dayal et al., 2013; Dekel et al., 2013; Lilly et al., 2013; Peng & Maiolino, 2014). In these models the traditional closed-box approach is extended to simultaneously take into account inflows and outflows, with various degrees of detail.

General properties of bathtub models

In an 'ideal' bathtub model, together with Eqs. 1.8–1.11, one generally assumes:

1. A linear star formation relation, SFR = ε M_g, with constant (or slowly varying) star formation efficiency (SFE) ε.

2. Outflow rate proportional to the SFR through a constant (or slowly varying) loading factor λ: $\Psi = \lambda$ SFR.

The simplest bathtub models are 'equilibrium' models (Finlator & Davé, 2008; Davé et al., 2011), which assume that the gas mass in the system does not change with time ($dM_g/dt = 0$). This assumption is justified by Davé et al. (2011) on grounds of its relevance to cosmological hydrodynamical simulations. Assuming equilibrium Eq. 1.8 reduces to

$$\Phi = (1 - R + \lambda)\ \mathrm{SFR} \quad \text{(in equilibrium)}. \tag{1.15}$$

Under these assumption at late times equation 1.12 reduces to

$$Z_g = \frac{p}{1 - R + \lambda} \quad \text{(in equilibrium)}, \tag{1.16}$$

which is remarkably similar to the closed-box solution (Eq. 1.13), but with the theoretical yield now replaced by a combination of the yield and the outflow loading factor. Finlator & Davé (2008) argue that Eq. 1.16, combined with a suitable mass-dependent outflow loading factor λ, can be used to successfully reproduce the shape of the mass-metallicity relation. In particular, at high masses the flattening of the mass-metallicity relation can be explained assuming $\lambda \to 0$, as expected for the most massive systems. At low masses, in order to reproduce the observed relation (which goes roughly as $Z \propto M_\star^{-0.3}$), one requires a loading factor $\lambda \propto M_\star^{-0.3}$, in rough agreement with theoretical modelling of (momentum-driven) stellar winds.

These simple models also successfully predict that a temporary departure from equilibrium generates a secondary dependence of the mass-metallicity relation on SFR (Finlator & Davé, 2008; Davé et al., 2011; Dayal et al., 2013). This is because a galaxy experiences an increase in its SFR and a decrease in its metallicity, due to dilution, whenever an increase in accretion takes place. This behaviour is independent of the detailed time evolution of the cosmological inflow rate, about which we have made no assumptions.

Despite these successes, Lilly et al. (2013) have highlighted that equilibrium may be a good assumption for gas-poor, chemically evolved, low-redshift galaxies, while it is not a good assumption for gas-rich dwarfs or galaxies at high redshift (see in particular Sec. 2.3 and 2.4 of Lilly et al. 2013 for a detailed discussion of the relevant timescales and Sec. 5 of Peng & Maiolino 2014 for an estimate of the equilibrium timescale for gas rich systems). Without assuming equilibrium, one may still obtain time-dependent solutions to the constitutive equations of the gas regulatory model, provided the time evolution of the accretion rate is specified.

Modelling the accretion rate

The simplicity of the framework offered by the bathtub model has encouraged several authors to seek analytical solutions for its fundamental equations. Unfortunately, if we do not assume the system is in equilibrium, the relation between metallicity and gas fraction (which can be interpreted as a natural 'clock' in the context of chemical evolution) will depend on the assumed time evolution of the inflow rate.

A notable special case is represented by the solutions obtained if one assumes the inflow rate to be proportional to the SFR (Matteucci & Chiosi, 1983; Recchi et al., 2008; Dayal et al., 2013; Kudritzki et al., 2015). This assumption is widely used because it leads to the simplest example of a non-equilibrium model which has a closed-form analytical solution for the relation between metallicity and gas fraction. The solutions of this model (summarised in Sec. 6.5.1) reach equilibrium at late times, as is generally the case in all non-equilibrium bathtub models, and correctly predict a secondary dependence of the mass-metallicity relation on the SFR (Dayal et al., 2013). However, while the other assumptions made in the context of the bathtub model may be justified, albeit approximately, on physical or observational grounds, there is no theoretical or observational reason to believe that the inflow rate should follow the same time evolution as the SFR.[8]

Although the dark matter accretion rate is stochastic on short timescales, simulations have determined that it follows a well-defined relation with mass and redshift of the form

$$\frac{dM_h}{dt} = \alpha M_h (1+z)^{\beta}, \tag{1.17}$$

where M_h is the halo mass and $\alpha \sim 0.030$ Gyr^{-1} and $\beta \sim 2.5$ (Dekel et al., 2013). For an Einstein-de-Sitter universe the Eq. 1.17 admits a particularly simple solution leading to

$$\dot{M}_h(z) = 0.03\ M_i\ e^{-a(z-z_i)}(1+z)^{2.5}. \tag{1.18}$$

where M_i is the mass of the halo at redshift z_i and $\dot{M}_h$ is the dark matter accretion rate at redshift z.

[8] Confusion often arises in the literature because, in equilibrium, all bathtub models predict the time evolution of the SFR to the follow that of the inflow rate (as in Eq. 1.15). However, this conclusion is only true when the system has reached equilibrium.

This analysis demonstrates that the halo accretion rate does not evolve very much over most of the age of the Universe (Dekel et al., 2013; Lilly et al., 2013). In particular, it changes by about a factor of 2 between z = 5 and 0.3. I neglect here the fact than only a fraction of the accreting baryons will reach the galaxy disc and are available for star formation, and this fraction might be a complex function of mass, redshift and perhaps other quantities (environment). Under these assumptions, Peng & Maiolino (2014) argue that the inflow timescale is much longer than all other timescales relevant to galaxy evolution and, therefore, it is an excellent approximation to assume the gas inflow rate to be constant in time. Assuming a constant inflow rate, Peng & Maiolino (2014) demonstrated that one can define a natural timescale for the chemical evolution of the system (the equilibrium timescale, τ_{eq}), given by

$$\tau_{\rm eq} \equiv \frac{1}{\varepsilon\,(1-{\rm R}+\lambda)}. \tag{1.19}$$

For t >> $\tau_{\rm eq}$ the system tends to the equilibrium metallicity given by Eq. 1.16. Exact analytical solutions for the time evolution of metallicity and other fundamental quantities in this model are presented for the first time in Belfiore et al. (2016) (Sec. 6.2.1).

Another possible way of modelling the accretion rate, widely used in the literature to model the metallicity gradient of the Milky Way, is to assume an exponential decrease with time. As discussed in more detail in Sec. 5.6.1, chemical evolution models aimed at reproducing the metallicity gradient in the Milky Way generally need to assume a faster assembly time for the inner disc, in order to mimic the theoretical expectation of inside-out growth. The standard procedure to implement inside-out growth in these models is to assume an exponentially declining accretion rate, with an infall timescale (τ_{inf}) which increases with galactocentric radius (Chiosi, 1980; Matteucci & Francois, 1989; Boissier & Prantzos, 1999; Chiappini et al., 2001; Weinberg et al., 2016). In the formalism of this section, this means assuming $\Phi = \Phi_0\ \exp(-{\rm t}/\tau_{\rm inf})$.

Recently Spitoni et al. (2016) have presented analytical solutions for this model and successfully applied it to the mass-metallicity relation. Rather interestingly, it can be demonstrated that the analytical solutions presented in Spitoni et al. (2016) assume the exact same functional form as the solutions for the constant infall case I presented in Belfiore et al. (2016)[9] if one replaces τ_{eq} with a new timescale $\tau_{\rm c}$ given by $\tau_{\rm c} = (\tau_{\rm eq}^{-1} - \tau_{\rm inf}^{-1})^{-1}$.

1.3.4 The chemical evolution of nitrogen

Since different chemical elements are released into the ISM on different time-scales, the study of abundance ratios of some key elements can provide more information on the gas flow and star formation history of a galaxy than the study of the abundance of one chemical species. For example, it has long been known that the [O/Fe] ratios in elliptical galaxies are consistent with the paradigm requiring these objects to form stars vigorously over a short time-scale at high redshift (Matteucci, 1994; Bernardi et al., 2003; Thomas et al., 2005, 2010). Unfortunately only a limited number of abundance ratios are readily accessible from optical spectroscopy of the ISM in nearby galaxies (see Sec. 1.4.2). In this thesis, therefore, I focus on one easily accessible abundance ratio of particular interest: the N/O ratio.

[9] This so far unpublished realisation was reached during a very fruitful week of discussions with my collaborator F. Vincenzo. This link between the formalism of bathtub models and that of models describing the chemical evolution of resolved regions in discs is particularly interesting, and will be explored in future work.

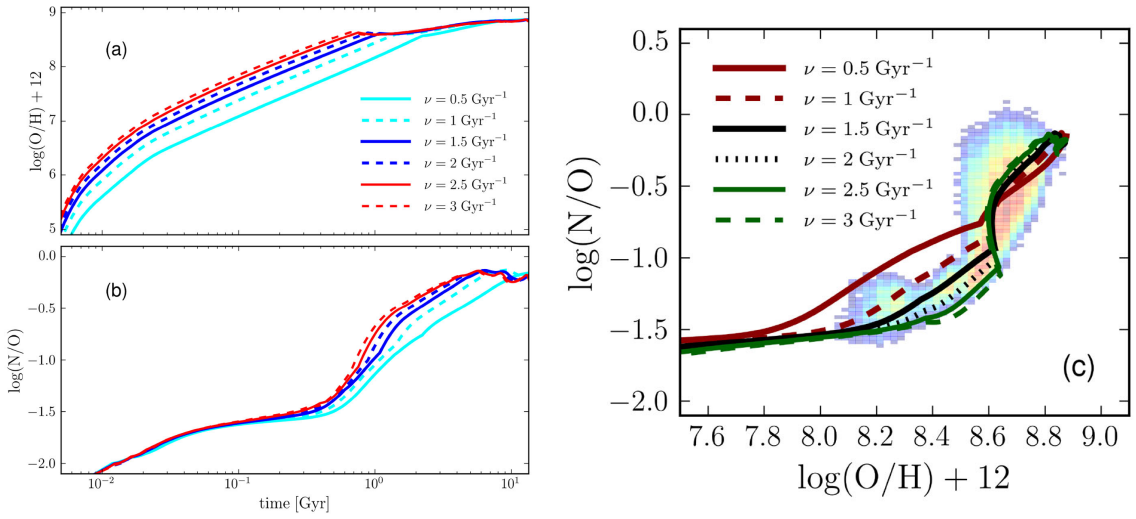

Figure 1.8: *Left*: The time evolution of the O/H (a) and N/O (b) ratios as a function of time for different SFEs (labelled ν in the figure). *Right*: The behaviour of model tracks in the O/H versus N/O plane for different SFEs (ν) superimposed on the locus occupied by star forming galaxies from SDSS (coloured contours). From Vincenzo et al. (2016a).

Elements like oxygen, carbon and sulphur have a primary nucleosynthetic origin, i.e. their nucleosynthetic yield is approximately independent from the amount of heavy elements already present in the galaxy. The nucleosynthetic origin on nitrogen, on the other hand, is more complex. It is predicted that in the low-metallicity regime most of the nitrogen has a primary origin and is generated in massive stars (Matteucci, 1986), although this inference remains controversial to date. This is because the computation of the nitrogen stellar yields for massive stars still suffers from large uncertainty, especially at very low metallicity, and none of the existing stellar evolutionary codes are able to provide the right amount of primary nitrogen, which is needed to reproduce the observed N/O plateau at very low metallicities. At higher metallicity nitrogen becomes a secondary nucleosynthetic product (i.e. the yield is proportional to the amount of heavy elements already present in the galaxy), since production of nitrogen depends on the previous amount of oxygen (and carbon) synthesised in stars via the CNO cycle. Moreover, since nitrogen is primarily produced by intermediate mass stars, it probes longer enrichment timescales relative to oxygen, which is promptly produced by short-lived massive stars.

Observations of single HII regions (Garnett, 1990; Nava et al., 2006; Berg et al., 2012) and data from large spectroscopic surveys of galaxies like SDSS show a constant N/O ratio (log(N/O) ~ -1.5) as a function of O/H ratio at low metallicity, and a superlinear slope for higher metallicity, where nitrogen production becomes secondary (Fig. 1.8, right, Edmunds & Pagel 1978; Vila-Costas & Edmunds 1993; Henry et al. 2000; Pérez-Montero & Contini 2009; Andrews & Martini 2013; Wu & Zhang 2013; Vincenzo et al. 2016a).

Given the different timescales for the release of oxygen and nitrogen into the ISM, the position of galaxies in the N/O versus O/H plane is sensitive to the timescale over which star formation has been occurring in galaxies. In Vincenzo et al. (2016a), for example, we used a chemical evolution model to follow the time-dependent evolution of oxygen and nitrogen (Fig. 1.8). This model assumes an exponential infall timescale, includes a treatment of outflows and takes into account the effect of stellar lifetimes. In this model, the timescale of star formation is determined by the assumed star formation efficiency (SFE = SFR/M_g, labelled ν in Fig. 1.8). The higher the SFE, the higher the

oxygen content in the galaxy at the moment when the first intermediate-mass stars die and secondary nitrogen production starts. Equivalently, at fixed metallicity, higher N/O tracks correspond to lower SFE. Importantly, the relation between O/H and N/O can in principle also be used to diagnose pristine gas inflows (Köppen & Hensler, 2005). In the case of truly pristine (zero metallicity) gas inflow, O/H would decrease but the N/O ratio remains unaffected. This effect is still evident in case of dilution by metal-poor gas which is not completely pristine (Belfiore et al., 2015).

1.4 Probing the ISM of galaxies via optical spectroscopy

The subject of this thesis is the study of SFR, excitation conditions and chemical abundances in nearby galaxies. I primarily exploit a set of diagnostics of the ionised interstellar medium available in the optical wavelength range, which are discussed in this section. The effect of interstellar dust on the study of emission lines is also briefly addressed here (Sec. 1.4.4).

While this dissertation is primarily focussed on the study of nebular line emission, the underlying emission of the stellar component in galaxies cannot be neglected. Stellar absorption features are not only a contaminant to accurate measurement of the line emission, but offer a wide range of probes of the age and metallicity of the underlying stellar population. Moreover, stellar emission shortward of the Lyman limit ($\lambda < 912$ Å) is the energy source of observed line emission, which depends sensitively on the assumed stellar spectrum at those wavelengths. Thus, the modelling and interpretation of emission lines properties in galaxies relies crucially on accurate stellar population models. Despite their importance, a discussion of the methodology and systematics involved in stellar population modelling is beyond the scope of this dissertation. The interested reader is referred to a recent review of the field by Conroy (2013).

1.4.1 HII region models

The energy source that allows HII regions to shine is UV light from massive O- or B-type stars. These hot stars emit copious amounts of ionising photons, which lead to photoionisation of hydrogen, the nebula's main constituent. Ionisation events by photons more energetic than the Lyman limit leave hydrogen ions with excess kinetic energy, which is rapidly thermalised by collisions with electrons and other ions. The resulting temperature distribution approaches a Maxwellian (but see Dopita et al. 2015), with typical nebular temperatures in the range 5000 K $< T_e <$ 20000 K.

Collisions of ions with thermal electrons may lead to electronic excitation. At typical nebular temperatures, hydrogen does not have readily accessible energy levels. Heavy elements, on the other hand, generally have low-lying energy levels corresponding to fine structure splitting (giving rise to IR lines). Transitions of energies of a few eV give rise to optical lines, including the most recognisable nebular lines of oxygen, nitrogen and sulphur[10], such as [OIII] $\lambda\lambda$4959,5007, [NII] $\lambda\lambda$6548,6583 and [SII] $\lambda\lambda$6717,6731. These lines are forbidden, as they cannot proceed via an electric dipole transition, and are therefore not re-absorbed within the nebula once they are emitted, thus contributing to cooling.

In a spherically symmetric nebular model, one may define a region of space inside which the photoionisation and recombination rates are balanced in thermal equilibrium (the Strömgen sphere).

[10] Forbidden lines are denoted by the name of the ion in square bracket followed by the wavelength of line emission (e.g. [OIII] λ5007). Permitted lines are denoted without brackets (e.g. HeI λ5875). Recombination lines are denoted by the name of the *recombined* species (e.g. HeI is emitted by the recombination of He^+).

Inside this region, the nebula is highly ionised. Cooling in the nebula takes place via a combination of line emission (mostly by collisionally excited metal ions) and continuum emission (via both free-free and free-bound emission). In nebulae of metallicity $Z/Z_{\odot} > 0.1$, the total cooling rate is largely dominated by line emission by collisionally excited metal ions. Because of the relation between metal lines and cooling in this regime, scaling up the metallicity of the nebula increases the cooling rate and lowers the nebular temperature.

The recombination spectrum of hydrogen

Ionisation equilibrium in the nebula is maintained by recombination events. The recombined species is generally left in a excited state, which decays to lower excited states (and eventually all the way to the ground state) by radiative transitions. This cascade process causes nebulae to emit prominently in the recombination lines of hydrogen (e.g. the Balmer series in the optical and the Paschen series in the near-IR) and helium. Recombination lines of metals ions are also emitted, but given their lower abundances they are weaker by several orders of magnitude, and generally undetectable in extragalactic sources.

The recombination spectrum of hydrogen is of particular importance because the relative ratios of the lines involved in the recombination cascade can be accurately modelled, from knowledge of the recombination cross section and relative transition probabilities. These ratios are only weakly dependent on the nebular temperature, but are influenced by the optical thickness of the nebula to Lyman series radiation. Two extreme cases can be considered, *case A* (optically thin nebula) and *case B* (optically thick nebula), which differ in the way recombinations to the ground level are treated. While in case A Lyman series radiation is free to escape the nebula and contribute to the observed spectrum, in case B Lyman radiation is assumed to be re-absorbed within the nebula, and lead to further ionisation. For typical HII regions, case B recombination is generally considered a more realistic assumption.

The structure of model nebulae

The intensity of the ionising spectrum incident onto the gas is generally quantified by defining a dimensionless *ionisation parameter*,

$$U(r) = Q/(4\,\pi\,r^2\,n_e\,c), \tag{1.20}$$

where Q is the rate of ionising photons emitted by the source, r is the distance between the gas and the source and n_e is the electron density. The ionisation parameter can be thought of the number of ionising photons per hydrogen atom.[11] The ionisation parameter, the chemical abundance of the gas and ionising stellar spectrum constitute the three parameters which determine the ionisation and temperature structure of the nebula. Model structures of ionised nebulae may be computed for different assumptions regarding these parameters via specialised photoionisation codes (e.g. CLOUDY, Ferland et al. 2013, MAPPINGS, Sutherland & Dopita 1993).

By solving for the structure of the nebula, one may determine which region of the nebula each emission lines originates from. High ionisation species, for example, originate from the inner regions

[11] Note that some authors (Kewley & Dopita, 2002; Levesque et al., 2010) define the ionisation parameter in units of cm s^{-1} as $q = Uc$.

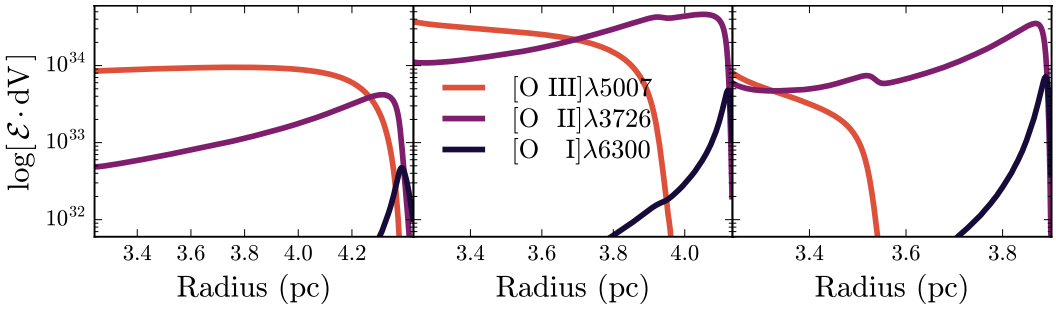

Figure 1.9: A model nebula calculated using the photoionisation code CLOUDY, with metallicity increasing from left to right and given by $\log(Z/Z_\odot)$= -1.0, -0.3, 0.0. The total emissivity of three oxygen transitions as a function of radius is shown. The model assumes logU = -2.5, and the input ionising spectrum is that of a 3 Myr simple stellar population (from FSPS, Conroy et al. 2009). As the metallicity increases, the nebular temperature decreases and the fraction of the nebula that emits in [OIII] also decreases. From Byler et al. (2016).

of the nebula, while low ionisation species come from the outskirts. The spectral shape of the ionising radiation determines the extent of the high-ionisation zone, but also the prevalence of partially ionised regions. In the next section I discuss some common diagnostics for nebular properties like temperature and density. It is important, however, to keep in mind that different regions *within* the nebula emit different lines. Hence diagnostics from particular ionic species may only trace the physical conditions of a specific part of the nebula (Fig. 1.9).

Nebular diagnostics: temperature and density

Suitable emission line ratios can be used as diagnostics of the temperature and density of the nebula.[12] In particular, the temperature of the nebula can be obtained by considering the ratio between lines emitted by a single ion from two energetically accessible levels with a difference in energy $\Delta E \sim k_B T_e$. A good temperature diagnostic should also not depend on density, which can be achieved by choosing transitions with high critical densities.[13] In the optical wavelength range [OIII] and [NII] are some of the most widely used ions with appropriate transitions. In this context, the weaker [OIII] λ4363 line is referred to as *auroral*, while the generally stronger [OIII] λ5007 line is referred to as *nebular*. Similar nomenclature is utilised for equivalent transitions for other species with equivalent electronic configuration. The ratios of auroral to nebular lines (such as [OIII] λ4363/[OIII] λ5007 or [NII] λ5755/[NII] λ6584) are sensitive to the electron temperature and roughly independent of density in the low-density regime.

[OIII] and [NII] emission probes different temperature zones within the nebula. [OIII] is mostly emitted in the high-ionisation zone, while [NII] emission origins from the low-ionisation zone, which also emits in [SII] and [OII]. Determination of electron temperature for the different ionisation zones is important in the context of determining chemical abundances. In this context, the abundances of all ionisation states of a specific element need to be accounted for. Moreover, even when considering ions which are predicted to originate from the same zone, several authors have found considerable temperature discrepancies (Kennicutt et al., 2003b; Bresolin et al., 2005; Esteban et al., 2009; Pilyugin

[12] See Osterbrock & Ferland (2006), chapter 5, and Draine (2011), chapter 18, for detailed discussions of this classical problem.

[13] The critical density is the density where the collisional de-excitation rate equals the radiative de-excitation rate. In a two-level model atom, at densities higher than critical the upper level is depopulated by collisional rather than radiative de-excitation.

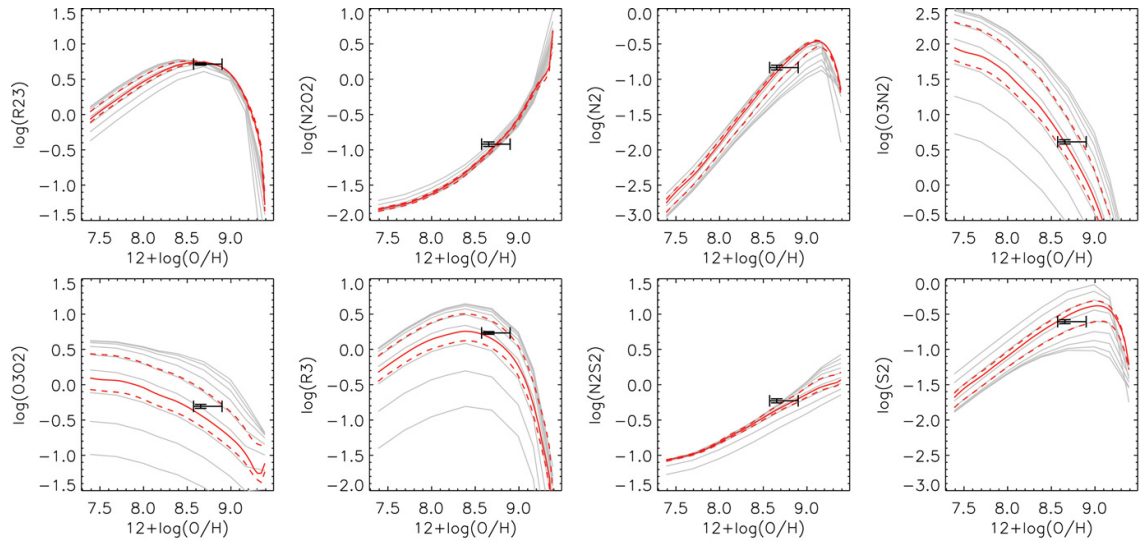

Figure 1.10: Examples of the relation between different strong line diagnostics as a function of metallicity derived from photoionisation models of Dopita et al. (2013). The different lines correspond to different values of the ionisation parameter. An example datapoint and associated uncertainty is shown in black, with the red lines corresponding to the best fit model (solid) and 1σ confidence limits (dashed). The double-valued nature of the R23 diagnostic is evident in the top-left panel. The N2O2 diagnostic is mostly insensitive to the ionisation parameter as shown in the second panel of the top row. O3N2, on the other hand, has a strong dependence on the ionisation parameter as evident from the right-most top panel. From Blanc et al. (2015).

et al., 2009; Binette et al., 2012; Berg et al., 2015). The physical cause for these discrepancies is not yet fully understood, but temperature inhomogeneities, chemical inhomogeneities and shocks may all be contributing factors.

Electron density in a nebula may be probed by collisionally excited lines that arise from levels of similar excitation energies, but with different radiative transition probabilities. These ratios are sensitive to the electron density in the density range around the critical density, while saturating in both the high- and low-density regimes. In the optical the ratio [SII] λ6717/[SII] λ6731 is the most widely used indicator and is sensitive to density variations in the range $n_e \sim 10^2 - 10^4$ cm^{-3}. The [OII] λ3729/[OII] λ3726 ratio is also a density tracer, however at medium spectral resolution, like in SDSS spectroscopy, the two lines are blended. In this thesis, and sometimes in the literature, the blend of these two lines is referred to [OII] λ3727. This is somewhat of a misnomer since it does not strictly abide to the conventional rule for labelling doublets.

1.4.2 The determination of chemical abundances

The T_e method

The most reliable way to measure gas phase oxygen abundance, at least in the sub-solar regime, is by determining the electron temperature of the nebula (the so-called T_e method, Pagel et al. 1992; Izotov et al. 2006) via detection of weak auroral lines (i.e. [OIII] λ4363, [NII] λ5755). Several auroral lines can be used to solve for the full structure of the nebula. If only one auroral/nebular ratio is available, the physical conditions of the other zones can be inferred from theoretical relations derived from photoionisation models (Garnett, 1992). The reliability of the T_e method, however, has been questioned in the high-metallicity regime, because of the possible effect of density and temperature fluctuations (Peimbert, 1967; Stasińska, 2005). The strong dependence of the auroral line emissivity

on temperature disproportionally enhances auroral with respect to nebular lines. This biases the overall temperature measurement high, and leads to an underestimate of the true abundance.

Strong line calibrators

Auroral lines are generally too weak ($\sim 100 - 1000$ times fainter than Hβ) to be detectable at solar metallicity and above with the typical sensitivity of large spectroscopic surveys, like SDSS, or in the high-redshift Universe. Several authors have therefore calibrated ratios of strong nebular lines to serve as metallicity tracers. These line ratios are only indirect metallicity tracers, as they are generally also influenced by the ionisation parameter, or changes in abundance ratios, if they consist of ratios between lines of different chemical species. In practice, however, they work quite well since in real HII regions these parameters are correlated (Kewley & Dopita, 2002; Levesque et al., 2010).

One of the most commonly used strong line metallicity diagnostics is the R23 index (Pagel et al., 1979; Pilyugin & Thuan, 2005), defined as

$$\mathrm{R23} = (\mathrm{[OII]}\ \lambda 3727 + \mathrm{[OIII]}\ \lambda\lambda 4959, 5007)/\mathrm{H}\beta. \tag{1.21}$$

In this definition, and others presented in this section, the required line ratios are assumed to have been corrected for the effect of interstellar extinction (see Sec. 1.4.4). The R23 ratio effectively measures the total cooling rate due to the brightest oxygen optical lines, and is thus expected to be sensitive to the nebular temperature. However, the relationship between this diagnostic and metallicity is double valued (see Fig. 1.10, top left panel). At low metallicity the cooling due to oxygen increases with chemical abundance. At higher metallicity, however, the temperature becomes too low for efficient excitation of the optical forbidden lines. In this regime, cooling proceeds instead via the fine-structure IR lines. Similar double-valued behaviour is exhibited by the S23 = ([SII] $\lambda\lambda$6717,6731 + [SIII] $\lambda\lambda$9069,9532)/Hβ diagnostic (Vílchez & Esteban, 1996), much less commonly used than R23 because optical surveys rarely cover the redder [SIII] lines. The double-valued nature of these calibrators implies that measurements of other line ratios are needed in order to choose the correct branch. In practice, this becomes difficult at intermediate metallicity, where the two branches merge, thus causing a large increase in the uncertainties associated with these calibrators in that metallicity regime.

Examples of other strong line diagnostics, which do not suffer (or do so only minimally) from this double-valued behaviour, include O3N2 = ([OIII] λ5007/Hβ)/([NII] λ6583/Hα), N2=[NII] λ6583/Hα (Alloin et al., 1979; Pettini & Pagel, 2004) and N2O2 = [NII] λ6548,6583/[OII] λ3727 (Kewley & Dopita, 2002). As further discussed in the next paragraphs, these line ratios are also sensitive to the relative N/O abundance ratio.

Strong line diagnostics have to be calibrated either empirically, via samples of HII regions with abundances measured by the T_e method, or theoretically, by making use of grids of photoionisation models. The choice of which methodology to use has a direct impact on the inferred oxygen abundance, as calibrators based on photoionisation models predict oxygen abundances that are $\sim$ 0.2-0.3 dex larger than those based on T_e-derived abundances (Kewley & Ellison, 2008; López-Sánchez et al., 2012). The underlying cause of this discrepancy is still hotly debated in the literature (Stasińska et al., 2006; Peña-Guerrero et al., 2012; Blanc et al., 2015), and may lie in deficiencies of the photoionisation models or in the problems associated with auroral line abundance determinations at high metallicity (as discussed above).

Moreover, strong line calibrators have different dependences on the ionisation parameter. This dependence can be taken into account by using a recursive technique (McGaugh, 1991; Kobulnicky & Kewley, 2004), can be minimised by choosing line ratios which are less sensitive to this effect (see Fig. 1.10), or can be explicitly marginalised over by making use of a fully Bayesian approach (Blanc et al., 2013b; Asari et al., 2016). Finally, as can be seen in Fig. 1.10, some strong line ratios, like O3O2=[OIII]λ5007/[OII]λ3727 (and partially also R3=[OIII]λ5007/Hβ), are good tracers of the ionisation parameter. Their relationship to metallicity is, therefore, only very indirect, and their use as metallicity diagnostics ought to be best avoided.

Two example strong line diagnostics: O3N2 and R23

In light of the discussion in the previous subsection, in this thesis I primarily use two strong line metallicity calibrations, based on different diagnostic ratios: O3N2 and R23. This choice is dictated by a desire to assess the systematic uncertainty introduced by the choice of calibration, without digressing in a detailed analysis of the merits and shortcomings of every one of the metallicity calibrations presented in the literature. Below I briefly discuss the two adopted calibrators in turn.

1. The Pettini & Pagel (2004) (PP04) metallicity calibration, based on the O3N2 index, has the advantage of varying monotonically with metallicity. It also relies on line ratios which are close in wavelength, thus minimising the uncertainty due to the extinction correction or imperfections in the flux calibration. The calibration is empirical in nature and is anchored to the abundances of 137 HII regions (of which 6 are derived by detailed photoionisation models, and the others via the T_e method). It suffers from a possible systematic uncertainty in the calibration in the super-solar metallicity regime. It should also be noted that, since [NII] and [OIII] originate from ions with a large difference in ionisation potential, this diagnostic ratio is systematically affected by variations in the ionisation parameter (see for example Blanc et al. 2015, Fig. 1.10), which are not calibrated. Moreover, the calibration assumes a one-to-one relation between the nitrogen and oxygen abundance, which is not necessarily a good assumption in the presence of a complex star formation history or gas flows (Sec. 1.3.4). Alternative calibrations of this diagnostics are presented by Marino et al. (2013) and Curti et al. (2017).

2. The calibration from Maiolino et al. (2008) (M08) based on the R23 parameter, is tied to abundances determined through the T_e method at low metallicity (12+log(O/H)<8.4). In this metallicity range the T_e method is deemed reliable (i.e. not suffering significantly from temperature fluctuation effects). At high metallicity (12+log(O/H)>8.4) the calibration is determined theoretically, by using the models of Kewley & Dopita (2002). In the high metallicity regime the M08 calibration gives similar abundances to those obtained using the calibration used by Tremonti et al. (2004) and the calibration of R23 presented by Kobulnicky & Kewley (2004), which solves recursively for metallicity and ionisation parameter.[14] The R23 diagnostic is more sensitive than O3N2 to possible inaccuracies in the extinction correction, due to the large difference in wavelength between [OII] λ3727 and the other two lines. However it is not sensitive to changes in the N/O ratio.

[14] In fact, the dependence of R23 on the ionisation parameter is relatively small on the upper branch of the R23-O/H relation (Kewley & Dopita, 2002; Blanc et al., 2015), which is where most of the data utilised in this thesis lie.

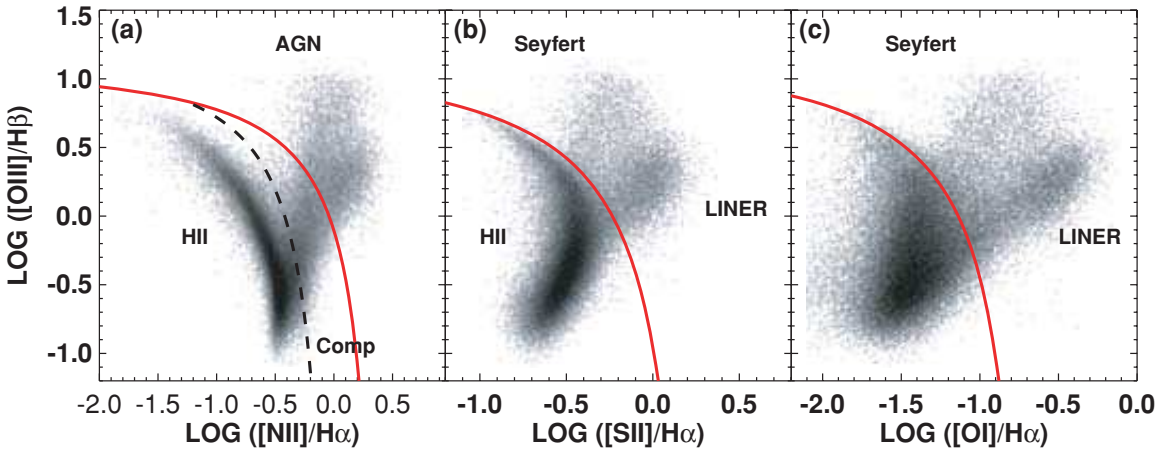

Figure 1.11: The [NII] BPT, [SII] BPT and [OI] BPT diagnostic diagrams populated by a large sample of SDSS star-forming galaxies. The Kewley et al. (2001) demarcation lines are shown in red in the three panels, while the revised division line by Kauffmann et al. (2003c) is shown as a dashed line in the [NII] BPT diagram. The bimodality between the left-hand and right-hand branches is evident in all the diagnostic diagrams, while the right-hand branch divides more clearly in its two sub-populations (Seyferts and LINERs) in the [SII] and [OI] diagrams. From Kewley et al. (2006).

Measuring the N/O ratio

The derivation of the N/O abundance ratio from the N2O2 line ratio is subject to smaller systematics than the measurement of the gas phase oxygen abundance. The advantage of using this line ratio lies in the similar ionisation potential of oxygen and nitrogen, which guarantees that $N^+/O^+ = N/O$ to high accuracy (Vila-Costas & Edmunds, 1993; Thurston et al., 1996). Pagel et al. (1992) provides a convenient formula to relate N^+/O^+ to the N2O2 calibrator, which has been verified theoretically using a five-level atom calculation,

$$\log(N^+/O^+) = \log(\mathrm{N2O2}) + 0.307 - 0.02 \cdot \log t_{\mathrm{NII}} - 0.726 \cdot \log {t_{\mathrm{NII}}}^{-1}, \tag{1.22}$$

where t_{NII} is the [NII] nebular electron temperature, which is assumed to be the same as the [OII] temperature (Stasińska, 1990; Garnett, 1992). In this thesis t_{NII} is estimated using the calibration provided by Thurston et al. (1996), which is based on R23. The effect of temperature on the calibration is, however, only very minor. The N/O abundance ratios obtained with this calibration are equivalent to the ones obtained using the more recent Pilyugin et al. (2010) method, based on a similar set of strong lines ratios.

It is worth noting that the N2O2 ratio has been suggested by same authors as an oxygen abundance diagnostic (Kewley & Dopita, 2002; Blanc et al., 2015), thanks to its minimal dependence on the ionisation parameter. However, this diagnostic only tracks oxygen abundance if a one-to-one relation between O/H and N/O is assumed. As discussed in Sec. 1.3.4, chemical evolution predicts different time evolution for oxygen and nitrogen. Hence, a one-to-one relation between the two abundances is not necessarily a good assumption.

1.4.3 The classical star formation-AGN division

The models discussed so far in this section refer to regions photoionised by massive stars. AGN, however, are also capable of photoionising the gas in galaxies. Due to their different spectral characteristics, AGN ionisation results in nebulae with line ratios substantially different from those generated

in HII regions. In the context of large spectroscopic surveys of galaxies, like SDSS, where a large fraction of the galaxy light is captured by a single optical fibre, one may use the different line ratios expected in the two cases to discriminate between line emission due to AGN and star formation.

The most widely used system for spectral classification of emission line galaxies is based on the diagnostic diagrams originally suggested by Baldwin et al. (1981) and Veilleux & Osterbrock (1987) (generally referred to as Baldwin-Phillips-Terlevich, or *BPT diagrams*). Standard BPT diagnostic diagrams rely on the line ratios [OIII] λ5007/Hβ versus [NII] λ6583/Hα ([NII] BPT), [SII] λ6717, 31/Hα ([SII] BPT) or [OI] λ6100/Hα[15]. This scheme has two key strengths: in z $\sim$ 0 Universe all the required lines lie in the easily accessible optical range and the vicinity in wavelength of the pairs of lines considered makes the scheme reddening insensitive.

Kewley et al. (2001) (K01) used population synthesis models together with photoionisation models to construct a division line in the BPT planes, arguing that sources lying above the inferred dividing line cannot be reproduced using star forming models alone. With the advent of the SDSS survey, it became even more apparent that galaxies lie in two well-defined sequences in the BPT diagram, leading to the characteristic 'sea gull' shape (Fig. 1.11). The left-wing sequence is associated with star-forming galaxies, while the right-wing sequence is associated with other ionisation mechanisms, including photoionisation by AGN (Type 2 Seyfert nuclei[16]), *low ionisation nuclear emission-line regions* (LINER) and shocks.

Kauffmann et al. (2003c) (K03) proposed a modification of the K01 line to better match the observational data derived from more than 10^5 galaxies from SDSS. The overall shape of this branch can be reproduced well by HII regions photoionisation models as the envelope of the expected line ratios for different values of metallicity and ionisation parameter for gas ionised by O and B stars (Kewley et al., 2001; Nagao et al., 2006; Stasińska et al., 2006; Byler et al., 2016).

The right-wing of the BPT diagram is known to show a bimodality, and is generally divided into an upper branch (the Seyfert branch) and a lower branch (the LINER branch). Kewley et al. (2006) studied this bimodality from an empirical perspective and concluded that the division between the two classes is most evident by using the [OI]/Hα and [SII]/Hα line ratios. Hence in this thesis the [SII]/Hα diagram, in combination with the Kewley dividing line, is used to distinguish between the Seyfert and LINER branches.

The LINER branch, accounting for up to a third of all galaxies (Ho et al., 1997; Cid Fernandes et al., 2010), is generally characterised by an ionisation mechanism significantly different from that of known Seyfert nuclei. Heckman (1980) first presented a detailed study of LINER emission, arguing that LINERs could represent the low-luminosity extension of the Seyfert population. However, as already discussed in Heckman (1980), both shock ionisation models (Dopita & Sutherland, 1995; Dopita et al., 2015) and photoionisation by a hard radiation field (Ferland & Netzer, 1983; Kewley et al., 2006) can be invoked to explain LINER emission. In more recent years, models for LINER-like emission due to shock excitation have been further applied outside the AGN framework to merging systems and ultra luminous infrared galaxies (ULIRGs, Rich et al. 2010, 2013).

A stellar source for LINER emission has also been proposed. Post-asymptotic giant branch (pAGB) stars represent a particularly promising explanation, since they are the natural product of

[15] From now on these lines will be referred to as just [OIII], [NII], [SII] and [OI].

[16] Type 1 AGN are characterised by the presence of very broad permitted lines in their spectra, while in Type 2 AGN permitted lines are of the same width as forbidden lines.

stellar evolution and have been shown to produce the required LINER-like line ratios, at least within the uncertainties of modern stellar population modelling (Binette et al., 1994; Cid Fernandes et al., 2010, 2011) and have long been associated with the observations of line emission in red sequence galaxies (Trinchieri & di Serego Alighieri, 1991). Moreover it has been found that extended LINER-like sources (Sarzi et al., 2010; Yan & Blanton, 2012; Singh et al., 2013) have radial profiles of line emission surface brightness shallower than r^{-2}. Some authors have argued that this represents evidence against ionisation from a central point source. The study of LINER-like excitation in galaxies on resolved scales is treated in much detail in chapter 3 of this thesis.

1.4.4 Dust and extinction

Dust is the part of the ISM which exists in solid form, mostly as grains of graphite and silicate of micron size (Draine, 2003). Dust plays a key role in the evolution of galaxies by depleting chemical elements out of the ISM, catalysing the formation of molecular hydrogen and contributing to the cooling of ionised nebulae. A fascinating subject of study in itself (see Draine 2011, chapters 21-26), for the purpose of this thesis dust is mainly a nuisance parameter, because of its obscuring effect. Focusing on the optical wavelength range, dust attenuates light (*extinction*), but also causes a change in the shape of the spectrum, by attenuating bluer wavelengths more than redder ones (*reddening*). The extinction at wavelength λ, measured in magnitudes, is defined as

$$A_\lambda = 2.5 \log(F^0_\lambda / F_\lambda), \tag{1.23}$$

where F^0_λ is the unattenuated flux and F_λ is the observed flux. The wavelength dependence of A_λ is generally expressed in terms of an *extinction curve* $k_\lambda = A_\lambda / E(B-V)$, where $E(B-V) = A_B - A_V$ is the so-called colour excess.

The extinction curve of the Milky Way can be determined by comparing the spectra of stars observed behind a substantial dust cover with those of unattenuated stars of a similar type. A convenient model for the Galaxy's extinction curve is provided by Cardelli et al. (1989), who suggest that variations around the mean extinction curve can be parametrised by the total-to-selective extinction in V-band, $R_V = A_V / E(B-V)$. R_V changes across lines of sights in the Milky Way (Mathis, 1990; Fitzpatrick, 1999), with a median value of $R_v \sim 3.1$.

For the purpose of correcting emission line fluxes, the theoretical ratios of Balmer lines (the Hα/Hβ ratio, or Balmer decrement, is generally used for this purpose) offer a direct way to measure E(B-V), provided the extinction curve is known. In detail, using Eq. 1.23 and the definition of E(B-V), the relation between the measured (F_λ) and intrinsic (F^0_λ) fluxes is given by

$$\frac{F_{H\alpha}}{F_{H\beta}} = \frac{F^0_{H\alpha}}{F^0_{H\beta}} 10^{-0.4\ E(B-V)[k_{H\alpha} - k_{H\beta}]}. \tag{1.24}$$

Since $F^0_{H\alpha}/F^0_{H\beta}$ is known from theory (2.87 for case B recombination at 10^4 K), E(B-V) can be calculated and Eq. 1.23 can be used to correct emission lines fluxes for the effects of extinction encountered along the line of sight.

For extragalactic sources the situation is considerably more complicated, as the 'effective extinction' curve will depend on the relative geometry of stars and dust (Natta & Panagia, 1984; Calzetti et al., 1994; Calzetti, 2001). While a simple dust screen generally produces the most reddening, a mixed star-dust geometry tends to generate a 'greyer' extinction curve (i.e. a larger R_V). Moreover,

the stellar continuum is generally found to have a lower reddening than the emission lines (Calzetti et al., 1994), possibly because young stars are more deeply embedded into gaseous and dusty structures. Finally, the Balmer decrement is only sensitive to modest extinction levels. When averaged over large scales, its value is biased towards lower extinction levels, since regions of lower attenuation will dominate the observed flux from the region.

Measuring the SFR

The Hα luminosity is directly proportional to the amount of ionising photons present in an HII region, assuming that the escape fraction of such photons is negligible. Since the massive stars which give rise to HII regions die on Myr timescales, the amount of ionising photons is a direct probe of the formation rate of massive stars. With suitable stellar population models, the relation between SFR and Hα luminosity may be calibrated, assuming knowledge of the stellar IMF. Similarly to the case of the average oxygen yield, discussed in Sec. 1.3.1, the SFR will be mostly affected by the fraction of massive stars assumed in different IMF parametrisations, and by the upper-mass cutoff of the IMF. A widely used parametrisation for the relationship between Hα and SFR, which is also adopted in this work, is given by Kennicutt (1998). Assuming a Salpeter IMF the SFR is given by

$$\mathrm{SFR}/(\mathrm{M}_\odot\ \mathrm{yr}^{-1}) = 7.9\ 10^{-42}\ \mathrm{L}_{\mathrm{H}\alpha}/(\mathrm{erg\ s}^{-1}), \tag{1.25}$$

where the conversion factor is computed for case B recombination at $\mathrm{T_e} = 10^4$ K. Aside from the systematic effect of the IMF and the uncertainties involved in the extinction correction, the SFR measured from Hα may be systematically affected by the stochastic sampling of the high-mass end of the IMF in the regime of very low SFR (Kennicutt & Evans, 2012).

1.5 Integral field spectroscopy of nearby galaxies

Highly multiplexed spectroscopic surveys like SDSS (York et al., 2000) have proved to be a transformational tool for the study of galaxy evolution. As already discussed in Sec. 1.1, the statistical power of the SDSS galaxy sample has shed light on the complex interplay of phenomena that shape the formation and evolution of galaxies – from their star formation and chemical enrichment, the impact of inflows and outflows, to the role of AGN, the effect of environment on galaxy properties and cessation of star formation (Kauffmann et al., 2003b,c; Brinchmann et al., 2004; Tremonti et al., 2004; Kewley et al., 2006; Asari et al., 2007; Mannucci et al., 2010; Peng et al., 2010; Thomas et al., 2010; Johansson et al., 2012). SDSS currently provides the most comprehensive picture of galaxies in the low-redshift Universe, against which theories of galaxy evolution are tested and properties of high redshift objects are compared.

Despite its successes, SDSS spectroscopy suffers from a considerable drawback, common to all surveys of galaxies that contain more than a few hundred objects: the light-gathering aperture (the 3″-diameter fibre in the case of SDSS) can only trace circum-nuclear galactic properties. In this way, the complex details of galactic structure (spiral arms, bulge, HII regions) are lost. Moreover, for nearby galaxies the derived properties may not be representative of the galaxy as a whole, since the fibre might just be targeting the galactic centre, or other areas of high surface brightness. Nearly all studies based on SDSS have to take this aperture effect into account in their analysis. For example, to obtain the total SFR in a galaxy one has to apply a large aperture correction to the SFR measured in

the central fibre. This correction is generally based on broadband optical (Brinchmann et al., 2004) or UV photometry (Salim et al., 2007), but remains difficult to calibrate accurately. Moreover, the kinematics of gas and stars, which probes the potential of the dark matter component and constitutes a powerful tracer of outflows, cannot be studied efficiently by using a single spectroscopic aperture. By investigating the full 2D spectroscopic structure of galaxies, integral field spectroscopy (IFS) provides the ideal observational tool to circumvent this problem.[17]

In the last decade the internal structure and kinematics of galaxies in the local universe have been successfully studied using IFS by a number of surveys, including SAURON (de Zeeuw et al., 2002), PINGS (Rosales-Ortega et al. 2010, Sec. 6.1.1), ATLAS^{3D}(Cappellari et al., 2011a), DiskMass (Bershady et al., 2010) and VENGA (Blanc et al., 2013a). These surveys have generally focussed on either small samples of nearby objects (PINGS, VENGA) or on a specific subclass of galaxies (early-type galaxies in the case of SAURON and ATLAS^{3D}). Other surveys, like DiskMass, have optimised their sample selection and instrument setup to investigate specific questions, but did not aim to provide an unbiased view of the galaxy population in the nearby Universe. The challenge of providing IFS data for a large sample of local galaxies has been addressed more recently by the CALIFA (Sánchez et al., 2012a) and SAMI (Croom et al., 2012) surveys, observing respectively 600 and 3400 galaxies.

At the same time, the development of IFS instruments in the near-IR has provided key observations of the spatially resolved properties of star forming galaxies as z $\sim$ 2. These observations have revealed that, despite the clumpy appearance and the high SFR, galaxies at these redshifts already display regular rotating discs (Förster Schreiber et al., 2009; Law et al., 2009), together with evidence for large-scale winds and outflows (Steidel et al., 2010; Genzel et al., 2011). Second-generation instruments with IFS capabilities are now available on large telescopes (for example KMOS, Sharples et al. 2006, and MUSE, Bacon et al. 2010) and are contributing to changing our view of the high-redshift Universe. Moreover, in the near future large ground-based and space telescopes (e.g., E-ELT, *JWST*) will also provide IFS capability as one of their core observing modes. In this context, it is clear that a large IFS survey of the local Universe is needed to provide a suitable benchmark for current and future high-z observations.

One of the three major programs of the fourth generation SDSS (SDSS-IV, Blanton et al., in prep.) is dedicated to a large IFS survey of local galaxies called MaNGA (Mapping Nearby Galaxies at Apache Point Observatory), which intends to provides the next step towards a statistically representative IFS survey of the nearby Universe. MaNGA plans to observe 10000 galaxies with average redshift $< z >= 0.03$, systematically covering galaxies out to 1.5 and 2.5 effective optical radii (R_e) in the wavelength range 3600 Å $< \lambda <$ 10300 Å. Chapter 2 is dedicated to a detailed discussion of different aspects of this large observational undertaking, from its hardware to data analysis.

1.5.1 Thesis aims

The power of the MaNGA survey lies in the combination of its large sample with the ability to spatially resolve internal structures in galaxies. Such dataset is now allowing us to move beyond a long-standing dichotomy in the observational study of galaxy evolution. On one side, observations of small samples

[17] Integral field spectroscopy refers to the experimental technique whereby several spectra of an extended source are obtained across a two-dimensional field one the sky. Different hardware solutions are possible to implement IFS, including an image slicer, lenslet array and fibres. A detailed discussion of the hardware used in the MaNGA IFS survey is presented in Sec. 2.1.1.

of bright nearby galaxies (e.g. SINGS, Kennicutt et al. 2003a) have provided us with outstanding detail regarding the distribution of star formation and chemical abundances in the local Universe. These studies, however, are fundamentally limited to probing only limited (and perhaps biased) subsamples of the overall galaxy population. At the other extreme, large surveys like SDSS have provided enormous statistics, albeit at the cost of treating galaxies as point sources. The aim of this thesis is to contribute to bridging this gap, and allow a characterisation of the distribution of line emission, star formation and chemical abundances in a large sample of galaxies ($\sim 10^3$) on $\sim$ kpc scales.

In chapters 3 and 4 I focus on the study for star formation and quiescence, and I aim to tackle the following questions.

1. Where do spatially resolved regions appear on classical BPT diagnostic diagrams, and how applicable are these diagnostics in distinguishing star-forming from quiescent regions?

2. How may we define 'quiescence' using spatially resolved spectroscopic data? How are quiescent regions distributed in galaxies?

3. Does the presence of a large number of quiescent regions correlate with other fundamental galaxy properties, such as stellar mass, SFR, colour, bulge-to-disc ratio?

4. How widespread is line emission on the red sequence and what powers the observed emission?

The ultimate goal of this study is to be able to identify trends with environment (Sec. 4.4 for a first look at the problem) and be able to quantify where and when the quenching process proceeds inside galaxies. The kpc-scale resolution of MaNGA, combined with its large sample, covering both the blue cloud, the red sequence and the sparsely-populated green valley, is ideal to conduct this type of study.

Chapters 5 and 6 of this thesis are dedicated to the subject of chemical abundances and chemical evolution modelling. In those chapters I aim to answer the following questions.

1. How does the metallicity radial gradient change as a function of mass and other fundamental galaxy properties (such as bulge-to-disc ratio, SFR)?

2. Can chemical abundances at large galacotcentric radii (R$>$ 2.0 R_e) provide evidence for direct accretion of pristine gas or metal transport via galactic fountains?

3. When appropriate knowledge of the gas content of galaxies is available, can the observed gas phase abundance gradient be used to constrain the importance of gas flows (inflows and outflows) over the history of a galaxy?

4. Can abundance ratios of chemical elements with different nucleosynthetic origin be used to shed light on the star formation and gas flow history of galaxies?

It is worth noting that a fundamental limitation to the study of chemical evolution in the MaNGA sample is the lack of spatially-resolved cold gas observations. In order to circumvent this problem, in chapter 6 I abandon the MaNGA sample and present a case study for a single nearby galaxy, for which a unique combination of IFS and cold gas data are available.

Chapter 2

The MaNGA survey

Partially adapted from 'P-MaNGA Galaxies: emission-lines properties - gas ionization and chemical abundances from prototype observations', F. Belfiore, et. al., 2015, MNRAS, 449, 867.

2.1 An overview of the MaNGA instrument and data

In this section I describe the overall properties of the MaNGA survey, in terms of its hardware, observing strategy, sample selection and data reduction, with a specific focus on the aspects which are most relevant to the study of the ionised ISM. MaNGA compares well with other ongoing IFS surveys (SAMI, CALIFA) in terms of information-gathering power and data quality. In particular, it offers a wider wavelength range than other surveys, by extending into the near-IR (Fig. 2.1). If one quantifies the survey information-gathering power by a product of the étendue (defined as the product of the system throughput, telescope collecting area and solid angle covered by the fibres) and the spectral resolution (R) of the survey, MaNGA compares favourably to other surveys thanks to its high system throughput, although SAMI is superior in its red arm thanks to its higher spectral resolution.

Details on the MaNGA instrument, including the design, testing, and assembly of the MaNGA fibre bundles are given in Drory et al. (2015). Wake et al. (in preparation) present the sample design, optimisation, and final selection of the survey. Details on the observing strategy and imaging quality requirements can be found in Law et al. (2015), while a discussion of the MaNGA science requirements, survey execution and initial data quality is presented in Yan et al. (2016b). The software and data framework as well as the reduction pipeline is described in Law et al. (2016). The spectrophotometric calibration procedure is described in Yan et al. (2016a). Details on the MaNGA data publicly released in SDSS Data Release (DR) 13 are presented in Albareti et al. (2016).

The MaNGA survey is an ongoing effort at the time of writing, having started on 1st July 2014 and being scheduled to run until 2020, utilising half of the dark time available in SDSS-IV. MaNGA observations are carried out by a team of professional observers at Apache Point Observatory (APO) and routinely supervised by members of the MaNGA team. The reduction of the MaNGA data is coordinated by the MaNGA data team. My contribution to this effort has been limited the study of the effect of error covariance introduced by the cube reconstruction algorithm (Sec. 2.1.4) and aspects of data validation, especially during the MaNGA prototype instrument phase (Sec. 2.3). The MaNGA

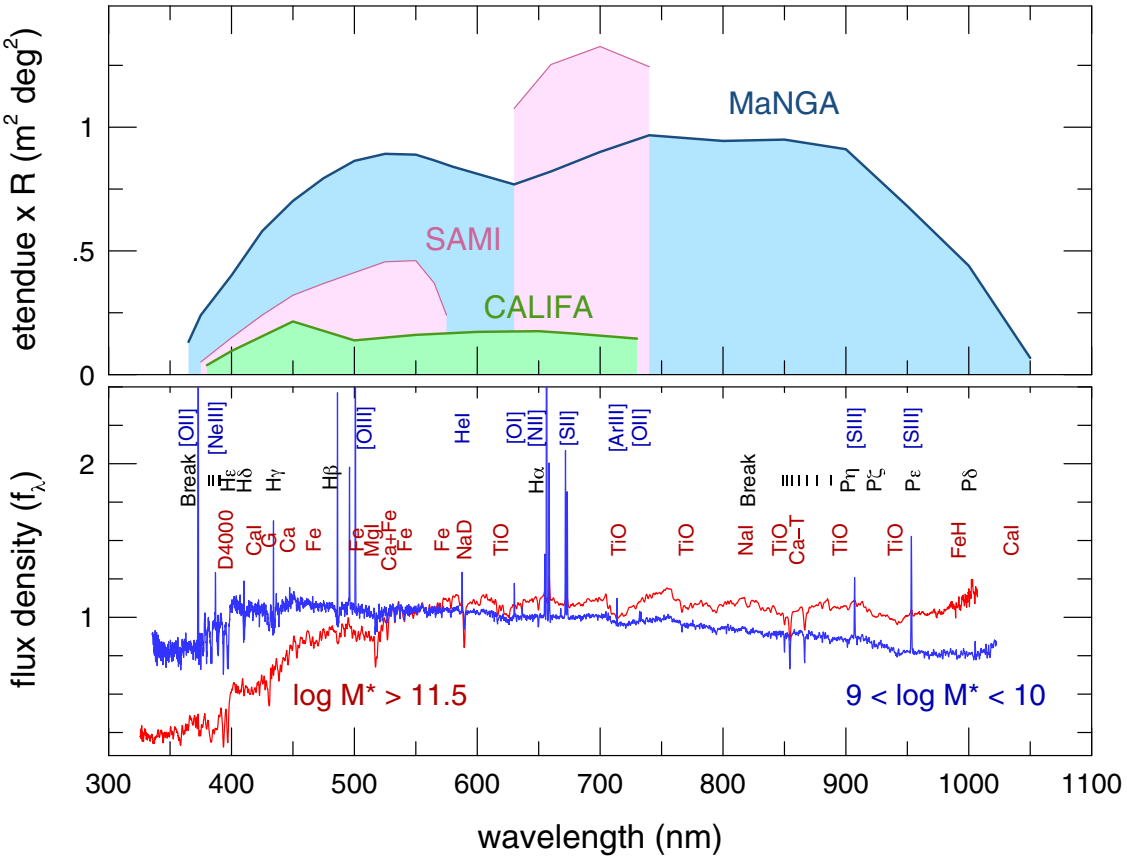

Figure 2.1: *Top*: MaNGA's information-gathering power, quantified by the products of the étendue and the spectral resolution (R) as a function of wavelength, compared to that of other modern IFS galaxy surveys. *Bottom*: Two examples of stacked z ∼ 0.15 spectra from the BOSS survey (Dawson et al., 2013), illustrating the available spectral features for ISM and stellar composition and kinematics available in the MaNGA wavelength range. From Bundy et al. (2015).

data analysis pipeline, which performs spectral fitting and derives physical parameters (e.g. line fluxes, kinematics etc) from the reduced datacubes, is an ongoing effort which I have been deeply involved in. The output of the MaNGA data analysis pipeline is undergoing quality control testing at the time of writing. In Sec. 2.2 I discuss the development of my own independent software and algorithmic framework to analyse the reduced MaNGA data. The results presented in this thesis are obtained by means of this custom-made analysis software.

2.1.1 The MaNGA instrument

The MaNGA survey makes use of the 2.5m telescope at APO in spectroscopic mode (Gunn et al., 2006). MaNGA uses the SDSS 'plate-cartridge' infrastructure, which has been adopted by SDSS since the start of operations. In short, an SDSS *plate* is a thin aluminium circular slab, with holes custom-drilled for every field at the positions of sources to be observed. Before each observation, plates are plugged with fibres (or fibre bundles in the case of MaNGA) and mounted onto a *cartridge*, which is a large cylindrical metal structure containing the fibre pseudo-slit and the necessary infrastructure to attach to the back of the telescope. Plates are plugged and mounted during the day. At night, the relevant cartridge is attached to the Cassegrain focus at the back of the telescope, observed and then swapped for a new cartridge with the subsequent plate.

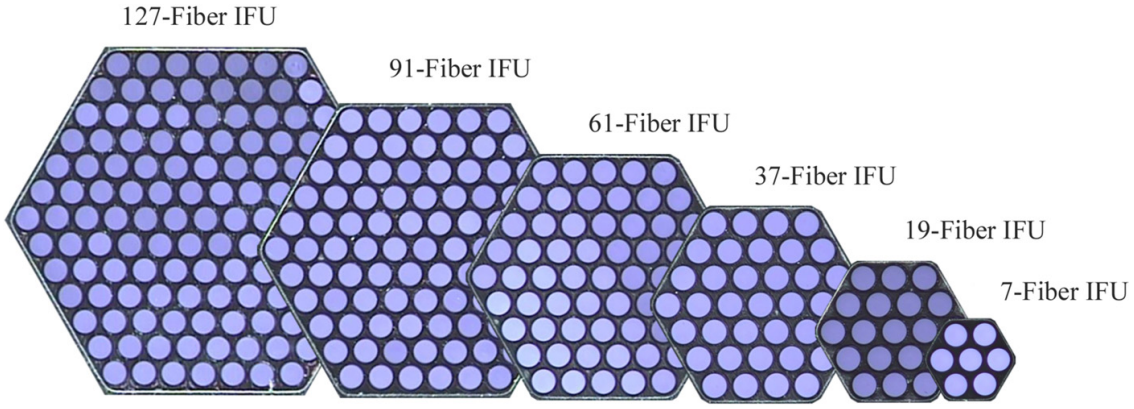

Figure 2.2: Photographs of six MaNGA IFUs from the first batch of survey-ready components. The photographs have been cropped to each IFU's hexagonal area and overlaid in this presentation. An example of each science IFU is shown, as well as a seven-fibre mini-bundle (far right), which is used for flux calibration. On each plate MaNGA observes 17 science IFUs with the following size distribution: two 19-fibre, four 37-fibre, four 61-fibre, two 91-fibre and five 127-fibre IFUs. Twelve 7-fibre IFUs are also observed for flux calibration. From Bundy et al. (2015).

The MaNGA instrument is a new piece of hardware, built by SDSS-IV to allow IFS observations using the existing plate-cartridge and telescope infrastructure at APO. The fundamental unit of the MaNGA hardware is a fibre bundle (or integral field unit, IFU), which consists of an hexagonal tightly-packed assembly of optical fibres (see Fig. 2.2). The MaNGA fibres have an inner light-sensitive core diameter of 120 μm (corresponding to 2.0″ at the telescope focal plane) and an outer diameter of 151.0 ± 0.5 μm including their protective buffers and cladding. The hexagonal packing strategy developed by Drory et al. (2015) was chosen over circular packing, which would maximise the filling factor of the bundle (Bland-Hawthorn et al., 2010; Bryant et al., 2011) adopted by the SAMI survey. While reaching a lower effective filling factor of $\sim$ 56%, the adopted hexagonal packing technique improves fiber throughput, decreases breakages, permits extremely regular fibre placement within each IFU and simplifies the dithering procedure (Sec. 2.1.2).

Each MaNGA cartridge hosts a total of 1423 fibres, subdivided into 17 'science' IFUs used for galaxy targets, ranging in size from 19 to 127 fibres (12.5 - 32.5″ diameter), twelve 7-fibre mini-bundles used for spectrophotometic calibration, and 92 single fibres used for sky subtraction. Each IFU can be deployed to target sources anywhere within the 3° diameter focal plane. The apparent size distribution of the targets on the sky motivates the adopted distribution of IFU sizes (two 19-fibre, four 37-fibre, four 61-fibre, two 91-fibre and five 127-fibre IFUs), chosen to guarantee the most efficient use of the fibres over the course of the survey, as discussed in Sec. 2.1.3.

IFUs feed light into the two dual-channel BOSS spectrographs (Smee et al., 2013), which maintain the same configuration as was used in SDSS-III. The collimated beams in each spectrograph are split with a dichroic and feed a blue (3600 - 6000 Å) and red camera (6000 - 10300 Å). Spectral resolution varies with wavelength, with an average resolving power $R = \delta\lambda/\lambda \sim 2000$. A detailed analysis of the variation of the spectral resolution as a function of wavelength is presented in Law et al. (2016) (Sec. 10.2) and Yan et al. (2016b) (Sec. 7.4), and is still a matter of ongoing improvement within the MaNGA collaboration.

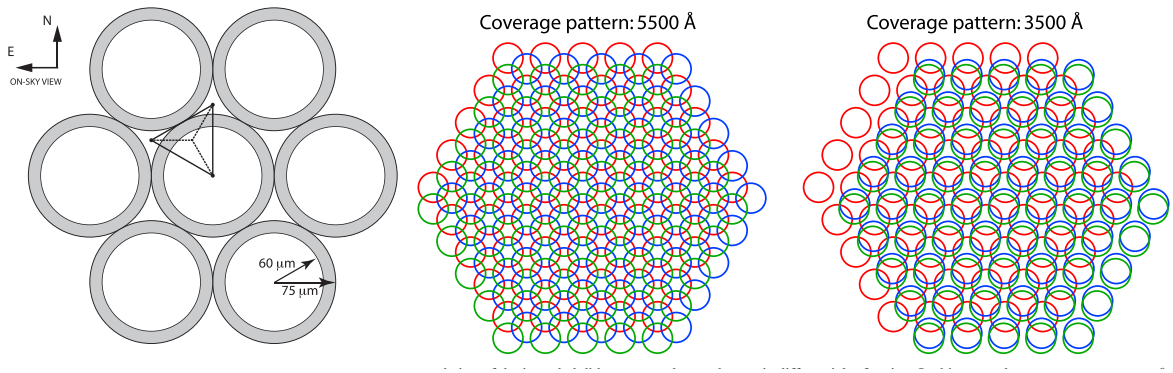

Figure 2.3: *Left*: Schematic diagram of the 7 central fibres within a hexagonally packed MaNGA IFU, showing the 120 micron diameter fibre core and surrounding cladding plus buffer. The triangular figure shows the relative positions of the three dither positions. *Middle and right*: Illustrative figure showing degradation of the intended dither pattern due to chromatic differential refraction. Each dither is shown in a different colour (red, blue, green). While the achieved dither pattern is nominal at the guide wavelength (central panel), at 3500 Å the dither pattern is severely degraded. From Law et al. (2015).

2.1.2 Observing strategy

Since the fibre bundles consist of 2″ diameter circular apertures separated by large interstitial gaps, each exposure will significantly undersample the point spread function (PSF, typically ∼1.5″ at APO) and produce a non-uniform response function across the face of each IFU. In MaNGA this problem is addressed by obtaining observations at three dither positions, in an regular triangular pattern (Fig. 2.3). The combination of three dithered exposures is referred to as a dither set.

Unfortunately, both the large field of view of the SDSS telescope and the wide wavelength range of the BOSS spectrographs introduce substantial complications to the dithering procedure. Atmospheric refraction causes astronomical sources to appear higher in the sky than the truly are. If exposures within the same dither set are observed at different hour angles, each exposure will be affected by atmospheric refraction in a different way, thus degrading the accuracy of the dither pattern. Even more importantly, refraction through the Earth's atmosphere is wavelength-dependent. This effect (differential atmospheric refraction) causes each spectroscopic fibre to effectively see a different part of the source at different wavelengths. The distortion introduced can be substantial compared to the fibre radius (particularly shortward of 4000 Å) and needs to be accounted for by the data reduction pipeline (Sec. 2.1.4). More problematically, since the three exposures in a given dither set may be obtained at different hour angles, the relative offset at a given wavelength will change between these three exposures and degrade the intended dither pattern coverage (see Fig. 2.3). Therefore the primary driver of the MaNGA observing strategy is to mitigate the adverse effect of atmospheric refraction on imaging quality. This is achieved by defining a set of hour angles within which all observations for a given set must be taken (see details in Law et al. 2015, Sec. 6.2, and Yan et al. 2016b, Sec. 5).

The total integration time per target is set by the requirement that MaNGA reach a signal-to-noise ratio (S/N) of 5 Å^{-1} fiber^{-1} in the r-band continuum at a surface brightness of 23 AB arcsec^{-2}. As described in Yan et al. (2016b), the typical integration time per plate to reach this target is around 3 hours in median conditions, but can range from 1.5 to 5 hours. An integration time of 15 minutes per exposure ensures that observations are shot-noise dominated for $\lambda >$ 3700 Å. Each dither set takes ∼ 48 minutes, and each completed plate will therefore consist of ∼ 6-21 individual exposures.

2.1.3 Sample selection

The MaNGA target selection is driven by the desire to optimise sample size, spatial coverage and spatial resolution, given the limited number of fibres available and the total duration of the survey. In order to provide a significant next step in terms of statistics and to be able to study properties of galaxies along three different independent axes (for example, mass, colour and environment), Bundy et al. (2015) conclude that a sample size of $\sim$ 10000 galaxies is needed. Kinematic features and interesting spatial structures (like bars, bulges, spiral arms) have scales of the order of $\sim$ 1 kpc. Given the 2″ size of the MaNGA fibres, recovering this scale means that the median galaxy target ought to be placed at redshift z $\sim$ 0.03.

The MaNGA sample is selected to be flat in stellar mass in the range $10^9 < M_\star/M_\odot < 10^{12}$, in order to have suitably large statistics for the high-mass end, where galaxies would be severely under-represented in a volume-limited sample. Due to the steepness of the mass function, there is a shortage of high-mass galaxies at very low redshifts. High-mass targets, therefore, generally need to be observed at higher redshifts.

MaNGA also requires uniform radial coverage in terms of a multiple of the galaxy effective radius (R_e). In order to compromise between spatial resolution and radial coverage, the sample is split in two subsamples: 2/3 of the sample is covered to 1.5 R_e (the *primary sample*) and 1/3 of the sample to 2.5 R_e (the *secondary sample*). A further optimisation step is performed to increase the number of galaxies in rare regions of the colour-magnitude diagram. The *colour-enhanced sample* is designed to add galaxies in regions of the $NUV - i$ versus M_i colour magnitude plane that are under-represented in the primary sample, such as high-mass blue galaxies and low-mass red galaxies, and constitutes 17% of total sample. The combination of the primary and the colour-enhanced sample is referred to as primary+.

MaNGA targets are selected from an extended version of the NASA Sloan Atlas (NSA `v1_0_1`[1], Blanton et al. 2011). The NSA is a catalogue of nearby galaxies, primarily based on the SDSS DR7 MAIN galaxy sample (Abazajian et al., 2009) but incorporating data from additional sources to increase the redshift completeness for nearby galaxies. The catalogue provides photometry in the five SDSS bands and in the *GALEX* NUV and FUV bands. Stellar masses are computed using a Chabrier (2003) initial mass function and using the `kcorrect` software package (version `v4_2`, Blanton & Roweis 2007) with Bruzual & Charlot (2003) simple stellar population models. Magnitudes are in the AB system and k-corrected to rest frame after correction for galactic extinction. Effective radii are measured from the SDSS photometry by elliptical Petrosian photometry in the r-band. In this catalogue and for the rest of this thesis we assume a ΛCDM cosmology with $H_0 = 70$ km s^{-1} Mpc^{-1}, $\Omega_m = 0.3$ and $\Omega_\Lambda = 0.7$.

The MaNGA target selection consists of a set of low- and high-redshift limits as a function of absolute i-band magnitude, M_i, within which galaxies are observed (the redshift limits are different for the primary and secondary samples, see Fig. 2.4, left). M_i is used instead of stellar mass in order to make the MaNGA sample selection independent of the systematics involved in calculating stellar masses, and thus easily reproducible. The redshift ranges are chosen to have a sufficient number of galaxies that can be covered to the required radial extent. Since the IFU size distribution is fixed, higher mass galaxies need to be observed at higher redshift in order to fit within the MaNGA IFUs.

[1] http://www.sdss.org/dr13/manga/manga-target-selection/nsa/

Compounded with the target density argument for high-mass systems presented above, these effects explain the overall shape of the redshift intervals seen in Fig. 2.4, left. In practice, the MaNGA selection function and the size distribution of IFUs has been optimised for best performance, as described in Wake et al., in prep.

The MaNGA sample is effectively volume-limited as a function of M_i (or colour and M_i for the colour-enhanced sample). Hence one can exactly define the volume over which any galaxy in the sample could have been selected and calculate a V_{max} (volume) weight. Application of the volume weights enables to correct the sample back to the volume-limited case (these weights are used in chapters 4 and 5). Additional complications arise if one wants to combine the primary+ and the secondary samples together and are discussed in Wake et al., in prep. By virtue of the sample selection, at each M_i (or stellar mass) MaNGA targets galaxies with a range of sizes so that, to first order, there is no correlation between M_i (or stellar mass) and IFU size allocation. This means that MaNGA probes the same spatial resolution in units of R_e at all masses,[2] although the physical resolution in kpc is mass-dependent (see Sec. 5.4.2).

A logical consequence of the above is that, at a fixed luminosity (or mass), the MaNGA sample contains galaxies covered by all bundle sizes. This means that galaxies with the smaller effective radii (in units of arcsec) are covered by the smallest bundles. Given that there is only a small change in redshift over the MaNGA selection function, galaxies with larger intrinsic sizes are preferentially allocated larger IFUs. This effect will introduce a very significant bias in any analysis that only uses galaxies observed with a certain IFU size. Unfortunately, the size of the IFU is a direct measure of the number of spatial elements available in the radial direction in a typical MaNGA galaxy, hence one needs to carefully consider the effect of resolution when the quantity of interest depends on the number of resolution elements per effective radius. In Sec. 5.4.2 I discuss this problem in detail, in the context of the determination of metallicity gradients in MaNGA galaxies.

2.1.4 Data reduction and calibration

The MaNGA data reduction pipeline is the main software tool responsible for producing sky-subtracted, wavelength and flux-calibrated datacubes for each galaxy (Law et al., 2016). The pipeline consists of two parts, so-called 2d and 3d stages.

The 2d reduction stage performs the standard stages for reduction of spectroscopic data, including bias subtraction, cosmic ray rejection, spectral extraction and flat fielding. Wavelength calibration is performed via neon-mercury-cadmium arc-lamp spectra and adjusted by fitting the centroids of bright sky lines. The final wavelength solution for each exposure is corrected to the vacuum heliocentric rest frame. Together with flux, an error extension is obtained for each fibre by taking into account read noise and Poisson noise and propagating them through the same reduction steps. A mask extension is also computed, which indicates the presence of cosmic rays or problems such as bad flat-fields, missing fibres, extraction problems, etc.

A first estimate of the LSF is obtained by fitting the width of arc-lines across wavelength. A correction is then applied in order to account for the effect of flexure, which causes the LFS to broaden slightly. This correction is computed by fitting the width of unblended strong sky lines. The obtained spectral resolution is a function of both both fibre number and wavelength, but has a median σ =

[2] This resolution is, however, systematically different between the primary+ and secondary samples.

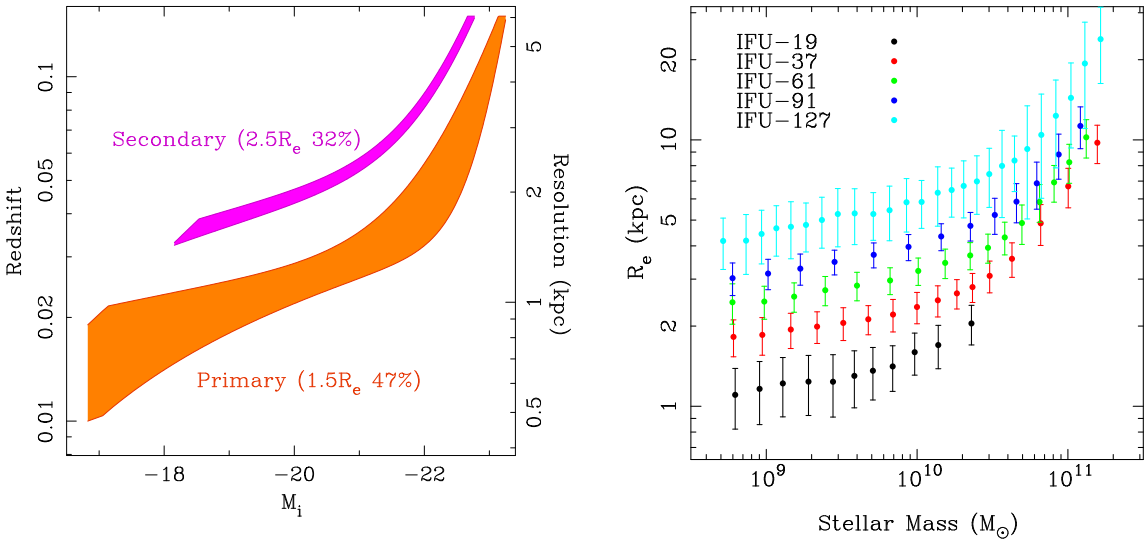

Figure 2.4: *Left*: The distribution of the primary and secondary sample in the M_i versus redshift plane. All the galaxies found within the shaded areas (orange for the primary, and violet for the secondary) are potential MaNGA targets. From Bundy et al. (2015). *Right*: The location in the radius - mass plane of MaNGA galaxies targeted with different IFU sizes (primary sample only for clarity, but an equivalent behaviour is present for the secondary sample). At fixed mass, larger IFUs are preferentially assigned to intrinsically larger galaxies. This effect introduces a significant bias when one selects a sub-sample of MaNGA galaxies based on IFU size. From Wake et al., in prep.

72 km s^{-1}.

Sky subtraction is performed by first creating a super-sampled model of the sky background by combining the spectra from all the sky fibres and then scaling it to the appropriate level for each IFU (the full procedure is described in Law et al. 2016). The quality of the sky subtraction was tested by using specially designed plates where all fibres where located on sky. The residuals from these plates after sky subtraction are very close to the expectations from Poissonian noise in line-free regions and slightly above Poissonian in regions affected by sky lines.

Flux calibration in MaNGA is performed following a different philosophy than adopted by previous SDSS single-fibre spectroscopy. In previous generations of SDSS the calibration needed to take into account both the flux lost by system losses (including both atmosphere and instrument) and the flux lost due to aperture effects. In IFS we do not desire to make an aperture correction, so we are only interested in a calibration which takes into account the system losses. In MaNGA this is achieved by targeting standard stars with 7-fibre mini-bundles with the same fibre size and fill factor as the science bundles. Although not all the light from the star is collected, because of the limited filling factor of the IFU, the relative flux ratios between the fibres in the bundle can be used to accurately model the position of the star within the IFU. Using an estimate of the PSF from the guider images, the profile of the star can be accurately fitted. The flux of the standard can then be accurate recovered leading to an estimate of the aperture loss separately from the system loss. The selected flux standards are late-F type main-sequence stars, with observed g-band magnitudes between 14.5 and 17.2. This magnitude range ensures that all the targeted stars lie in the galactic halo and are beyond most of the galactic dust. In order to obtain the flux calibration vector, their spectra are fitted with a combination of Kurucz stellar models reddened according to the dust map of Schlegel et al. (1998) and matched to the SDSS r-band PSF magnitude.

The accuracy of the flux calibration is dictated by the requirement to calculate accurate lines ratios across the wide MaNGA wavelength range, so that the calibration uncertainty does not dominate the uncertainty in the derived SFR, obtained from extinction-corrected Hα flux. Yan et al. (2016a) find that MaNGA meets this requirement, and in particular that MaNGA's relative calibration is accurate to 1.7% between the wavelengths of Hα and Hβ and to 4.7% between [OII] λ3727 and [NII] λ6584.

The 3d stage of the pipeline gathers all the exposures for a single objects, performs astrometric calibration and produces the final datacube. Astrometry is computed for each fibre taking into account its position within the fibre bundle from laboratory measurements, differential atmospheric refraction and other optical factors. Further astrometric registration is performed by matching to SDSS photometry.

In order to produce a datacube the fibre fluxes, errors and astrometric positions are combined using an image-generating algorithm that constructs a final datacubes with 0.5″ spatial sampling. In the case of MaNGA a flux-conserving variant of Shepard's algorithm is used, employing a Gaussian weighting function. This procedure is identical to that implemented for CALIFA observations (Sánchez et al., 2012b; Husemann et al., 2013). Since cube reconstruction scrambles the error vectors from single fibres across different spaxels,[3] the error vectors of nearby pixels are strongly covariant. Law et al. (2016) find that spaxels separated by 0.5″ have correlation coefficients of ~ 0.85, decreasing to < 0.1 (i.e., nearly uncorrelated) at separations of >2″. Spatial covariance is therefore important when one generates a binned spectrum using nearby spaxels (Sec. 2.2.1). Law et al. (2016) find that the correct noise vector can be obtained using an approximate fitting function of the form

$$N_{\rm true}/N_{\rm no\ covar} = 1 + \alpha \log(N_{\rm bin}), \tag{2.1}$$

where $N_{\rm true}$ is the true noise, $N_{\rm no\ covar}$ is the noise computed by error propagation assuming spaxels to be independent (i.e. neglecting covariance), α is a coefficient found to be ~ 1.62 and $N_{\rm bin}$ is the number of spaxels in the bin.

After one takes into account the effects of cube reconstruction, the final PSF of the MaNGA datacubes is a weak function of the observational seeing, and is well described by a Gaussian with FWHM of 2.54″.

2.2 Spectral fitting

Each spaxel in a MaNGA datacube can be modelled as a spectrum consisting of two broadly independent components: the stellar continuum emission and a set of nebular emission lines. The emphasis in this thesis is on emission line properties. However, an accurate measurement of the emission line fluxes and kinematics cannot be obtained without constructing an accurate model for the underlying stellar continuum. The spectral fitting problem is well-known since the advent of large spectroscopic datasets, like SDSS (Tremonti et al., 2004; Oh et al., 2011). IFS data extends the problem by providing spatial as well as spectral information. The consequences of this extra degree of freedom are discussed in this section.

2.2.1 The choice of binning scheme

Since the typical galaxy profile spans a large dynamic range in surface brightness, in the case of spatially resolved spectroscopic observations it is common practice to bin the data and trade S/N with

[3] A spaxel is a spatial pixel with the associated spectral information.

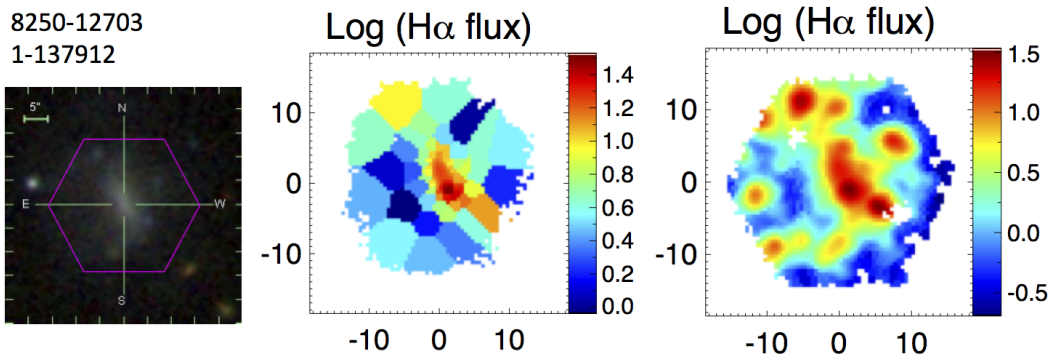

Figure 2.5: The effect of two different binning schemes on a low-surface brightness galaxy with strong emission lines (MaNGA-ID 1-137912). The left panel shows an SDSS $g-r-i$ cutout. The middle panel shows the Hα flux obtained by binning the galaxy spectra with a Voronoi binning scheme based on the continuum S/N. This results in large bins which dilute the highly clumpy line emission. The right panel shows the effect of using the procedure outlined in Sec. 2.2.2, where the line emission is recovered on a different binning scheme from that adopted for the continuum. The resulting Hα map now demonstrates the presence of highly clumpy line emission features.

spatial resolution. Different binning schemes have been presented in the literature (radial, Voronoi as in Cappellari & Copin 2003, intensity-based as in Sánchez et al. 2012b, etc.). Each carries its advantages and disadvantages and might be more suitable for specific science goals. In particular, the Voronoi binning procedure (Cappellari & Copin, 2003) has proved particularly popular, since it generates convex bins of optimal size that reach a target, maximally uniform S/N. In the case where scientific exploitation of the data requires a minimum S/N, and where the signal does not have clumpy substructure, this binning choice proves extremely successful. Previous work, however, was mostly focused on early-type galaxies, and used the continuum S/N to determine the binning for both stellar features and emission lines (Emsellem et al., 2004; Sarzi et al., 2005). With the advent of large scale IFS surveys comprising all galaxy types (like in MaNGA) we need to reassess the merit of a binning scheme in relation to both the continuum and the emission lines. A number of factors need to be assessed in order to make this choice.

1. Reliable emission line parameters depend crucially on accurate continuum subtraction. This is most evident for the Balmer lines, which lie above stellar Balmer absorption features, but also crucially important for weak lines in the blue part of the spectrum, which is very rich in stellar features (see inset in Fig. 2.6 for some examples).

2. The line emission surface brightness profile does not necessarily follow the continuum profile, hence a binning scheme optimising the continuum S/N may be inefficient for studying emission lines. This is less of a problem for early-type galaxies, where previous work has shown that line emission generally follows the continuum (Sarzi et al., 2010). It becomes a major issue, however, for blue galaxies with conspicuous HII regions, but very weak continuum (Fig. 2.5 for an example).

3. Line emission can be clumpy and concentrated in very bright regions but also very weak and diffuse. A binning scheme which mixes flux from a bright regions into a neighbouring diffuse region, with the aim of increasing its S/N, would unnecessarily mix regions with different physical properties. On the other hand, a scheme which does not attempt to bin in regions of diffuse emission risks losing the diffuse signature in the noise.

In the context of MaNGA, I have experimented with a few possible schemes to overcome the problems above.

1. Spaxel-by-spaxel analysis of continuum and emission lines (i.e. no binning).
2. Voronoi binning based on continuum S/N for both continuum and line emission (like in ATLAS^{3D}).
3. Voronoi binning on the continuum and subsequent spaxel-by-spaxel analysis for the emission lines.
4. Voronoi binning on the continuum, subtraction of the continuum on a spaxel-by-spaxel scale and subsequent Voronoi binning on the Hα S/N (as described below).

The latter procedure was found to be the best at meeting the conflicting goals described above, and has been implemented in the custom-designed analysis pipeline described in the next section.

2.2.2 The fitting algorithm

I extract emission line fluxes and stellar population indices from the MaNGA data through a customised spectral fitting procedure, which models both the stellar continuum and the nebular emission lines.[4] The basic steps implemented in this procedure are described below.

1. I perform an initial Voronoi binning (Cappellari & Copin, 2003) of the MaNGA datacubes based on the continuum S/N in the 6000-6200 Å range. I choose a S/N target of 6 (per 69 km s^{-1} channel), which is well suited to extracting reliable kinematics from the continuum (but not sufficient to derive higher Gauss-Hermite moments of the the stellar line of sight velocity distribution). I do not include in the binning procedure spaxels with S/N <1. The effect of noise covariance between spaxels is taken into account by modifying the original Voronoi binning procedure of Cappellari & Copin (2003) and scaling the binned noise vector according to Eq. 2.1.
2. The resulting binned spectra are fitted with a set of simple stellar population (SSP) models using penalised pixel fitting (PPXF, Cappellari & Emsellem 2004). A window of 1200 km s^{-1} around the expected position of emission lines (taking into account the galaxy redshift) is excluded from the fit. Strong sky lines are also masked. A set of 36 templates from the MIUSCAT SSP library (Vazdekis et al., 2012), spanning a wide range in stellar age (from 60 Myr to 15 Gyr) and four metallicities ([Z/H]=0.2, 0.0, -0.4, -0.7) is used as basis set for the fitting. For each spaxel I fit for a Gaussian line of sight velocity distribution (and derive the velocity [$v_\star$] and velocity dispersion [$\sigma_\star$] of the stellar component). The stellar templates are fitted together with dust extinction (using a Calzetti et al. 2000 extinction law) and a set of additive polynomials up to the 4th order, to take into account possible residual imperfections in the relative spectrophotometry. It is important to acknowledge that the use of additive polynomials

[4] The MaNGA data analysis pipeline, performing a similar set of tasks, was still being developed during the time of my PhD. All the results presented in this thesis are thus based on a spectral fitting code written by me and run locally on a machine in the Kavli Institute for Cosmology in Cambridge. Parts of this code have since been adapted and integrated into the MaNGA analysis pipeline. Comparisons checks of some of the derived quantities (like emission line fluxes) with the first science-grade products of the MaNGA data analysis pipeline (as of November 2016) reveal good correspondence with my results at the percent level.

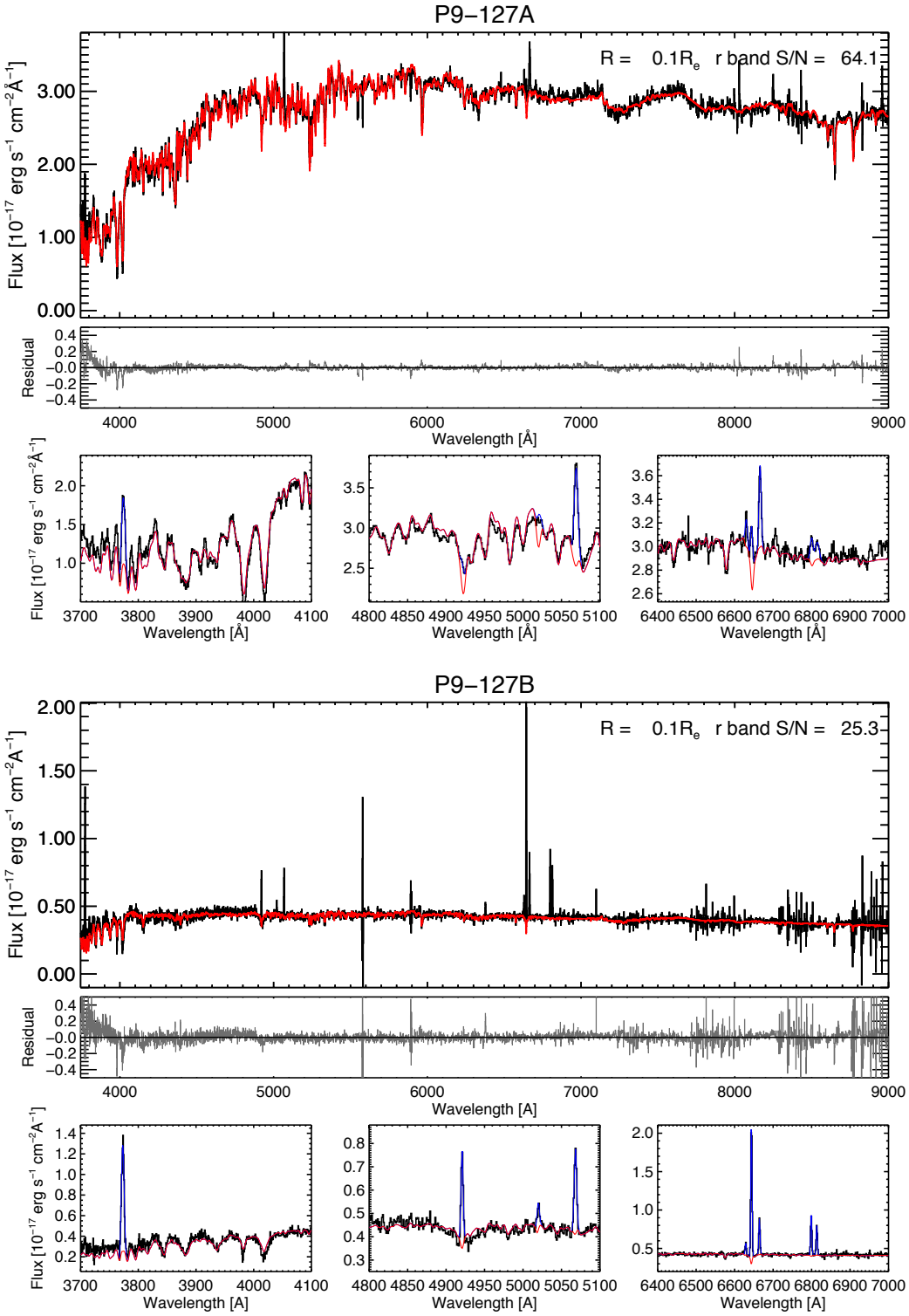

Figure 2.6: Spectral fitting of two spectra, corresponding to Voronoi bins in the central regions of two P-MaNGA galaxies: P9-127B and P9-127A. For each galaxy, the top panel shows the spectrum (black) with the SSP fitting (red). Fit residuals are shown in the middle panel. The smaller panels at the bottom show the details of the fit in three narrow wavelength ranges: around 4000 Å (note the prominent [OII] λ3727 unresolved doublet), 5000 Å (with prominent Hβ and [OIII] $\lambda\lambda$4945,5007 lines) and 6700 Å(with prominent Hα, [NII] $\lambda\lambda$6548,6584 and [SII]$\lambda\lambda$6717,6731 lines). The observed spectrum is in black, the SSP fit in red and the emission line fit (summed to the SSP fit) in blue. Note that the blue fit is sometimes not clearly visible in the plot due to absorption infill (for example in the case of the Hβ line for P9-127A), even though the line is well detected. The galactocentric distance in units of R$_e$ and the S/N in the r-band (from fit residuals) is shown in the top right corner. From Belfiore et al. (2015).

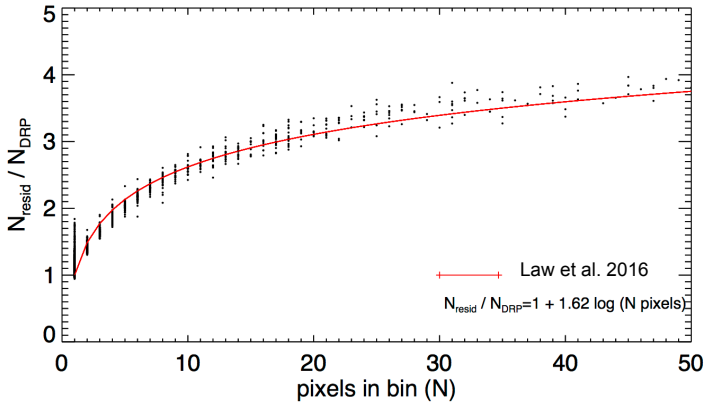

Figure 2.7: The relation between the noise obtained from the fit residuals (N_{resid}) and the noise vector obtained from the data reduction pipeline neglecting the effect of spatial covariance between pixels (N_{DRP}) as a function of number of spaxels in a Voronoi bin. The relation from Law et al. (2016) is plotted in red (Eq.2.1) and constitutes a good representation of the observed trend, demonstrating that the effects of spatial covariance in the data are well-characterised by this approximation.

3. Since the binning on the continuum S/N is not ideal for studying the emission lines, the best-fit continuum within each bin is scaled according to the flux in the 6000-6200 Å range and subtracted from the observed spectrum on a spaxel-by-spaxel basis. An emission-line-only datacube is obtained on the original spaxel grid. This procedure is not ideal, since it assumes that the shape of the continuum, and in particular the absorption infill, is the same within the Voronoi bin. However it has the advantage of providing a physical model for the continuum even when the low S/N in the individual spaxels would have made such measurement highly uncertain.

4. After this step, a second Voronoi binning based on the S/N around Hα is performed. The S/N around Hα is estimated by summing the flux around the expected position of the Hα line in a 600 km s^{-1} window. Spaxels that had been previously rejected by the continuum-based Voronoi binning for having undetected continuum are also considered at this stage, after subtracting the median flux in the 6000-6200 Å range. After extensive testing an Hα S/N target of 4 was implemented and spaxels with S/N < 1 were rejected. This choice only leads to a moderate amount of binning, and is found to be appropriate for MaNGA data in order not to mix light from the bright HII regions with light from the diffuse component.

5. For each bin the emission lines are simultaneously fitted with a set of Gaussians, one per line. To increase the ability to fit weaker lines, the velocities of all lines are tied together. In this way the stronger lines are used to constrain the kinematics of the weaker ones. In the case of the [OIII] $\lambda\lambda$4959,5007 and [NII] $\lambda\lambda$6548,83 doublets their dispersions are tied together and their amplitude ratios are fixed to the theoretical ratios. Fluxes are obtained by integrating the Gaussian best fit to the line. Errors on the flux are derived from the formal errors on the amplitude and dispersion of the Gaussian fit.

6. The reddening for the gas component is calculated from the Balmer decrement, for those spaxels where both Hα and Hβ are detected with S/N > 3, and a Calzetti et al. (2000) reddening curve with $R_V = 4.05$. The theoretical value for the Balmer line ratio is taken from Osterbrock & Ferland (2006), assuming case B recombination (Hα/Hβ = 2.87). The use of the extinction curve

of Cardelli et al. (1989) (or the modification by O'Donnell 1994) with $R_V = 3.1$ yields very similar results across the MaNGA wavelength range. Emission line fluxes are then corrected for the effect of reddening using the derived extinction map.

Based on Monte Carlo simulations of model data to which a suitable noise model was added and based on analysis of repeat observations, I conclude that, when an emission line is detected with S/N > 3, the uncertainties calculated by my pipeline are realistic under a wide range of conditions.[5] The uncertainties are less reliable for galaxies with stronger continuum and older stellar populations, for which an accurate continuum subtraction plays a key role. Simulations show that this spectral fitting procedure is able to recover line fluxes with negligible bias and less than 0.12 dex error for S/N > 3 for all strong lines except Hβ, which suffers from larger errors ($\sim$ 0.2 dex) and a small positive bias (generally less than 0.08 dex), possibly due to the uncertainties associated with the continuum subtraction.

To test the reliability of the emission line fluxes, the fitting procedure detailed above has been repeated using the Bruzual & Charlot (2003) templates (used in previous work with SDSS data, Tremonti et al. 2004) for a set of P-MaNGA data (see Sec. 2.3). The resulting fit residuals and emission line fluxes obtained with the Bruzual & Charlot (2003) templates were found to be in good statistical agreement with those obtained using MIUSCAT templates.

To evaluate the effect of the approximate treatment of noise correlation between different spaxels when building the Voronoi bins, I estimated of the noise 'a posteriori' using the standard deviation of the fit residuals in the r-band. While this noise estimate will be affected by template mismatch, it should represent an upper limit on the true noise. This noise is plotted against the noise obtained for each bin neglecting covariance. The resulting relation between the measured noise and that estimated from neglecting covariance is well-represented by Eq. 2.1 (Fig. 2.7), demonstrating that the error estimation on the line fluxes is not substantially affected by the effect of spatial covariance.

Emission lines equivalent widths (EW) are calculated for each line by dividing the line emission by its neighbouring continuum, and are defined to be positive in emission. Note that all EWs are measured after correction for continuum absorption, i.e. I consider the *emission component* of the EW.

2.3 The MaNGA prototype instrument and data

The MaNGA prototype instrument (P-MaNGA) refers to a preliminary version of the MaNGA hardware that was used to conduct engineering tests and develop the data reduction and analysis strategy. Key hardware questions addressed by the P-MaNGA run include the number of fibres allocated to sky subtraction and flux calibration, the method used for flux calibration (use of mini-bundles versus larger fibres), and the determination of the optimal density of fibres across the slit (and thus the total number of fibres available). P-MaNGA observations were taken in December 2012 and January 2013, and included three galaxy plates, each targeting 6 galaxies. These targets were chosen for specific testing reasons and do not match the MaNGA target selection described in Sec. 2.1.3. Each plate was observed to a different depth, in variable seeing conditions, as reported in Belfiore et al. (2015).

[5] In case of a spectral line S/N is defined as the *amplitude* of the fitted Gaussian divided by the average noise in a nearby bandpass.

Sky subtraction was limited by the discovery of a substantial coma aberration in one of the BOSS spectrograph, which was subsequently fixed before the start of survey operations. Moreover, the flux calibration accuracy is limited to ~ 10 %, because single large fibres were used instead of fibre bundles. The sub-standard performance of the flux calibration obtained in P-MaNGA was the deciding factor driving the manufacture and adoption of mini-bundles for flux calibration.

Despite the limitations of this dataset, P-MaNGA observations have resulted in a set of scientific papers demonstrating the strengths of the MaNGA instrument for the study of emission lines (Belfiore et al., 2015), spectral fitting (Wilkinson et al., 2015) and stellar population indices (Li et al., 2015). In particular, in Belfiore et al. (2015) I made use of the analysis pipeline described in Sec. 2.2.2 and studied the excitation property of the gas via standard BPT diagnostic diagrams. An example of the wealth of information available in the P-MaNGA dataset is presented in Fig. 2.8. The details of the P-MaNGA analysis are not further discussed in this thesis, since they are largely superseded by the studies presented in chapters 3 and 5 of this thesis, which are based on large samples of MaNGA survey galaxies.

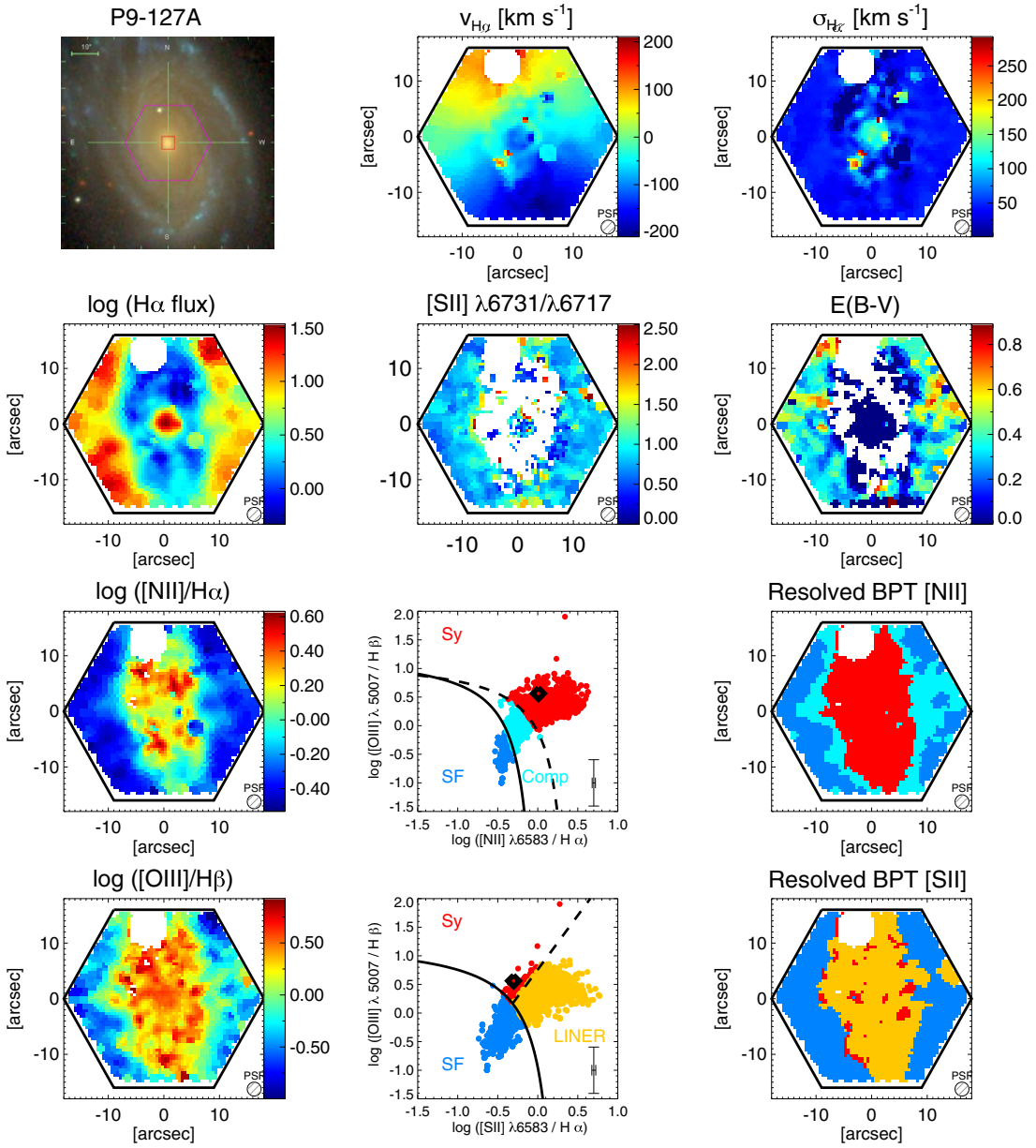

Figure 2.8: Maps of several key quantities for galaxy P9-127A, observed as part of the P-MaNGA program. From the top left: (i) A g-r-i colour-composite image from SDSS, with the positions of the P-MaNGA IFU (purple hexagon) and the SDSS 3 arcsec-diameter fibre (red box) shown. (ii) Map of the Hα velocity (in units of km s^{-1}). (iii) Map of the Hα velocity dispersion (σ), corrected for instrumental dispersion (in units of km s^{-1}). (iv) Map of the log of the Hα flux, in units of 10^{-17} erg s^{-1} cm^{-2} Å^{-1}. (v) Map of the flux ratio of the [SII] doublet ([SII] λ6731/[S II] λ6717). This diagnostic is a proxy for electronic density in the gas. (vi) Map of E(B-V) of the gas obtained from the Balmer decrement. (vii) Map of the flux ratio log([NII] λ6584/Hα). (viii) Classical BPT diagram using the [N II] λ6584/Hα and [OIII] λ5007/Hβ line ratio. The open diamond corresponds to the line ratios obtained from the Sloan 3 arcsec-diameter fibre. The median error is shown in the bottom-right corner. (ix) Map of the excitation mechanism of the gas as traced by the [NII] BPT diagram. The colour-coding reflects the position of each region in the BPT diagram and corresponds to the same colour of the spaxels (SF, Inter, and Sy) in the [NII] BPT diagram. (x) Map of the flux ratio log([O III] λ5007/Hβ). (xi) Classical BPT diagram using the [SII] $\lambda\lambda$6717, 31/Hα and [OIII] λ5007/Hβ line ratio. Each point corresponds to a Voronoi bin within the galaxy. The open diamond corresponds to the line ratios obtained from the Sloan 3 arcsec-diameter fibre. The median error is shown in the bottom- right corner. (xii) Map of the excitation mechanism of the gas as traced by the [SII]-BPT diagram. The colour-coding reflects the position of each region (SF, Sy, LINER) in the [SII] BPT diagram. The PSF of the P-MaNGA data is represented in all maps in the bottom-right corner. Adapted from Belfiore et al. (2015).

Chapter 3

Emission lines diagnostic ratios: why some galaxies are LIERs

Based on 'SDSS IV MaNGA - Spatially resolved diagnostic diagrams: A proof that many galaxies are LIERs', F. Belfiore et al., 2016, MNRAS, 461, 3111.

The properties of galaxies in terms of their star formation activity are observed to follow a bimodal distribution, often expressed in terms of a red sequence and blue cloud (Sec.1.2.2, Strateva et al. 2001; Blanton et al. 2003b; Baldry et al. 2004, 2006). These two sequences are separated not only in their integrated optical and UV colours (Wyder et al., 2007), but also in their stellar populations (e.g Kauffmann et al., 2003b), cold gas content and ionised gas properties (Kewley et al., 2006; Saintonge et al., 2011).

Galaxies in the blue cloud are characterised by an emission line spectrum typical of classical HII regions, with nebular line ratios varying mostly as a function of metallicity and ionisation parameter (Sec. 1.4.3, Kewley et al. 2001; Levesque et al. 2010). Conversely, galaxies on the red sequence are either completely devoid or host only low levels of residual line emission (e.g. Phillips et al., 1986; Goudfrooij, 1999; Sarzi et al., 2010), with line ratios generally inconsistent with those expected from star formation. These spectra are characterised by strong low-ionisation transitions (e.g. [OI] λ6300, [SII] $\lambda\lambda$6717,31) and display the characteristic line ratios of LINERs (Heckman, 1980).

Originally associated with weak active galactic nuclei (Kauffmann et al., 2003c; Kewley et al., 2006; Ho, 2008), LINER emission has recently attracted increasing amounts of attention. Spatially resolved observations have demonstrated that LINER-like emission is not confined to nuclear regions in galaxies, but often appears to be extended on kpc scales (Sarzi et al., 2006, 2010; Singh et al., 2013), especially in early-type galaxies. In these galaxies, several authors have argued that the extended LINER-like emission is consistent with photoionisation by hot evolved stars (and in particular pAGB stars), which become the main source of ionising photons in quiescent regions after star formation has ceased (Binette et al., 1994; Stasińska et al., 2008; Cid Fernandes et al., 2011; Yan & Blanton, 2012). While observational support for the 'stellar hypothesis' for LINER emission is mounting, previous work has been limited by lack of spatial resolution (e.g. Yan & Blanton, 2012), wavelength coverage (e.g. Sarzi et al., 2010) or small sample size (e.g. Singh et al., 2013).

In this chapter we make use of a large sample of 646 galaxies of all morphological types and

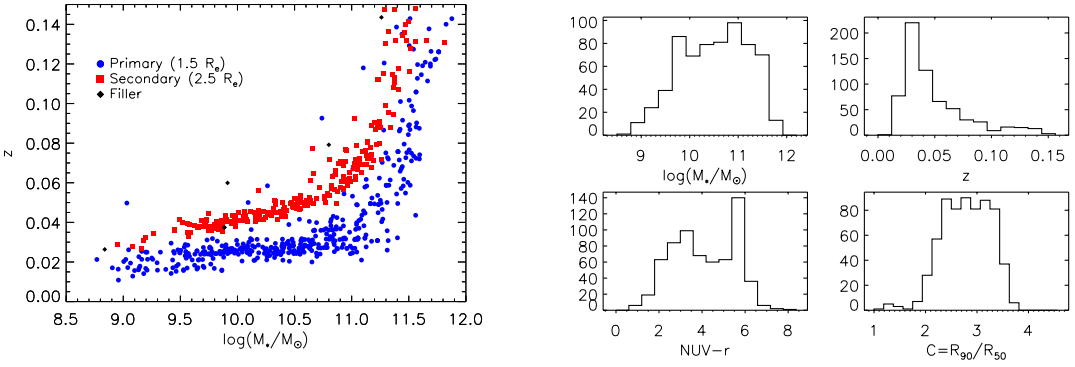

Figure 3.1: *Left*: The MaNGA sample used in this chapter in the stellar mass-redshift plane. Due to the fixed size distribution of the MaNGA bundles and the fact that MaNGA observes galaxies out to a fixed galoctocentric distance in terms of R_e, higher mass galaxies are preferentially observed at higher redshift. For an equivalent reason the secondary sample (radial coverage out to 2.5 R_e) is preferentially observed at higher redshift at fixed stellar mass. A handful of galaxies have been observed while not fitting in either the primary or secondary sample selection functions and are designed as 'filler'. *Right*: Histogram distributions of stellar mass, redshift, $NUV-r$ colour and concentration parameter ($C = R_{90}/R_{50}$, where R are Petrosian radii) for the galaxy sample used in this chapter. We note that our sample is roughly flat in stellar mass in the range $\log(M/M_\star) > 9.0$, has median redshift $< z >\sim 0.037$ and samples well both the blue cloud and the red sequence.

covering a wide range in stellar mass ($10^9 - 10^{12}$ $M_\odot$) observed with IFS to map the excitation properties of the ionised gas and study the occurrence and properties of LINER-like emission. We make use of data from the SDSS-IV MaNGA survey (Sec. 2, Bundy et al. 2015). Crucially for the aim of this work, MaNGA's observed wavelength range (3600 -10300 Å) covers all the strong nebular lines used in the standard BPT (Baldwin et al., 1981; Veilleux & Osterbrock, 1987) excitation diagnostic diagram. Moreover, the large and well-defined sample, combined with the uniform spatial coverage of MaNGA (covering galaxies out to at least 1.5 effective radii [R_e]), allows us to study ionised gas across both the red sequence and the blue cloud at kpc spatial resolution.

The MaNGA data was reduced using version `v1_3_3` of the MaNGA reduction pipeline (Law et al., 2016). The stellar mass and redshift distribution of the sample used for this work is shown in Fig. 3.1. The sample includes all MaNGA galaxies observed before April 2015 (first 8 months of survey operations) and consists of 646 unique galaxies (not taking into account the possible presence of smaller companions/satellites within a single MaNGA bundle). The properties of this sample compare well with the properties of the full MaNGA parent sample in terms of stellar mass coverage (approximately flat in stellar mass for $\log(M_\star/M_\odot) > 9$) and redshift ($< z >\sim 0.037$). Spectral fitting was applied to the reduced MaNGA datacubes according to the procedure described in Sec. 2.2 to obtain line fluxes and resulting errors, stellar population indices and measurements of the extinction correction based on the Balmer decrement. In this chapter, given the vicinity in wavelength of the ratios of lines considered, line fluxes are not corrected for the effects of extinction unless otherwise stated.

3.1 Emission line diagnostic diagrams and the role of LI(N)ER excitation

3.1.1 Hot evolved stars as sources for LI(N)ER emission

Motivated by earlier work on line emission on the red sequence (Phillips et al., 1986; Trinchieri & di Serego Alighieri, 1991), Binette et al. (1994) studied the ionising spectrum due to pAGB stars predicted by the stellar population models of Bruzual & Charlot (1993), demonstrating that they can lead to LI(N)ER-like line ratios. pAGB stars in this context include all the stages of stellar evolution subsequent to asymptotic giant branch, including the hydrogen burning, white dwarf cooling and intermediate phases (see Stanghellini & Renzini 2000 for a detailed discussion). Since the time spent by stars in the pAGB phase is a strong function of the core mass, only stars within a rather small mass range (core mass 0.55-0.64 $M_{\odot}$, or initial mass 1-3 $M_{\odot}$) appear as planetary nebulae (Tylenda & Stasinska, 1989; Weidemann, 2000; Buzzoni et al., 2006). In the case of pAGB stars with smaller core masses, the hydrogen ionisation temperature is reached too slowly and only after the material expelled during the AGB phase has already been lost to the general ISM. These stars have been referred to as 'lazy pAGB' stars. pAGB stars are generally hot, with typical temperatures around 30 000 K, and are thus ideal candidates as sources of ionising and UV photons. Indeed, stellar population models demonstrate that these stars are the main source of the ionising photon background in galaxies once star formation has ceased (Binette et al., 1994).

The low Hα equivalent widths (EW(Hα) $<$ 3 Å) observed in most early type galaxies are compatible with the expectations from reprocessing of the ionising radiation from hot evolved stars (Binette et al., 1994; Stasińska et al., 2008; Cid Fernandes et al., 2011), although some controversy persists in the literature as to whether equivalent widths larger than 1 Å can be powered solely by stellar emission. Theoretically, this is a difficult question to address, since several uncertainties remain in our modelling of pAGB evolution, including the initial-final mass relation and the residual envelope mass (O'Connell, 1999; Stanghellini & Renzini, 2000).

In this section we compute the time evolution of the EW(Hα) after a starburst predicted by population synthesis models (by C. Maraston) including a treatment of the pAGB phase. The pAGB phase is included following the stellar tracks for the pAGB phase based on the calculations of Stanghellini & Renzini (2000), and make use of the fuel consumption theorem to compute the post-main sequence evolution, as detailed in Maraston (1998, 2005). In this context, the *fuel* consumed by a specific phase of stellar evolution is defined to be the amount of stellar mass to be converted in luminosity (where the helium mass is suitably scaled with respect to hydrogen to take into account the different energy release, Maraston 1998).

In Fig. 3.2 we show the predicted ionising photon flux and EW(Hα) for this model. The reference model shows the time evolution of a starburst, demonstrating the precipitous decline in the ionising photon flux and EW(Hα) following the death of massive OB stars. The inclusion of the pAGB phase generates ionising photons in old populations as soon as the pAGB phase contributes a sizeable amount of fuel. We note that the exact time after which the pAGB phase starts consuming sizeable amounts of fuel ($\sim$ 2 Gyr in this model) is strongly dependant on the details of the calculation and the adopted stellar tracks. The reference pAGB model produces an ionising photons flux of $Q_{\rm ion} \sim 10^{41} (M_{\star}/M_{\odot})$ and an EW(Hα) $\sim$ 0.8 Å. These values are consistent with the range of predictions obtained in

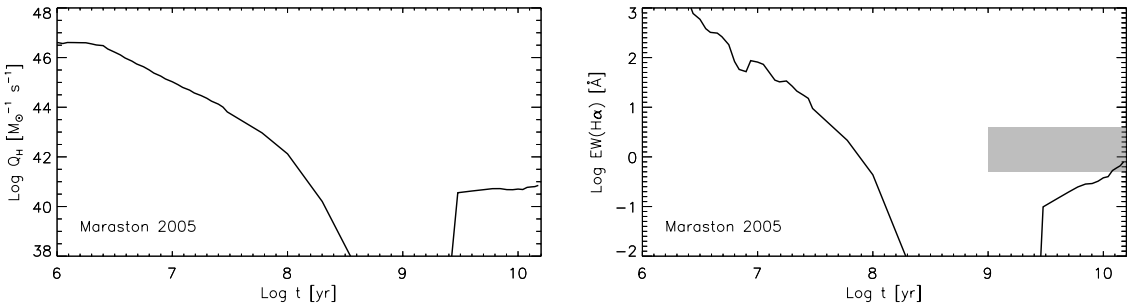

Figure 3.2: The ionising photon flux (Q_H) per unit stellar mass and the equivalent width of Hα as a function of age after the starburst for Maraston (2005) stellar population models, using pAGB (including planetary nebulae) model tracks based on Stanghellini & Renzini (2000). The ionising flux and EW(Hα) due to the young stellar population declines quickly after the burst. Physically motivated choice of pAGB parameters predict an EW(Hα) in the range 0.5 - 3.0 Å at late times, corresponding to the shaded in grey in the right panel.

previous modelling of the pAGB phase presented in the literature (Binette et al., 1994; Cid Fernandes et al., 2011).

In order to gain some physical understanding of the uncertainties involved in the values calculated, we also calculate a simple ad-hoc pAGB prescription, where the ionising flux of the evolved population depends on two free parameter: the fuel consumed during the pAGB phase and the *mean* effective temperature of pAGB stars (where the average is intended to be a time-average; this approach was already followed in Maraston & Thomas 2000 to model the UV spectra of elliptical galaxies). Either a small increase in the fuel consumption or an increase in the mean temperature with respect to those assumed in the reference model would increase the predicted EW(Hα). A realistic choice of parameters (fuel in the range $6 \cdot 10^{-3} - 6 \cdot 10^{-2}$ $M_\odot$ and mean temperature in the range 25000 – 40000 K) leads to EW(Hα) in the range 0.5-3.0 Å (represented by the shaded region in Fig. 3.2).

3.1.2 LI(N)ERs host old stellar populations

In further support of the stellar hypothesis for LI(N)ER emission legacy SDSS spectroscopy has shown that LI(N)ER galaxies have substantially older stellar populations than any other spectral type (Kauffmann et al., 2003c; Kewley et al., 2006), including Seyfert galaxies. In order to allow for a direct comparison between large spectroscopic samples like legacy SDSS and the new MaNGA data, we show in Fig. 3.3a,c the BPT diagnostic diagrams for the SDSS main galaxy sample (Strauss et al., 2002). Emission line fluxes and spectral indices are taken from the MPA-JHU catalogue (Brinchmann et al., 2004; Kauffmann et al., 2003c; Tremonti et al., 2004), and the demarcation lines shown are from Kewley et al. (2001) and Kauffmann et al. (2003c).

The middle and right panels of Fig. 3.3 show the average value of the age-sensitive spectral indices $D_N(4000)$ and Hδ_A as a function of position in the BPT diagram. $D_N(4000)$ (also referred to as the '4000 Å break') is calculated here by adopting the definition in Balogh et al. (1999). The break results from the combination of the Balmer break with a number of metal lines in a narrow wavelength region. In hot stars, these metals are multiply ionised and the break will be small (and dominated by

the Balmer break), while as cooler stars start to dominate the stellar population the break increases due to metal-line blanketing. Therefore $D_N(4000)$ is a sensitive probe of the overall ageing of the stellar population, and is roughly independent of metallicity for ages less than 1 Gyr. The equivalent width of $H\delta_A$ (defined by Worthey & Ottaviani 1997) is primarily sensitive to stars of intermediate spectral type (A to early F) and thus increases until about 300-400 Myr after the burst (post-starburst population) and then decreases again at later times (Kauffmann et al., 2003b; González Delgado et al., 2005). At late ages, both indices are known to depend both on the age and the metallicity of the stellar population (Thomas et al., 2004; Korn et al., 2005; Thomas & Davies, 2006).

As evident from Fig. 3.3a,c, LI(N)ER emission in the central region of galaxies, as probed by legacy SDSS, is associated with high $D_N(4000)$ values and low EW($H\delta_A$), hence ruling out the presence of young stars (younger than 1 Gyr) in LI(N)ER regions.

3.1.3 The role of diffuse ionised gas (DIG)

Diffuse ionised gas (DIG) with LINER-like ratios is observed surrounding the plane and filling in the regions between HII regions in the Milky Way and other spiral galaxies (Reynolds, 1991; Martin, 1997; Martin & Kennicutt, 1997; Hoopes & Walterbos, 2003; Rossa & Dettmar, 2003; Oey et al., 2007; Haffner et al., 2009; Blanc et al., 2009; Flores-Fajardo et al., 2011). This gas is warm (10^4 K), low density (10^{-1} cm^{-3}) and has low ionisation parameter. Its ionisation source is not yet well understood, but is generally compatible with photoionisation by radiation from stellar sources (O and B stars, but possibly also hot evolved stars), filtered and hardened by photoelectric absorption by gas in the disc. Study of the DIG in external galaxies remains difficult because of its low surface brightness, however extensive work on edge-on galaxies (see for example the prototype case of NGC 891 as studied in Rand et al. 1990; Rossa et al. 2004; Bregman et al. 2013) has demonstrated that DIG emission is detectable up to several kpc from the disc midplane. DIG with LINER-like emission is also observed in regions of low surface brightness across the disc of star forming galaxies (Walterbos & Braun, 1994; Oey et al., 2007). The distinction between bright HII regions and DIG is therefore somehow ill-defined, since the spectroscopic properties of the gas vary gradually and continuously as a function of line emission surface brightness (Martin, 1997). Moreover, since DIG is pervasive in star forming galaxies, its presence will affect the line ratios measured for star forming regions in the limit of low surface brightness. The binary classification of regions between LINER and star forming discussed in this chapter is thus to be intended only as a first order division, because of the inevitable presence of DIG contamination.

3.1.4 From LINER to LIER

Evidently several different physical processes can be responsible for LI(N)ER-like emission in galaxies. Studies of the central few parsecs in nearby galaxies (Ho et al., 1997; Shields et al., 2007) demonstrate that LINER emission on those scales can be associated with nuclear accretion phenomena, in particular weak, radiatively inefficient AGNs (see for example the review from Ho 2008). However, LI(N)ER-like emission on larger scales is far from trivial to interpret. With few exceptions (e.g. NGC 1052, Pogge et al. 2000) AGN-related LINERs do not show elongated structures analogous to ionisation cones in Seyfert galaxies.

Moreover, at the typical scales probed by the SDSS fibre and by the MaNGA PSF (few kpc)

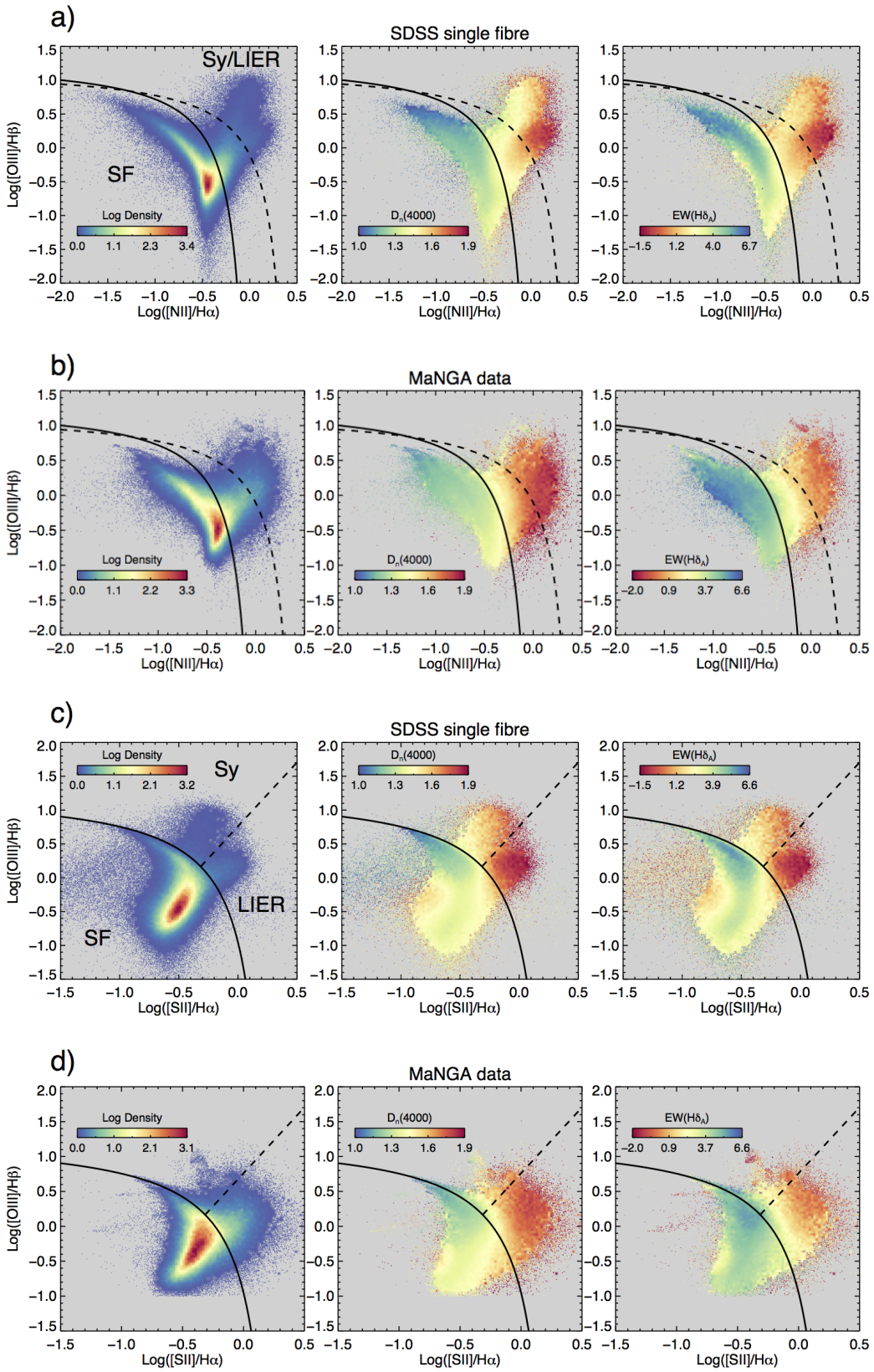

Figure 3.3: The BPT diagnostic diagrams based on [NII]/Hα (top) and [SII]/Hα (bottom) for the galaxies in the MPA-JHU legacy SDSS sample and MaNGA sample used in this work. The three panels in each row show respectively the density of galaxies (left), the average $D_N(4000)$ (middle) and EW($H\delta_A$) (right) across the BPT diagram. The demarcation lines are discussed in Sec. 3.2. For each plot, both axes have been divided in 100 intervals thus creating small bins in the 2D space. Bins containing more than 20 galaxies are represented by the average value of the quantity (or total number density). For bins containing less than 20 galaxies, the individuals values of each galaxy are shown. For the SDSS legacy data, emission line fluxes and stellar population indices are taken from the MPA-JHU catalogue (Brinchmann et al., 2004; Tremonti et al., 2004).

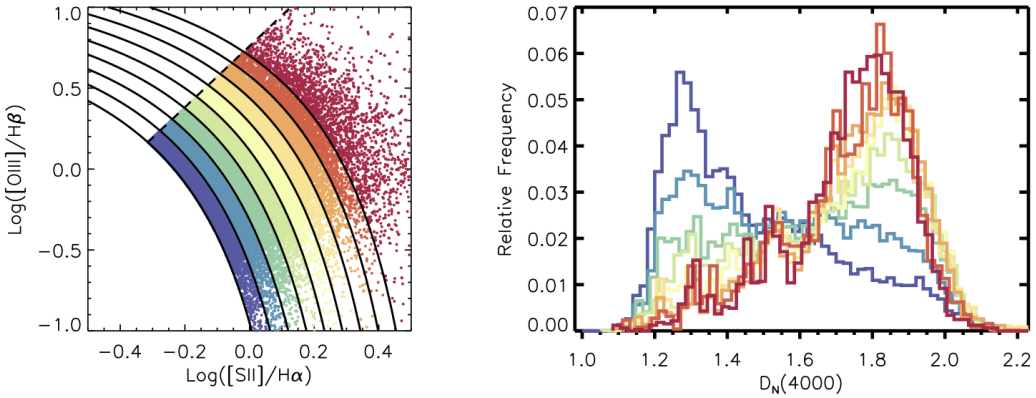

Figure 3.4: A zoom-in in the LIER region of the [SII] BPT diagram. Following Kewley et al. (2006), we draw a set of curves parallel to the demarcation curve of Kewley et al. (2001) to define the distance from the SF sequence. Successive curves are separated by a 0.05 dex interval in log([SII]/Hα) and log([OIII]/Hβ). The right panel shows the histograms of the $D_N(4000)$ distribution as a function of distance from the SF sequence (the colour-coding is the same as in the left panel, with red being furthest from the star forming sequence). Within the LIER spaxels, a clear transition is observed in $D_N(4000)$ as a function of distance from the SF sequence.

the predicted Hα emission from pAGB stars is comparable to or higher than that expected from a weak AGN. To perform an order of magnitude estimate, let us assume a specific ionisation flux from pAGB stars of $Q_{ion} = 10^{41}(M_*/M_\odot)$ (in line with the models in Sec. 3.1.1) and an average stellar mass surface density of $\Sigma_* = 10^3$ $M_\odot$ pc^{-2} (typical of elliptical galaxies or bulges). Under these assumptions, and assuming that all the ionising photons are absorbed in the gas, a 1 kpc^2 region will radiate $L_{H\alpha} \sim 10^{38}$erg s^{-1}. This is of the same order of magnitude as the typical Hα luminosity of well-studied low-accretion rate AGN classified as LINERs (for example, Ho 2008 quotes an average Hα luminosity for LINER AGN of $L_{H\alpha} \sim 5.0 \cdot 10^{38}$erg s^{-1}). Therefore, on the scales probed by MaNGA, LINER-type AGN photoionisation will only be energetically dominant in the very central regions, if at all.

This fact has two important consequences: 1) kpc-resolution surveys (like SDSS or MaNGA) are not suitable for detecting and studying low-luminosity (LINER-type) AGN via their optical line emission, 2) the attribute 'nuclear' in the LINER acronym is misleading when not referred to true nuclear ($\sim$ 100 parsec size) scales. In recognition of the latter, for the rest of this work we drop the 'N' in LINER and refer to low ionisation emission-line regions as 'LIERs'[1].

3.2 Excitation morphologies of emission line galaxies

3.2.1 The BPT diagram on kpc scales

In Fig. 3.3b,d we show the BPT diagnostic diagrams for all the individual spaxels in the current MaNGA sample which have S/N > 2 in all the relevant strong emission lines and S/N > 5 on the continuum. We have checked that similar results are obtained using a different S/N cut or a cut on the error of the considered line ratios (Juneau et al., 2014).[2]

[1]Coincidentally, one might argue this is a more fitting-sounding acronym, in recognition of the long-lasting misclassification of these sources as AGN in surveys like legacy SDSS.

[2]This cut selects approximately $3 \cdot 10^5$ spaxels. Note, however, that spaxels in MaNGA are not statistically independent due to the effects of the PSF and the datacube generation algorithm. On average, considering nearby spaxels, there are

The left panels show the density distribution of all the MaNGA spaxels on the [NII] and [SII] BPT diagrams. In both diagrams the star forming (SF) sequence is clearly visible, together with the less populated right-hand branch. As will be discussed in detail in the following sections (and demonstrated in Cid Fernandes et al. 2011), the S/N cuts imposed above have a strong effect on the fraction of LIER-like spaxels which can be plotted in this diagram, since LIER-like emission is characterised by low surface brightness of line emission.

The middle and right panels of Fig. 3.3b,d show the same sample of spaxels colour-coded by the mean $D_N(4000)$ and EW($H\delta_A$) in each bin. The 'right-hand' sequence in the [NII] BPT diagram and the LIER space in the [SII] BPT diagram show stellar indices typical of old stellar populations (high $D_N(4000)$ and low EW($H\delta_A$)), similarly to what is observed in legacy SDSS (Fig. 3.3a,c). Given the adopted S/N threshold, using Monte Carlo simulations we estimate the maximum uncertainties for spectral indices to be respectively 0.03 for $D_N(4000)$ and 0.5 Å for EW($H\delta_A$).

Compared to the single fibre SDSS data, in the spatially resolved MaNGA data young stellar populations (i.e. low $D_N(4000)$ and high EW($H\delta_A$)) spread towards larger values of [SII]/Hα, [NII]/Hα, and larger [OIII]/Hβ. The result is that young stellar populations extend slightly beyond the adopted demarcation lines between star forming galaxies and AGN/LIERs, in particular in the [SII] BPT diagram, suggesting a potential misclassification of SF regions as dominated by AGN photoionisation in this area of the BPT diagram.

In Fig. 3.4 we focus on the LIER area of the [SII] BPT diagram and draw a set of parallel lines (distanced by 0.05 dex) to define an effective distance from the star forming sequence (compare with a similar study of SDSS LIERs in Kewley et al. 2006). The right panel of Fig. 3.4 demonstrates the existence of two populations of LIER regions with distinct stellar populations. At small distances from the SF sequence, LIER emission is characterised by young ages ($D_N(4000) \sim 1.3$), while moving outwards from the SF sequence we see the emergence of a second populations of LIER regions with much older stellar populations ($D_N(4000) \sim 1.9$). The younger age LIER population is virtually absent in single fibre SDSS data, and is therefore only seen with the larger radial coverage and spatial resolution of MaNGA. We will see in the next sections that this population of LIER regions is mainly associated with diffuse ionised gas and extra-planar emission in star forming galaxies.

We note that the Seyfert branch is underpopulated in MaNGA with respect to legacy SDSS. This is due to a combination of selection effects. Importantly, legacy SDSS observes has much superior statistics in terms of sampling galactic central regions, where AGN ionisation will dominate. Moreover, since Seyferts are rare, they are on average at larger distances than probed by the MaNGA survey and thus more common in SDSS.

3.2.2 A new classification scheme based on spatially resolved line emission

Simple demarcation lines in the BPT diagrams have been the main classification tool to distinguish star formation from other sources of ionisation in several studies based on the SDSS and more distant galaxy samples (Kauffmann et al., 2003c; Tremonti et al., 2004; Kewley et al., 2006, 2013; Shapley et al., 2015). However, a large amount of previous investigations using IFS (see for example Rich et al. 2010; Sharp & Bland-Hawthorn 2010; Singh et al. 2013; Davies et al. 2014; Belfiore et al. 2015; Gomes et al. 2015a) have demonstrates that emission line classifications based on single fibre spec-

approximately 20 spaxels per each PSF element.

troscopy can be systematically biased. In particular, previous IFS work has highlighted the diversity of the ionisation structure within single galaxies. Such diversity is particular dramatic in 'peculiar' galaxies, such as mergers and galaxies hosting AGNs. But 'regular' galaxies can also be characterised by different excitation processes in different galactic regions. In this section we propose a systematic classification of the 'excitation morphologies' of galaxies, based on the large MaNGA sample currently available. The philosophy behind this scheme is to represent a natural extension of the classifications based on single-fibre spectroscopy, while attempting to correct for significant aperture biases.

In Fig. 3.5 we illustrate with some prototypical examples the types of ionisation structures observed in MaNGA galaxies and our proposed revised classification scheme.

Star forming (SF) galaxies

The galaxy in Fig. 3.5a (MaNGA-ID `1-114306`) is a typical star-forming galaxy. Its prominent spiral arms are populated by bright star-forming regions, which at the MaNGA kpc resolution generally consist of several classical HII regions (Mast et al., 2014), evident in the Hα flux map. The vast majority of spaxels are classified as star forming using either the [SII] and [NII] BPT diagrams.

Galaxy `1-636015` (Fig. 3.5b) shows the typical ionisation structure of strongly star forming edge-on discs. While the disc itself is characterised by SF line ratios, moving above and below the disc we observe a transition to LIER excitation. The change in excitation conditions can be interpreted as a transition from HII-dominated ionisation in the disc to DIG, as discussed in Sec. 3.1.3, and possibly shocks (Fogarty et al., 2012; Ho et al., 2016). We note that LIER emission consistent with DIG is also sometimes observed in MaNGA in SF galaxies in inter-arm regions (Zhang et al., 2017).

For the purpose of this work, since we aim at a general galaxy classification scheme, LIER-like DIG is considered a constituent part of the ionised gas in normal SF galaxies. We therefore do not assign a different class to SF galaxies where LIER-like DIG is detected in the outer/inter-arm regions. Thus, operationally a galaxy is defined as SF if a region of the size of the MaNGA PSF in the galaxy centre is classified as star forming.

Central LIER (cLIER) galaxies

The galaxy in Fig. 3.5c (MaNGA-ID `1-155926`) exemplifies a galaxy class showing LIER emission at small galactocentric radii and a transition to SF line ratios further out. Observations of the nuclear regions (e.g. with SDSS single fibre spectroscopy) would classify this galaxy as LI(N)ER, but would miss the star formation in the disc. We denote this class of galaxies 'central LIER' (cLIER). In order to define a galaxy as cLIER, we require the LIER emission in the centre to be spatially extended (i.e. larger than the MaNGA PSF, indicated in the bottom-right corner of the maps in Fig. 3.5), and at the same time star forming regions to be clearly detected at larger radii (larger than one PSF). After an initial automatic classification the maps for all galaxies were visually inspected to confirm the robustness of the classification to the effect of noise/marginal line detections. As a class of galaxies cLIERs have not yet been subject of a systematic investigation in the literature, although they can be related to the small samples presented in previous work (e.g. Gomes et al., 2015b,a; James & Percival, 2015).

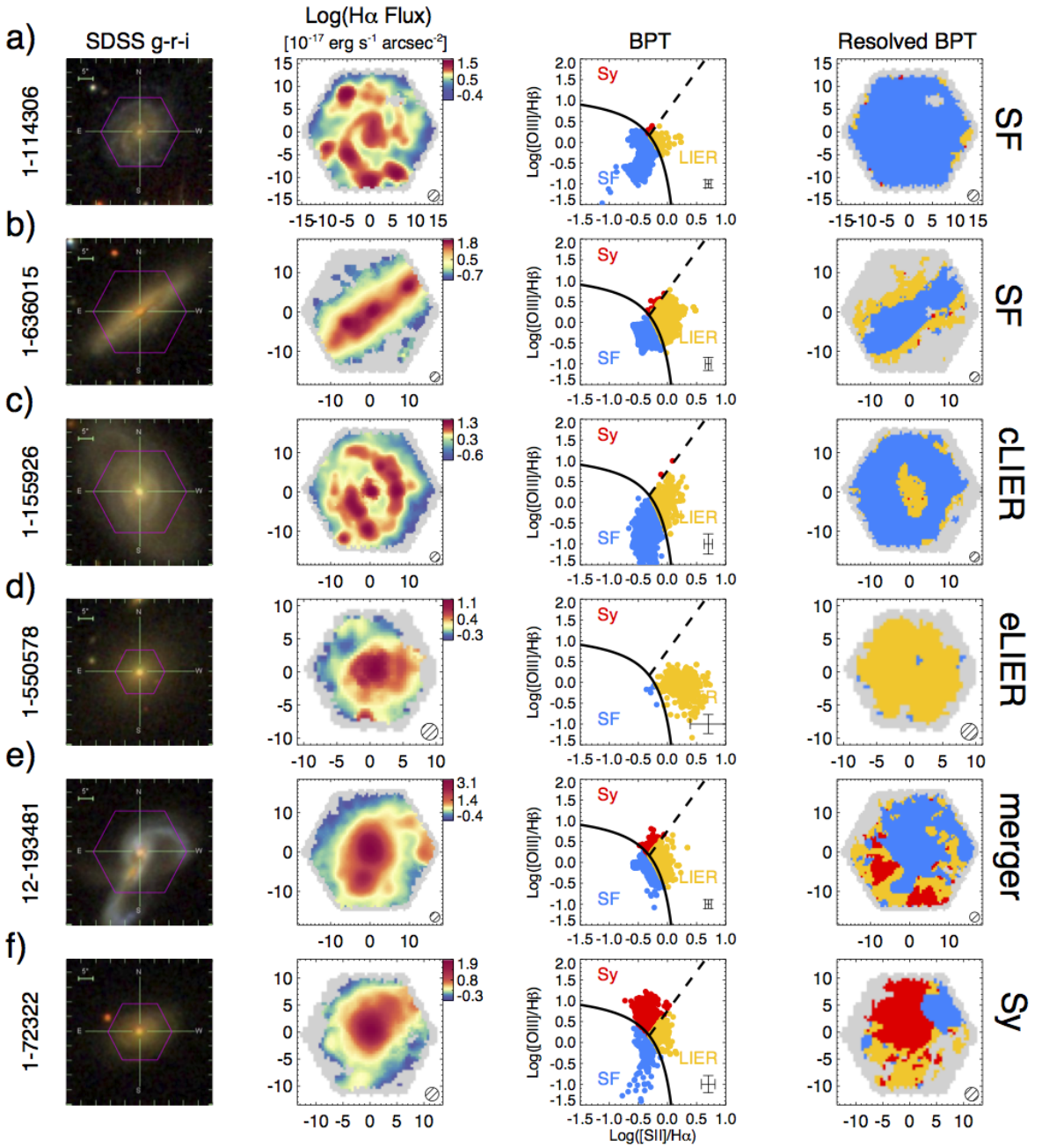

Figure 3.5: Examples of the different gas excitation conditions observed in MaNGA galaxies. Following the classification scheme described in the text, from top to bottom, galaxies are classified as follows: (a) `1-114306` star forming (SF); (b) `1-636015` star forming with clear extra-planar LIER emission; (c) `1-155926` LIER central (cLIER); (d) `1-114928` LIER extended (eLIER); (e) `12-193481` peculiar (merger); (f) `1-72322` Seyfert (Sy). Each row shows, from right to left (1) a $g-r-i$ image composite from SDSS with the MaNGA hexagonal FoV overlaid. (2) A map of Log(Hα Flux), with histogram stretching of the colour-bar. (3) The [SII] BPT diagram showing the position of each spaxel (and typical line ratio uncertainties in the bottom right corner). (4) A map of the galaxy colour-coded according to the position of individual regions with the same colour-coding as in (3). The MaNGA PSF is shown as a hatched circle in the bottom right corner of the MaNGA maps. The greyed area corresponds to the FoV of the MaNGA bundle.

Extended LIER (eLIER) galaxies

The galaxy in Fig. 3.5d (MaNGA-ID 1-550578) is a typical example of an early type galaxy showing extended LIER emission. This is the class of LI(N)ERs that has received the most attention in the literature, especially through the contributions of the SAURON and ATLAS^{3D} projects (Sarzi et al., 2006, 2010) and more recently the CALIFA team (Kehrig et al., 2012; Singh et al., 2013; Papaderos et al., 2013), and for which the non-AGN nature of LIER emission has the strongest support. We will refer to these galaxies as 'extended LIER' (eLIER). We consider a galaxy to be an eLIER if it does not show signs of star formation at any galactocentric distance and its central regions are classified as LIER.

Mergers and interacting systems

In order to highlight the complications arising in 'peculiar' systems, we show the MaNGA observations of a major merger of two star forming galaxies in Fig. 3.5e (MaNGA-ID 12-193481). The central regions and most of the tails of the individual merging galaxies are dominated by SF line ratios, while a large fraction of the more diffuse gas shows line ratios falling beyond the SF sequence in the BPT diagram (both LIER-like and Seyfert-like). Shocks, non-virial motions and outflows are likely to play a major role in the ionisation structure of this type of systems (see further discussion in Sec. 3.5.3). In the analysis presented in this chapter we exclude mergers from our sample of 'normal' galaxies.

Seyfert galaxies

Seyfert galaxies generally display large regions photoionised by the nuclear source (photoionisation cones), extending from the nucleus to kpc scales, often associated with disturbed gas kinematics (outflows and other non-virial motions). In Fig. 3.5f (MaNGA-ID 1-72322) we show an example of a Type 2 Seyfert galaxy. The excitation structure appears complex, featuring LIER ratios and also SF regions outside the area photoionised by nuclear emission. Seyfert galaxies (i.e. galaxies where the central PSF is classified as Seyfert using the [SII] BPT diagram) are excluded from further analysis presented in this chapter.

Line-less galaxies

Finally, some galaxies do not show any detectable significant line emission. We will refer to these galaxies as 'line-less'. In the literature, galaxies are often defined as 'line-less' if their emission lines do not meet a set S/N level (e.g Brinchmann et al., 2004). However, we consider that a definition which is independent from the depth of the data would be preferable. In this work, therefore, a galaxy is defined as line-less if the mean EW(Hα) within 1.0 R_e is less than 1 Å. The chosen EW has the advantage of corresponding closely to the sensitivity limit of the MaNGA data. However, we stress that the chosen numerical value does not have a physical motivation and is chosen purely for convenience. We further comment on the definition of line-less galaxies in Sec. 3.3.3.

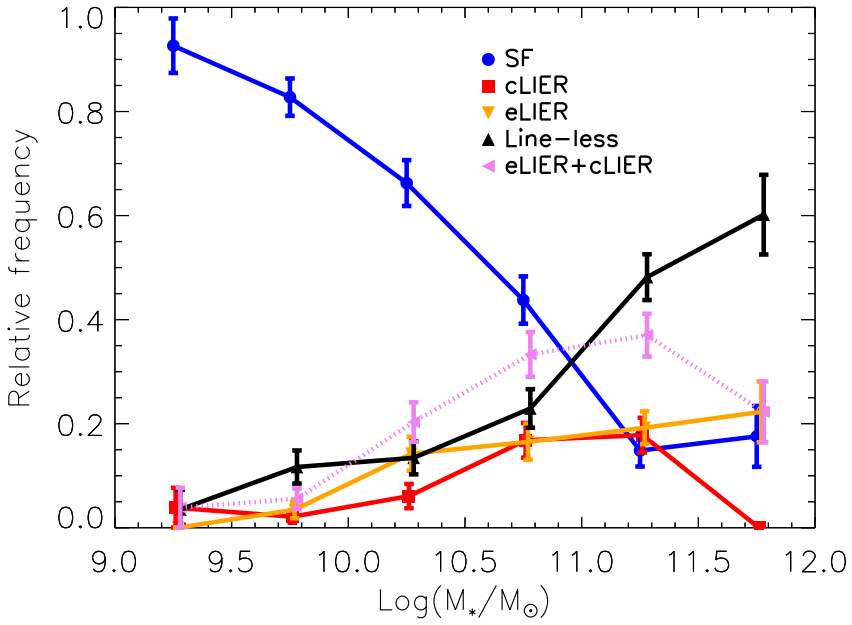

Figure 3.6: The fraction of normal galaxies (excluding interacting galaxies, mergers and AGN) in the current MaNGA sample classified as star-forming (blue), central LIER (red), extended LIER (orange) and quiescent (black) as a function of stellar mass. The sum of both eLIER and cLIER classes is also shown (dotted magenta line). Galaxies with ambiguous BPT classification have also been excluded. The MaNGA sample is selected to be representative of the total galaxy population in each stellar mass bin for $\log(M_\star/M_\odot) > 9$ and appropriate volume corrections have been applied to the current sample to correct for effect of the MaNGA selection function. Errors shown are the formal counting errors.

3.2.3 Summary of galaxy classes

The excitation properties of local galaxies, as probed by MaNGA, follow surprisingly regular radial patterns on kpc scales. Apart from the complex ionisation conditions observed in peculiar and active systems (interacting galaxies and Seyferts), the presence of spatially resolved LIER ionisation increases gradually in importance from SF galaxies to cLIER and eLIER galaxies. Moreover, not all possible combinations of excitation properties are observed. For example, there are no galaxies with a line-less central region and star formation at larger radii, nor face-on[3] galaxies with a SF nucleus and extended areas of LIER excitation in the disc.

In Fig. 3.6 we show the fraction of galaxies in the SF, eLIER, cLIER and line-less classes as a function of stellar mass. Mergers, interacting galaxies, Seyfert and galaxies with an ambiguous BPT class have been excluded from this plot. The total number of galaxies in each class in the current sample is as follows: SF (314), cLIER (57), eLIER (61), line-less (151), others (including Seyfert, mergers and unclassified galaxies: 63). The MaNGA sample is not volume-limited as a whole, but it is volume limited in each bin in i-band absolute magnitude. Hence the fraction of galaxies in each class per stellar mass bin are roughly representative of the total galaxy population at $z \sim 0$ (neglecting possible evolution within the MaNGA redshift range $0.01 < z < 0.15$).

Fig. 3.6 reproduces the well-know increase in the red fraction (here generally represented by quiescent and eLIER galaxies) as a function of mass (e.g. Peng et al., 2010). Intriguingly the fraction of both eLIER and cLIER galaxies is consistent with zero for $\log(M_\star/M_\odot) < 10$ and increases to 15%

[3]As described in Sec. 3.2.2, LIER excitation often dominates at large distances from the disc midplane in edge-on SF galaxies.

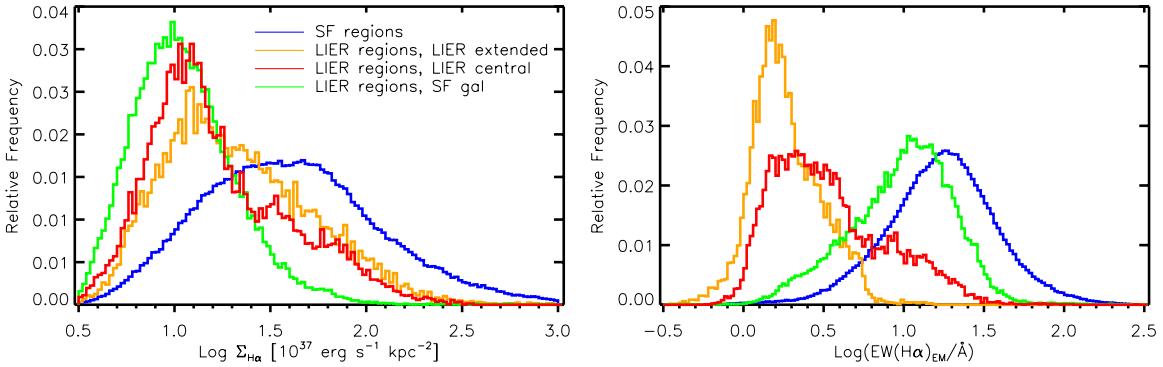

Figure 3.7: Histograms of the distribution of Hα surface brightness and the equivalent width of Hα (in emission) for MaNGA spaxels. Spaxels of different classes are colour-coded differently following the legend in the left panel. The blue histograms correspond to spaxels classified as SF (independently of galaxy class). LIER spaxels are subdivided in three classes, depending on the galaxy type: LIER extended (or eLIER, in orange), LIER central (cLIER, in red) and SF galaxies (in green).

in the mass bins $10.5 < \log(M_\star/M_\odot) < 11.5$. Overall each of the two LIER galaxy classes (eLIER and cLIER) represents roughly half of the total number of galaxies that would have been classified as LI(N)ER using only nuclear spectra. The total LIER galaxy populations (eLIER and cLIER) is shown as a dotted line and constitutes around $\sim 30\%$ of the galaxy population for $10.5 < \log(M_\star/M_\odot) < 11.5$, roughly consistent with previous estimates based on single-fibre spectra (Cid Fernandes et al., 2011). A in-depth discussion of the morphology, colours and dynamical properties of each galaxy class is presented in chapter 4.

3.3 Hα emission profiles

3.3.1 Hα surface brightness and equivalent width distributions

The intensity of the Balmer recombination lines of hydrogen is proportional to the ionising photon flux, assuming that all ionising photons are absorbed by the gaseous component. The escape fraction for Lyman continuum photons in late-type galaxies in the local Universe is generally very low. Yet there is some evidence that the escape fraction might be larger in early-type galaxies, if ionising photons are produced by old stars and the gas distribution is patchy (e.g. Papaderos et al., 2013). Bearing this in mind, we first investigate the distribution of Hα surface brightness and equivalent width (EW) as a function of the *local* ionisation conditions. More specifically we divide the MaNGA spaxels in four classes

1. SF spaxels in any galaxy type (blue in Fig. 3.7).
2. LIER spaxels in SF galaxies (green in Fig. 3.7).
3. LIER spaxels in eLIER galaxies (orange in Fig. 3.7).
4. LIER spaxels in cLIER galaxies (red in Fig. 3.7).

This choice is motivated by the observation that HII regions have similar nebular properties in all galaxies, while the excitation mechanism leading to LIER emission might be different as a function of galaxy class. Both the red and orange histograms refer to regions of spatially resolved LIER-like

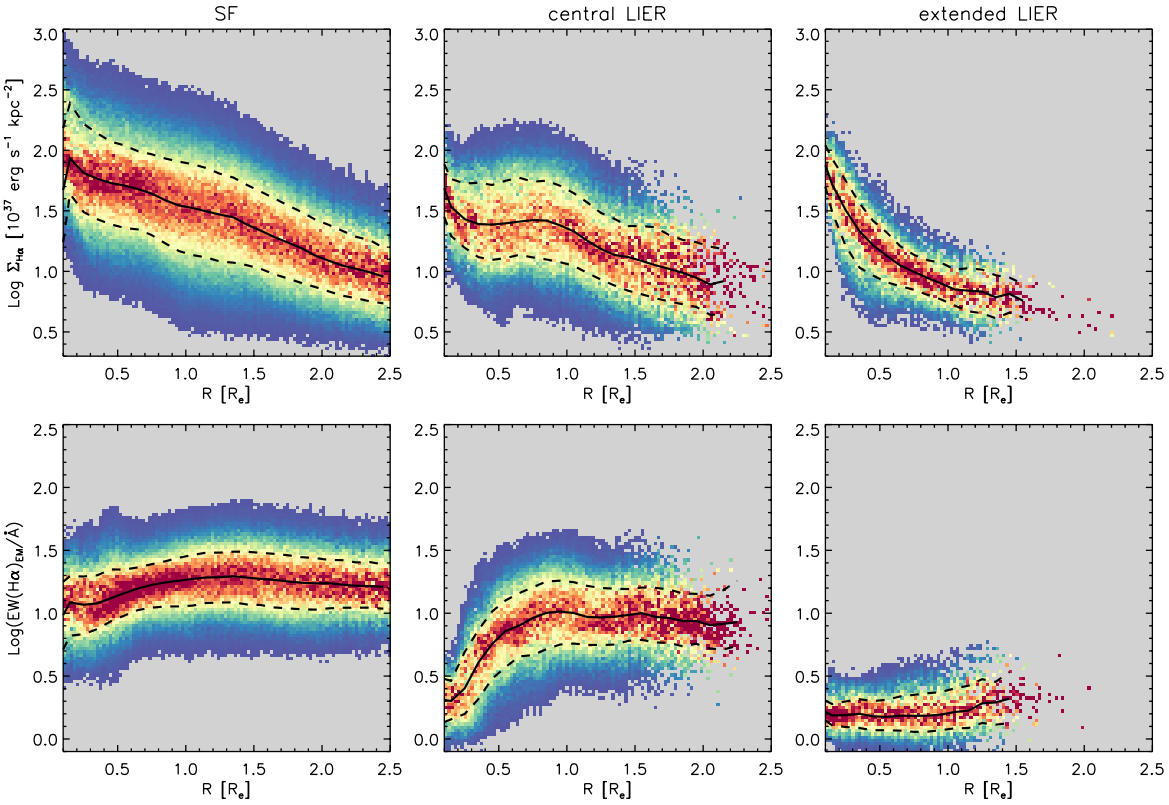

Figure 3.8: Gradients of Hα surface brightness (top) and EW(Hα) in emission (bottom) as a function of deprojected radius in units of effective radius. The spaxels are binned in the 2D space and only bins with more than 4 spaxels are shown. The density distributions are normalised at each radius. The black solid line represent the median at each radius, and the dashed lines represent the 25th and 75th percentiles.

emission (in cLIER and eLIER galaxies respectively), while the green histogram refers to (mostly extra-planar) diffuse LIER-like emission in SF galaxies. Spaxels that are classified as having Seyfert-like ionisation are not considered in this section.

The distribution of Hα surface brightness (left panel of Fig. 3.7) highlights two important facts:

1. SF regions have surface brightness on average 0.4 dex higher than LIER regions, independently of galaxy class.

2. LIER regions in any galaxy type have a similar Hα surface brightness distribution, with LIER regions in SF galaxies having a slightly lower average surface brightness and less prominent high surface brightness tail. The sharp low surface brightness cutoff for all spaxel classes is due to the sensitivity limit of the MaNGA observations.

These observations motivate our earlier remark that sensitivity limitations affect more strongly the LIER region of the BPT diagram than the SF sequence. Moreover, even though LIER emission is fainter than line emission due to star formation, if we assume it is present as a diffuse background, it can contribute a non-negligible fraction of the line flux observed in SF regions. We quantify the effect of LIER-like DIG in SF galaxies in more detail in Zhang et al. (2017).

The EW(Hα) has been used by several authors to distinguish between ionisation due to star formation and AGN (characterised by high EW(Hα)) and ionisation due to a smooth background of hot evolved stars (EW(Hα)$<$ 3 Å). Moreover, Cid Fernandes et al. (2011) have shown that the emission

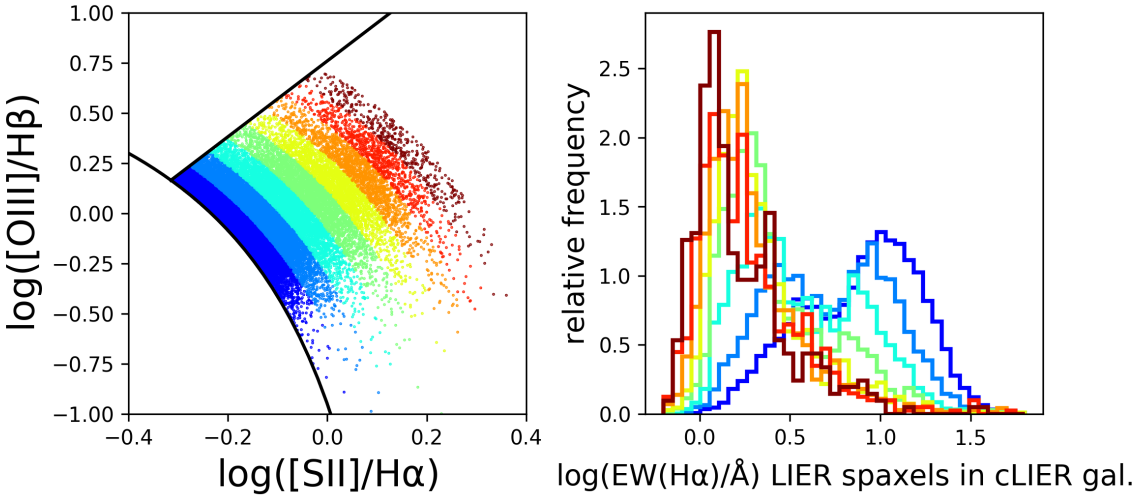

Figure 3.9: A zoom-in in the LIER region of the [SII] BPT diagram in cLIER galaxies, demonstrating that regions close to the demarcation line show EW(Hα) values comparable to SF galaxies. We draw a set of curves parallel to the demarcation curve of Kewley et al. (2001) to define the distance from the SF sequence. Successive curves are separated by a 0.05 dex interval in log([SII]/Hα) and log([OIII]/Hβ). The right panel shows the histograms of the EW(Hα) distribution as a function of distance from the SF sequence (the colour-coding is the same as in the left panel, with red being furthest from the star forming sequence).

line galaxy population in SDSS is clearly bimodal in EW(Hα), and that 3 Å is a useful empirical separation between the two populations.

In Fig. 3.7 (right panel) we show the EW(Hα) of the MaNGA spaxels following the classification presented at the start of this section. The distribution of EW(Hα) for MaNGA spaxels is clearly bimodal, with two independent peaks at log(EW(Hα)) $\sim$ 0.3 and log(EW(Hα)) $\sim$ 1.3, in excellent agreement with results from SDSS single-fibre spectroscopy, and clearly separating regions characterised by LIER emission from regions characterised by SF line ratios. We note that the MaNGA sensitivity limit and the arbitrary cut at 1.0 Å used to define line-less galaxies will affect the distribution of low EW spaxels.

The LIER spaxels in eLIER galaxies have on average lower EW(Hα) than LIER spaxels in cLIER galaxies. In particular, the EW(Hα) distribution for cLIERs (red in Fig. 3.7) shows a prominent tail at large EW, which is an effect of the contamination from star forming regions on approaching the LIER-star formation interface. This contamination can be clearly demonstrated by focusing on the LIER spaxels in cLIER galaxies and showing their EW(Hα) as a function of the distance from the Kewley et al. (2001) demarcation line (to be compared with Fig. 3.4). In Fig. 3.9 we demonstrate that LIER spaxels in cLIER galaxies close to the SF sequence show a bimodal EW(Hα) distribution, with a peak at values typical of star forming regions. As regions move away from the SF sequence, the EW(Hα) decreases to the values observed in eLIERs. Most spaxels in cLIER galaxies, however, are found close to the SF sequence in the BPT diagram. It is therefore important to acknowledge the presence of residual star formation in these regions. While shocks may play a role in generating the observed line ratios, we do not observe any other independent piece of evidence in favour of the presence of shocks, even in these central regions (see Sec. 3.5.3).

On the other hand, even in eLIER galaxies a small number of localised regions display EW(Hα)

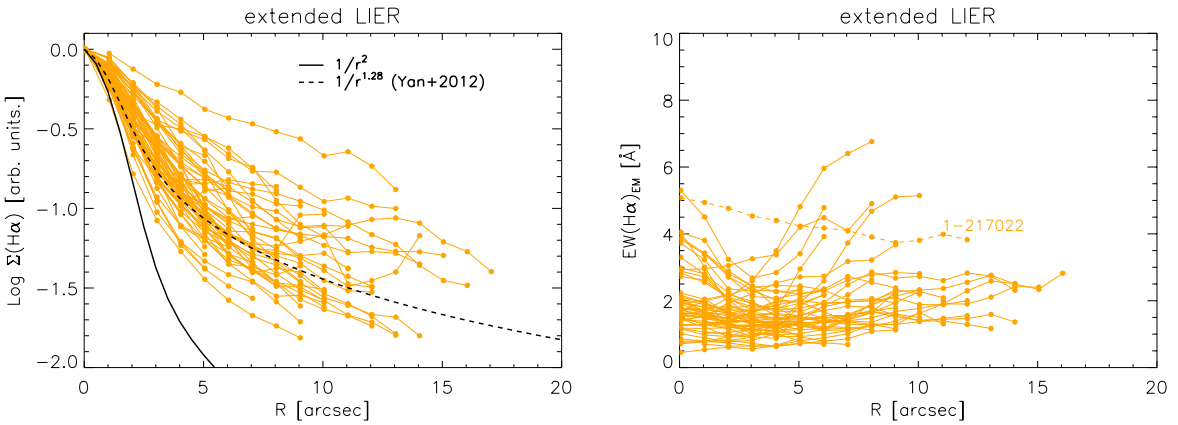

Figure 3.10: Hα surface brightness normalised to the central Hα flux (left) and EW(Hα) (right) profile as a function of deprojected radius (in arcsec) for eLIER galaxies. In the left panel, the solid line represents a $1/r^2$ model convolved with the median MaNGA PSF, representing the prediction from ionisation from a central source assuming constant cloud number density, effective area and filling factor as a function of radius. The dashed line represent the best-fit profile for red LIER galaxies from Yan & Blanton (2012), corresponding to $1/r^{1.28}$. The right panel shows the remarkably flat EW(Hα) distribution for eLIER galaxies. Galaxy `1-217022`, standing out as having high EW(Hα) with respect to the rest of the class, is studied in detail in Cheung et al. (2016).

> 3Å. These spaxels generally correspond to well-defined bisymmetric structures in the equivalent width maps resembling an integral sign (as observed also in the SAURON survey by Sarzi et al. 2006, 2010). Examples of these features in the MaNGA data are presented in Cheung et al. (2016).

The spaxels associated with LIER emission in SF galaxies (i.e. DIG, green in Fig. 3.7), show higher EW than other LIER regions. This can be interpreted as the result of the fact that the local stellar continuum is not the source of the ionising radiation, which instead comes from leakage of ionising photons from star forming regions elsewhere in the galaxy. Since most of these LIER regions are extra-planar, the continuum emission is weak, which translates into high EW.

3.3.2 Hα radial gradients

In Fig. 3.8 we show the radial gradients for the Hα surface brightness (top panels) and EW(Hα) (bottom panels) as a function of deprojected galactocentric radius (in units of effective radius R_e), for SF, eLIER and cLIER galaxies.

For eLIER galaxies the Hα surface brightness decreases steeply with radius, following the rapid drop of the stellar continuum. The fact that the line emission follows the continuum becomes clearer by looking at the radial gradient of the EW(Hα), which shows a nearly flat profile with narrow dispersion around a low value ($\sim$ 1.5 Å). Note, however, that the median EW(Hα) may be biased high because of the S/N cut imposed on line emission, as the MaNGA sensitivity limit corresponds roughly to EW(Hα) $\sim$ 1.0 Å.

For SF galaxies the radial distribution of Hα surface brightness shows a larger dispersion and decreases more slowly with galactocentric radius. The EW(Hα) has a much higher mean value than for eLIERs (typically > 10 Å), with a relatively constant profile as a function of galactocentric radius, and with a weak, but significant drop toward the central region, associated with some contribution from the bulge to the central continuum emission. Since for SF galaxies the EW(Hα) is a good proxy of the specific SFR (the SFR per unit mass), we conclude that the mean specific SFR is only weakly

dependent on galactocentric radius, although it decreases slightly in the central regions ($R < 1.0\ R_e$). This is in agreement with the observations of a spatially resolved relation between stellar mass surface density and SFR (Cano-Díaz et al., 2016).

cLIER galaxies (central panels in Fig. 3.8) have more complex gradients. In the central region their EW(Hα) approaches the same low values observed in eLIERs, pointing towards a similar excitation mechanism in such regions, while the outer regions (where star formation occurs) have a higher EW(Hα), although generally slightly lower than in SF galaxy discs, suggesting some intrinsic differences in terms of age of the stellar population and mixture between ongoing and evolved stellar populations. The Hα surface brightness has a complex profile resulting from a combination of steeply declining central profile and an increase in flux at the radius where the LIER-star formation transition occurs. In the stacked profile presented in Fig. 3.8 the effect is evident as a large increase in dispersion at $0.5 < R/R_e < 1.0$, due to the fact that the LIER-star formation transition occurs at different radii in different galaxies.

Several authors (Sarzi et al., 2010; Yan & Blanton, 2012; Singh et al., 2013) have investigated the radial profile of line emission in LIER galaxies as a means of testing the hypothesis of illumination from a central source. To compare with these studies we show here the radial profiles of Hα surface brightness ($\Sigma_{H\alpha}$) for eLIER galaxies. We do not show the equivalent plot for cLIERs because the transition to SF regions at $0.5 < R/R_e < 1.0$ means that only the central profiles, which are more heavily affected by beam smearing, could be used for this test.

Fig. 3.10, left panel, shows the $\Sigma_{H\alpha}$ gradients normalised to the central Hα flux as a function of the deprojected distance from the galaxy centre for eLIER galaxies. The black solid line represents a $1/r^2$ intensity profile, convolved with the median MaNGA PSF, which is the expected surface brightness profile in case of photoionization by a central source (e.g. AGN) assuming a constant cloud number density and volume filling factor as a function of radius. Unfortunately cloud number densities and filling factors are not readily determined from the available data. Hence a line surface brightness profile shallower than $1/r^2$ provides only a weak indication regarding the origin of line emission in eLIER galaxies. Interestingly, although the individual galaxy profiles show significant scatter, our data is in general agreement with the $1/r^{1.28}$ profile found by indirect means by Yan & Blanton (2012). In Fig. 3.10 we also show the EW(Hα) profiles for individual eLIER galaxies, demonstrating the flatness of the profiles on a galaxy by galaxy basis and with few galaxies showing EW(Hα) > 3 Å. Galaxy `1-2117022`, which shows and unusually high average EW, is discussed in detail in (Cheung et al., 2016).

3.3.3 Are galaxies really line-less?

So far we have defined 'line-less' galaxies as galaxies with mean EW(Hα) < 1.0 Å within 1.0 R_e. The chosen EW value is motivated by the wish to detect all the strong lines needed for BPT classification with adequate S/N at the typical depth of the MaNGA data and does not represent a physical boundary. Moreover, since we impose a cut on Hα, other lines might still be detectable in what we defined 'line-less' galaxies, especially [NII], [OIII] and [SII], which are enhanced with respect to Balmer lines in the LIER regime. If we make the assumption that line-less galaxies represent the continuation to lower EW of the eLIER population, it is interesting to explore the consequences for the EW(Hα) distribution for the combined eLIER and line-less classes.

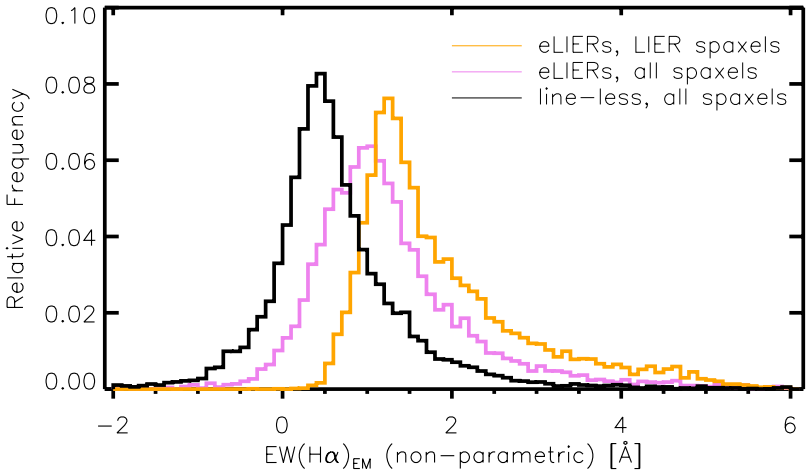

Figure 3.11: Histogram of the distribution of EW(Hα) (in emission) calculated using the non-parametric method. Orange denotes regions with S/N > 2 on all the [SII] BPT lines in eLIER galaxies (which are hence classified as LIERs in the [SII] BPT diagram). Violet corresponds to all regions within eLIER galaxies, and black to all regions in line-less galaxies.

Deriving EW(Hα) for line-less galaxies is a non-trivial exercise, as the continuum dominates the line emission and an accurate fit to the Balmer absorption is thus necessary. Moreover, at low flux level, the adopted Gaussian fitting strategy to recover emission line fluxes becomes biased, as the line shape becomes poorly defined. In order to attempt a measurement of the residual line emission in line-less galaxies we therefore perform the following: 1) The Hα flux is calculated using the same binning scheme as the stellar continuum, in order to get the most accurate continuum subtraction possible, 2) The Hα flux is calculated by performing a straight sum of the flux of the continuum-subtracted spectrum in a 600 km s^{-1} window around the expected position of the Hα line, taking the redshift of the source into account, and when detected, the measured velocity of the line. We refer to the line fluxes obtained this way as the 'non-parametric' fluxes. We have checked that at high flux levels the line fluxes obtained from Gaussian fitting agree with the non-parametric fluxes.

In Fig. 3.11 we show the EW(Hα) distribution obtained using non-parametric fluxes for the eLIER and line-less galaxies. Including spaxels with S/N < 3 on the BPT strong lines lowers the median EW(Hα) for eLIER galaxies from 1.6 Å to 1.1 Å. The median EW(Hα) for line-less galaxies is 0.5 Å.

Further work, including deeper observations or stacking of the available MaNGA data, will be useful to decisively confirm the presence of residual line emission in 'line-less' galaxies. The findings in this sections suggest that imposing a S/N cut sufficient to reliably measure all the BPT lines excludes a tail of lower EW(Hα) regions. The overall distribution of EW(Hα) for LIERs is therefore likely to be biased high because of the adopted S/N cut.

3.4 Line ratio gradients

As discussed in Sec 1.4.1, line ratios can be used as probes of the fundamental parameters of the gas and the ionising radiation field: the gas electron density (n_e), ionisation parameter (U), gas phase metallicity (Z) and hardness of the ionisation field (α). The flux ratio of the [SII] doublet, [S II] λ6731/[S II] λ6717, constitutes as direct probe of the gas electron density, with the ratio expected to vary from ~ 0.7, for $n_e \sim 10^{1.5}$ cm^{-3} to ~ 2.0, for $n_e \sim 10^4$ cm^{-3} (Osterbrock & Ferland, 2006). The

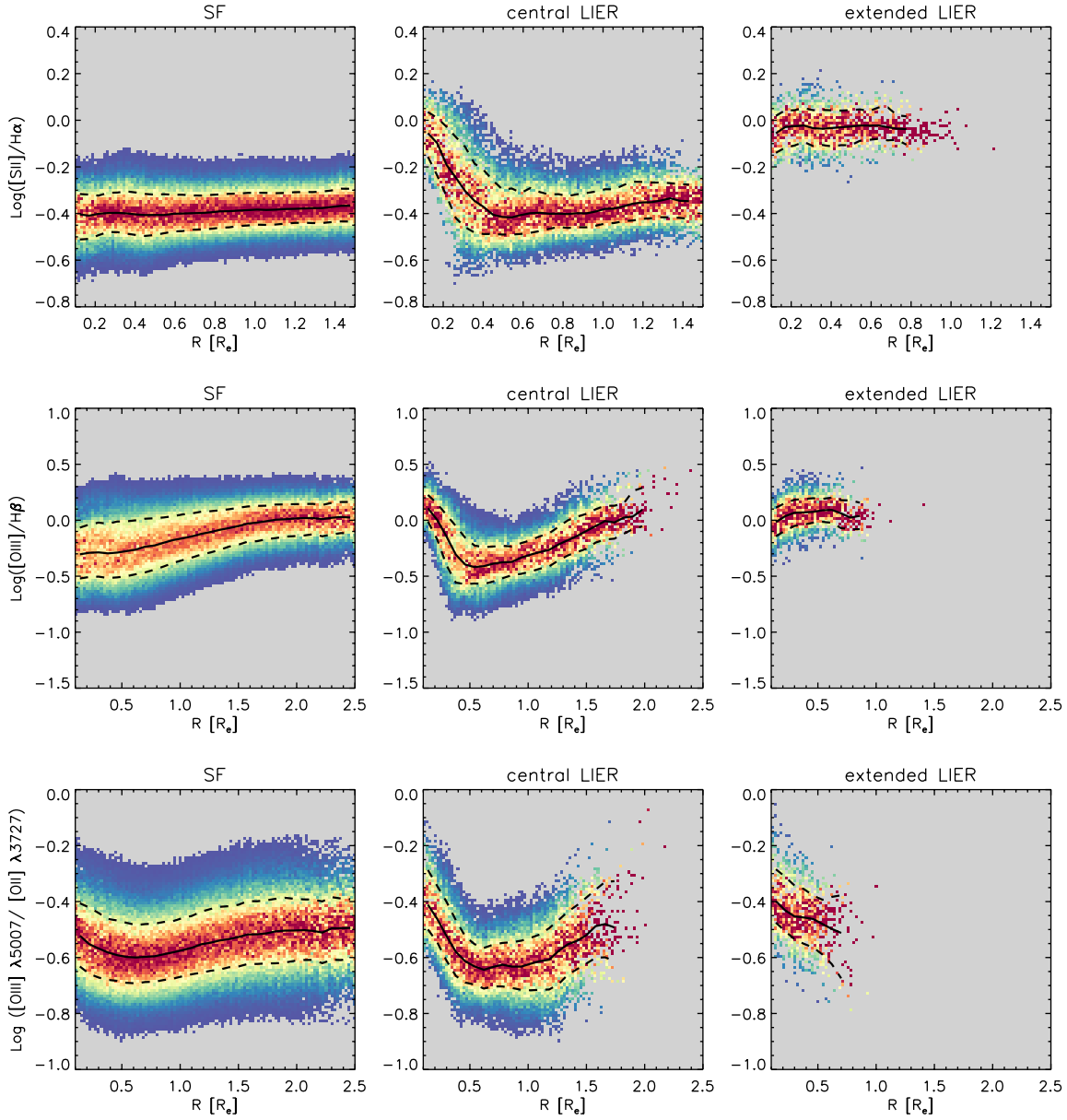

Figure 3.12: Gradients of different diagnostic ratios as a function of deprojected radius in units of R_e for SF, cLIER and eLIER galaxies. From top to bottom: (1) [OII]/Hβ, (2)[SII]/Hα and (3)[OIII]/[OII]. The spaxels are binned in the 2D space and only bins with more than 4 spaxels are shown. At each radius the distributions are normalised so that the colour-coding represents the density of points at that radius. The red colour is fixed to represent the mean of the distribution at each radius. The black solid line represent the median at each radius, and the dashed lines represent the 25th and 75th percentiles.

sensitivity of this ratio saturates at the low electron density value for most regions in MaNGA galaxies (both SF and LIERs), causing the [SII] doublet ratio to appear artificially flat as a function of radius for all galaxy classes. The median [SII] ratio for SF galaxies is 0.725, corresponding to a density $n_e \sim 10^{1.5}$, close to the lower limit at which the line ratio saturates.

In Fig. 3.12 we show the gradients of [SII]/Hα for different galaxy classes. Since [SII] is a low ionisation line, emitted primarily in the partially-ionised region of the gas cloud, [SII]/Hα is a good tracer or the importance of low-ionisation species and thus provides a good separation between star formation and LIER ionisation. The power of this diagnostic is demonstrated in Fig. 3.12 by the effective bimodality between the SF (log([SII]/Hα) ~ -0.4) and LIER locus (log([SII]/Hα) ~ -0.05).

Both the [OIII]/[OII] and [OIII]/Hβ line ratios are sensitive to the ionisation parameter and the hardness of the ionisation field. [OIII]/Hβ has a more pronounced metallicity dependence than [OIII]/[OII], which is roughly proportional to U, for both HII regions (Diaz et al., 2000) and harder AGN or old stellar population spectra (e.g. Yan & Blanton, 2012). In order to account for the large wavelength difference between [OIII] λ5007 and [OII] λ3727 we perform an extinction correction based on the Balmer decrement to measure the [OIII]/[OII] ratio. Fig. 3.12 shows the gradients in [OIII]/[OII] and [OIII]/Hβ for SF, cLIER and eLIER galaxies. By selection, regions dominated by LIER ionisation in both cLIERs and eLIERs show common line ratios, characterised by higher [OIII]/[OII] and [OIII]/Hβ than SF galaxies. Remarkably, for eLIERs the gradient in [OIII]/Hβ is nearly flat and the [OIII]/[OII] gradient is only weakly decreasing as a function of radius (~ 0.2 dex decrease over 1 R_e).

The ionisation parameter, being directly proportional to the ionising photon flux, constitutes a constrain on the geometry of the excitation source. Assuming the electron density to be approximately constant over the range of radii covered by MaNGA, the ionisation parameter should go down as $1/r^2$ in the same radial range in the case of point source illumination (e.g. a central AGN). However, several caveats apply this arguments. Firstly, the electron density is likely to decrease with radius, although most likely following a more shallow power law than r^{-2} (Sarzi et al., 2010). Moreover, in nearby resolved narrow line regions of Seyfert galaxies the ionisation parameter is generally found to be roughly constant as a function of radius, and also to be remarkably constant across different sources (e.g. Veilleux & Osterbrock, 1987; Veron-Cetty & Veron, 2000). A variety of models have been proposed to explain these observations, the most successful of which are dusty radiation pressure-dominated AGN models (Dopita et al., 2002; Groves et al., 2004a,b). In these models, for ionisation parameters greater than $U \sim \alpha_B/(c\ \kappa_d) \sim 10^{-2}$, where α_B is the case B recombination coefficient for hydrogen and κ_d is the dust effective opactiy, the narrow line region is radiation pressure-dominated (Dopita et al., 2002). In this regime the ionisation parameter of the line-emitting clouds remains roughly constant as a function of radius.

The ionisation parameters implied by the observed [OIII]/[OII] ratio in eLIER is $U \sim 10^{-4} - 10^{-3}$ (Binette et al., 1994; Stasińska et al., 2008), which is 1-2 orders of magnitude lower than the critical value of the ionisation parameter which would lead to radiation-pressure domination. Thus even for classical LINER-type AGN, radiation pressure is predicted to be negligible. We conclude that the observed flat profiles in the ionisation parameter-sensitive line ratio [OIII]/[OII] are not consistent with a low-ionisation parameter, weak AGN scenario. Overall, the MaNGA data are in good agreement with previous studies of gradients of line ratios in elliptical galaxies, which generally demonstrates very shallow or flat line profiles outside the central 100 pc (Annibali et al., 2010; Papaderos et al., 2013; Sarzi et al., 2010; Yan & Blanton, 2012).

3.5 Discussion

3.5.1 Energetics: powering the observed line emission in LIER galaxies

As discussed in Sec. 3.1.4, typical weak AGN do not emit sufficient energy in ionising photons to explain the observed line emission in LIER galaxies. pAGB stars, on the other hand, represent a diffuse source of ionising photons, which must be present in galaxies with old stellar populations. Although further work is needed to reduce the uncertainties in current modelling of the late stages of stellar evolution (e.g. O'Connell, 1999), considering the uncertainty in the modelling parameters, Hα EWs of 0.5 - 2.0 Å can be generated by the pAGB stellar component. The tight correlation between the observed continuum and line emission in LIERs, and the fact that the EW(Hα) observed in LIER regions lies in the range predicted by the models is strong evidence in favour of the stellar hypothesis for LIER emission.

This conclusion should not be considered at odds with studies of truly nuclear LINERs on $\sim$ 100 parsec scales. For example Ho (2008) estimates that on the scales of 100-200 pc covered by the Palomar spectroscopic survey, pAGB stars can only account for $\sim$ 30-40% of the emission observed in LI(N)ER nuclei. On these small scales a weak AGN could indeed be the main source of ionising photons. However, at the resolution of surveys like MaNGA (or within the 3″ SDSS fibre), a possible LINER AGN contribution is generally subdominant beyond the central resolution element.

Strong gradients and localised features in either the equivalent width and/or diagnostic line ratios are generally not expected if LIER emission is attributed to diffuse stellar sources. Indeed, the flat gradients and low observed EW(Hα) are consistent with this scenario. However, even in eLIER galaxies, a small number of regions lie in the upper tail of the EW(Hα) distribution with EW(Hα) = 3-6 Å (Fig. 3.8). Interestingly, these features generally correspond to localised features, often of bisymmetric morphology ('integral sign', Sarzi et al. 2006; Cheung et al. 2016). The self-similarity of these structures points towards a likely common origin. A possible explanation lies in the relative geometry of the ionising stellar sources and the gas cloud absorbers. If the gas clouds are not randomly distributed around the stars but preferentially concentrated along coherent structures on kpc scales (discs, ionisation cones, etc.), then diffuse ionisation sources like pAGB stars can be sufficient to explain the higher observed equivalent widths. Non-uniform dust concentration might also play a role in defining these structures. On the other hand, shocks provide a natural mechanism to generate localised features in line emission maps. A prediction of the shock scenario is that localised equivalent width enhancements should be accompanied by a systematic change in line ratios and, possibly, by an increase in the gas velocity dispersion due to unresolved velocity gradients.

Finally, other sources of ionising radiation, such as low-mass X-ray binaries and extreme horizontal branch stars, have been found to be a subdominant contribution with respect to pAGB stars by at least one order of magnitude (Sarzi et al., 2010; Yan & Blanton, 2012). Their contribution to the relevant energy budget is thus overall negligible unless the number of pAGB stars has been largely over-predicted by models. An interesting note on this topic is represented by the fact that *Hubble Space Telescope (HST)* imaging of nearby LIERs (like M31, Ciardullo et al. 1988; Heckman 1996, which in a MaNGA-like observation would appear as a cLIER, or the nearby elliptical galaxy M32) struggles to account for the number of UV bright stars and planetary nebulae predicted by stellar population models (Brown et al., 1998, 2008; Rosenfield et al., 2012; Pastorello et al., 2013). At the moment it is not clear whether these inconsistencies are due to observational bias, limitations of the theoretical

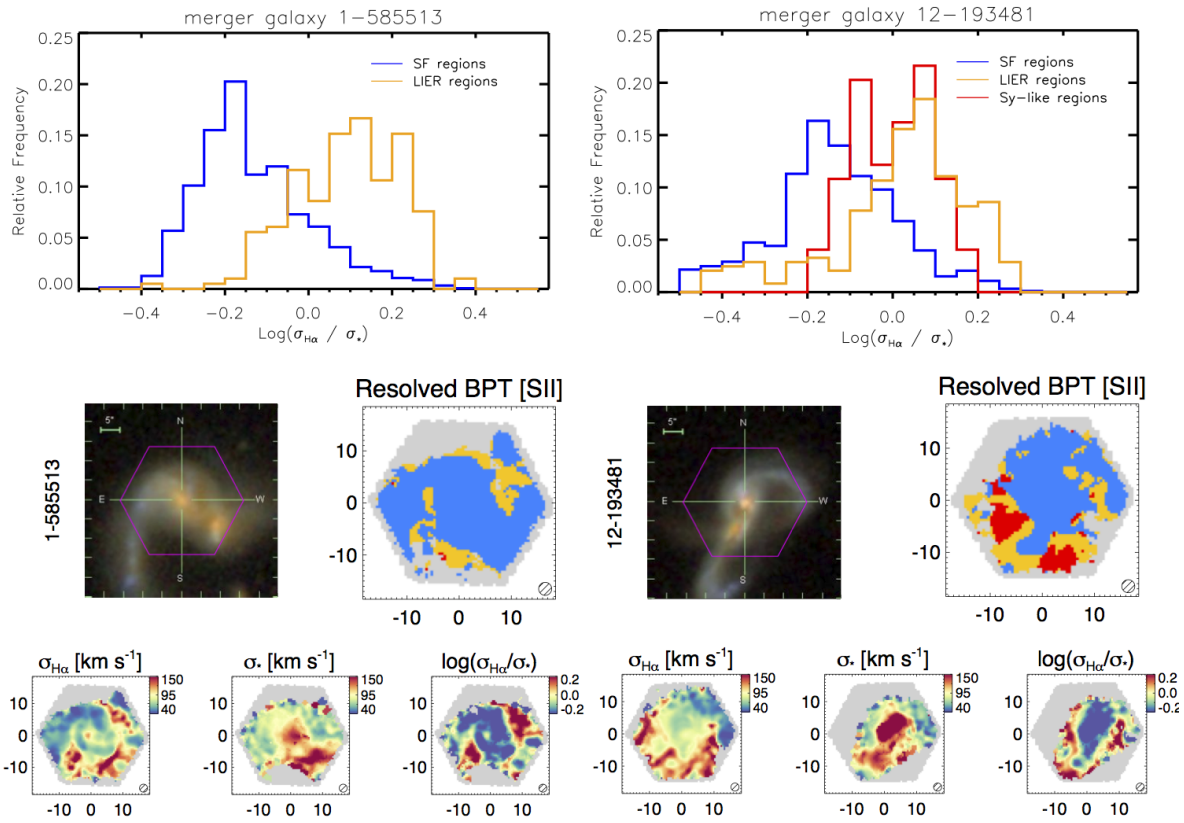

Figure 3.13: An illustration of the properties of LIER-like emission in two major mergers. The top panels show the $\log(\sigma_{H\alpha}/\sigma_\star)$ ratio for the SF (blue), LIER-like (orange) and Seyfert-like (red) spaxels, demonstrating the fact the dispersion in LIER-like regions in mergers is dominated by non-gravitational motions. In the second row we show the $g-r-i$ SDSS composite image and the resolved BPT diagram, based on the position of galactic regions in the [SII] BPT diagram, as in Fig. 3.5. In the third row we show the Hα and stellar velocity dispersion maps, together with a map of the $\log(\sigma_{H\alpha}/\sigma_\star)$ ratio.

models or both. Clearly more work is needed in this area to be able to conclusively associate the LIER emission to the UV stellar sources powering it.

3.5.2 Local ionisation conditions and the state of the LIER gas

The question of the relative distance and geometry of ionising sources and line emitting gas in LIER galaxies is crucial to the correct interpretation of the MaNGA observations presented in this chapter, but is a difficult one to address. Both Sarzi et al. (2010) and Yan & Blanton (2012) present detailed discussions of the predicted ionising photon profiles under a variety of model assumptions. Sarzi et al. (2010), for example, discuss the predicted EW(Hα) profile in the case of a spherically symmetric stellar model, following a Dehnen (1993) density profile, and a thin gas disc. If one assumes an infinite mean free path for the ionising photons, this model predicts an EW(Hα) profile which increases with radius (see Sarzi et al. 2010, Fig. 10). A smaller mean free path for the ionising photons leads to shallower profiles of EW(Hα), as the line emission becomes more tightly coupled to the 'local' ionising sources. However, as the mean free path approaches zero, this model predicts an EW(Hα) profile as steep as 1/R, because the line flux becomes directly proportional to the stellar density. A shallower profile can be obtained by assuming early type galaxies to have disky stellar profiles, an assumption that finds observational support in the findings of the ATLAS^{3D} team, who highlight that

fast-rotator early type galaxies have intrinsic shapes very similar to disc galaxies (Weijmans et al., 2014)

Assuming that a single pAGB star emits the reference value of 10^{47} ionising photons per second and an electron density of 10^2 cm^{-3}, in agreement with the measured [SII] double ratio, for logU = 10^{-4} (consistent with the observed values of [OIII]/[OII] in LIERs, as discussed in Binette et al. 1994 and Stasińska et al. 2008) the mean separation between ionising source and gas cloud must be of order of a few parsecs, thus further justifying the 'locality' assumption discussed above. If both gas and stars lie in a disc-like structure, such close separations can be naturally achieved.

In this scenario, geometry is also a likely explanation for EW(Hα) lower than 3 Å, which can be explained by a more spherical stellar profiles, in addition to relaxing the assumption that all photons are absorbed 'locally'. In galaxies devoid of gas is possible that a fraction of the ionising photons escape the galaxy altogether. In fact, in the pAGB scenario is it harder to justify the *absence* of line emission than its presence. In chapter 4 we present a discussion of the possible reasons for lack of line emission in line-less galaxies.

3.5.3 The case for shock excitation in interacting/merging galaxies

Shocks are the results of several astrophysical phenomena likely to occur in galaxies, including supernovae explosions, AGN winds and the interaction of a jet with the ISM. It is well known that the BPT diagram does not represent a good test for shock ionisation, as shock models cover larger areas of both the LIER and SF sequences (Allen et al., 2008; Rich et al., 2010, 2011; Ho et al., 2014; Alatalo et al., 2016). Moreover, just like for the case of a weak AGN, the presence of shocks does not imply that they must be the main source of ionising photons in galaxies. Conversely, while the pAGB scenario may account for the observed line ratios and energetics, the presence of shocks cannot be conclusively ruled out.

Previous work has considered a correlation between line ratio and velocity dispersion a good test for shock ionisation (Monreal-Ibero et al., 2006; Rich et al., 2011, 2014). In the case of LIER galaxies at kpc resolution this test is of difficult interpretation due to the possible complex kinematics of the gas and to resolution effects. A potentially more promising way for identifying shocks is looking for a localised increase in the velocity dispersion of the gas compared to that of the stars. Since the gas is generally dynamically colder than the stars, due to its ability to dissipate non circular motions, and the fact that the thermal broadening of the gas at 10^4 K is a negligible contribution to its velocity dispersion, a large increase in the gas velocity dispersion compared to the stellar dispersion is a possible signature of shocks.

Here we only discuss the potential of the method in isolating shocked regions in interacting galaxies in the current MaNGA sample. As briefly discussed in Sec. 3.2.2, gas rich mergers show localised regions of LIER-like (and even Seyfert-like) emission. In Fig. 3.13 we show the histograms of $\log(\sigma_{\mathrm{H}\alpha}/\sigma_\star)$ for SF spaxels (blue), LIER-like (orange) and Seyfert-like (red) in two major mergers (MaNGA-ID `1-585513` and `12-193481`). LIER emission in merging systems shows systematically higher gas velocity dispersion compared to the stars, and, as demonstrated by the maps of velocity dispersion of gas and stars, this increase is highly localised in regions of LIER and Seyfert-like emission. These observations support the presence of LIER-like shock excitation in merging systems, consistently with the strong LIER-like emission observed in ULIRGs, (Monreal-Ibero et al., 2006; Alonso-

Herrero et al., 2010), most of which are strongly starbursting merging systems, large-scale outflows (Lipari et al., 2004) and regions at the jet-ISM interface (Cecil et al., 2000). We note, however, that in the low-z Universe merging systems are very rare and constitute a statistically negligible part of the overall galaxy population, although they may be more commonly observed at higher redshift.

Chapter 4

The spatially resolved transition from star formation to quiescence

Based on 'SDSS IV MaNGA - The spatially resolved transition from star formation to quiescence', F. Belfiore et al., 2017, MNRAS, 446, 2570; and partially on 'SDSS IV MaNGA - Spatially resolved diagnostic diagrams: A proof that many galaxies are LIERs', F. Belfiore et al., 2016, MNRAS, 461, 3111.

In the previous chapter we have discussed LIER emission and presented evidence that this phenomenon is not related to nuclear activity, but simply a consequence of presence of a diffuse UV background due to evolved stellar populations. This conclusion leads us to reconsider the conventional definition of *quiescence* as absence of nebular line emission. Namely, both LIER and line-less regions (EW(Hα) < 1 Å) can be defined as 'quiescent' (or 'passive'), to highlight the fact that they do not host current star formation, as traced by the dominant component of line emission.

An alternative definition of quiescence may rely on probes of star formation on longer timescales, such as the so-called 4000-Å break ($D_N(4000)$, Balogh et al. 1999) which is a sensitive tracer of the age of the stellar population. More specifically, while $D_N(4000)$ is also sensitive to metallicity effects (for stellar population older than 1 Gyr), the combination of $D_N(4000)$ and the stellar index EW(Hδ_A) is less sensitive to the effect of metallicity and has been used in the literature as a probe for the galaxy's star formation history (e.g. Kauffmann et al., 2003b,a; Li et al., 2015). With the MaNGA data we can exploit both line emission and stellar indices to classify individual regions within galaxies as either star forming or quiescent, and correlate this classification with other resolved properties.

In the first part of this chapter we discuss the relation between excitation conditions and stellar indices on spatially resolved scales 4.1, highlighting the strong correlation between LIER emission and stellar indices characteristic of old stellar populations. In the second part (Sec. 4.2), we discuss how galaxies that differ in their excitation morphologies (SF, cLIER, eLIER and lines-less) behave with regards to fundamental galactic properties and how this classification fits within the bimodal galaxy population.

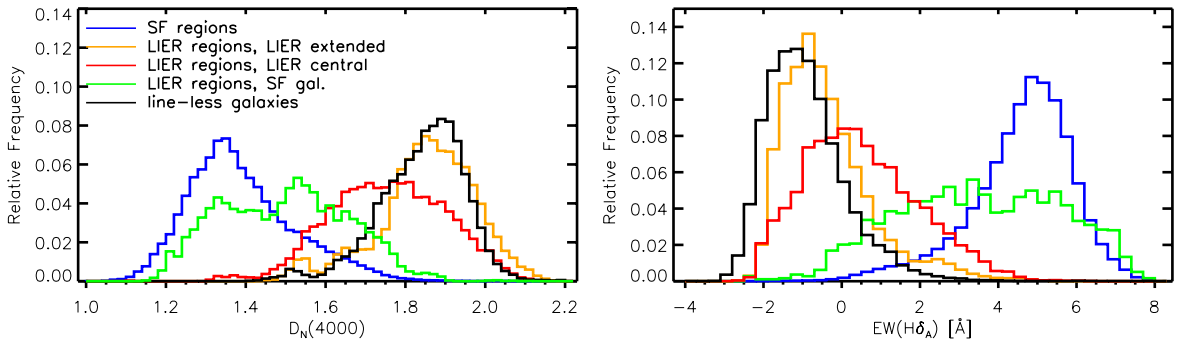

Figure 4.1: Histograms of the distribution of $D_N(4000)$ and EW($H\delta_A$) in MaNGA spaxels. Spaxels of different classes are colour-coded differently following the legend in the left panel. The blue histograms correspond to spaxels classified as SF in SF galaxies. LIER spaxels are subdivided in three classes, depending on the galaxy they belong to: eLIER (orange), cLIER (red). Finally, spaxels were line emission is not detected (line-less) are plotted in black.

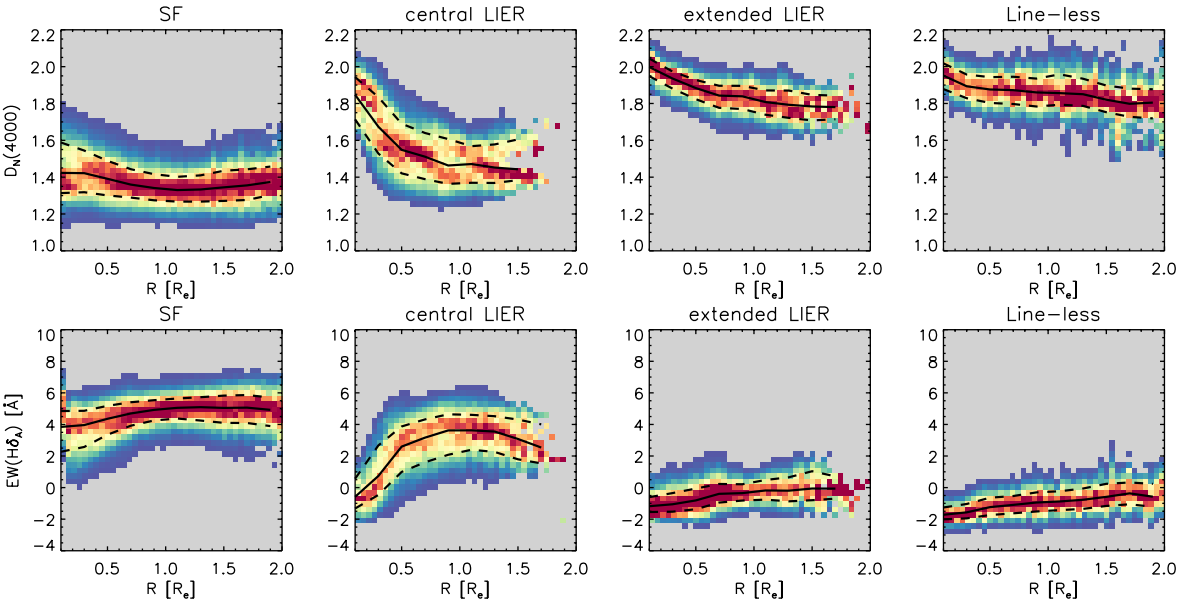

Figure 4.2: Gradients of $D_N(4000)$ (top) EW($H\delta_A$) (bottom) and as a function of deprojected effective radius for MaNGA galaxies split according to the emission-line based classification introduced in Sec. 3.2.2. The spaxels are binned in the 2D space and only bins with more than 10 spaxels are shown. At each radius the distributions are normalised so that the colour-coding represents the density of points at that radius, with the red colour fixed to represent the mean of the distribution at each radius. The black solid line represent the median at each radius, and the dashed lines represent the 25th and 75th percentiles.

4.1 From nebular lines to stellar indices: tracing star formation and quiescence

4.1.1 Age-sensitive indices

In Sec. 3.1.2 we argued that LIER emission is associated with old stellar population, as traced by the stellar population indices $D_N(4000)$ and EW($H\delta_A$) in legacy SDSS spectroscopy as well as in the spatially resolved MaNGA data. In this section we further study differences in the distribution and radial gradients of these age sensitive stellar population indices in the MaNGA data. We split the MaNGA spaxels in the four classes defined in Sec. 3.3.1: 1) SF spaxels, 2) LIER spaxels in cLIER galaxies, 3) LIER spaxels in eLIER galaxies and 4) LIER spaxels in SF galaxies. Moreover, in this

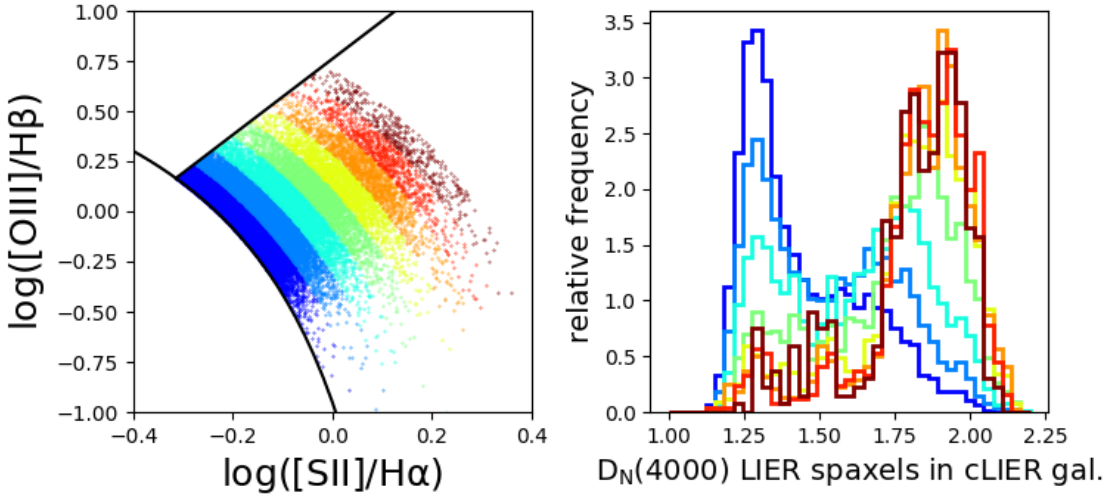

Figure 4.3: A zoom-in in the LIER region of the [SII] BPT diagram in cLIER galaxies, demonstrating that regions close to the demarcation line show $D_N(4000)$ values typical to SF galaxies and that moving away from the demarcation line the regions get older. LIER regions are subdivided by a set of parallel line to the demarcation curve of Kewley et al. (2001) to define the distance from the SF sequence. Successive curves are separated by a 0.05 dex interval in log([SII]/Hα) and log([OIII]/Hβ). The right panel shows the histograms of the $D_N(4000)$ distribution as a function of distance from the SF sequence (the colour-coding is the same as in the left panel, with red being furthest from the star forming sequence).

section we additionally consider spaxels with reliable continuum but undetected line emission in line-less galaxies.

Fig. 4.1 shows the histogram distribution of $D_N(4000)$ and EW(Hδ_A) for the MaNGA spaxels divided in the classes defined above. SF regions in SF galaxies have stellar population indices consistent with young stellar populations ($D_N(4000) \sim 1.3$ and EW(Hδ_A) ~ 5).

On the opposite end of the spectrum, LIER spaxels in eLIER galaxies and line-less spaxels are characterised by old stellar populations. In fact, the presence or absence of line emission does not have any effect on the stellar populations in these systems: i.e. the stellar populations properties of eLIER and line-less galaxies are fully consistent with each other.

LIER regions in cLIER galaxies show $D_N(4000)$ and EW(Hδ_A) distributions which are intermediate between SF and eLIER/line-less galaxies. Intermediate values of these indices require careful modelling since in these regime both indices are sensitive to both metallicity and stellar age. It is important to note that, even in the LIER regions of cLIER galaxies, the distribution of $D_N(4000)$ is strongly bimodal. The peak at low $D_N(4000)$, corresponding to the SF stellar populations, decreases as we move away from the SF sequence, while the high-$D_N(4000)$ peak increases in importance, as shown in Fig. 4.3. This behaviour is equivalent to that observed for the EW(Hα) distribution in LIER regions of cLIER galaxies, and points to the presence of SF regions even within the canonical Kewley et al. (2001) demarcation line.

As anticipated in Sec. 4.2.1 (and Fig. 4.5) the only LIER regions that clearly host young stars ($D_N(4000) < 1.5$) correspond to LIER regions in SF galaxies, associated with DIG in both extra-planar and inter-arm regions in spirals.

In order to put this analysis into context it is important to remember that the different galaxy classes have different stellar mass distributions. Because of the well-known downsizing effect, lower

mass galaxies are also younger and thus it is possible that SF galaxies appear on average younger than cLIERs because cLIERs occur more frequently at higher mass (see Fig. 3.6). We have therefore divided the sample in stellar mass bins and checked that the trends presented in Fig. 4.1 are preserved. This is indeed the case because, while on average the stellar populations of all galaxy classes become older with increasing stellar mass, the relative stellar indices differences between classes of spaxels are preserved in each stellar mass bin ($10 < \log(M_\star/M_\odot) < 11.5$). At the extremes of the stellar mass distribution we do not have enough galaxies of each class to be able to perform this test.

4.1.2 Age radial gradients

Fig. 4.2 shows gradients of $D_N(4000)$ and EW($H\delta_A$) for MaNGA galaxies of different classes. A detailed study of the dependence of stellar population properties gradients on other galactic properties is presented in Goddard et al. (2016). Here we only comment on the qualitative differences between gradients in galaxies classified according to our emission-line based classification.

1. SF galaxies have flat $D_N(4000)$ and EW($H\delta_A$), consistently with the fact that young stellar populations are present at all radii. Older stellar populations are found for a subset of the most massive galaxies in the nuclear regions (galaxies with $\log(M_\star/M_\odot) > 10.5$, corresponding to an increase in dispersion for $r < 0.5\ R_e$), which can be associated with an older bulge component.

2. eLIER and line-less galaxies show slowly radially decreasing $D_N(4000)$ and increasing EW($H\delta_A$), consistent with previous study of age profiles in early type galaxies (Wilkinson et al., 2015; Li et al., 2015). However the observed gradient in the two stellar indices is due to a combination of both metallicity and age effects and a combined analysis is needed to reliably disentangle the two.

3. cLIER galaxies show a clear transition between old stellar populations in the inner (LIER) region and young stellar populations in the outer (SF) regions.

Goddard et al. (2016) make use of full spectral fitting (Heavens et al., 2000; Panter et al., 2004; Fernandes et al., 2005; Gallazzi et al., 2006; Sánchez-Blázquez et al., 2011; Wilkinson et al., 2015; McDermid et al., 2015) to derive age and metallicity of the stellar population, thus largely mitigating the age-metallicity degeneracy. However the bimodality observed in stellar population between 'young' ($D_N(4000) < 1.5$) and 'old' ($D_N(4000) > 1.5$) is very robust to metallicity effects (Wilkinson et al., 2015).

The gradients in stellar indices discussed above are diluted due to the combination, within each galaxy class, of galaxies with different properties (masses, environments etc.). However, given the well-defined differences in stellar indices gradients between the different galaxy classes, an emission-line based classification appears to capture a sharp distinction between young (SF), transitioning (cLIER) and quiescent (eLIER and line-less) galaxies, with other properties (like stellar mass) representing a smooth variation in addition to the basic trend presented here.

4.1.3 The $D_N(4000)$ - $H\delta_A$ plane

In Fig. 4.4a we plot the MaNGA spaxels divided by galaxy class (SF, cLIER, eLIER and line-less) in the $D_N(4000)$ versus EW($H\delta_A$) plane. Model tracks (computed by C. Maraston), based on Maraston

& Strömbäck (2011) stellar population models, are shown for a burst of star formation (with solar metallicity, solid black line in all panels) and three models with continuous, exponentially declining star formation (where the SFR decline timescale, τ, is varied in the range 0.1-10 Gyr). Except for the increase in EW($H\delta_A$) observed in the burst model at young ages (< 1 Gyr), stellar population age increases going from top-left to bottom-right. The black dotted models in the eLIER and line-less panels correspond to a burst of twice solar metallicity, and confirm that metallicity does not substantially affect the position in the $D_N(4000)$ versus EW($H\delta_A$). In all panels, the burst model defines an envelope in $D_N(4000)$-EW($H\delta_A$), with continuous SFR models occupying regions at lower $D_N(4000)$ for a fixed EW($H\delta_A$) value.

Continuous star formation models are an excellent representation of the data for SF galaxies, with the model with τ=10 Gyr passing through the locus of the data. The data for cLIERs is bimodal in the $D_N(4000)$ versus EW($H\delta_A$) plane, spanning the full range of stellar ages. The peak at $D_N(4000) \sim 1.4$ is well-fitted by continuous SFR models with a decline timescale of several Gyr. The second peak ($D_N(4000) \sim 1.7$), indicative of an intermediate age stellar population, is harder to fit with the available models, as the data lie above the burst model track. On-going star-forming regions embedded in old stellar populations may also produce the observed intermediate values of stellar indices. The case of nuclear star forming ring, which occur in 20% of spirals (Knapen, 2005) may also be relevant here (Sarzi et al., 2007), as many cLIERs present similar features in their Hα maps.

The stellar populations of eLIERs and line-less galaxies are indistinguishable in the $D_N(4000)$-EW($H\delta_A$) plane, and are well-fitted by the burst model at old (> 10 Gyr) ages. While the locus of the data does not require significantly α-enhanced stellar populations, α-enhancement can successfully explain the observed spread to higher EW($H\delta_A$) at fixed $D_N(4000)$ (dashed model track in eLIER panel, Thomas et al. 2004, 2011).

In Fig. 4.4b we show the same plot, but colour-coded by the fraction of spaxels classified as LIER across the $D_N(4000)$ versus EW($H\delta_A$) plane. The results demonstrate the strong correspondence between LIERs and old stellar populations, with cLIERs showing a transition from LIER-dominated central regions to SF-dominated outskirts.

4.2 LIER galaxies within the bimodal galaxy population

The tight correlation between line emission and stellar populations discussed in the previous section leads us to further investigate the emission-line based galaxy classification in the context of the broader physical properties of galaxies. In this section we address the question of how emission line-based galaxy categories (SF, cLIER, cLIER and line-less) fit within the overall galaxy bimodality in terms of their fundamental properties (colours/morphology/kinematics). For example, can we interpret the SF, cLIER, eLIER and line-less galaxies sequence of increasing 'quiescence' as an evolutionary sequence? Where does the gas in eLIER galaxies come from and what makes these galaxies different from line-less galaxies?

4.2.1 Integrated colours and star formation rates

The physical origin of the colour bimodality in the galaxy population lies in the idea of using galaxy colour as 'clocks'. Both UV and blue colours evolve quickly once O and B stars disappear from the

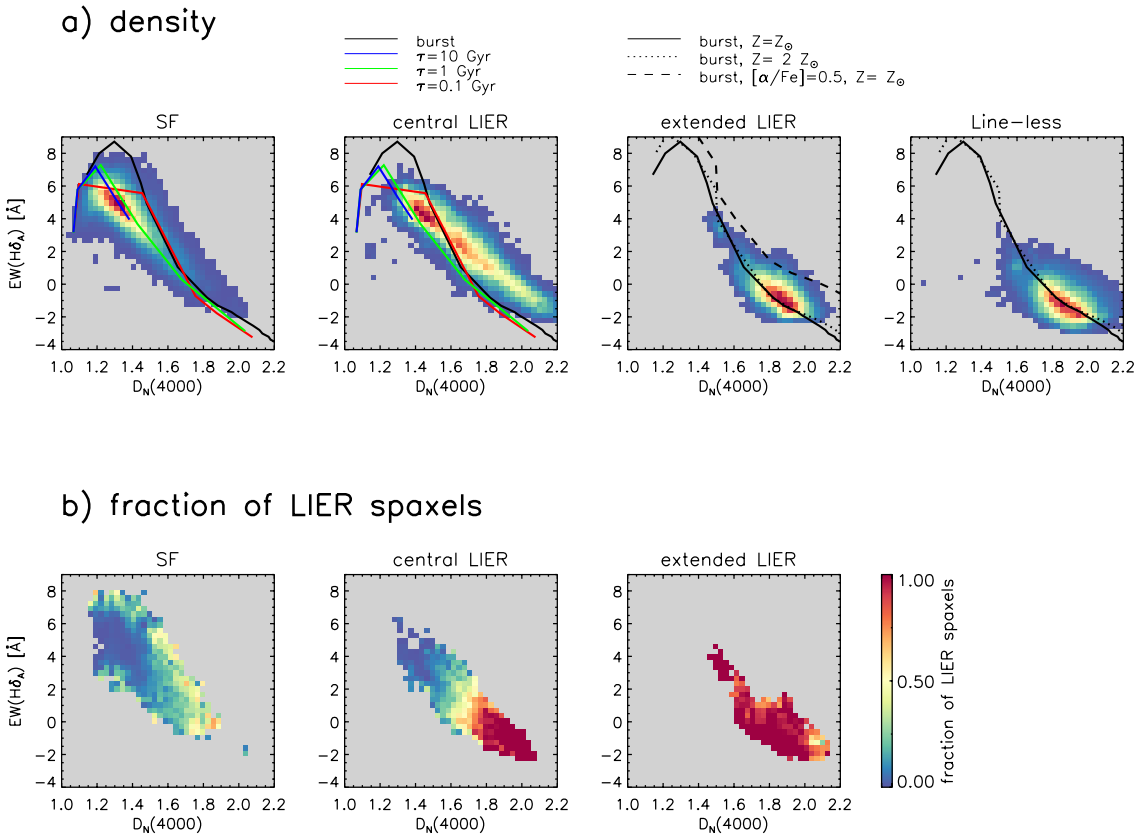

Figure 4.4: (a) Density plot in the $D_N(4000)$ versus $EW(H\delta_A)$ plane for spaxels in the different galaxy classes (SF, cLIER, eLIER and line-less) defined in Sec 3.2.2. Different burst and continuous SFR models based on Maraston & Strömbäck (2011) stellar population models are overplotted (details in the legend). (b) Same as (a) but with the colour-coding reflecting the fraction of spaxels classified as LIER in each region of the $D_N(4000)$ versus $EW(H\delta_A)$ plane.

galaxy spectrum. In particular, NUV emission declines more slowly than Hα ($\sim 10^6 - 10^7$ yr), but faster than blue optical continuum ($\sim 10^9$ yr), making UV-optical colours a sensitive probe to the fading of young stellar populations.

Fig. 4.5 shows the $NUV - r$ versus M_i (i-band absolute magnitude) diagram for the current MaNGA sample, with galaxies sub-divided according to the emission line-based classification scheme introduced in this work. We observe that SF galaxies constitute the vast majority of the blue cloud ($NUV-r < 4$), while line-less and eLIER galaxies are concentrated on the red sequence ($NUV-r > 5$). The most striking feature of Fig. 4.5 is that a large fraction of cLIER galaxies (~40 %) are found in the green valley ($4 < NUV-r < 5$), with the remaining ones also lying at intermediate UV-optical colours (the mean $NUV - r$ for cLIERs is 4. 1 with a standard deviation of 1.0 mag).The prevalence of cLIER galaxies in the green valley is not surprising, since the integrated colours are affected by both the light from the red, old, LIER-like central regions and light from the blue, star forming disc, thus generating the observed intermediate integrated colours. The separation of cLIER galaxies from the blue cloud is less evident when using optical colours (for example $u - r$ or $g - r$ instead of $NUV - r$). Indeed, using $g - i$ colours, cLIER galaxies are consistent with lying on the red sequence, and have equivalent colour to eLIERs and line-less galaxies. Further details on the UV-optical colours of different galaxy classes are summarised in Table 4.1.

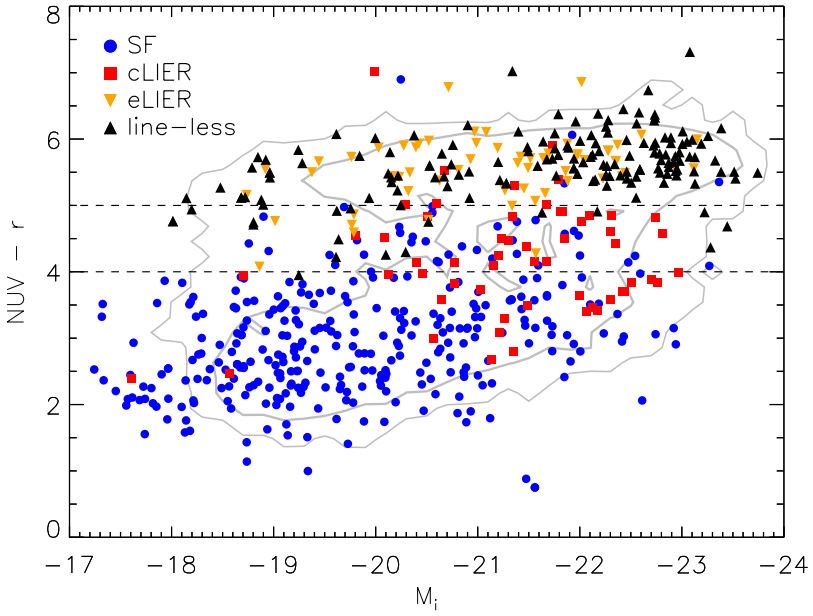

Figure 4.5: MaNGA galaxies in the $NUV - r$ versus M_i (colour-magnitude) diagram. Galaxies are subdivided according to the emission line-based classification introduced in Sec. 3.2.2. Contours represent galaxy density in the MaNGA parent sample, while dashed lines provide a division between the red sequence ($NUV - r > 5$), green valley ($4 < NUV - r < 5$) and blue cloud ($NUV - r < 4$). The green valley is preferentially occupied by cLIER galaxies, while eLIER and line-less galaxies are mostly found on the red sequence ($NUV - r > 5$).

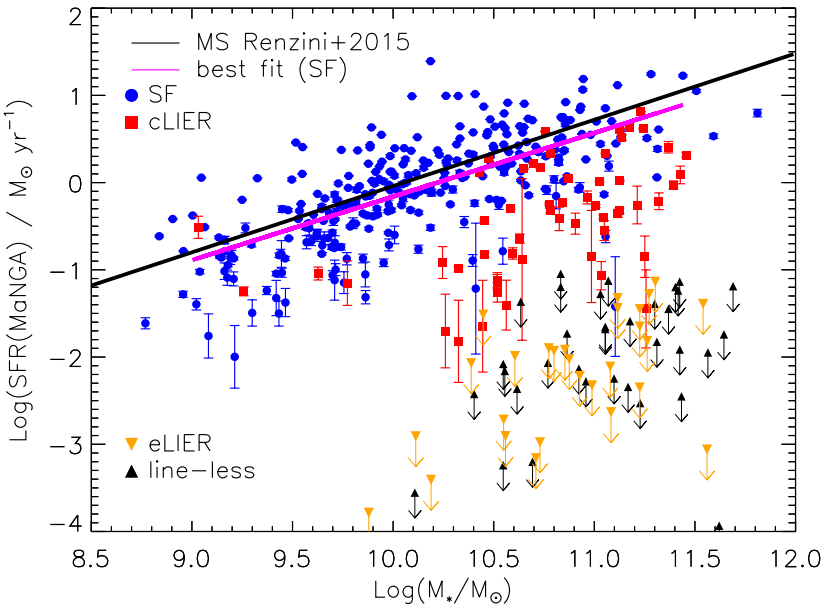

Figure 4.6: The SFR-$M_\star$ plane for MaNGA galaxies. The SFR is derived is from the extinction-corrected Hα flux. The black line represent the 'main sequence' for star forming galaxies from legacy SDSS spectroscopy (Renzini & Peng, 2015). The magenta line represents the best fit 'main sequence' using the star forming galaxies in the MaNGA sample.

Fig. 4.6 presents an even more striking illustration of the transitional nature of cLIER galaxies, by representing the MaNGA galaxies in the SFR-$M_\star$ plane. The SFR is calculated from the extinction-corrected Hα flux within the MaNGA bundle and using the Kennicutt (1998) conversion factor. The simplest approach to computing SFR would be to exclude regions (spaxels) which are not classified as star forming by making use of a hard cut on a BPT diagnostic diagram. We consider this approach partly unsatisfactory because of the rather arbitrary nature of the demarcation lines. Instead we suggest a framework where the total Hα flux is the combination of a contribution from HII regions, related to star formation, and a contribution from old evolved stars (LIERs) and LIER-like diffuse ionised gas. In order to disentangle the two components we rely on their different lines ratios, following a similar approach to Blanc et al. (2009). In this work we choose to use [SII]/Hα, which is the most sensitive line ratio to the presence of LIER emission (see Sec. 3.4). Defining f_{SF} to be the fraction of Hα flux due to star formation and f_L the fraction of Hα flux due to LIERs, we have

$$f_{SF} + f_L = 1, \qquad \left(\frac{[SII]}{H\alpha}\right) = f_{SF}\left(\frac{[SII]}{H\alpha}\right)_{SF} + f_L\left(\frac{[SII]}{H\alpha}\right)_L, \tag{4.1}$$

where $\left(\frac{[SII]}{H\alpha}\right)_{SF} = 0.4$ and $\left(\frac{[SII]}{H\alpha}\right)_L = 0.9$ are the characteristic line ratios for star forming regions and LIERs, respectively, whose numerical values are obtained from the data presented in Sec. 3.4. To calculate the SFR we solve for f_{SF} for each spaxel and then sum the total Hα luminosity due to star formation within the FoV of each MaNGA galaxy. We note that this approach leads to very similar numerical results to a hard cut on SF spaxels based on a BPT demarcation line. For example, using the K01 demarcation line in the [SII] BPT diagram to classify SF spaxels, and only using those spaxels in the SFR calculation, leads to SFR which strongly correlate with our estimate for purely SF galaxies (Pearson correlation coefficient of 0.997). The SFR calculated using the LIER correction is, on average, systematically larger by only 0.03 dex from that computed using only SF spaxels with a average scatter of 0.07 dex.

Our SFR estimates are also in excellent agreement with the SFR reported in the MPA-JHU catalogue (Brinchmann et al., 2004), based on legacy SDSS spectroscopy (Pearson correlation coefficient of 0.8, dispersion of 0.4 dex). The offset from the one-to-one relation is substantially larger for cLIERs (0.5 dex) than SF galaxies (0.07 dex), which is not surprising given the poor leverage of the SDSS 3″ fibre in calculating the SFR in cLIERs.

Fig. 4.6 demonstrates that SF galaxies lie on the star formation main sequence (Brinchmann et al., 2004; Salim et al., 2007; Peng et al., 2010; Renzini & Peng, 2015), while the cLIER galaxies lie systematically below it, although above the passive galaxy population, consisting of eLIERs and line-less galaxies. For reference we plot the main sequence at $z \sim 0.1$ from Renzini & Peng (2015) (black solid line in Fig. 4.6), obtained from legacy SDSS spectroscopy, and the best fit line to the SF galaxy population using the current MaNGA sample (with $9 < \log(M_\star/M_\odot) < 11.5$, magenta line in Fig. 4.6), given by

$$\log\left(\frac{SFR}{M_\odot yr^{-1}}\right) = -7.5 \pm 0.2 + (0.73 \pm 0.02)\log\left(\frac{M_\star}{M_\odot}\right). \tag{4.2}$$

Considering the differences in sample selection and methodology for calculating stellar mass and SFR, results from legacy SDSS are in excellent agreement with the MaNGA result presented here. At a fixed stellar mass, cLIER galaxies lie on average 0.8 dex below the main sequence defined by the star forming population, although they actually spread across the entire green valley with large scatter.

Table 4.1: Classification statistics of emission line galaxies in the $NUV-r$ colour-magnitude diagram and mean (± standard deviation) for selected UV and optical colours. Appropriate volume weights have been applied to correct for the MaNGA selection function.

Galaxy class	Blue cloud $NUV-r<4$	Green Valley $4<NUV-r<5$	Red sequence $NUV-r>5$	$NUV-r$ $\mu\pm\sigma$	$u-r$ $\mu\pm\sigma$	$g-r$ $\mu\pm\sigma$
SF	92%	7%	1%	2.8 ± 0.8	1.6 ± 0.4	0.55 ± 0.16
cLIER	48%	39%	13%	4.1 ± 1.0	2.2± 0.3	0.74 ± 0.10
eLIER	0	19%	81%	5.4 ± 0.6	2.5 ± 0.2	0.78 ± 0.09
line-less	1%	14%	85%	5.5 ± 0.7	2.4 ± 0.2	0.76 ± 0.09

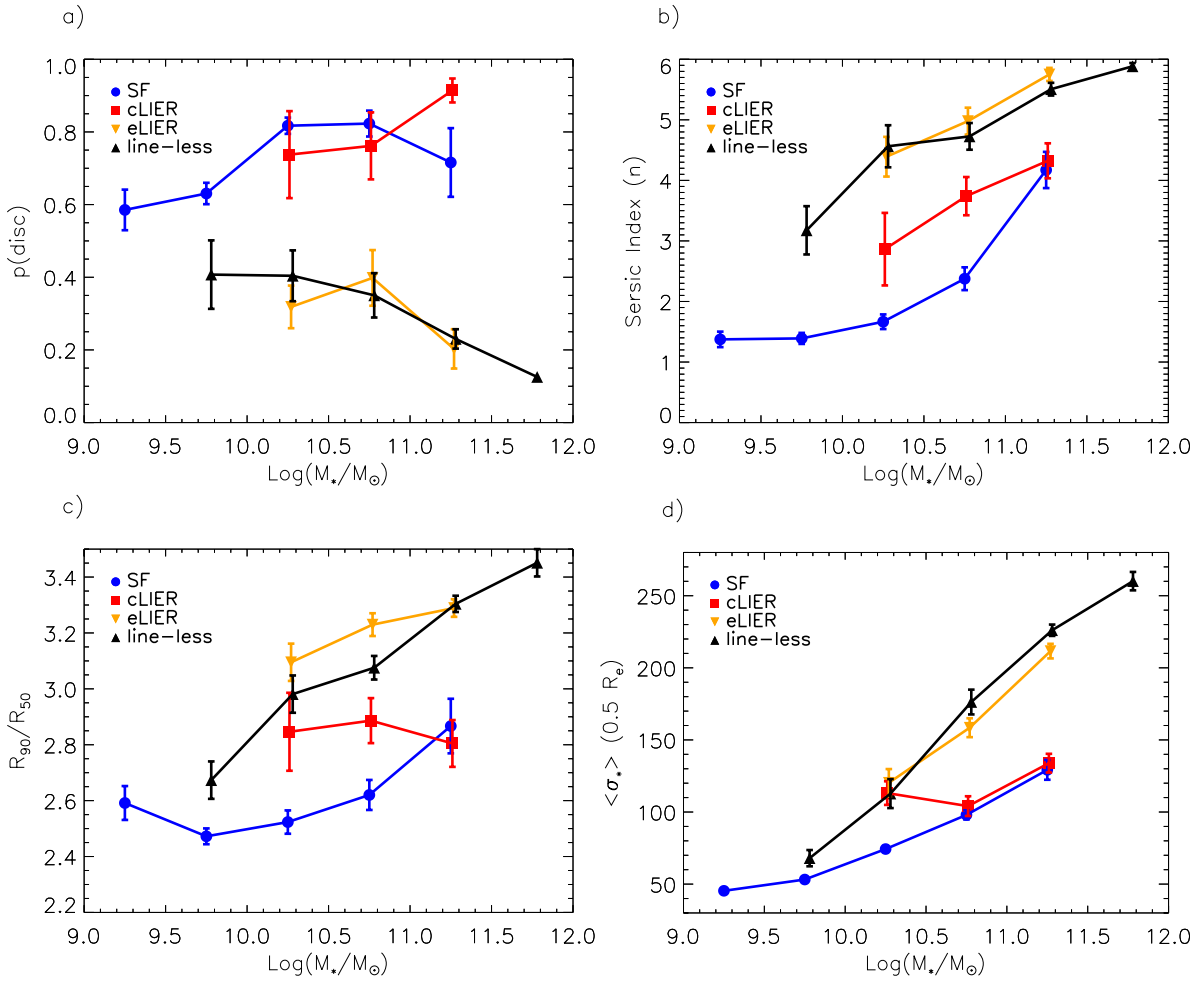

Figure 4.7: *(a)* Average disc vote fraction from Galaxy Zoo 2 (Willett et al., 2013) in bins of stellar mass for MaNGA galaxies of different classes. The vote fraction can be interpreted as a probability and has been statistically de-biased to account for the increasing difficulty of detecting fainter morphological features at higher redshift following Willett et al. (2013). *(b), (c)* Average Sérsic index and concentration (defined as R_{90}/R_{50}, where R are Petrosian radii) in bins of of stellar mass. Sérsic parameters and Petrosian radii are obtained from the Nasa-Sloan Atlas (Blanton et al., 2011) and are based on legacy SDSS r-band imaging. *(d)* Average stellar velocity dispersion within 0.5 R_e in bins of stellar mass. Velocity dispersions are calculated from the MaNGA data and R_e is the Sérsic r-band effective radius from the NSA catalogue.

Summarising, the key results from this section are the following: 1) eLIER and quiescent line-less galaxies are indistinguishable in terms of colours; 2) Most green valley galaxies are not such because of dust reddening or globally intermediate stellar populations, but are associated with galaxies (cLIERs) in which quiescent (non-SF) central regions co-exist with outer star formation. These galaxies lie in the transition region between the star formation main sequence and quiescent galaxies.

4.2.2 Morphological type

The traditional morphological dichotomy between early-type (ETG, E and S0) and late-type galaxies (LTG, spirals), as implemented in the revised Hubble classification (chapter 1, Sandage 1961), is based on the presence of spirals arms, and/or dust lanes when galaxies are seen edge on. Subsequent revisions to this classification, including recent advanced made possible by IFS observations, have conclusively demonstrated that a large fraction of ETG contain disks seen at a variety of inclinations (dubbed as 'fast rotators' by the ATLAS^{3D} project). Only the most massive end of the early type galaxy population is populated by true dispersion dominated systems ('slow rotators'), with very little ordered angular momentum (Emsellem et al., 2007, 2011; Cappellari et al., 2011a). Extensions to higher redshift (Bundy et al., 2010) seem to confirm this general picture.

Visual morphological classifications from the Galaxy Zoo 2 project (Lintott et al., 2008; Willett et al., 2013), based on legacy SDSS imaging, were used to subdivide MaNGA galaxies into ETG and LTG. In particular, we make use of the detailed classification from Galaxy Zoo 2, which asked its volunteer citizen scientists to identify several morphological features (spirals, bars etc) in SDSS three-colour image cutouts. Individual classifications are processed as detailed in Willett et al. (2013) and statistically 'de-biased' to take into account the fact that is it harder to identify fine morphological features for smaller, fainter galaxies. The nature of the Galaxy Zoo vote fractions means that they can be interpreted as conditional probabilities, though one needs to take into account that not all parameters are estimated for all galaxies, given the decision tree nature of the Galaxy Zoo 2 classifications. Vote fractions for certain questions (hence features) are only computed if previous questions in the decision tree are 'well-answered' (as detailed in Willett et al. 2013, Sec. 3.3 and Table 3).

In Fig. 4.7 (a) we plot the median trends in bins of stellar mass for the de-biased probability of the presence of disc or other feature[1] in our MaNGA galaxy sample, classified according to the emission line-based classification. In order to study trends as a function of stellar mass, we correct for the effect of the MaNGA selection function, using the volume weights discussed in Sec. 2.1.3. The error bars represent the error on the mean in each mass bin. The results from the Galaxy Zoo 2 classifications demonstrate that eLIER and line-less galaxies have mutually consistent morphologies and are visually classified as early type galaxies. SF and cLIER galaxies, on the other hand, also have mutually consistent disc fractions and are consistent with being late type galaxies. Although outliers are present in either direction (SF galaxies with no disc features or line-less galaxies classified as discs), these do not dominate the sample averaged trends.

Interestingly, previous work based on Galaxy Zoo has highlighted the fact that when galaxies are classified into a red sequence and blue cloud using optical colours, the red sequence hosts a substantial fraction of red ('anemic') spirals (Bamford et al., 2009; Masters et al., 2010). cLIER galaxies, because of their substantially redder optical colours than the mean of the blue cloud (see Table 4.1) and their disc-like morphology, may appear as 'red spirals' in integrated colours. This class of galaxies represents a natural link between normal spirals and lenticular (S0) galaxies, as suggested in the revised 'trident' morphological classification van den Bergh (1976) and further updated by Cappellari et al. (2011a).

Further support towards a relation between the anemic spiral class and cLIERs is given by the fact that anemic spirals in single-fibre spectroscopy (Masters et al., 2010) are often classified as LIERs,

[1]Task 1 in Galaxy Zoo 2, addressing the question: *Is the galaxy simply smooth and rounded, with no sign of a disc?*

have lower EW(Hα) than SF galaxies, present older mean stellar ages (Tojeiro et al., 2013), and are found to be an insignificant fraction of the total spiral population for $M_\star < 10^{10}$ $M_\odot$ (Wolf et al., 2009), while representing as much as 40% of the spiral population at the highest masses ($M_\star > 10^{10.8}$ $M_\odot$, Masters et al. 2010).

4.2.3 The importance of the bulge

Morphological features such as spiral arms and bars only capture one aspect of the complex problem of morphological classification of galaxies. Another characteristic generally associated with the study of galaxy morphology is the presence and importance of a central spheroidal component (the bulge). Unfortunately, although parametric bulge-disc decomposition is a well-established technique, studies based on photometry alone are limited by the well-known intrinsic degeneracies in the method (Rybicki, 1987; Gerhard & Binney, 1996). Although potentially even more biased, 'cheaper' proxies such as the concentration index (here defined as $C = R_{90}/R_{50}$ where R are Petrosian radii) or a galaxy-averaged Sérsic index have often been used on large photometric samples to provide an observationally more well-defined estimate of the importance of the bulge/spheroidal component. As a complement to these photometric indicators we also study the central stellar velocity dispersion extracted from the MaNGA data, which is a direct proxy for the depth of the bulge gravitational potential.

In this context, it is important to note that, if the bulge is defined kinematically, the classical lenticular (S0) morphological class is found to span a wide range in bulge fraction, forming a sequence essentially parallel to the classical increase in bulge fraction from Sc to Sa for LTGs (Cappellari et al., 2011b; Krajnović et al., 2013; Cappellari, 2016). Indeed, it is arguable whether the traditional S0 morphological classification is in itself meaningful, as IFS surveys have demonstrated that the photometry alone is a very poor predictor of the degree of rotational support for ETG, with S0 likely to be classified as classical dispersion dominated ellipticals when viewed at low inclinations (e.g Emsellem et al., 2011).

In Fig, 4.7 (b), (c), (d) we show the average Sérsic index, concentration and stellar velocity dispersion within 0.5 R_e ($< \sigma_\star >$) as a function of galaxy class in bins of stellar mass. In each bin, an average value is plotted only if there are more than four galaxies in the bin. As expected from their early-type morphology, both line-less and eLIER galaxies show higher Sérsic indices, concentration and $< \sigma_\star >$ than cLIER and SF galaxies in all stellar mass bins. cLIERs have Sérsic indices, concentrations and $< \sigma_\star >$ intermediate between eLIER/line-less and SF galaxies, consistent with the idea of being the subset of disc-dominated galaxies with largest bulge component at each stellar mass. For purely SF galaxies Sérsic index, concentration and $< \sigma_\star >$ all increase as a function of mass, matching those of cLIER galaxies in the mass bin $11.0 < \log(M_\star/M_\odot) < 11.5$. When using the central velocity dispersion as a tracer of the bulge potential we recover the same overall trends as for pure photometric tracers, like Sérsic index and concentration, thus confirming that our results are not dominated by the uncertainty in the photometry.

4.3 Kinematic misalignment

Kinematic decoupling between the gaseous and stellar components has been observed to be common in local ETGs (Bertola et al., 1999; Sarzi et al., 2006; Davis et al., 2011), with hints of this behaviour

being already present at high redshift (Wisnioski et al., 2015). The distribution of misalignments between the gas and stars is a direct probe of the origin of the gas in ETG. Theoretically, a newly formed gas disc is predicted to precess due to the effect of the gravitational potential of the stars, with gas precessing faster at smaller radii, where the torque is larger. Cloud-cloud collisions will also work to realign the differently precessing gas rings, and the system will eventually settle into a configuration where the gas and stellar components are either aligned or misaligned by 180°. The relaxation time for this process was initially predicted to be of order of the dynamical time (Tohline & Durisen, 1982; Lake & Norman, 1983), however recent work based on hydrodynamics in the cosmological framework has highlighted that misalignments might persist on much longer (several Gyr) timescales (van de Voort et al., 2015), mostly because of the effect of continuous cosmological accretion. This longer relaxation timescale also provides a better fit to the misalignment distributions presented in the literature (Davis & Bureau, 2016). For weakly triaxial systems stable gaseous orbits are allowed both in the plane containing the long and intermediate axes and the plane of the short and intermediate axis (Franx et al., 1991). If the origin of the gas is external, therefore, the distribution of the gas-stars kinematic misalignment should display three peaks, respectively at $0, 90, 180°$, with the peak around 90° being weaker and scaling with the degree of triaxiality.

In this section we derive the kinematic position angle (PA) of both gas and stars following the procedure in Krajnović et al. (2006). In short, having fixed the kinematical centre to the photometric one, the algorithm constructs a bi-antisymmetric version of the velocity field and compares it with the observed velocity field. The resulting PA is thus only representative of the axis of symmetry of the velocity field and the measurement does not imply that the galaxy is best fitted with a thin disc model.

In our sample four eLIER galaxies present particularly complex gaseous kinematics with no obvious symmetry axis and have been excluded from the following analysis. Two of these galaxies show approaching/trailing features while other two show evidence for extreme changes in the direction of rotation of the gas (MaNGA-ID `1-38167`, `1-274663`). The remaining eLIER galaxies display a wide range of gas velocity field patterns. While some are consistent with disc rotation, in other systems the velocity field appears disturbed. Overall, the large majority of galaxies in this class show coherent velocity shear patterns, showing both red- and blue-shifted emission. These gas flows are not always associated with large scale rotation. In Cheung et al. (2016), for example, we propose a biconical outflow model for an eLIER galaxy (MaNGA-ID `1-217022`), which has recently been subject to a minor merger event, as demonstrated by the presence of a nearby companion and the detection of neutral gas via the NaD absorption feature.

The observed distribution of stars-gas misalignment for the eLIER galaxies in our sample is shown in Fig. 4.8, with 30 out of 49 galaxies having misalignments larger than 30°. Making the appropriate volume corrections, necessary in order to take into account the MaNGA selection function, we infer that $65 \pm 7\%$ of eLIERs are misaligned with $|\phi_{\rm stars} - \phi_{\rm gas}| > 30°$. This number is significantly larger from that inferred by the SAURON and ATLAS^{3D} surveys (Sarzi et al., 2006; Davis et al., 2011). However, both surveys adopt a pure morphological selection, thus including galaxies with residual star formation into their sample, which would not be classified as eLIERs. Galaxies with detectable star formation (SF and cLIERs) have a misalignment distribution strongly peaked at zero (Fig. 4.8, bottom panel, only $11 \pm 2\%$ with $|\phi_{\rm stars} - \phi_{\rm gas}| > 30°$). Thus a small contamination from SF or cLIER galaxies can bring our result in line with previous work. Moreover our results confirm the theoretical prediction for the case of external accretion, as the observed distribution of misalignments for eLIERs

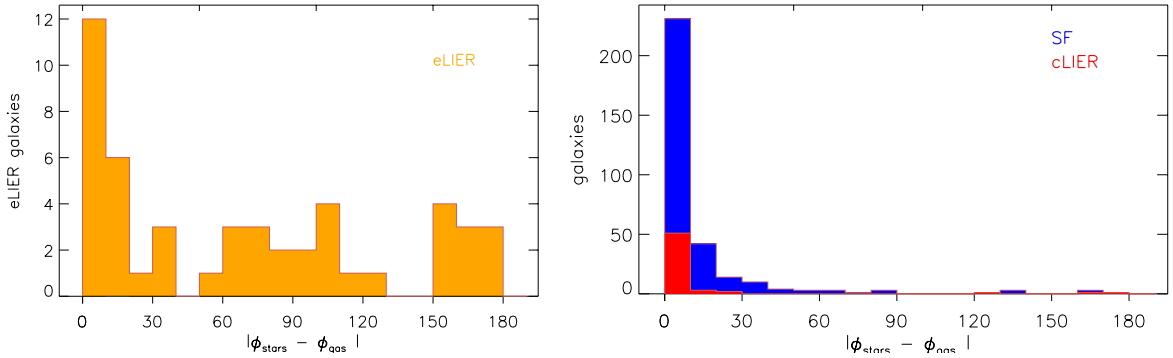

Figure 4.8: Histograms of the distribution of kinematic misalignments between the position angle of the major axis of the stellar component and of the ionised gas for the eLIER galaxies (left) and SF and cLIER galaxies (right) in the current MaNGA sample.

is peaked at 0, 90 and 180°.

In absence of internal processes (i.e. stellar mass loss), the misalignment histogram is predicted to be *symmetric* around 90° (Davis & Bureau, 2016). Making the assumption of isotropic accretion and long relaxation times, one would naively expect 150/180~83% of galaxies to have misalignments larger than 30°. The presence of a stronger peak at zero and the fact that the number of misaligned galaxies is lower than a naive estimate for isotropic accretion implies that internal processes are also likely to play a role, although secondary, in shaping the observed misalignment distribution. In particular, stellar mass loss will not only inject into the ISM some amount of gas sharing the same kinematic properties as the parent stars. This pre-existing disc would also create additional torque on the accreted misaligned gas and contribute to realign it with the stellar kinematic field (Sarzi et al., 2013; Davis & Bureau, 2016). Both effects would contribute to increase the fraction of aligned galaxies.

4.4 The effect of environment

Fundamental properties of the bimodal galaxy population, including colour, SFR and passive fraction are found to depend both on stellar mass and environment (Sec. 1.2.3, Blanton et al. 2005a; Baldry et al. 2006; Peng et al. 2010). Using data from legacy SDSS, it has been demonstrated that the change in EW(Hα) distribution as a function of environment is predominantly due to a change in the relative number of SF and passive galaxies (Balogh et al., 2004). If one restricts the study to star forming galaxies, the EW(Hα) (or equivalently the specific SFR) is observed *not* to depend on environment, i.e. if a galaxy forms stars on the main sequence, environments does not effect its SFR (Peng et al., 2010), which is consistent with the finding that stellar population ages do not depend on environment (Thomas et al., 2010). Passive galaxies with measurable EW of line emission (eLIERs in our classification), however, have long been associated with inefficiently accreting active galactic nuclei (e.g Kauffmann et al., 2003c; Kewley & Ellison, 2008). Therefore their role as red sequence galaxies with residual gas has not yet seen suitably discussed in the context of environmental studies.

In this work we have highlighted the similarities of eLIER to line-less galaxies in terms of the stellar populations and morphological properties. Given these observed similarities, it is logical to ask whether environment plays a role in the presence or absence of line emission on the red sequence. Some evidence in this direction was reported by Sarzi et al. (2006), who found a small difference in

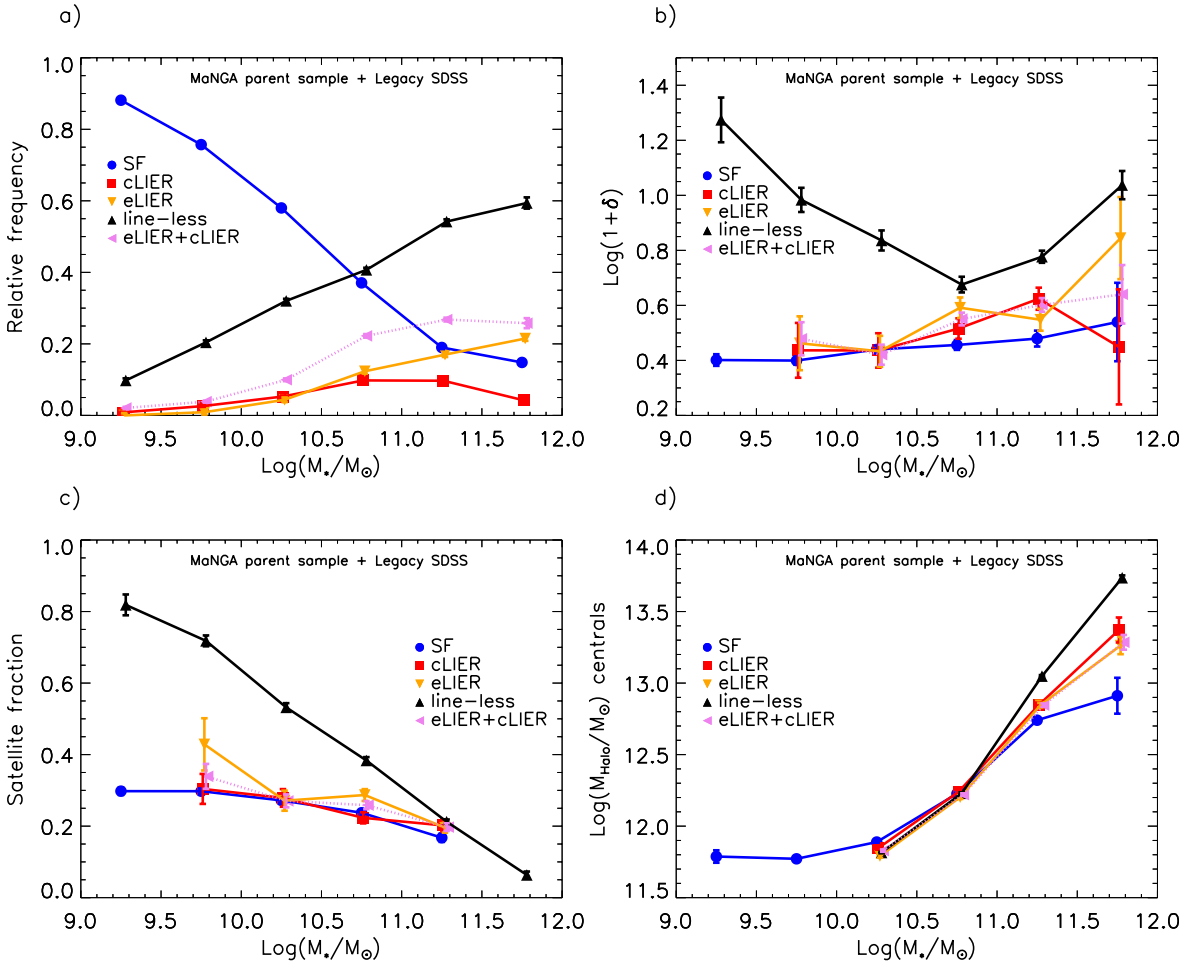

Figure 4.9: *(a)* The relative frequency of galaxies in different emission-line based classes derived from the MaNGA parent catalogue and legacy SDSS spectroscopy in bins of stellar mass. *(b)* Average overdensity as a function of stellar mass for galaxies of different emission line classes, based on the MaNGA parent catalogue and SDSS legacy spectroscopy. *(c)* Average fraction of galaxies classified as satellites in the Yang et al. (2007) group catalogue for each emission-line based galaxy class as a function of stellar mass. The galaxy sample is taken from the MaNGA parent sample, complemented with SDSS legacy spectroscopy. *(d)* Average halo mass for galaxies classified as central in the Yang et al. (2007) group catalogue for each emission-line bases galaxy class as a function of stellar mass. The galaxy sample is taken from the MaNGA parent sample, complemented with SDSS legacy spectroscopy. In each plot the error bar represents the error on the mean and only bins containing more than 4 galaxies are shown. The dotted line (eLIER+cLIER) refers to the union of both cLIER and eLIER classes.

the fraction of detected line emission between ETGs in the Virgo cluster compared to the field.

In order to address this question with a large sample of galaxies, in this section we make use of the MaNGA parent galaxy sample (Wake et al., *in prep.*), and study the emerging trends as a function of different environmental measures. We do not use the MaNGA data directly because the sample of LIER galaxies currently available is too small to reliably study environmental trends in several stellar mass bins. The MaNGA parent sample, on the other hand, includes all galaxies from the NSA catalogue which match the MaNGA target selection criteria ($\sim$ 30000 galaxies). We use legacy SDSS spectroscopy (Strauss et al., 2002), and make use of the line flux measurements from the MPA-JHU catalogue (Kauffmann et al., 2003c; Brinchmann et al., 2004; Tremonti et al., 2004) to compute the BPT classifications of each galaxy. In order to study trends as a function of stellar mass we correct for the effect of the MaNGA selection function.

In order to adapt the cLIER/eLIER distinction to single-fibre legacy SDSS, which does not cover the outer regions of galaxies, we make use of the integrated UV-optical colours, based on the findings in Sec. 4.2.1 above. We assume that both cLIERs and eLIERs would appear as LIER galaxies in single-fibre spectroscopy. A galaxy appearing as LIER in single-fibre spectroscopy is classified as cLIER if it lies on the blue cloud or the green valley ($NUV - r < 5$) and eLIER if it lies on the red sequence ($NUV - r > 5$) using UV-optical colours. We make use of the MaNGA parent sample instead of the full legacy SDSS in an attempt to minimise the role of aperture effects in this classification, an effect which is otherwise difficult to quantify. According to Sec. 4.2.1, our mixed spectroscopic + photometric eLIER/cLIER distinction introduces a 19% contamination for eLIERs and 13% contamination for cLIERs. Similarly, in the attempt to replicate in the best possible way the MaNGA-based classification, galaxies with EW(Hα) < 1.0 Å within the 3″ SDSS fibre are considered line-less. Seyfert AGN, as identified using the [SII] BPT diagram, are excluded from this analysis.

In Fig. 4.9(a) we show the fraction of galaxies in each class as a function of mass in the MaNGA parent sample. This figure is to be compared with Fig. 3.6, which shows the equivalent figure based on the MaNGA sample. Qualitatively the mass trends for each class are similar, however some differences are also present. In particular, the classification based on legacy SDSS finds less LIER galaxies than in the MaNGA data, which might be due to residual aperture effects.

In order to study environmental effect, we make use of adaptive aperture environmental measure presented in Etherington & Thomas (2015). The cosmic density ρ field is calculated using a cylinder centred on each galaxy and with length of 1000 km s^{-1} and radius given by the distance to the fifth nearest neighbour more luminous than $M_r < -20.26$ (where M_r is the k-corrected r-band magnitude). The environment estimator is cast in terms of an overdensity ($\delta = (\rho - \rho_m)/\rho_m$) relative to the average density of tracer galaxies ρ_m, and is most sensitive to scales around 2 Mpc (Etherington & Thomas, 2015).

We further make use of the environmental information provided by the Yang et al. (2005, 2007) group catalogue. The catalogue is based on a halo-finding algorithm applied to the NYU-Value Added Catalogue (Blanton et al., 2005a), based on legacy SDSS DR7 data. Galaxies belonging to the same dark matter halo are defined to constitute a 'group' (where the term group is used here irrespective of the number of galaxies in the association). The most luminous galaxy in each group is defined to be the 'central', while the other galaxies in each group are defined to be 'satellites'. Note that, following this definition, centrals do not need to necessarily lie at the geometric centre of the dark matter halo. Several galaxies are assigned to haloes that contain no other galaxy within them; these galaxies are called centrals even though no satellites are detected in SDSS (although deeper observations might reveal their presence). The halo mass (M_{halo}) is calculated for each group by Yang et al. (2007) considering the characteristic integrated luminosity (above some flux limit, and corrected for incompleteness) of the group members calibrated against the dark matter masses derived from models.

In Fig. 4.9(b) we show the mean environmental density as a function of stellar mass for each galaxy class (SF, cLIER, eLIER and line-less). The plot demonstrates that 1) At fixed stellar mass, line-less galaxies always live in denser environments than eLIER galaxies. The relative difference in environmental density between the two galaxy classes is large at both the lowest and highest stellar masses, with a minimum difference at $M_\star \sim 10^{10.5}$ $M_\odot$. 2) There is only a marginal difference in environmental density between SF galaxies and cLIER or eLIERs, with eLIERs living in marginally denser environments.

For the purpose of the study of line emission in the overall galaxy population, the most striking feature of of Fig. 4.9(b) is the large difference in environmental density between eLIERs (i.e. red sequence galaxies with line emission) and line-less galaxies (i.e. red sequence galaxies with EW(Hα) < 1.0 Å). *The legacy SDSS data demonstrates clearly that the lack of line emission on the red sequence is associated with higher environmental densities.* We discuss the physical processes that could be responsible for this phenomenon in Sec. 4.5.2.

Fig. 4.9(c) demonstrates that line-less galaxies have a substantially higher satellite fraction than any other galaxies class at all stellar masses lower than $M_\star \sim 10^{11}$ $M_\odot$. Hence the increase in the environmental density of line-less galaxies at low stellar masses is mostly driven by the fact that these galaxies are preferentially satellites.

At high stellar masses, on the other hand, line-less central galaxies have a higher mean halo mass than other galaxy classes (Fig. 4.9(d)). Higher mass haloes tend to have a higher number of satellites and also to be more strongly clustered, thus explaining the increase in environmental density at the high mass end. The figure also shows that in the highest mass bin, SF galaxies reside in lower-mass haloes than LIER galaxies (both eLIERs and cLIERs).

4.5 Discussion

4.5.1 Inside-out quenching and the nature of cLIER galaxies

A slow quenching pathway for late type galaxies

The properties of cLIERs are such that they can be considered objects in transition (in the process of being 'quenched') from the star forming blue cloud towards the quiescent red sequence. The MaNGA spatially resolved data further demonstrate that star formation in these galaxies terminates from the inside out, with LIER emission appearing in the central regions, while star formation continues in the disc. The quenching process is not only evident via the lack of detected star formation in diagnostic diagrams, but also in the stellar population properties, as LIER emission is strongly correlated with old stellar populations (Sec. 4.1).

The process leading to the quenching of the central regions is likely to be gentle, since it does not involve a change in the overall morphology and kinematics of the galaxy, although it is associated with the presence of a large central spheroidal component. cLIER galaxies are thus consistent with the idea of a 'slow quenching mode' for LTGs (e.g. Schawinski et al., 2014; Smethurst et al., 2015). Different lines of evidence point towards the need of a such a 'slow quenching' pathway for LTGs, associated with the increasing importance of the bulge component. Cappellari et al. (2013), for example, argue that the quenching process involved in the production of fast rotator ETGs needs to increase the bulge size, while at the same time removing the gas reservoir and/or shutting down star formation and maintaining the flatness of the disc at large radii. Moreover galaxies in the green valley are known to host larger bulge components than galaxies on the blue sequence of the same mass (Schiminovich et al., 2007). At higher redshift, Bell et al. (2012) and Bundy et al. (2010) argue for a similar slow quenching pathway initiated by gradual changes in internal structure.

A possible quenching mechanism, much discussed in the literature (e.g. Wake et al., 2012; Bluck et al., 2014), assumes the higher central spheroidal masses to be directly connected to the cause of galaxy starvation via AGN radio-mode feedback. Indeed, larger bulge/spheroid masses imply larger

black hole masses, hence higher capability of halo heating through radio-mode episodes (Heckman & Best, 2014), which in turn may result into lack of gas cooling onto the host galaxy.

The interruption of the inflow of cold gas onto the galaxy ('strangulation'), due to either heating of the gas in the halo or via halo mass shock heating, could lead to an inside-out quenching signature, assuming that the remaining cold gas is consumed more quickly in the central regions of galaxies. As illustrated by Leroy et al. (2008) the efficiency of star formation (i.e. the number of stars formed per unit gas mass) is not constant across galaxy discs (see Sec. 1.2.1), but is observed to steadily decrease with galactocentric distance, thus making this scenario a viable option.

Secular processes and bulge growth

Alternatively, the larger bulge masses, together with the implied slow timescale for the quenching process, may argue in favour of secular processes (i.e. mechanisms internal to the galaxies) playing a role in the quenching process in cLIERs. Bars, for example, tend to funnel gas towards towards the galactic central regions, thus contributing to the formation of (pseudo)bulges (Kormendy et al., 2010; Simmons et al., 2013; Cheung et al., 2013). Moreover, simulations show that the torques and stresses created by both bars and bulges on the cold gas component can lead to lower star formation efficiency, especially in the regions swept up by the bar (Emsellem et al., 2014; Fanali et al., 2015). Indeed, bar fraction is known to correlate with the galaxy's stellar mass and colour and specific SFR (Nair & Abraham, 2010; Masters et al., 2011), in the sense of redder and more massive, lower specific SFR discs having higher bar fraction. Moreover, bar fraction is observed to be higher in HI-poor galaxies (Masters et al., 2012), although no similar investigation of the molecular gas content of a large sample of barred and unbarred galaxies has been possible to date (see Saintonge et al. 2012 for the largest sample to date).

Using the current MaNGA sample, for galaxies with $\log(M_\star/M_\odot) > 10$ the bar fraction (defined as disc galaxies with $p_{bar} > 0.3$ from Galaxy Zoo 2) is $32 \pm 5\%$ for the SF discs, and $41 \pm 11\%$ for the cLIERs. We thus conclude that the difference in bar fraction between the two classes is not significant with the current sample size, and a larger sample is needed to observationally test the relative occurrence of bars in SF galaxies are cLIERs.

Models predicts that disc instabilities represent the dominant contribution to the formation of bulges in massive galaxies ($M_\star > 10^{10}$ $M_\odot$, De Lucia et al. 2011). Disc stability can be parametrised in terms of the stability parameter (Q, Toomre 1964), which in the case of gas+stars systems can be extended to include the two components (Jog & Solomon, 1984; Elmegreen, 1995; Martig et al., 2009; Romeo & Wiegert, 2011). The presence of a significant bulge goes towards increasing the stability of a cold gas disc to gravitational collapse. Indeed, results from the COLD-GASS survey (Saintonge et al., 2011) demonstrate that galaxies with significant bulges have lower star formation efficiencies (Saintonge et al., 2012). Spatially resolved observations of the gas component for the MaNGA sample would be crucial in testing the role of the bulge in driving the star formation efficiency in different galaxy classes.

Star formation efficiency for cold gas is found to be systematically lower in ellipticals (Martig et al., 2013; Davis et al., 2014) and in the bulge of our own Galaxy (Longmore et al., 2013). Therefore, the absence of the star formation in the central regions of cLIERs could be due to a significantly lower star formation efficiency, even in presence of a large molecular gas reservoir. In a similar fashion the central molecular zone in the Milky Way is found to have a star formation efficiency approximately 10

times lower than the Milky Way disc. In fact, the Milky Way itself is a likely cLIER candidate, given its inferred green valley optical colours and SFR lower than expected from the star formation main sequence (Mutch et al., 2011).

In this context, secular evolution processes (interaction with a bar or spiral density waves) and radial flows represent a possible explanation for the presence of cold gas in the central regions of cLIERs, which is required in order to explain the observed LIER emission. The kinematic correspondence between the stars and gas, which is preserved in the central regions of cLIER galaxies, further supports a scenario where the gas in the central region of cLIER galaxies is either integral part of the disc or has been acquired from it. Indeed, the absence of line-less bulges in the current sample is a strong indication that central regions of bulge + disc systems are always more gas rich than galaxies on the red sequence, and points towards the importance of the star forming disc as a possible reservoir of gas in these systems.

In summary, cLIER galaxies are consistent with both a scenario of slow gas exhaustion and a scenario of reduced star formation efficiency in the bulge, driven by dynamical processes. The presence of larger bulges in cLIER galaxies argues against a fast evolutionary track linking these galaxies to the blue cloud, but rather a slow evolutionary process. The cold gas content of the central regions of cLIERs is not known, however some amount of gas must be present in order to allow for the observed LIER emission. This gas shares the same kinematics of the star forming disc and is thus possibly driven into the central regions by bars or other disc instabilities. Follow-up resolved studies of the cold gas content of bulge + disc systems are needed in order to shed further light into the reasons for the absence of star formation in the central regions of cLIERs.

4.5.2 Ionised gas on the red sequence and the nature of eLIER galaxies

Origin of the gas in red galaxies

It has long been argued that red sequence galaxies have a large and plentiful source of ionised gas in their old stellar populations. Stellar evolution predicts that an old stellar population returns on the order of half its stellar mass to the ISM over a Hubble time (Ciotti et al., 1991; Padovani & Matteucci, 1993; Jungwiert et al., 2001). Mass return is dominated by stellar mass loss during the evolution of intermediate and low mass stars along the red giant branch and the post AGB phases. Padovani & Matteucci (1993) predict that, for a Salpeter IMF, a 15 Gyr old population will lead to a mass loss rate per unit stellar mass of

$$\dot{M}_\star = 2.3 \cdot 10^{-12}\ M_\odot\ yr^{-1}. \tag{4.3}$$

The mass of ionised gas can be estimated from the Hα luminosity as

$$M_{HII} = 2.3 \cdot 10^3 \left(\frac{L_{H\alpha}}{10^{38}\ erg\ s^{-1}}\right)\left(\frac{10^2\ cm^{-3}}{n_e}\right) M_\odot. \tag{4.4}$$

For typical integrated Hα luminosities observed in eLIERs, this implies a mass of about $\sim 10^4 - 10^5$ $M_\odot$. Therefore, for eLIER galaxies of mass of $\sim 10^{10.5}$ $M_\odot$, the typical nebular line luminosities can easily be accounted for by gas injected into the ISM by stellar mass losses over a timescale of only a few million years. However, the kinematic signatures of the ionised gas are expected to be similar to those of the parent stars. This predictions is at odds with the observational evidence that a large

fraction ($\sim$ 65 %) of eLIER galaxies are kinematically misaligned. Thus stellar mass loss can only be responsible for a minor fraction of the gas associated with LIER emission. Instead it is likely that the gas supplied by stellar mass loss is quickly transferred into the hot X-ray emitting phase, with only a small fraction succeeding to cool. Indeed, the standard paradigm of the ISM in red sequence galaxies assumes that supersonic motion of the ejecta through the ambient hot medium generates a strong shock that thermalises the gas to the kinetic temperature of the stars, $\sim 10^6 - 10^7$ K, on a timescale of $\sim 10^5 - 10^6$ yr (Sanders, 1981; Mathews, 1990; Sarzi et al., 2013). Episodic AGN activity could also be responsible for balancing cooling (Ciotti & Ostriker, 2007; Schawinski et al., 2007; Cheung et al., 2016) and maintaining the gas in a hot state.

In summary, the existence of a large population of red sequence galaxies with EW(Hα) $<$ 1Å and the same stellar population properties as eLIERs suggests that stellar mass loss cannot be the main source of cool gas in these galaxies. This inference is confirmed by the fact that in our sample of eLIERs external accretion is required in at least 65 % of the population to explain the observed kinematic misalignment between gas and stars.

The role of environment on the red sequence

As discussed in Sec. 4.4, environmental effects are known to play a key role in determining the passive fraction of galaxies (Dressler, 1980; Peng et al., 2010). In this work, we have shown that, in addition to determining the passive faction, environmental effects also affect the presence of line emission, and thus the cold gas content, in red sequence galaxies. In particular, we have demonstrated that red sequence galaxies with small or undetected line emission (EW(Hα) $<$ 1 Å) live in denser environments, both as centrals and satellites, than eLIERs of the same mass.

At the high end of the stellar mass function line-less galaxies are mostly the central galaxies in high-mass haloes. Their position within a large halo would both impede accretion of external cold gas and heat up the gas recycled via stellar evolution, thus leaving the galaxy line-less. Analysis of the stellar kinematics of the MaNGA data further demonstrates that at high masses most galaxies classified as slow rotators are line-less, as expected from the kinematics-density relation (Cappellari et al., 2011b). These galaxies are known to host X-ray haloes, whose temperature is consist with that expected from the thermalization of the kinetic energy of stellar ejecta (Sarzi et al., 2013). These central, massive, slowly-rotating line-less galaxies represent the striking endpoint of galaxy evolution.

At the low mass end, environment is known to play a crucial role in making galaxies line-less, albeit via a different route (e.g. Geha et al., 2012). We demonstrate in Fig. 4.9 that for $M_\star < 10^{10}$ $M_\odot$ more than 70 % of line-less galaxies are satellites, in contrast with the much lower satellite fraction for eLIERs ($\sim$ 40 %). Satellites are generally not thought to accrete gas after falling into the hot environment of galaxy overdensities (or anyhow to accrete at a substantially lower rate than centrals, Kereš et al. 2009) and are likely to undergo some amount of ram-pressure stripping as they enter a massive halo. Moreover, while at first the merger rate is enhanced as galaxies fall into rich haloes, once the galaxies virialise the large velocity dispersion within cluster considerably suppresses the subsequent merger rate (van Dokkum et al., 1999), thus making it harder to obtain gas from gas rich mergers. While it is possible that some amount of dense gas survives the infall event and allows the satellite galaxy to continue forming stars for a timescale comparable to the depletion time (Wetzel et al., 2013), once star formation ceases the strong environmental effects are likely to seriously disrupt the diffuse gas component and finally leave the galaxy line-less.

4.6 Additional material

We present here SDSS $g-r-i$ composite images and Hα flux maps all the cLIER and eLIER galaxies used in chapters 3 and 4.

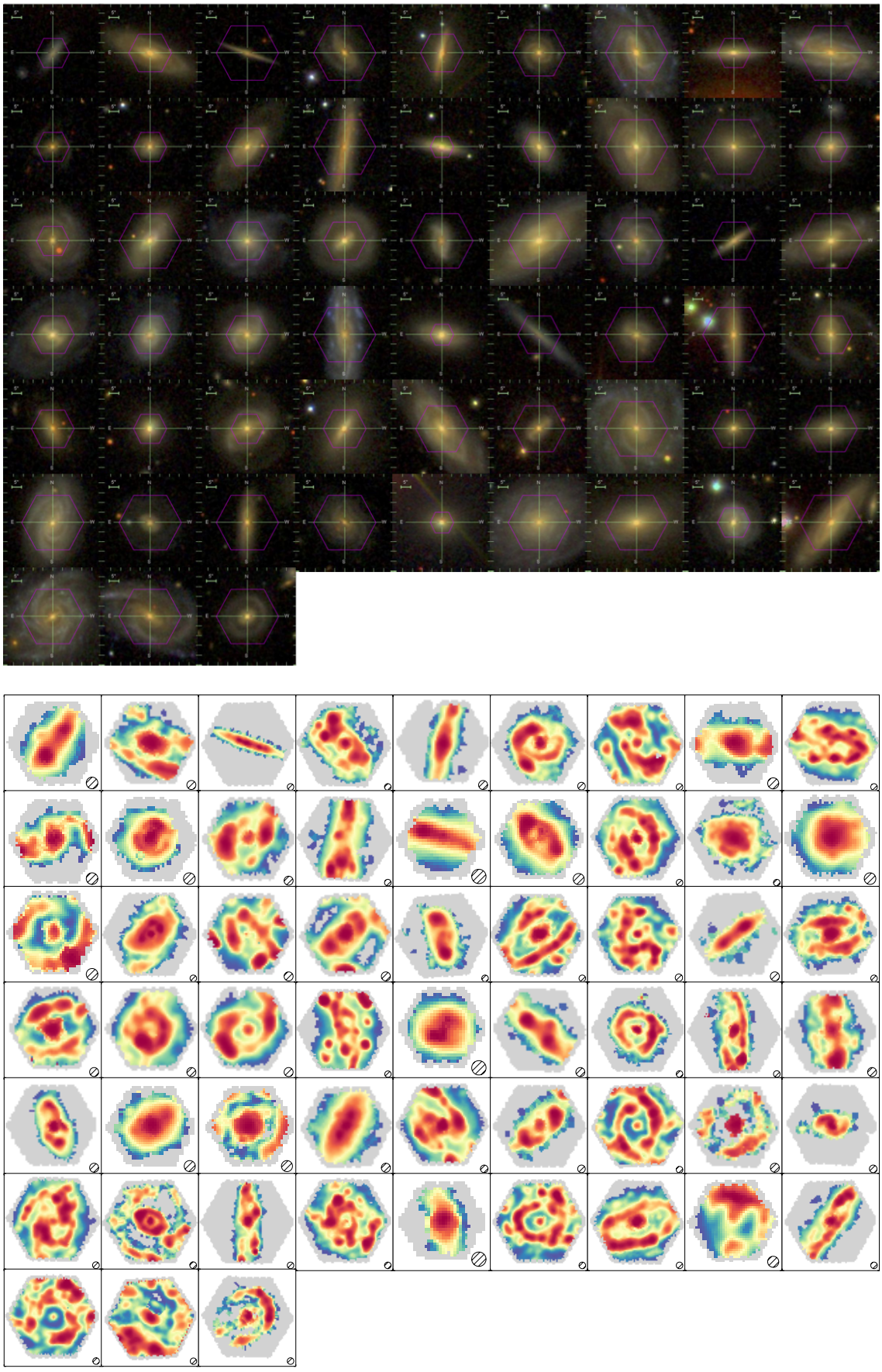

Figure 4.10: *Top*: SDSS g-r-i colour composite images (with MaNGA IFU bundle FoV superimposed) for the sample of cLIER galaxies studied in this work. *Bottom*: MaNGA Hα flux maps for the sample of cLIER galaxies studied in chapters 3 and 4.

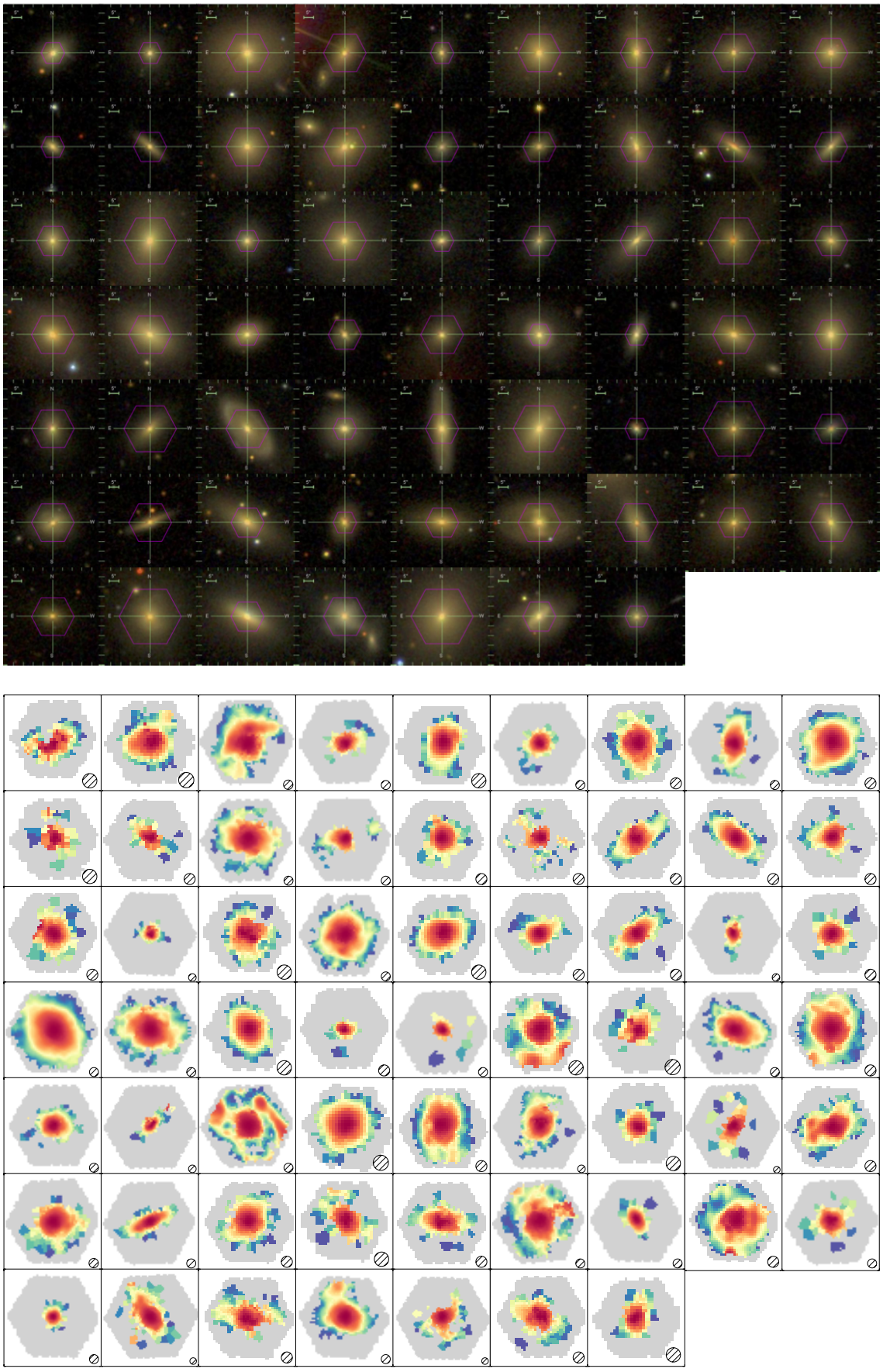

Figure 4.11: *Top*: SDSS g-r-i colour composite images (with MaNGA IFU bundle FoV superimposed) for the sample of eLIER galaxies studied in this work. *Bottom*: MaNGA Hα flux maps for the sample of eLIER galaxies studied in chapters 3 and 4.

Chapter 5

Metallicity gradients in the local Universe

Based on 'SDSS IV MaNGA - The shape of the gas metallicity and nitrogen abundance gradients in the local Universe' , Belfiore et al., 2017, MNRAS, 469, 151

Metals are direct products of stellar nucleosynthesis, thus making chemical evolution studies a powerful approach to understanding star formation and gas flows in and out of galaxies. The existence of tight relationships between stellar mass and gas phase oxygen abundance (the mass-metallicity relation, Lequeux et al. 1979; Tremonti et al. 2004), and the more recent identification of secondary scaling relations between stellar mass, metallicity and SFR, (Mannucci et al., 2010; Andrews & Martini, 2013) or gas content (Hughes et al., 2013; Bothwell et al., 2013, 2015, 2016) have paved the way to the development of a theoretical picture where the metallicity is regulated by the interplay between inflows of pristine gas, star formation and star formation-driven outflows (so called 'gas regulatory' or 'bathtub' models, Sec. 1.3, Erb 2008; Dayal et al. 2013; Lilly et al. 2013; Peng & Maiolino 2014).

The radial distribution of metals in galaxies is of particular interest because of its direct relation to the unknown radial profile of gas accretion, which in terms drives the inside-out growth of discs (Larson, 1976; Matteucci & Francois, 1989; Boissier & Prantzos, 1999; Pezzulli & Fraternali, 2016). Models of the metallicity gradient, which typically assume a simple radial dependence of the accretion rate (leading to inside-out growth) and no radial flows are capable of reproducing the observed metallicity gradients (Chiappini et al., 2001; Fu et al., 2009). Individual models, however, vary substantially in their most fundamental predictions. Some models, for example, predict a steepening of the metallicity gradients with time (Chiappini et al., 2001; Mott et al., 2013), while others predict the opposite (Mollá et al., 1997; Prantzos & Boissier, 2000; Fu et al., 2009; Pilkington et al., 2012b). Observations of high-redshift galaxies may provide more direct evidence regarding the time evolution of the metallicity gradients (Jones et al., 2013; Wuyts et al., 2016). Current studies at high redshift, however, are still limited to small sample sizes.

Alternatively, abundance ratios of elements of different nucleosynthetic origin can be used to gain further insight into the history of star formation and chemical enrichment in galaxies (Sec. 1.3.4). For example, the ratio between oxygen (mostly produced on short timescales by massive stars dying as Type II supernovae) and iron (mostly produced on long timescales by Type Ia supernovae) or nitrogen (produced by low- and intermediate-mass stars, Renzini & Voli 1981; Vincenzo et al. 2016a) can be used as probes for the average timescale of star formation in a stellar system.

Observationally it is well-known that in the local Universe disc galaxies present a negative metallicity gradient (Vila-Costas & Edmunds, 1992; Oey & Kennicutt, 1993; Zaritsky et al., 1994; van Zee et al., 1998; Moustakas et al., 2010). Only recently, however, sufficiently large samples of galaxies have become available to securely quantify the slope of the metallicity gradient (Moran et al., 2012; Sánchez et al., 2014; Pilyugin et al., 2015; Ho et al., 2015; Sánchez-Menguiano et al., 2016), and study its dependence on other galactic properties. Earlier studies, based on multi-slit spectroscopy, suffered from poor spatial sampling and difficulty in excluding regions which are not dominated by ionisation from massive stars. IFS of star forming galaxies and HII regions, as pioneered by the early studies of Rosales-Ortega et al. (2010) and Sánchez et al. (2012b), has been shown to be an ideal tool to circumvent these difficulties and provide accurate measurements of chemical abundances over the whole optical extent of nearby galaxies.

In this chapter we present a new study of the shape of the gas phase oxygen and nitrogen abundance gradient in the nearby Universe, based on IFS data from the SDSS-IV MaNGA (Sec. 2, Bundy et al. 2015) survey. Our aim in this chapter is to provide a statistically robust reference for modellers aiming to reproduce the evolution of abundance gradients and their shape in the nearby Universe. Unlike previous work in this area, the MaNGA galaxy sample is approximately flat in stellar mass and its simple selection function makes it possible to perform accurate volume corrections (Sec. 2.1.3), making this the first study of the metallicity gradient in nearby galaxies to use a *representative* sample of nearby galaxies over the whole mass range $10^9 - 10^{11.5}$ $M_\odot$. Moreover, this work represents a significant increase in sample size with respect to previous studies, as we derive metallicity gradients for a total of 550 galaxies, thus obtaining greater statistical power in studying the slope and shape of the metallicity gradient and other fundamental galactic properties.

5.1 The MaNGA galaxy sample

We select galaxies from a parent sample of 1392 galaxies observed by MaNGA within the first ~ 2 years of operation, corresponding to the publicly available SDSS data release 13 (DR13, Albareti et al. 2016). Higher level data products and emission line fluxes are obtained follwing the procedure described in Sec. 2.2. Following the revised galaxy classification scheme proposed in Sec. 3.2.2, we classify galaxies according to their emission line properties based on the [SII]/Hα versus [OIII]/Hβ BPT (Baldwin et al., 1981; Veilleux & Osterbrock, 1987; Kewley et al., 2001) diagram as:

- *Line-less galaxies*: No detected line emission (equivalent width [EW] of (Hα) < 1.0 Å within 1.0 R_e).
- *Extended LIER galaxies (eLIER)*: galaxies dominated by low ionisation emission-line regions (LIERs) at all radii where emission lines are detected. No evidence for any star forming regions.
- *Central LIER galaxies (cLIER)*: galaxies where LIER emission is resolved but located in the central regions, while ionisation from star formation dominates at larger galactocentric distances.
- *Star forming galaxies*: galaxies dominated by star formation in the central regions and at all radii within the galaxy disc.

For the remainder of this chapter we select the galaxies with the following properties:

1. Classified as star forming or cLIER, i.e. all galaxies that display star formation at some or all radii.

2. Major to minor axis ratio (b/a) greater than 0.4, to exclude highly inclined systems.

3. $9.0 < \log(M_\star/M_\odot) < 11.5$ primary+ and secondary sample MaNGA galaxies.

4. Interacting and merging galaxies are excluded since both observations and simulations confirm that interacting and merging galaxies have systematically flatter metallicity gradients due to gas mixing (Kewley et al., 2010; Rich et al., 2012). In particular, we exclude galaxy pairs, defined as galaxies within the SDSS spectroscopic catalogue with projected separation < 100 kpc and line-of-sight velocity difference of < 500 km s^{-1}. In order to exclude late-stage mergers, where the small separation between the two galaxies prevents SDSS from having spectroscopic coverage of both galaxies, we make use of the visually classified merger catalogue from the Galaxy Zoo merger project (Holincheck et al., 2016). We exclude galaxies with a merger probability $p_{merger} > 0.4$.

Fig. 5.1 displays the position of the selected MaNGA galaxies in the redshift-mass plane, with the full DR13 sample also displayed in grey. As discussed in Sec. 2.1.3, MaNGA observes larger (hence generally more massive galaxies) at higher redshifts, in order for these galaxies to be covered to the appropriate galactocentric distance with the available IFUs. For the same reason, the secondary sample targets are always observed at higher redshift with respect to primary+ sample targets of the same luminosity.

After applying the cuts described above to the MaNGA DR13 sample we obtain a sample of 550 galaxies (334 primary+ sample, 216 secondary; blue circles and red triangles in Fig. 5.1 respectively).

5.2 Deriving the abundance gradient

5.2.1 Identifying star forming regions

The formation of new stars in galaxies can be traced by observations of HII regions, where photoionisation equilibrium is maintained by radiation from embedded hot massive O and B stars. Apart from classical, discrete HII regions, galaxies are observed to contain low surface brightness DIG, sometimes also referred to as warm ionised gas (Reynolds, 1984; Hoopes & Walterbos, 2003; Oey et al., 2007). The ionisation and energetics of DIG are a subject of active research. A combination of radiation leaking from classical HII regions, massive stars in the field and radiation from hot evolved stars may all be required to reproduce the observed properties of the DIG (Martin, 1997; Oey & Kennicutt, 1997; Hoopes & Walterbos, 2003; Zhang et al., 2017). In particular, spectroscopic studies of the DIG in the Milky Way (Reynolds et al., 1995; Madsen et al., 2006) and external galaxies (Rand et al., 1990; Martin, 1997; Rossa & Dettmar, 2003) demonstrate that DIG shows emission line ratios typical of LIERs, thus requiring a combination of lower ionisation parameter and a harder ionisation field than HII regions. Since metallicity diagnostics are calibrated on HII regions models, it is necessary to minimise the contribution of DIG when measuring chemical abundances from emission line ratios.

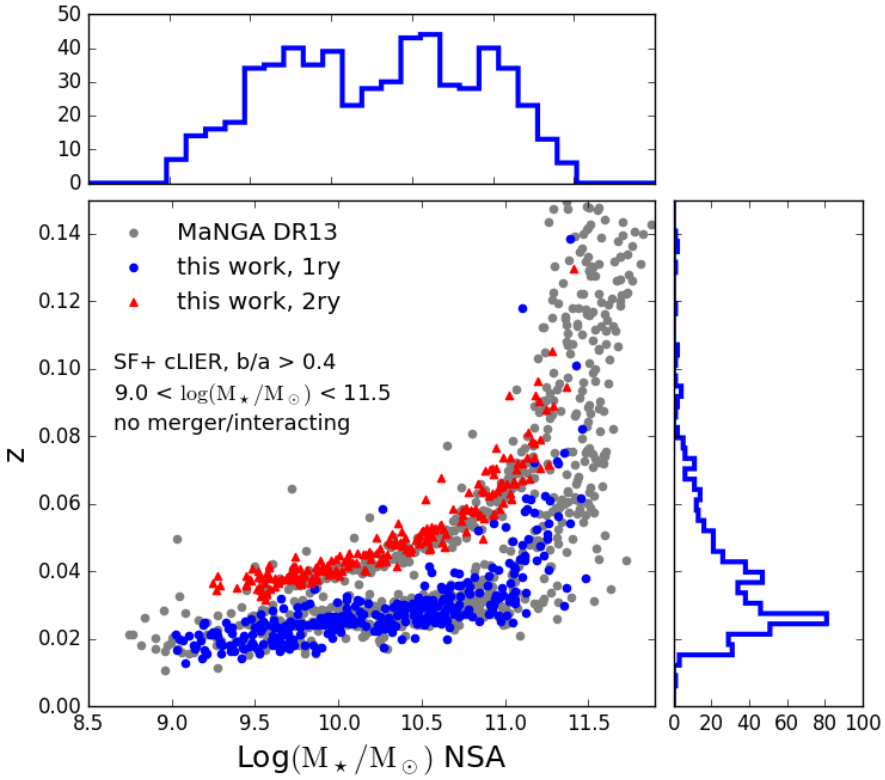

Figure 5.1: The MaNGA sample used in this chapter in the redshift-$M_\star$ plane. The full MaNGA DR13 sample is plotted in grey, while galaxies selected for the study of gas-phase metallicity (SF and cLIER galaxies, b/a > 0.4 and 9.0 < log($M_\star/M_\odot$) < 11.5) are plotted in blue circles (primary+ sample), red triangles (secondary sample). The redshift and stellar mass distributions for the full sample used in this work are shown as blue histograms.

HII regions have typical sizes of tens to a few hundreds parsecs and are thus not resolved by MaNGA (at the median redshift of 0.03 the MaNGA PSF FWHM corresponds to 1.5 kpc). In this chapter we make use of diagnostic line ratios to separate star forming regions (which are assumed to be collections of unresolved HII regions) and DIG. In particular, we exclude regions which are not classified as star forming using the [SII]/Hα versus [OIII]/Hβ BPT diagram and the Kewley et al. (2001) demarcation line. As demonstrated in chapter 1, this criterion successfully excludes extra-planar and inter-arm regions in star forming galaxies. This criterion also excludes the central regions of cLIER galaxies, which, by definition, display LIER line ratios. For these galaxies we compute metallicity profiles which are effectively centrally truncated. We note that, despite the exclusion of regions dominated by DIG, the diffuse gas component may affect the line ratios measured for HII regions, especially in the low surface brightness regime, where the contamination from DIG is expected to be most severe.

Previous work has also demonstrated that there exists a tight relation between diagnostic line ratios and EW(Hα) in emission, in the sense that LIERs have EW(Hα) < 3 Å in emission (Cid Fernandes et al., 2011; Sánchez et al., 2015). After applying the BPT cut described above and also requiring S/N > 3 on the metal lines required to measure chemical abundances, only 0.3% of spaxels considered have EW(Hα) < 3 Å and 3% have EW(Hα) < 6 Å. The exclusion of these spaxels from further analysis does not change any of the subsequent results presented in this chapter.

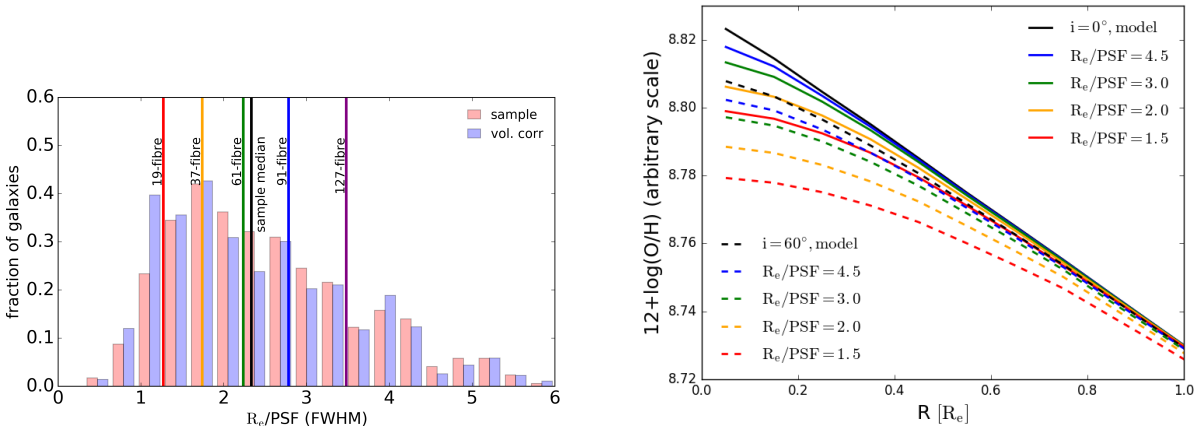

Figure 5.2: *Left*: Histogram of the ratio of the effective radius of MaNGA targets and the MaNGA PSF (FWHM). The red histogram represents the full MaNGA sample used in this work, while the blue histogram represents the volume-corrected distribution. Since MaNGA observes galaxies to a fixed galactocentric distance in units of R_e independently of the galaxy brightness, the volume correction does not introduce a large change in the underlying distribution. The coloured vertical lines represent the median values of R_e/PSF for the whole sample (R_e/PSF = 2.3) and for bundles of different sizes (19-fibre: 1.3 , 37-fibre: 1.7, 61-fibre: 2.2, 91-fibre: 2.8, 127-fibre: 3.5). *Right*: The effect of inclination and beam smearing on a model metallicity gradient, computed from a projected 3D exponential flux model for two emission lines. Solid lines refer to a face-on disc ($i = 0°$) while dashed lines are for $i = 60°$. Lines of different colour represent the effect of varying R_e/PSF, as detailed in the legend.

5.2.2 The effect of spatial resolution

Observed metallicity gradients can be systematically affected by the 'beam smearing' effect of the PSF. This effect is increasingly important at higher redshift and for marginally resolved galaxies (Yuan et al., 2013; Mast et al., 2014; Stott et al., 2014; Wuyts et al., 2016), but also affects the measurement of the metallicity gradient at the typical resolution of the MaNGA data. In the MaNGA survey galaxies are observed out to a fixed galactocentric radius in units of R_e, hence MaNGA bundles of different sizes have systematically different R_e/PSF ratios: larger bundles afford more resolution elements per R_e. By virtue of the MaNGA target selection, to first order there is no correlation between the galaxy luminosity (or stellar mass) and the size of the bundle it has been allocated. This means that, on average, R_e/PSF does not depend on stellar mass within the MaNGA sample (see also Sec. 5.4.2). This conclusion does not hold if one is interested in physical distance, i.e. kpc/PSF, which depends systematically on mass within the MaNGA sample, as more massive galaxies are observed at higher redshift (Sec. 2.1.3).

In Fig. 5.2, left, we show the distribution of the R_e/PSF ratio for the MaNGA sample used in this work (red histogram). The median R_e/PSF is 2.3 (varying from 1.3 for the 19-fibre bundles to 3.5 for the 127-fibre bundles). Applying a volume correction (blue histogram) does not have a large effect on the R_e/PSF distribution, since R_e/PSF is to first order independent of galaxy luminosity by selection.

In order to study the effect of beam smearing in a model situation we construct a 3D model of an exponential disc, with vertical scale height corresponding to an oblateness of q=0.13, as assumed in Sec. 5.2.4. We then rotate the model to different inclinations (i = $0, 30, 45, 60, 75°$) and generate 2D on-sky projections by summing the flux along the line-of-sight. For each projection, we convolve the resulting 2D image with a Gaussian PSF with FWHM corresponding to R_e/PSF = $1.5, 2.0, 3.0, 4.5$, in order to cover the range of parameter space relevant to the MaNGA data. Since metallicity is a function of line ratios, we perform this procedure for two different flux maps (corresponding in this

example to the [NII] and [OIII] lines), chosen to generate a metallicity gradient with a slope of -0.1 dex R_e^{-1}. Since R_e is the only spatial scale in the problem the beam smearing effect depends only on the ratio between R_e and the resolution element (R_e/PSF) and the assumed slope of the metallicity gradient.

Fig. 5.2, right panel, shows the effect of beam smearing on the metallicity gradient for the $i = 0°$ (solid lines) and $i = 60°$ (dashed lines) model. The colour of the lines represents different amount of beam smearing, while the black lines representing the result from using the un-convolved 2D projected models. From this simulation we conclude that

1. The effect of beam-smearing is increasingly important at smaller galactocentric radii for all inclinations.

2. Even with no beam smearing, in this simple model, inclination generates a flattening of the metallicity gradient, since flux from different galactocentric radii is summed when the model is projected in the plane of the sky. A residual dependence of the mass-metallicity relation on inclination, likely caused by this effect, is indeed observed in SDSS single-fibre abundances (Tremonti et al., 2004). Our toy model does not take into account differential extinction, which would further attenuate the flux from the central, metal-rich regions and thus produce an even more significant flattening of the metallicity gradient.

For each of the models produced we fit a linear metallicity gradient and study the effect of inclination and beam smearing on the recovered slope for models of different inclinations as a function of R_e/PSF. Since the central regions of galaxies are the most affected by beam smearing, we attempt a fit to the recovered metallicity gradient in two different radial ranges: (1) between 0.5 and 2.0 R_e and (2) over the whole considered radial range (0.0-2.0 R_e). As expected, we observe a systematic flattening in the metallicity gradient with decreasing R_e/PSF and also with increasing inclination, even for large values of R_e/PSF. This motivates the exclusion of highly inclined systems (b/a <0.4, or $i < 68°$) in this chapter. Moreover, the inclusion of the central regions ($R < 0.5\ R_e$) in a linear fit to the metallicity gradient causes a significant systematic flattening of the derived slope. We therefore recommend the exclusion of the central regions in order to recover the intrinsic metallicity gradient in the MaNGA sample. The systematic bias in the recovered metallicity gradient with respect to the true gradient increases for steeper model gradients (in units of dex R_e^{-1}), but the qualitative conclusions of this sections remain valid.

The toy model presented above does not aim to reproduce the details of the nebular emission in real galaxies. Several important factors are not taken into account, including the clumpy and non-uniform flux distribution of line emission, the effect of dust (and thus of differential extinction across the galaxy disc) and the systematic change in the property of line emission from classical HII regions to the diffuse ISM (Zhang et al., 2017). The latter effect, in particular, implies that star forming regions are increasingly contaminated by lower surface brightness DIG as the physical resolution of the observations is degraded. These possible systematic effects should be taken into account when comparing the results derived in this work with observations derived at much higher spatial resolution. Further analysis of the resolution effects in the MaNGA sample is presented in Sec. 5.4.2.

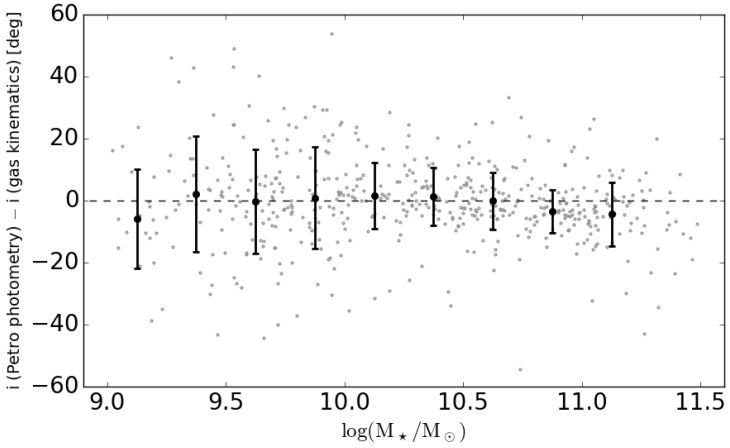

Figure 5.3: The difference between the inclination calculated from elliptical Petrosian photometry and that obtained from fitting the gas kinematics with a thin-disc model (see Westfall et al., in prep). The black points show the median in 0.25 dex mass bins, with the respective standard deviation represented by the error bars.

5.2.3 The determination of disc inclination

In this chapter the inclination of the disc is derived from the axis ratios (b/a) obtained by performing elliptical Petrosian photometry (from the NSA catalogue, Sec. 2.1.3). In order to estimate the effect of errors on the inclination on the metallicity gradient, we use the toy model galaxy described in Sec. 5.2.2. We set up models with different inclinations (0, 30, 45, 60, 75°) and recover the slope of metallicity gradient assuming the measured inclination is affected by a Gaussian error of 10°. The resulting difference between the true and measured slope of the metallicity gradient after 1000 noise realisations are computed. Even though the distributions have a positive tail (i.e. a tail where the inferred slope is flatter than the measured one), their median agrees with zero (no systematic difference between measured and true slope) to better than 0.01 dex R_e^{-1}. We therefore conclude that random errors on the inclination consistent with those expected from the photometric determination do not affect the results presented in this paper.

A more serious concern is represented by possible systematic biases in the determination of b/a. For low-mass galaxies ($\log(M_\star/M_\odot) < 9.5$) the axis ratio can be ill-defined due to clumpiness, lopsidedness, weak continuum heavily contaminated by line emission and small sizes compared to the PSF. At the high-mass end ($\log(M_\star/M_\odot) > 10.5$), on the other hand, the bulge becomes a concern, as light from the central spheroidal component may bias the measurement of the disc b/a. In order to prove that these effects do not bias the inclinations measured from photometry for our sample we have compared the Petrosian inclinations with the inclinations derived by fitting a thin-disc model to the gas velocity field (by K. Westfall). Fig. 5.3 shows the comparison between the kinematic and Petrosian inclinations, demonstrating that the two estimates of inclination are in good agreement over the whole mass range, despite significant dispersion ($\sim 16°$ at the low mass end to $\sim 19°$ at the high mass end). We conclude that the systematic median difference between Petrosian and kinematic inclination is always small ($< 6°$), even in low-mass systems.

5.2.4 Measuring the gradient

Following the classification of spaxels as star forming (Sec. 5.2.1), the gas phase metallicity is derived using the Maiolino et al. (2008) (M08) R23 and Pettini & Pagel (2004) (PP04) O3N2 metallicity calibrations described in Sec. 1.4.2 for each spaxel in which the relevant line ratios are detected with S/N > 3. Similar S/N cuts are applied in order to measure the N/O ratio, by making use of the calibration discussed in Sec. 1.4.2. To determine radial abundance gradients we calculate the deprojected distance of each spaxel. The inclination was derived from the measured semi-axis ratio (b/a) by assuming a constant oblateness of q = 0.13 (Giovanelli et al., 1994) according to

$$\cos^2(i) = \frac{(b/a)^2 - q^2}{1 - q^2}. \tag{5.1}$$

The choice of the correct scale length to normalise the abundance gradient in disc galaxies is not obvious. We seek a definition of scale length which is both robust and physically motivated. To this aim, we adopt the elliptical Petrosian effective radius (henceforth R_e), which is the most robust measure of the photometric properties of MaNGA galaxies provided by the NSA catalogue. We discuss in Sec. 5.4.1 the effect of choosing a different normalising radial scale length.

For each galaxy we compute the benchmark metallicity gradient in the radial range 0.5-2.0 R_e, unless otherwise stated (although not all galaxies are covered to 2.0 R_e). cLIER galaxies do not have valid profiles in the central regions, as described in Sec. 5.2.1. However, the effect of these centrally truncated profiles is quite small as most of the LIER emission is confined within 0.5 R_e and the benchmark metallicity gradient is computed in the range 0.5-2.0 R_e. This radial range is used to minimise the effects of inclinations and beam smearing on our gradient measurements (see Sec. 5.2.2), but also in light of the fact that significant deviations from a linear fit are observed at both smaller and larger radii (Sánchez et al., 2014; Sánchez-Menguiano et al., 2016).

In order to fit a straight line model to the metallicity gradient, we derive the azimuthally averaged metallicity in radial bins of 0.1 R_e and perform an unweighted least-squares linear fit. A gradient is not computed for galaxies with less than four valid metallicity data points in this radial range 0.5-2.0 R_e. The errors on the metallicity gradient are derived by a bootstrapping analysis. The residuals from the initial line fit are drawn randomly and with replacement and applied to data, which is then refitted with a straight line model. For each galaxy the process is repeated 1000 times and the standard deviation of the bootstrapped gradient is taken to be the formal error.

5.3 The shape of the oxygen and nitrogen abundance gradients

5.3.1 The mass dependence of the metallicity gradient

Fig. 5.4 (top) shows the dependence of the metallicity gradient on stellar mass. Here the metallicity gradient is measured in the radial range 0.5 - 2.0 R_e with the M08 R23 calibration. Individual gradients are plotted as grey points, while the median metallicity gradient in 0.25 dex bins of stellar mass is plotted as red points with associated error on the mean. We note that the scatter in the value of the metallicity gradient at fixed mass is relatively large and increases with mass, going from 0.08 dex R_e^{-1} at the low-mass end to 0.15 dex R_e^{-1} at the highest masses. The metallicity gradients of NGC 628 (see chapter 6) and the Milky Way (data from Genovali et al. (2014), as described in Sec. 5.5.2) are plotted as yellow stars and fit within the scatter observed in the MaNGA sample.

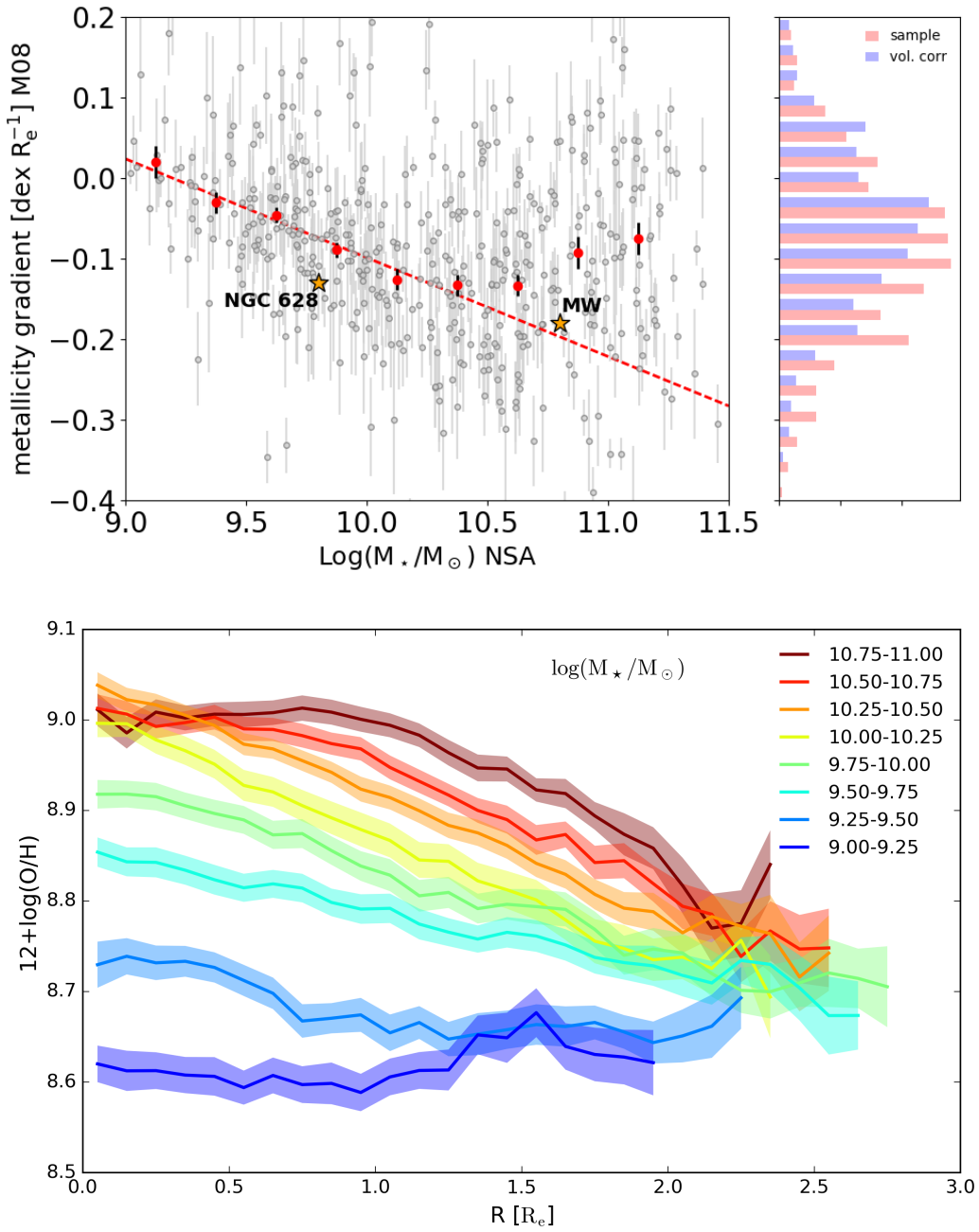

Figure 5.4: *Top*: The metallicity gradient (measured in the radial range 0.5 - 2.0 R_e) using the M08 calibration based on R23 as a function of stellar mass. The red points represent the median measurements in 0.25 dex stellar mass bins with corresponding errors. The red dashed line is a straight line fit to the median gradient as a function of mass for $\log(M_\star/M_\odot) < 10.5$. The stars represent the metallicity gradients measured for NGC 628 (see chapter 6) and the Milky Way (from Genovali et al. (2014), as described in Sec. 5.5.2). The histogram on the right represents the distribution of metallicity gradients for the full sample (red) and for a volume weighted sample (blue). *Bottom*: The shape of the metallicity gradient (using the M08 calibration based on R23) in 0.25 dex mass bins from $\log(M_\star/M_\odot) = 9.0 - 11.0$. For each mass bin the shaded region represents the error on the median gradient.

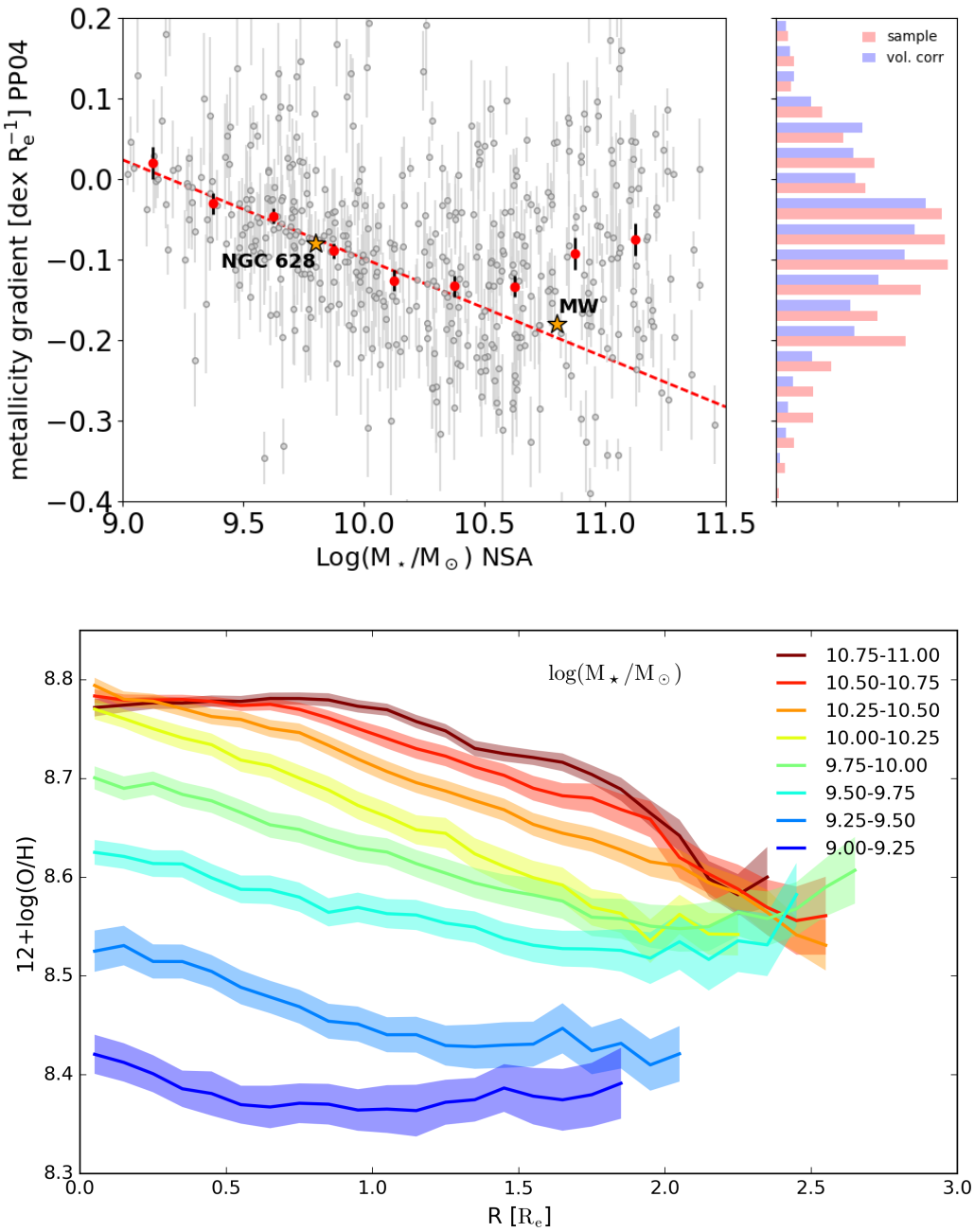

Figure 5.5: Same as in Figure 5.4 but for the Pettini & Pagel (2004) O3N2 metallicity calibrator.

We observe that the slope of the oxygen abundance gradient becomes increasingly negative with stellar mass, going from roughly flat at $\log(M_\star/M_\odot) = 9.0$ to -0.14 dex R_e^{-1} at $\log(M_\star/M_\odot) = 10.5$. In the stellar mass range $9.0 < \log(M_\star/M_\odot) < 10.5$ the relation between the slope of the gradient and $\log(M_\star)$ is well fitted by a straight line with negative slope (red dashed line). Galaxies of higher mass show an inversion of this trend, displaying shallower, but still negative gradients.

In Fig. 5.4 (top) we also show the histogram distribution of all the measured gradients (red) and the derived distribution after applying the volume weights (blue), thus representing our inference for the gradient distribution in a volume-limited sample. The mean and scatter of the metallicity gradient distribution for the MaNGA sample is $\mu = -0.08$ and $\sigma = 0.12$ using the M08 calibration. In the case of a volume-limited sample (in the stellar mass range $10^9 - 10^{11.5}$ $M_\odot$), low-mass galaxies, which display flatter gradients, are preferentially up-weighted. This effect causes an overall flattening of the volume-averaged metallicity gradient, which we infer to have mean $\mu = -0.06$ and scatter $\sigma = 0.12$.

An equivalent trend between metallicity gradient and stellar mass is observed using the Pettini & Pagel (2004) metallicity calibration based on O3N2 (see Fig. 5.5, top). In this case the mean and scatter of the metallicity gradient for the MaNGA sample are $\mu = -0.08$ and $\sigma = 0.10$ ($\mu = -0.07$ and $\sigma = 0.10$ after volume correction).

In Fig. 5.4 (bottom) and 5.5 (bottom) we show the stacked profiles for the metallicity gradient (using the M08 R23 and the PP04 O3N2 calibrations respectively) for galaxies of different stellar masses. The profiles are obtained by computing the robust estimate of the median profile (using Tukey's biweight, Beers et al. 1990) and standard deviation within each mass bin. Shaded regions represent the error on each stacked profile, which take into account the number of galaxies contributing at each radius. For each mass bin a profile is computed only if more than 12 galaxies have a valid measured profile at that radius.

The mass-metallicity relation is responsible for the zero-point vertical offset between the different profiles. Aside from the vertical offset, the figure highlights the differences in *shape* in the metallicity profiles for galaxies of different stellar masses. In particular, we observe that

1. Galaxies with $\log(M_\star/M_\odot) < 9.5$ have flatter profiles than higher mass galaxies in the full radial range probed by our observations.

2. Galaxies with $\log(M_\star/M_\odot) > 10.5$ show a flattening in the central regions ($R < 0.5\ R_e$). While these are the regions of the metallicity profile most affected by beam-smearing, they are also flatter with respect to the inner regions of lower mass galaxies. Since R_e/PSF does not depend on mass, the observed flattening is highly significant in a differential sense.

The same qualitative features regarding the shape of the metallicity profile are observed by making use of the Pettini & Pagel (2004) metallicity calibrator, despite the differences in normalisation of the oxygen abundance scale. We note that the choice of radial range used to compute the slope of the metallicity gradient has an effect on the measured slope, especially for higher mass galaxies, as they show strongly flattened profiles out to 1.0 R_e. A steeper slope of the metallicity gradient is naturally obtained if a larger fraction of the central regions is excluded from the linear fit for high mass galaxies. We have checked that the features discussed above are preserved if we exclude cLIER galaxies from the stacks. Their contribution in anyway small, except in the highest mass bins.

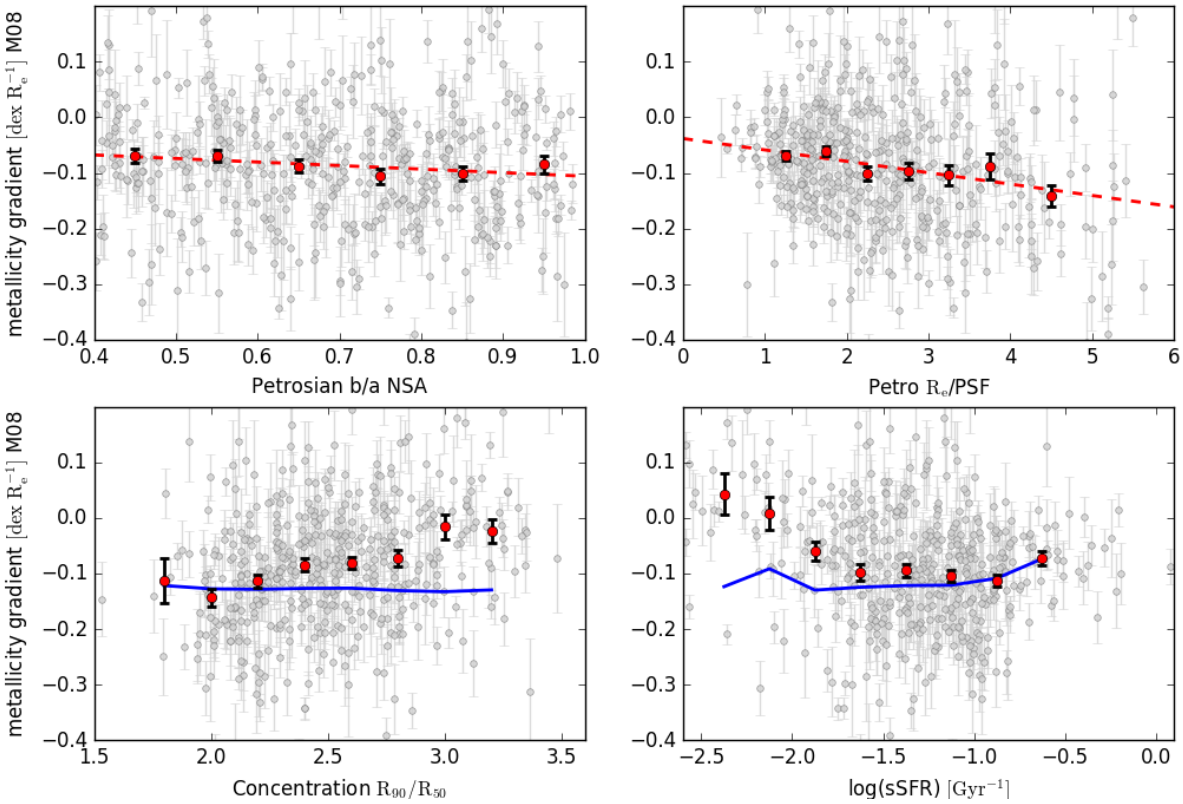

Figure 5.6: The slope of the metallicity gradient as a function of axis ratio (b/a, from elliptical Petrosian photometry), R_e/PSF (FWHM), as a measure of the beam smearing effect, concentration (R_{90}/R_{50}) and specific star formation rate (sSFR [Gyr^{-1}]) using the M08 metallicity calibrator based on R23. The red dashed lines are a linear fit to the binned data (red data points with error bars). The blue solid lines in the lower panels are the expected metallicity gradient for each bin if stellar mass was the only driving parameter, predicted using the relation between the metallicity gradient and stellar mass from Sec. 5.3.1.

5.3.2 Dependence of the metallicity gradient on secondary parameters

In Fig. 5.6 we study the dependence of the metallicity gradient in the radial range 0.5-2.0 R_e on several secondary parameters. Using the current sample selection, the metallicity gradient has a weak negative dependence on inclination (parametrised by the elliptical Petrosian axis ratio, b/a) and a clear negative dependence on the number of PSF FWHM within one R_e (top panels in Fig. 5.6). By fitting a straight line relation between the slope of the metallicity gradient and b/a we obtain that the gradient steepens by 0.03 dex R_e^{-1} going from b/a of 0.4 to face-on galaxies. Performing the same procedure with the PSF/R_e dependence, we obtain that the gradient steepens by 0.08 R_e^{-1} going from 1.5 to 3.5 PSF/R_e (corresponding roughly to the expected resolutions for the 19-fibre and the 127-fibre bundles respectively).

In the bottom panels of Fig. 5.6 we show the dependence of the metallicity gradient on galaxy concentration (a proxy for the bulge fraction, defined as R_{90}/R_{50}, where R are Petrosian radii containing 50% and 90% of the light respectively) and specific SFR (sSFR = SFR/$M_\star$). The SFR is calculated from the extinction-corrected Hα emission for the whole galaxy, as discussed in Sec. 4.2.1. The data shows a positive correlation of metallicity gradient with concentration, in the sense of more highly concentrated galaxies having flatter gradients. The dependence between metallicity gradient

and sSFR is flat for log(sSFR) > -1.5 Gyr^{-1}, but galaxies with lower sSFR show remarkably flatter metallicity gradients.

Both concentration and sSFR correlate with stellar mass, in the sense that galaxies with higher concentration and lower sSFR also have higher stellar mass. In order to test the relation of these secondary parameters with the metallicity gradient, it is thus necessary to control for the effect of stellar mass. Making use of the observed relation between stellar mass and metallicity gradient, for each bin in concentration or sSFR we calculate the slope of the metallicity gradient expected from its median stellar mass. The resulting predicted slopes are plotted as blue solid lines in the lower panels of Fig. 5.6. This exercise demonstrates that stellar mass is consistent with being the main driving parameter of the metallicity gradient for low concentrations and high sSFR galaxies (C <2.6, log(sSFR) > -1.5 Gyr^{-1}), but galaxies of high concentration and low sSFR show flatter gradients than expected from the stellar mass dependence alone. We have checked that the deviations from the expected gradient observed for high concentration and low sSFR galaxies persist when using the PP04 O3N2 calibration.

5.3.3 The mass dependence of the N/O abundance ratio

Fig. 5.7 (top) shows the dependence of the log(N/O) gradient (measured in the radial range 0.5 - 2.0 R_e) on stellar mass. Individual gradients are plotted as grey points, while the median gradient in 0.25 dex bins of stellar mass is plotted in red symbols, with associated errors. The distribution of log(N/O) gradients for the whole sample (red) and for a volume-corrected sample (blue) are plotted as histograms on the right of panel of Fig. 5.7 (top), demonstrating that the log(N/O) gradient is slightly steeper than the average metallicity gradient, and is affected by similar scatter (mean log(N/O) gradient of -0.07 dex R^{-1} with scatter of 0.09 dex). In contrast to the metallicity gradient, the log(N/O) gradient is observed to steepen with stellar mass over the whole observed stellar mass range. The steepening represents, however, only a modest effect (-0.02 dex R_e^{-1} per dex in stellar mass).

Contrary to the behaviour of the metallicity gradient, the log(N/O) abundance ratio does not flatten in the innermost regions of massive galaxies (Fig. 5.7, bottom), where a flattening of the oxygen abundance gradient is observed. In fact, we detect a *steepening* of the N/O ratio gradient in the inner regions of the most massive galaxies in the sample, as further discussed in the next section.

5.3.4 The behaviour at small and large radii

In this section we focus on a quantitative comparison of the changes in slope of the metallicity and N/O gradients for galaxies of different masses as a function of radius.

To do so, we define three radial ranges 0.0-0.5 R_e, 0.5-2.0 R_e and 2.0-3.0 R_e respectively and study both the distribution of the metallicity profiles in individual galaxies and the results from a stacking analysis in stellar mass bins. We stack metallicity profiles in four stellar mass bins 0.5 dex wide (Fig. 5.8). Each profile is normalised to the median value of all profiles in that bin at 1.0 R_e, in order to mitigate the effect of the mass-metallicity relation. We then fit each profile with a straight line in the three different radial ranges considered (shown as red, black and blue dashed lines in Fig. 5.8, left). The slopes obtained from fitting the stacks are compared with the distributions obtained by fitting individual galaxy profiles shown as histograms in Fig. 5.8. The red, black and blue histograms correspond to the radial ranges 0.0-0.5 R_e, 0.5-2.0 R_e and 2.0-3.0 R_e respectively. The slopes obtained

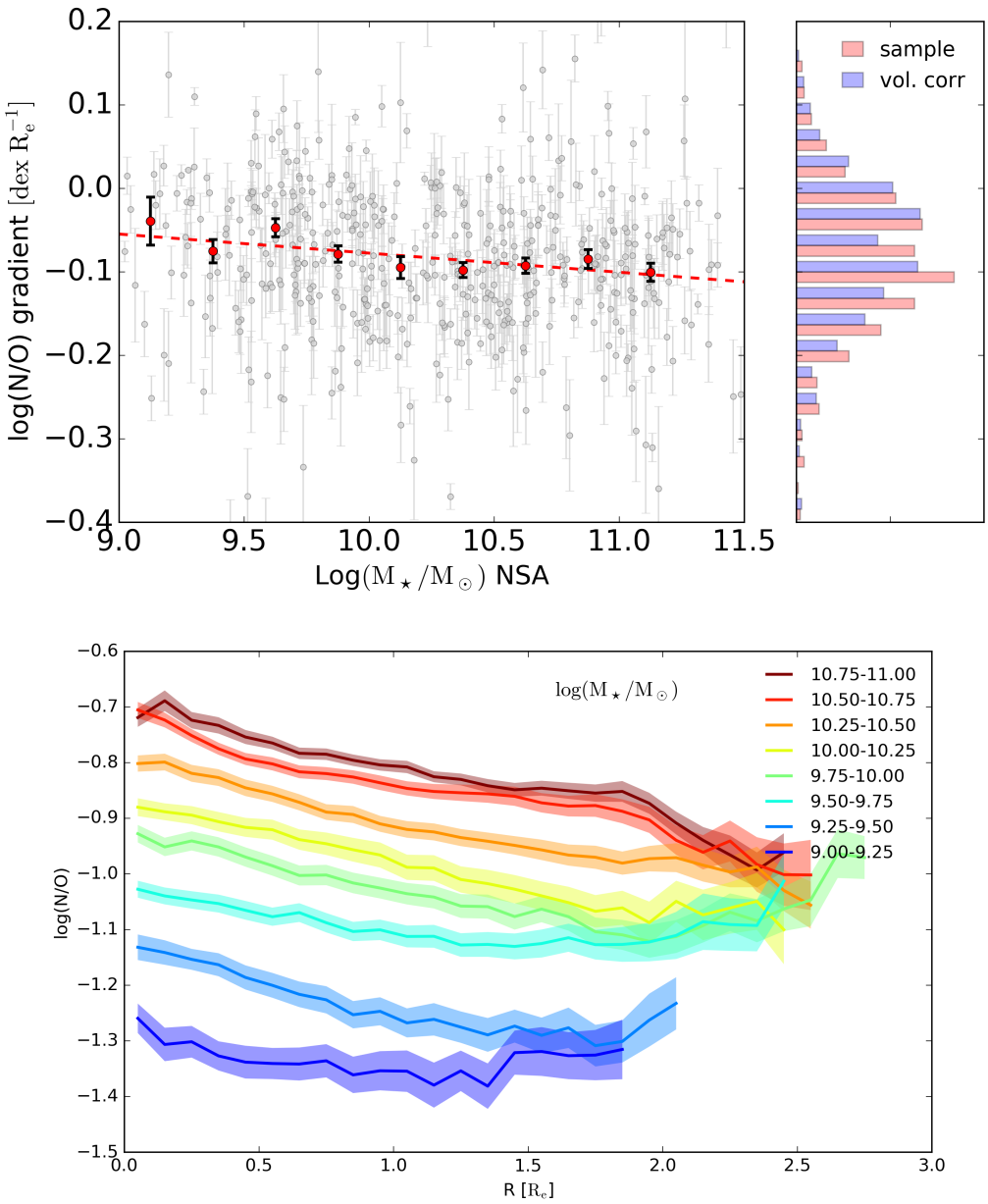

Figure 5.7: *Top*: The log(N/O) gradient (measured in the radial range 0.5 - 2.0 R_e using the Pagel et al. (1992) calibration based on N2O2) as a function of stellar mass. The red points represent the median measurements in 0.25 dex stellar mass bins with corresponding errors. The red dashed line is a straight line fit to the median gradient as a function of mass. The histogram on the right represents the distribution of log(N/O) gradients for the full sample (red) and for a volume-weighted sample (blue). The volume-weighted distribution is fitted with a Gaussian with mean of -0.16 dex R_e^{-1} and σ = 0.09 dex R_e^{-1}. *Bottom*: The shape of the log(N/O) gradient in 0.25 dex mass bins from log($M_\star/M_\odot$) = 9.0 − 11.0. For each mass bin the dashed region represents the error on the median gradient.

from fitting the stacks are shown as horizontal dashed lines and their value and uncertainty is quoted in the bottom right corner of each panel.

This analysis demonstrates that inner regions of massive galaxies (log($M_\star/M_\odot$) 10.5-11.0) have flatter O/H profiles than the same regions of less massive galaxies. In particular, while for the highest mass bin the slope in the inner region is marginally consistent with being flat, for lower-mass galaxies the slope in the inner regions is statistically consistent with that measured in the 0.5-2.0 R_e range.

At large radii, a flattening of the metallicity gradient with respect to the value 0.5 < R/R_e < 2.0

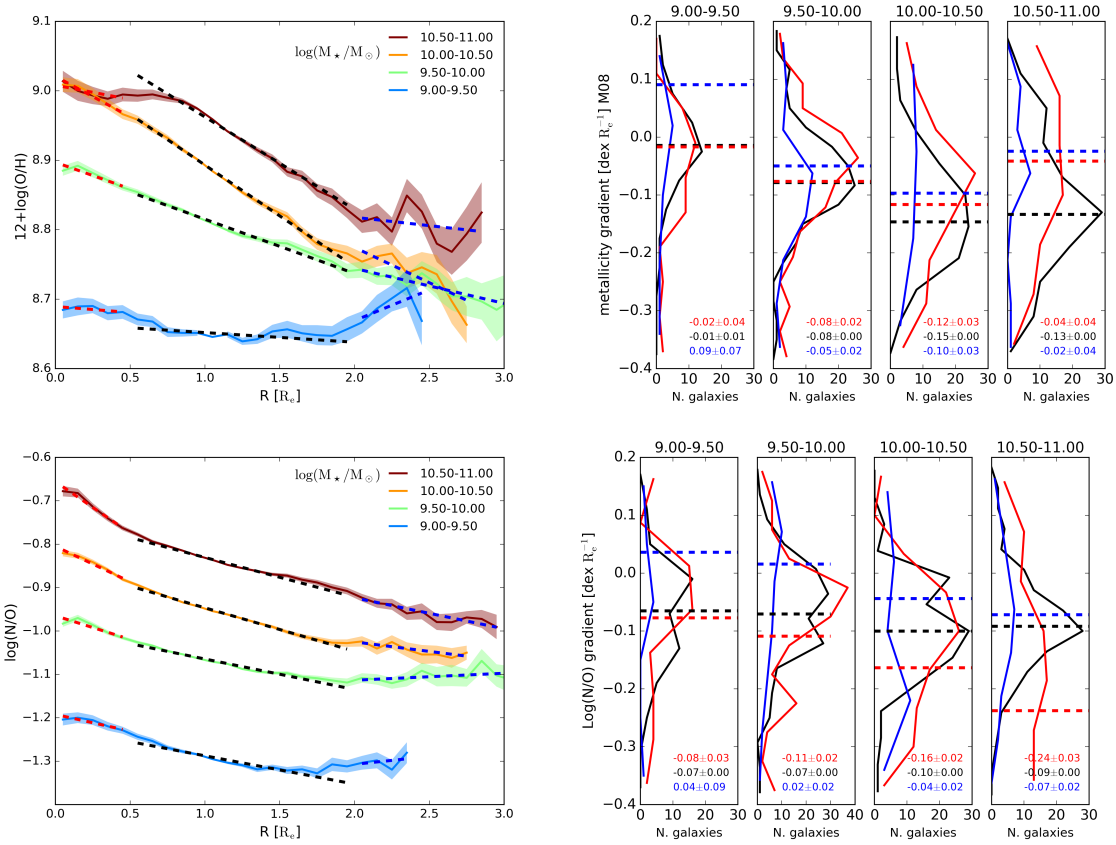

Figure 5.8: *Top-left*: Stacked metallicity profiles in four stellar mass bins and straight line fits in three radial ranges: 0.0-0.5 R_e (red), 0.5-2.0 R_e (black) and 2.0-3.0 R_e (blue). *Top-right*: Histogram distributions of the slope of the metallicity gradient measured in three different radial range, 0.0-0.5 R_e (red), 0.5-2.0 R_e (black) and 2.0-3.0 R_e (blue), for the four mass bins (mass of the bin indicated above each panel). The slopes obtained from fitting the stacks are also shown as dashed lines, and their values and error is reported in the bottom-right corner of each panel. *Bottom*: Same as the top panels, but for the N/O profiles.

is detected for $\log(M_\star/M_\odot) > 9.5$, although with varying degrees of significance. In particular, for galaxies in the mass bins $\log(M_\star/M_\odot) = 9.5$-10.0 and 10.0-10.5, the gradient at large radii is still negative and only marginally flatter than in the $0.5 < R/R_e < 2.0$ radial range. For the lowest stellar mass bin the metallicity gradient at large radii is slightly inverted, although with low significance. The observed distribution of the slopes of the metallicity gradients at large radii (as shown in the histograms of Fig. 5.8 right) are broad, highlighting the advantage of using the stacked profiles. Applying a volume correction to these distributions only has a small effect in each mass bin, since the volume corrections are mass-dependent.

The behaviour of the log(N/O) ratio gradient with mass and radius is shown on the bottom panels of Fig. 5.8. Similarly to the metallicity gradient, the log(N/O) gradient flattens at large radii, with the middle two mass bins showing the most significant flattening with respect to the slope in the $0.5 < R/R_e < 2.0$ radial range. In contrast to the metallicity gradient, the log(N/O) ratio gradient steepens in the inner regions of galaxies with increasing mass. This steepening is especially evident for $\log(M_\star/M_\odot) > 10.5$.

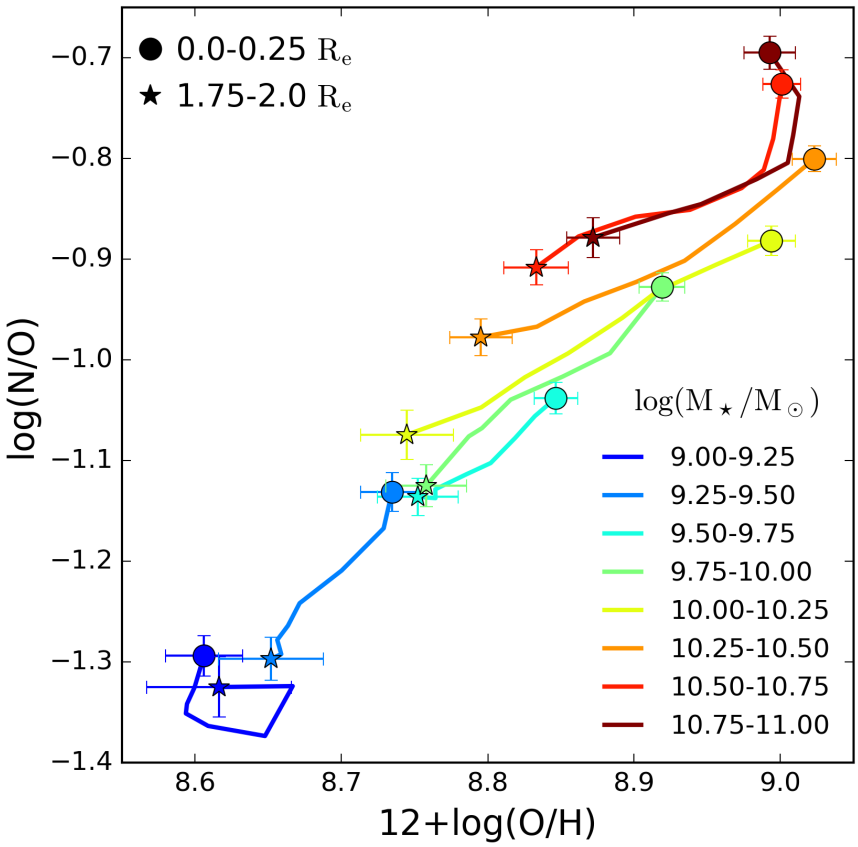

Figure 5.9: The relation between log(N/O) and metallicity (12+log(O/H)) as a function of both stellar mass and radius. The radial profiles in both metallicity and N/O are stacked in stellar mass bins of width 0.25 dex. The coloured solid lines represent the location of the stacked radial profiles in the log(N/O) versus 12+log(O/H) plane, with circles representing the innermost radial bin (0.0-0.25 R_e) and the stars representing the outermost radial bin (1.75-2.0 R_e).

5.3.5 The relation between oxygen and nitrogen abundance

In Fig. 5.9 we show the relation between metallicity (using the M08 R23 calibration) and the N/O ratio. All the valid spaxels in the MaNGA data have been divided in 8 bins of 0.25 dex according to the total stellar mass of the galaxy. For each mass bin, spaxels have been subdivided according to galactocentric distance (normalised to Petrosian R_e) in 8 radial bins. For each radial bin the median log(N/O) is plotted as a function of median metallicity (different colours indicate the different stellar mass bins). For each stellar mass, the innermost radial bin ($0.0 - 0.25$ R_e) is plotted with a filled circle and the outermost radial bin ($1.75 - 2.0$ R_e) with a star. Representative errors bars are plotted for these bins.

The derived relation between O/H and N/O agrees with previous work, showing a super-linear dependence of nitrogen on oxygen abundance at super-solar metallicity. A plateau is expected at log(N/O) $\sim$ -1.4 for lower metallicities, which are, however, not well represented in the MaNGA data (see Sec. 1.3.4). Fig. 5.9 also confirms the results of previous sections, by demonstrating the flattening of both N/O and O/H gradients at lower stellar masses (particularly evident for the $9.0 < \log(M_\star/M_\odot) < 9.25$ bin). The flattening of the metallicity gradient in the inner regions of massive

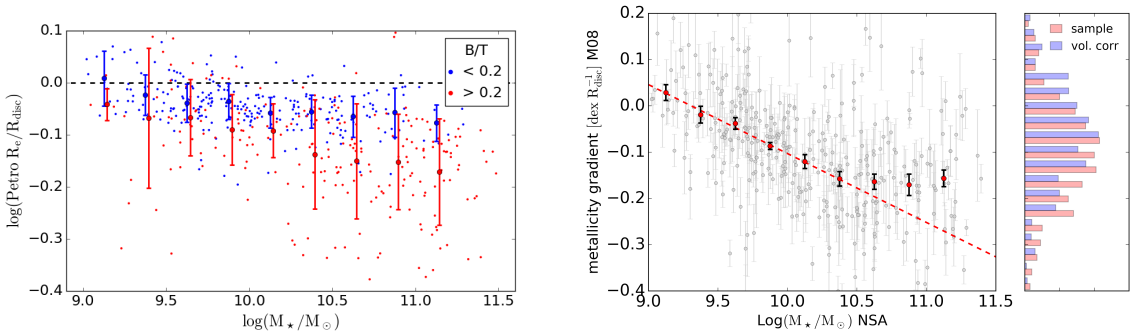

Figure 5.10: *Left*: The difference between the elliptical Petrosian and the disc effective radius as a function of stellar mass. Blue and red points correspond respectively to galaxy with bulge/total (B/T) ratios of < 0.2 and > 0.2. The larger dots with error bars correspond to the median and standard deviations of the two samples as a function of stellar mass. Note that the difference between the two measures of the effective radius increases as a function of B/T. *Left*: The metallicity gradient (measured in the radial range 0.5 - 2.0 R_{disc} using the M08 calibration based on R23) as a function of stellar mass, using the disc-only effective radius from the Simard et al. (2011) catalogue. The red points represent the median measurements in 0.25 dex stellar mass bins with corresponding errors. The red dashed line is a straight line fit to the median gradient as a function of mass for $\log(M_\star/M_\odot) < 10.5$. The histogram represents the distribution for the MaNGA sample (red) and for a volume-weighted sample (blue).

galaxies, which is however *not* accompanied by a flattening of the N/O ratio, is also evident (for example in the $10.75 < \log(M_\star/M_\odot) < 11.00$ bin, which shows an increase in N/O but not O/H moving towards the inner radii).

The key result from Fig. 5.9 is that the scatter in the O/H versus N/O relation correlates with galaxy mass. In particular, at a fixed local O/H, outer regions of more massive galaxies have higher N/O than inner regions of less massive galaxies, at least for $\log(M_\star/M_\odot) > 9.5$. Possible physical processes responsible for this effect are discussed in Sec. 5.6.3.

5.4 Sources of systematic error

In this section we discuss possible sources of systematic error in the determination of chemical abundances and their radial gradients in the MaNGA data.

5.4.1 The choice of radial scale length

Throughout this chapter we have used the Petrosian effective radius as the normalising scale length to measure metallicity gradients. From a theoretical perspective, however, the disc effective radius (or equivalently the scale length of the exponential disc) may represent the preferred length scale for normalising the metallicity gradients. The distinction is important because our sample contains bulge + disc systems, and the presence of a bulge affects the measured Petrosian (or Sérsic) effective radius by making it smaller than the disc effective radius. This effect is particularly important at high masses, where the bulge represents a more significant mass component in galaxies. Observationally, however, the determination of disc effective radius is less robust than the Petrosian radius determination for the MaNGA sample. Bulge-disc decompositions are often not unique, and bulges of $\sim$ kpc size may be only marginally resolved at the MaNGA median redshift.

In order to test the effect of using a disc-only effective radius, we cross-matched the MaNGA sample with the Simard et al. (2011) catalogue of bulge-disc decompositions based on the SDSS

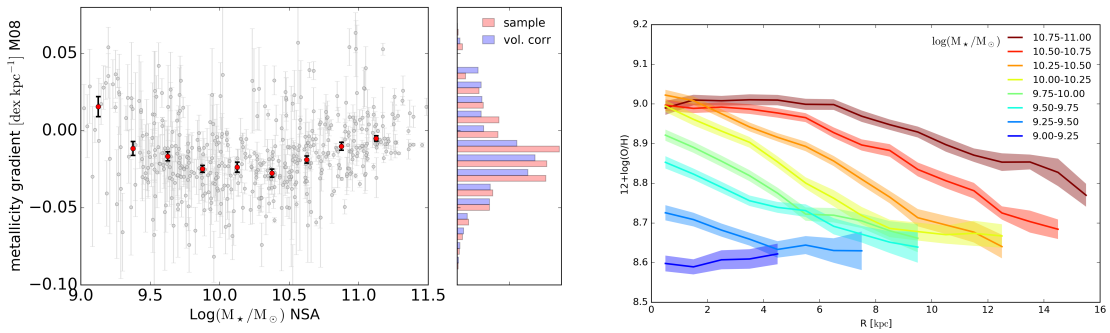

Figure 5.11: Same as Fig. 5.4, but calculating the metallicity gradient in units of dex kpc^{-1}.

photometry.[1] We obtain a positional match for 543 out of the 579 galaxies in our sample. From the Simard catalogue we extract the r-band disc-only effective radii for our sample. In Fig. 5.10 (left) we compare the NSA Petrosian and Simard et al. (2011) disc-only effective radii, colour-coding galaxies according to the bulge/total (B/T) ratio (blue for B/T < 0.2 and red for B/T > 0.5). We note that the disc effective radii are always larger than the elliptical Petrosian effective radii, with the difference increasing as a function of stellar mass at fixed B/T. Moreover, higher B/T galaxies have a larger difference between the disc-only and elliptical Petrosian effective radii.

In Fig. 5.10 (right) we show the dependence of the metallicity gradient on stellar mass obtained if the disc-only effective radius from Simard et al. (2011) is used instead of the galaxy-wide Petrosian effective radius as a normalisation for the distance. We confirm the qualitative trends observed in Sec. 5.3.1: a log-linear decrease of the gradient slope with stellar mass, and a flattening of this relation for $\log(M_\star/M_\odot) > 10.5$. In contrast with the results from Sec. 5.3.1, however, the slope of the metallicity gradient does not flatten again for the highest-mass galaxies but remains roughly constant at ~ -0.16 dex R_{disc}^{-1}. Moreover, for all masses the derived gradients are steeper than those obtained normalising by the Petrosian radius, since the Petrosian radius is systematically smaller than the disc effective radius.

For $\log(M_\star/M_\odot) < 10.5$ the median metallicity gradient as a function of mass is well-fitted by a straight line relation between the metallicity gradient ($\Delta \log(O/H)$) and stellar mass for the M08 calibration, of the type $\Delta \log(O/H) = a + b\ \log(M_\star/M_\odot)$. We obtain best fit parameters $a = 0.15$ (± 0.02) and $b = -0.14$ (± 0.02).

To facilitate comparisons with previous work on abundance gradient which did not adopt any scale length normalisation we also present the results obtained measuring the metallicity gradient in units of dex kpc^{-1}. Dropping any radial normalisation introduces a *strong* dependence of beam smearing on stellar mass, hence making it more difficult to interpret mass trends in the MaNGA data. Moreover, since in MaNGA galaxies are observed out to a fixed radial distance in units of R_e, galaxies of different masses are covered to different physical distances.

The results obtained by not including a radial normalisation are summarised in Fig. 5.11, which demonstrates that several features of the analysis presented in this chapter remain valid when metallicity gradients are measured in units of dex kpc^{-1}. Namely, gradients for $\log(M_\star/M_\odot) \sim 9.0$ are flat or marginally inverted, the metallicity gradient steepens with stellar mass until $\log(M_\star/M_\odot) \sim 10.5$, while becoming flatter again, but still negative, for higher masses. The change in shape of the metal-

[1] We use the version of the catalogue where the bulge Sérsic index is fixed at n=4.

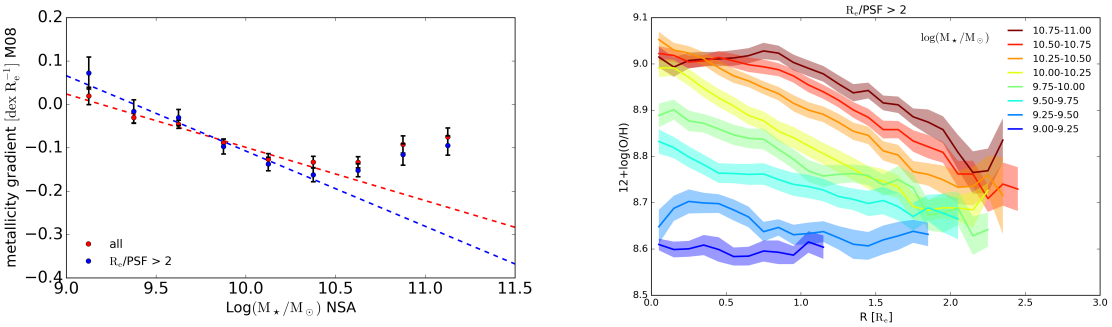

Figure 5.12: *Left*: The dependence of the metallicity gradient on stellar mass using the whole MaNGA sample selected in this work (red) and the the sub-sample of galaxies with R_e/PSF >2 (blue). Each data point represents the median gradient for the relevant mass bin and the error bars represent the error on the median. The dashed lines represent the best fits linear for the relation in the range $9.0 < \log(M_\star/M_\odot) < 10.5$. *Right*: Stacked metallicity gradients as a function of stellar mass using the sub-sample of galaxies with R_e/PSF >2.

licity gradient as a function of radius and mass is also evident in the metallicity stacks (Fig. 5.11, right), with higher mass galaxies showing a clear flattening in the central regions and intermediate mass galaxies displaying a flattening at large radii.

5.4.2 The effect of spatial resolution

To further the discussion in Sec. 5.2.2, in this section we take an empirical approach to quantifying the effect of spatial resolution on the measurement of the metallicity gradient in the MaNGA sample by considering sub-samples differently affected by beam-smearing.

First, we consider measuring the metallicity gradients for a sub-sample of galaxies with R_e/PSF > 2.0. This cut selects 61% of the sample (338 galaxies), but biases the selection, as it preferentially excludes galaxies observed with the two smallest fibre bundles (19 and 37-fibre IFUs). Selecting MaNGA galaxies based on IFU size generates a surface brightness bias as described in Sec. 2.1.3, since at fixed luminosity MaNGA only observes a narrow redshift range. Within this redshift range, galaxies observed with larger bundles have lower surface brightness, since they have larger effective radii on the sky. Aware of this potential bias, we perform the same analysis presented in Sec. 5.3.1 and measure the metallicity gradient using the M08 calibration on this sub-sample of well-resolved galaxies. The resulting slopes of the metallicity gradient and stacked metallicity profiles as a function of stellar mass are presented in Fig. 5.12. We observe the sub-sample of galaxies with R_e/PSF > 2.0 has steeper gradients than the whole sample, but the effect is small and within the statistical error for all mass bins. We note that galaxies with R_e/PSF > 2.0 in the lowest mass bin show a marginally inverted gradient. In the right panel of Fig. 5.12 we show the stacked metallicity profiles for the R_e/PSF > 2.0 and demonstrate that this sub-sample reproduces the main features observed for the whole sample. Namely we further confirm that the flattening of the metallicity gradient in the central regions of massive galaxies is not due to beam smearing effects.

We further test the effect of beam smearing on our results by comparing the metallicity gradients obtained using the primary and secondary samples separately. These two MaNGA sub-samples are selected to both be representative of the local galaxy population, with the secondary sample observing galaxies to larger galactocentric distance, thus affording fewer resolution elements per R_e. For both samples the MaNGA selection uses all bundles sizes at each luminosity (or stellar mass), thus affording

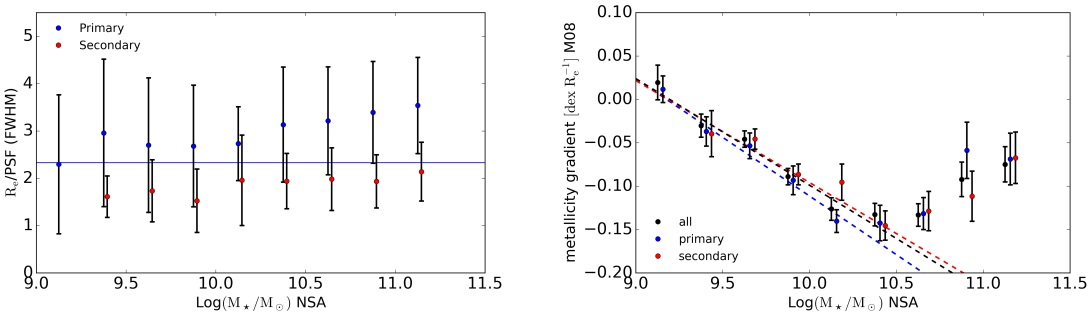

Figure 5.13: *Left*: The dependence of resolution (in terms of R_e/PSF) on stellar mass for the primary (blue) and secondary (red) MaNGA samples. At all masses the secondary sample, which covers galaxies out to 2.5 R_e, offers lower resolution than the primary sample (covering galaxies out to 1.5 R_e). *Right*: The dependence of the metallicity gradient on stellar mass using the whole MaNGA sample selected in this work (black) and for the primary (blue) and secondary (red) samples separately. Each datapoint represents the median gradient for the relevant mass bin and the error bars represent the error on the median. The dashed lines represent the best fits for the range $9.0 < \log(M_\star/M_\odot) < 10.5$.

a roughly constant number of resolution elements per effective radius as a function of stellar mass. This fact is demonstrated by the left panel of Fig. 5.13, which shows the median R_e/PSF as a function of stellar mass for the primary and secondary samples respectively. The resulting median slopes of the metallicity gradient as a function of stellar mass for each sub-sample and for the full MaNGA sample are plotted in the right panel of Fig. 5.13, demonstrating that the secondary sample leads to slopes that are statistically consistent with the primary sample for almost every mass bin. In conclusion, the observed trend between the shape of the metallicity gradient and stellar mass appears robust to the effect of resolution.

5.4.3 The contamination from DIG

The ubiquitous presence of DIG in star forming galaxies generates a contamination of the line ratios from HII regions which we are not able to remove at the median resolution of MaNGA. The results presented in this chapter, however, are likely to be robust to the effect of DIG contamination for the following reasons. First, DIG biases the measurement of metallicity in different directions depending on the calibrators used. As demonstrated in Zhang et al. (2017), DIG contamination biases the metallicity low when using the R23 calibrator, while it biased it high when using the [NII]/Hα ratio, and it generates an increase in scatter, but negligible bias when using the O3N2 calibrator. Since the relative trends highlighted in this study are preserved using different calibrators, the trends cannot be driven by DIG contamination. In the case of the central galactic regions, moreover, the surface brightness of line emission is generally high enough to prevent any significant DIG contamination.

The case of outer regions of disc is more difficult to assess, since in these regions of low surface brightness DIG could have a more significant effect. However, we have checked that the flattening is detected using both R23, O3N2 and [NII]/Hα metallicity calibrators, in addition to the N2O2 indicators, tracing the N/O ratio. Hence it is highly unlikely to be due entirely to the contamination from DIG. More detailed resolved spectroscopy of the outer regions of discs at high spatial resolution would be advantageous to directly assess the contribution of DIG to measurements of metallicity at large radii.

5.5 Comparisons to previous work

5.5.1 The metallicity gradient in nearby galaxies

The slope of the metallicity gradient in other IFS surveys

Recent IFS observations of nearby galaxies (Rosales-Ortega et al., 2011; Sánchez et al., 2012b, 2014; Ho et al., 2015; Sánchez-Menguiano et al., 2016; Pérez-Montero et al., 2016) have provided large datasets suitable for studying the shape of the metallicity gradients in the nearby Universe. To illustrate the source of possible differences with previous work, we compare our results with Sánchez-Menguiano et al. 2016 (SM16), one of the latest studies of abundance gradients based on the CALIFA survey (Sánchez et al., 2012a), based on a final sample of 129 galaxies. SM16 obtains an average metallicity gradient of -0.11 ± 0.07 dex R_e^{-1} using the PP04 calibration (but a lower value of -0.08 ± 0.09 dex R_e^{-1} when considering only HII regions identified via a clump-finding algorithm). This result is comparable in both average slope and scatter with the one presented in this work (-0.08 dex R_e^{-1} for both the R23 and O3N2 calibrations), although in case of the directly comparable method for selection of star forming spaxels SM16 reports a slightly steeper gradient.

In order to draw a fair comparison, it is important to note that CALIFA observes more nearby galaxies with a larger IFU, resulting in an average of $\sim$ 11 resolution elements per R_e (using the effective radii for the sample used in SM16 and a FWHM of 2.5″ for CALIFA, as described in Garcia-Benito et al. 2015). The CALIFA data is thus much less affected by beam smearing than the data used in this work (which has an average PSF/R_e = 2.3). A further important difference between this work and SM16 is that the CALIFA sample is not representative for galaxies of $\log(M_\star/M_\odot) < 9.65$, because of the adopted diameter-selection strategy (Walcher et al., 2014). This difference in sample selection, and thus in the stellar mass distribution, between the CALIFA and MaNGA samples leads to a significant bias when computing a median gradient if, as shown in Sec. 5.3.1, the metallicity gradient has a dependence on stellar mass. In particular, the larger number of low-mass galaxies in the MaNGA sample is likely to be a significant contribution to the shallower gradient measured by MaNGA with respect to CALIFA. This effect is further accentuated if we apply a volume correction to the MaNGA sample.

The stellar mass dependence of the metallicity gradient

In this chapter we present the first clear detection of a strong, albeit non-linear, dependence of the metallicity gradient on stellar mass in the nearby Universe (Sec. 5.3.1). This dependence was not unambiguously detected in the previous, smaller samples, although hints in this direction were already present in the literature (Vila-Costas & Edmunds, 1992; Zaritsky et al., 1994; Garnett et al., 1997). More recently Pérez-Montero et al. (2016) have made a marginal detection of the dependence between the O/H and N/O gradients and stellar mass, qualitatively similar to the one observed in this work. In particular, they observe a trend towards shallower gradient for both log(O/H) and log(N/O) for low-mass (late-type) galaxies. Additionally for log(O/H) (but not log(N/O)) they also observe a trend towards shallower gradients for high-mass (early type) star forming galaxies.

As an aside, we note that the results from González Delgado et al. (2015) for the stellar metallicity gradients derived from full spectra fitting of the CALIFA data point towards the existence of a similar mass trend as presented in this work (see their Fig. 12 and 13 for a direct comparison). Namely

González Delgado et al. (2015) obtain the steepest gradients for $\log(M_\star/M_\odot) \sim 10.5$ and a gradual flattening for galaxies of lower and higher mass. Goddard et al. (2017) reach similar conclusions based on a full spectral fitting analysis of the MaNGA data. Namely, they detect a general steepening of the mass-weighted stellar metallicity gradient with stellar mass.

We note that the results presented in this paper apply only to star forming galaxies. Early-type galaxies are found to have different metallicity gradient profiles (Pastorello et al., 2015; González Delgado et al., 2015; Goddard et al., 2017), which are more strongly influenced by the merger history of the system and the accreted stellar component (Coccato et al., 2011; Greene et al., 2015).

The shape of the metallicity gradient at small and large radii

We confirm, with much larger statistics that in previous work, the change in *shape* of the metallicity gradient as a function of radius and mass, namely a flattening at small radii for higher mass galaxies and a mild flattening at large radii especially evident for $\log(M_\star/M_\odot) > 10.0$. These features were already detected in small samples of galaxies by previous work (Belley & Roy, 1992; Bresolin et al., 2009; Werk et al., 2010, 2011; Rosales-Ortega et al., 2011; Bresolin et al., 2012) and confirmed by the extensive studies presented by the CALIFA collaboration (Rosales-Ortega et al., 2012; Sánchez et al., 2014; Sánchez-Menguiano et al., 2016). In addition to confirming the change in shape of the metallicity gradient, in this work we also present evidence for the flattening of the N/O ratio gradient at large radii and the steepening of the N/O in the central regions of massive galaxies.

It is interesting to note that studies using both CALIFA and MaNGA data have highlighted a correlation between metallicity and local stellar mass surface density (Sánchez et al., 2014; Barrera-Ballesteros et al., 2016) and have interpreted galaxy metallicity gradients as a direct result from such a correlation. Our results, however, clearly show that the stellar surface density cannot be the only driver of metallicity, since the metallicity profiles we observe deviate from exponentials in both the inner regions of massive galaxies and the outer regions of galaxies of all masses. While in the case of the inner regions of massive galaxies, the presence of the bulge complicates a direct comparison between metallicity and the disc mass profile, the flattening of the metallicity gradient at large radii necessarily implies a deviation from the relation between mass surface density and metallicity observed across the inner regions of the disc. As discussed further in Sec. 5.6, the fact that the flattening of the metallicity gradient at large radii is not consistent with a 'local' relation between metallicity and stellar mass surface density can be explained invoking feedback processes that lead to the redistribution of metals from the inner to the outer regions.

5.5.2 Abundance gradients in the Milky Way

A direct comparison of our result with the oxygen abundance gradients measured in the Milky Way is a difficult task for a variety of reasons, including (1) the use of different tracers and calibrations, often tracing different elements, (2) the presence of substantial dust obscuration in the Milky Way disc, (3) the uncertainty on the galactocentric distance of the measured tracers and on the Milky Way scale length itself.

With regards to metallicity tracers, studies of the present epoch abundance gradient in the Milky Way have been carried out using HII regions (via measurements of optical emission lines, radio recombination lines and collisionally excited lines, leading to somewhat discrepant results, see for example

Henry & Worthey 1999; Rudolph et al. 2006; Blanc et al. 2015), O- and B-type stars (Smartt & Rolleston, 1997; Rolleston et al., 2000), Cepheids (Luck et al., 2003; Pedicelli et al., 2009; Lemasle et al., 2013; Genovali et al., 2014), open clusters (Magrini et al., 2009; Yong et al., 2012) and planetary nebulae (Maciel & Quireza, 1999; Stanghellini et al., 2006). The results of these studies lead to metallicity gradients generally in the range -0.03 to -0.08 dex kpc^{-1}.

Given their young ages (< 200 Myr) and their accurate distance measurements, Cepheids are generally considered the best tracers of the present day chemical make-up of the Galaxy. The largest compilation of Cepheid abundance data (Genovali et al., 2014) leads to an abundance gradient of -0.06 dex kpc^{-1}, or -0.18 dex R_e^{-1} using the Milky Way scale length from Bovy & Rix (2013).[2] We can compare this measurement with the gradient predicted for a galaxy of the mass of the Milky Way (assumed here to be $\log(M_\star/M_\odot) = 10.8$, Bovy & Rix 2013) based on the results of this work (Sec. 4.2.2) which is -0.17 dex R_e^{-1}. Considering the systematics involved and the large scatter in the metallicity gradient observed in our sample at each stellar mass, we consider these values to be in excellent agreement.

Studies of the abundance gradient in our Galaxy based on different tracers points towards the possibility of a flattening of the metallicity gradient at large radii ($R > 10$ kpc, see for example Pedicelli et al. 2009 using Cepheids, Vílchez & Esteban 1996 using HII regions or Magrini et al. 2009 using open clusters), although this claim is contested by other authors using the same tracers (see, for example, the discussion in Stasińska et al. 2012). Using the scale length from Bovy & Rix (2013), the observed flattening in the Milky Way metallicity gradient would occur at $\sim 2.8\ R_e$, a somewhat larger galactocentric distance to the flattening detected in this work for $R > 2.0\ R_e$. Interestingly, a flattening is also reported in the Milky Way for the N/O ratio from HII regions (Vílchez & Esteban, 1996).

5.6 Discussion

5.6.1 Chemical evolution models and 'inside-out' growth

Chemical evolution studies have provided some of the earliest evidence in support of the theories of disc formation in the cosmological framework and 'inside out' growth (Chiosi, 1980; Matteucci & Francois, 1989; Boissier & Prantzos, 1999; Chiappini et al., 2001), since the difference in assembly time across the galactic disc naturally produces a metallicity gradient. The inside-out growth scenario is further supported by observations of colour gradients (Bell & de Jong, 2000; Muñoz-Mateos et al., 2007) and spectroscopically-inferred age profiles of disc galaxies (Pérez et al., 2013; González Delgado et al., 2015; Ibarra-Medel et al., 2016).

It is important to note that other factors beyond the radial variation in assembly time can play a crucial role in determining the metallicity gradient. As demonstrated by Goetz & Koeppen (1992) from a purely analytical perspective, metallicity gradients can also be generated by a radial dependence of the metal yield (which, assuming that nucleosynthetic physics is universally constant, implies a change in the stellar initial mass function, IMF) or a radial dependence of the star formation efficiency (SFE= SFR/M_{gas}). Leaving aside any possible IMF variation (which remains to date a highly speculative suggestion), different assumptions regarding the radial variation of the star formation efficiency have been investigated by classical chemical evolution models. Differences in the parametrisation of the

[2] Genovali et al. (2014) measure [Fe/H], so the quoted gradient is also affected by the radial dependence of the [O/Fe] ratio.

SFE are not merely a technical detail: they are at the core of the different predictions for the time evolution of the metallicity gradient presented in the literature. In particular, models where the SFE is assumed constant as a function of radius generally predict a steepening of the metallicity gradient with time (Matteucci & Francois, 1989; Chiappini et al., 2001), while models that assume a decrease of the SFE with radius generally predict a flattening with time (Boissier & Prantzos, 1999; Mollá & Díaz, 2005), although this distinction is not always clear cut (see for example the discussion in Mott et al. 2013).

On top of these effects, radial flows and gas recycling from the hot halo (which is dependant on the overall efficiency of ejective feedback) can act to flatten (or, albeit for rather contrived choices of parameter, steepen) pre-existing metallicity gradients (Lacey & Fall, 1985; Schönrich & Binney, 2009; Pezzulli & Fraternali, 2016). Recent progress in semi-analytical modelling (Fu et al., 2009) and hydrodynamical simulations performed in a cosmological context (Pilkington et al., 2012a; Gibson et al., 2013) have demonstrated the fundamental role that metal recycling via galactic fountains has on the metallicity gradient. These effects of feedback and recycling ought to be more extreme in low-mass galaxies, where outflows play a larger role in regulating the star formation and gas supply.

It is beyond the scope of this chapter to revisit the predictions of classical chemical evolution models in light of the new observations presented here. We wish, however, to comment on the fact that the clear detection of a steepening of the metallicity gradient with stellar mass (between 0.5 R_e and 2.0 R_e) has important consequences for our understanding of the time evolution of metallicity gradients. In a simple model of chemical evolution, chemical enrichment, time and mass growth are tightly linked. In this sense lower mass galaxies can be interpreted as the 'progenitors' of the higher mass star forming galaxies (note that this equivalence is only true in a limited sense, since the physical conditions of low-mass high-redshift galaxies are assumed to be different from the low-redshift equivalents). In a simple inside-out growth model (with no radial flows and no wind recycling) and a SFE profile which decreases as a function of radius (as observed in local galaxies, Leroy et al. 2008) the metallicity gradient should initially (i.e. in low-mass galaxies) be steep, as star formation occurs primarily in the central regions, and subsequently flatten, as star formation proceeds in the outer regions of the disc. Moreover, in this scenario, the flattening should occur 'inside-out', with central regions reaching their equilibrium metallicity earlier than outer regions (see Sec. 1.3.3 and next subsection), as is indeed observed in this work. Hence, some contribution from ejective feedback may be necessary to reproduce the flat abundance gradients observed in the lowest-mass galaxies in our sample. In these galaxies the shallower gravitational potential well may favour the launching of large scale galactic winds, reducing the amount of low angular momentum gas that turns into stars in the central regions of the disc (Brook et al., 2012).

5.6.2 Interpreting the shape of the metallicity gradient

It is a general property of chemical evolution models accounting for infall, star formation and outflows to evolve towards an equilibrium metallicity at late times (Sec. 1.3.3). The concept of an equilibrium chemical abundance has been discussed extensively in recent literature focussing on the study of 'bath-tub' chemical evolution models (Sec. 1.3.3, Davé et al. 2011; Lilly et al. 2013; Peng et al. 2015). Within this framework, the flattening of the mass-metallicity relation at high masses (Tremonti et al., 2004) and the flattening of the metallicity gradient in the central regions of massive galaxies can

be ascribed to the general behaviour of evolved systems to reach an equilibrium abundance at late times, corresponding to low gas fractions. Given the time delay between the production of oxygen and nitrogen, the nitrogen abundance keeps increasing even if the global metallicity reaches an equilibrium value, resulting in the different behaviours of the oxygen and N/O gradients in the central regions of massive galaxies. Interestingly, gradual dilution of the interstellar medium in the central regions of massive galaxies is predicted by some models (Yates & Kauffmann, 2014) and might contribute to explaining the observed flattening and/or marginal inversion of the metallicity gradient in the very central regions of the most massive galaxies in our sample, while not affecting our conclusion for the N/O ratio.

The flattening of the metallicity gradients at large galactocentric radii deserves a more detailed discussion. The outer regions of galaxies are an ideal laboratory to study disc assembly at the current epoch, since these regions are characterised by extreme conditions: high gas fractions, long dynamical timescales and low stellar surface density. These properties indicate that outer disc regions are relatively un-evolved, a realisation that stands in contrast with the relatively high observed chemical abundances (8.7 <12+log(O/H) <8.9, for the M08 R23 calibration). Indeed, our data shows that at large radii the profiles of galaxies of different masses tend to converge to a common metallicity, similar in value to the metallicity observed throughout the disc of the low-mass galaxies in our sample. This value of metallicity is much higher than than the metallicity floor of $\sim 1\%$ $Z_{\odot}$, found in metal-poor galaxies in the local Universe (Izotov et al., 2006; Morales-Luis et al., 2011), which is expected to be set by direct accretion of gas from the cosmic web at z~0 (Danforth & Shull, 2005; Arnaud et al., 1994; Sánchez Almeida et al., 2014).

The common metallicity observed in the MaNGA data at large radii may reflect the fact that chemical enrichment initially happens quickly, especially for systems with a high star formation efficiency (see for example Fig. 5 in Vincenzo et al. 2016a). Outer discs, however, are likely characterised by low star formation efficiencies and previous work has argued against the self-enrichment scenario, pointing out that the current level of star formation is insufficient to explain the observed high abundances, even when extrapolated back for a Hubble time (Bresolin et al., 2012).

As an alternative to in-situ production, metals in the outer regions of the disc may originate from the highly-enriched regions of the inner disc through either radial flows or re-accretion of enriched coronal gas. In the enriched infall scenario, the observed metals at large radii are most likely the result of a 'wind recycling' process, where the halo gas is progressively enriched by outflows from the more star forming inner regions of the disc, cools and falls back onto the disc over a $\sim$ 1 Gyr timescale, as predicted in recent hydrodynamical simulations (Oppenheimer et al., 2010; Christensen et al., 2016; Muratov et al., 2016; Armillotta et al., 2016). This scenario, however, does not provide a natural interpretation of the common metallicity observed in MaNGA galaxies at large radii. Further modelling of galactic fountains and their effect of chemical abundances may help to shed more light on this question.

5.6.3 The N/O ratio gradient

Chemical evolution models taking into account stellar lifetimes and metallicity-dependant yields predict that the nitrogen abundance radial gradient ought to be steeper than that for O/H. The prediction is a direct consequence of the time delay between oxygen and nitrogen production, causing the differ-

ence in the production rate of nitrogen between the inner and the outer regions of the disc to be even larger than that for oxygen (Matteucci & Francois, 1989). Another important prediction of modelling the N/O ratio is that the position of systems in the O/H versus N/O plane depends chiefly on the SFE (Mollá et al., 2006; Vincenzo et al., 2016a). Lower SFE delays the production of nitrogen at fixed oxygen abundance, thus causing low SFE regions to lie at higher N/O at fixed O/H (Sec. 1.3.4).

The results from Sec. 5.3.5 can thus be interpreted as a consequence of the different star formation efficiency between the central and the outer regions of discs. For example, in Fig. 5.9 we observe that the central regions of galaxies in the mass range $\log(M_\star/M_\odot) = 9.5 - 9.75$ have the same oxygen abundance as the outer disc ($R = 1.75 - 2.0\ R_e$) of galaxies in the mass range $\log(M_\star/M_\odot) = 10.5 - 10.75$. However, the N/O ratio corresponding to the outer disc of the higher mass bin is ~ 0.15 dex higher, possibly due to systematically lower SFE in the outer discs.

Metal redistribution via wind recycling, which we have already considered in the context of the flattening of the O/H gradient at large radii, will also have an effect in the N/O versus O/H plane. Indeed, higher N/O ratios in the outer disc of massive galaxies may also be interpreted as a consequence of the pollution of galaxy outskirts with some amount of high-metallicity, high-N/O gas from the central regions. Upon mixing with the lower-metallicity gas at larger radii, the metallicity of the infalling gas is significantly diluted, while its N/O ratio only decreases slightly in mixing because of the highly non-linear relation between O/H and N/O (see for example the models presented in Köppen & Hensler 2005). Therefore, in this case the N/O ratio acts as a tracer of the original metallicity of the gas polluting the outer regions. Further modelling, taking into account the combined effect of radial variations in SFE and metal redistribution will be needed in order to fully exploit the information encoded in the O/H versus N/O plane.

Chapter 6

Where are the metals? - A galaxy-wide metal budget

Based on 'Galaxy gas flows inferred from a detailed, spatially resolved metal budget', F. Belfiore, R. Maiolino & M. Bothwell, MNRAS, 2016, 455, 1218.

Metals are produced by stellar nucleosynthesis and act as a fossil record of a galaxy's star formation and gas flows history. Simple analytical models relating metal abundances to SFR and gas flow rates have been presented by several authors (Sec. 1.3, Erb 2008; Lilly et al. 2013; Dayal et al. 2013; Peng & Maiolino 2014; Ascasibar et al. 2014) with the aim of explaining the scaling relations observed in statistical samples of galaxies. More detailed chemical evolutionary models have been successfully exploited to reproduce the observed chemical abundances, gas content and SFR of the solar neighbourhood, the Milky Way or nearby disc galaxies (Colavitti et al., 2009; Marcon-Uchida et al., 2010; Spitoni & Matteucci, 2011). The common aim of chemical evolution studies is to use chemical abundances observed today to infer the gas flow history and star formation history of the system. For example, in order to reproduce the chemical abundances of the Milky Way, a two-stage inflow model is generally invoked. The bulge is assumed to have formed at early times during a first inflow phase, while the disc is assumed to form inside-out during a second inflow phase (Matteucci & Francois, 1989; Boissier & Prantzos, 1999; Naab & Ostriker, 2006; Williams et al., 2009). Hydrodynamical simulations of disc galaxies generally agree with the inside-out disc formation model (Pilkington et al., 2012b). Chemical abundances can also provide clues on the relative importance of additional evolutionary processes in galaxies, including stellar migration, gas flows within the disc and large scale galactic fountains.

Current large IFS galaxy surveys (eg. CALIFA, Sánchez et al. 2012a; SAMI, Croom et al. 2012; MaNGA, Sec. 2, Bundy et al. 2015) offer great potential for extending the study of resolved chemical abundances to much larger galaxy samples. Using optical IFS data, the chemical abundance of the ISM can be derived by analysing gas emission lines (Sec. 1.4.2), while insight into the metallicity of the stellar population can be obtained using Lick indices, or applying spectral decomposition techniques (Sánchez-Blázquez et al., 2014; Cid Fernandes et al., 2011). The CALIFA survey has recently delivered important insights on the distribution of metals within star-forming galaxies, providing the strongest evidence so far for a universal gas phase abundance gradient (Sánchez et al., 2014) out to

2.0 R_e, as already suggested in previous work (Vila-Costas & Edmunds, 1992; Bresolin et al., 2009, 2012). The results of a new study of the shape of the metallicity gradient using a large sample of galaxies from MaNGA survey has been presented in chapter 5 of this thesis.

Observations of resolved gas metallicity, however, cannot be uniquely related to specific chemical evolutionary models, unless measurements of the gas and stellar content are also available. This work presents one of the first attempts to combine chemical abundances from IFS with gas mass measurements from millimetre/radio observations for a single galaxy (NGC 628) on the same spatial scales, along with stellar mass surface density and stellar metallicities. We are therefore able to constrain the metal budget both as a function of radius, and for the galaxy as a whole, out to 3 R_e. Since we have access to information on radial gradients of the relevant physical quantitates, we obtain an overall metal budget free from aperture effects, which affected previous work based on metallicities estimated from observations of galaxy central regions (for example from the SDSS galaxy sample, York et al. 2000; Abazajian et al. 2009).

Empirical studies of the metal budget in the z = 0 Universe, presented by several authors, agree in concluding that the total mass of metals produced by galaxies cannot be accounted for by the metals observed in stars and the ISM (Pettini et al., 1999; Ferrara et al., 2005; Bouché et al., 2007; Peeples & Shankar, 2011; Zahid et al., 2012; Peeples et al., 2014). Large amounts of metals (between 35% and 90%) must be residing in the intergalactic medium, but also in the diffuse halo gas and in the circumgalactic medium (CGM). Although recent observational efforts have led to a better characterisation of the metallicity of the gas in the hot halo phase (Tumlinson et al., 2011, 2013), a robust metal budget for these phases is still missing. Cosmological hydrodynamical simulations which include chemical evolution in a self-consistent way generally agree with the empirical studies above, and highlight that the fraction of missing metals is strongly dependant of the sub-grid feedback prescription (Wiersma et al., 2011; Pilkington et al., 2012b).

The aim of this chapter is to investigate in detail how many metals are lost and hence assess the severity of the 'missing metal problem' in NGC 628. This information also provides tight constraints on the outflow loading factor (i.e. the ratio between SFR and outflow rate) *averaged* over the galaxy lifetime. The results are expected to provide simulators with new constraints on the net effect of gas flows in disc galaxies on resolved scales.

6.1 Overview of the data

NGC 628 is a nearby ($D \approx 7.3$ Mpc, $z = 0.00219$) nearly face-on ($i \approx 7^\circ$) spiral galaxy (Fig. 6.1). Table 6.1 summarises some of its basic properties. NGC 628 is a good example of an isolated galaxy (no encounter in the last Gyr; see Kamphuis & Briggs 1992), displaying typical grand-design structure. The following sections describe the observations of NGC 628 that have been used in this work.

6.1.1 Integral field spectroscopy

In this study we make use of IFS observations of NGC 628 taken as part of the PINGS survey (Rosales-Ortega et al., 2010; Sánchez et al., 2011; Rosales-Ortega et al., 2011). The survey was carried out using the 3.5-m telescope at the Calar Alto observatory, with the Potsdam Multi-Aperture Spectrograph in PPAK mode (Kelz et al., 2006). The PPAK fibre bundle corresponds to a field of view of $75'' \times$

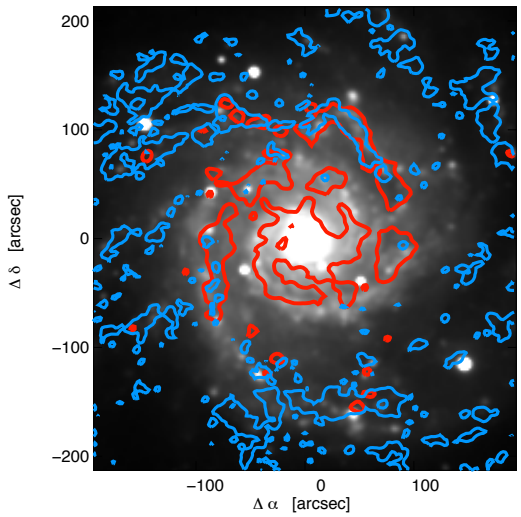

Property	Value
Name	NGC 628, M 74
RA	$00^h59^m50.1^s$
Dec	$-07°34'41.0''$
Type	SAc
Distance (adopted)	7.3 Mpc
i	7°
R_e	$67'' = 2.4$ kpc
scale	36 pc arcsec^{-1}

Figure 6.1: *Left*: optical image of NGC 628 (r-band from SDSS) with superimposed contours of HI (from the THINGS survey, in blue) and CO surface brightness (from the HERACLES survey, in red). The red contours correspond to a molecular hydrogen surface mass density of 10 $M_\odot$ pc^{-2}, while the blue HI contour correspond to a neutral hydrogen surface mass density of 12 $M_\odot$ pc^{-2}. *Right*: Table with general properties of NGC 628.

65″ and consists of 331 science fibres of 2.7″ diameter packed in an hexagonal pattern, leading to a filling fraction of 65%. The data covers the spectral range between 3700 Å - 7100 Å, with a spectral resolution of FWHM ∼ 8Å. Due to the large projected size of the galaxy (10.5′×9.5′) the data consists of a mosaic of observations taken on 6 different nights over a period of 3 years. The final size of the mosaic is of $6' \times 7'$. We estimate the PSF to have a FWHM of approximately 3″.

The reduced datacube was analysed according to the procedure outlined in Sec. 2.2, but with some modifications with respect to the parameters used for the MaNGA data. In short, for each spaxel, we fit a linear combination of single stellar population templates, after correction for systemic velocity and instrumental dispersion, using penalised pixel fitting (Cappellari & Emsellem, 2004). We used a grid of 29 SSP templates, generated by using Maraston & Strömbäck (2011) models based on the empirical STELIB spectral library (Le Borgne et al., 2003). After subtracting the stellar continuum, the emission lines spectrum is fitted with a set of Gaussian functions, one per emission line (using least-squares minimization). The doublets [OIII] $\lambda\lambda$4959,5007 and [NII] $\lambda\lambda$6548,6584 are set to have the same velocity and velocity dispersion and the ratio of their intensities is fixed to the theoretical one. We apply a signal to noise cut to the emission line maps generated above, imposing a S/N larger than 5 for Hα and Hβ. This threshold is intentionally high to exclude regions of diffuse emission (mainly inter-arm regions) where the Hα emission might not be ascribed to bona-fide HII regions. We also discard regions where both the [OII] and the [OIII] line are undetected.

We use the standard ionisation diagnostic diagram (BPT diagram, Sec. 1.4.3, Baldwin et al. 1981; Veilleux & Osterbrock 1987; Kewley et al. 2001; Kauffmann et al. 2003c) to identify galactic regions as star-forming and discard regions that lie above the Kewley et al. (2001) demarcation line in the [OIII]/Hβ versus [SII]/Hα diagnostic diagram. All of the discarded spaxels are found in the inter-arm regions and present LINER-like ionisation. We note that such regions are only 5% of the total, and their exclusion does not affect our final results. Emission line fluxes are corrected for extinction as described in Sec. 1.4.4 and the gas phase metallicity is calculated using two strong line ratios calibrators: the Maiolino et al. (2008) (M08) calibrator based on R23 and the Pettini & Pagel (2004)

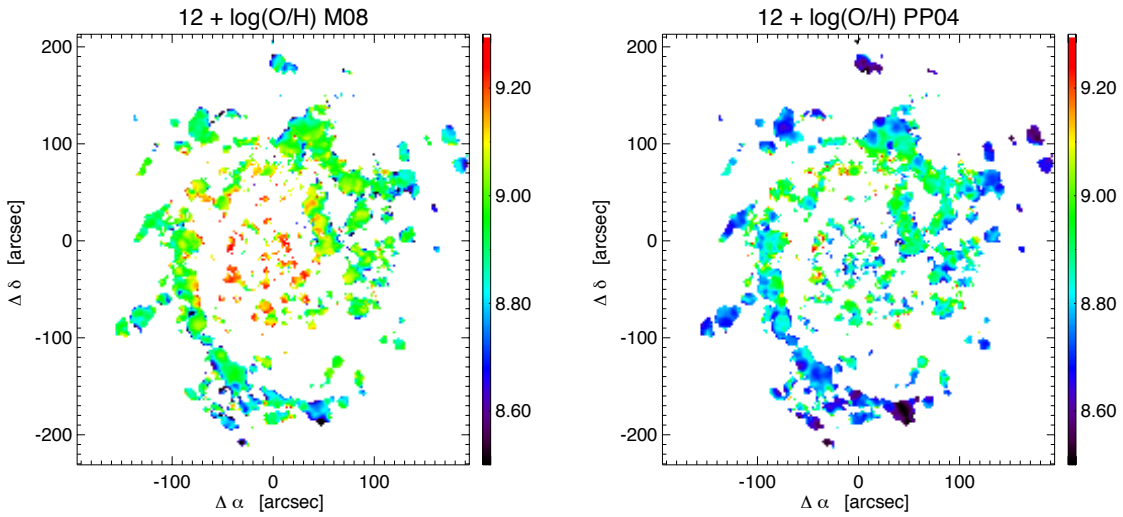

Figure 6.2: Maps of the gas metallicity in NGC 628 using the Maiolino et al. (2008) (M08) calibration based on R23 (left) and the Pettini & Pagel (2004) (PP04) calibration based on O3N2 (right). Only spaxels that lie below the Kewley et al. (2001) demarcation line in the [OIII]/Hβ versus [SII]/Hα BPT diagram are included.

(PP04) calibrator based on O3N2 (see the discussion in Sec. 1.4.2). The resulting metallicity maps are shown in Fig. 6.2. For reference, the photospheric solar oxygen abundance, as derived by Asplund et al. (2009), is 12 + log(O/H) = 8.69, or equivalently $Z_{\odot}(O) = 0.00585$. Note that we are referring to Z as the oxygen abundance by mass. The total metal content (fraction by mass of elements heavier than helium) in the Sun is 0.0142.

6.1.2 HI 21 cm observations

We used observations of the 21 cm line from THINGS (The HI Nearby Galaxy Survey, Walter et al. 2008). This survey comprises 34 nearby galaxies observed with the VLA, at high spectral (< 5.3 km s^{-1}) and spatial resolution. NGC 628 was observed using the B, C and D configurations with a combined on-source integration time of $\sim$ 10 hr. We use the publicly available[1] 'robust' weighted map (the 'robust' weighting scheme is used to achieve a sensitivity close to natural weighting while preserving a resolution close to uniform weighting, see Walter et al. 2008 for details), which has a beam size of $\approx 6''$ ($B_{min} = 5.57'', B_{maj} = 6.8''$). The 1σ noise per 2.6 km s^{-1} channel is 0.66 mJy beam^{-1}, corresponding to a sensitivity of ≈ 0.5 M$_{\odot}$ pc^{-2}, sufficient to trace the atomic hydrogen in all regions where it constitutes the dominant component of the ISM.

6.1.3 CO(2 -1) observations

Observations of the CO(2 -1) transition we used to infer the molecular gas content. Maps are obtained from the publicly available[2] HERA CO-Extragalactic Survey (HERACLES, Leroy et al. 2009). HERACLES is a survey of 48 nearby galaxies using the HERA multi-pixel receiver on the IRAM 30 m telescope, with $13''$ angular resolution and 2.6 km s^{-1} spectral resolution. The 1σ sensitivity of the map is estimated to be ≈ 3 M$_{\odot}$ pc^{-2} (with the Galactic conversion factor discussed in Sect. 6.1.7).

[1] http://www.mpia.de/THINGS/Data.html
[2] http://www.mpia-hd.mpg.de/HERACLES/Data.html

Table 6.1: Multi-wavelength observations of NGC 628 used in this chapter to supplement the IFS mosaic from Rosales-Ortega et al. (2010).

Telescope	Filter/Receiver	$\lambda_{\rm eff}$ [Å]	Bandwidth [Å]	PSF FWHM [″]	Reference
GALEX	FUV	1516	268	4.3	Morrissey et al. (2007)
	NUV	2267	732	5.3	”
SDSS	u′	3540	599	1.49	Abazajian et al. (2009)
	g′	4770	1379	1.34	”
	r′	6222	1382	1.16	”
	i′	7632	1535	1.03	”
	z′	9060	1370	1.13	”
2MASS	J	1.235 [μm]	0.162 [μm]	2.5	Skrutskie et al. (2006)
	H	1.662 [μm]	0.251 [μm]	2.5	”
	K_s	2.159 [μm]	0.262 [μm]	2.5	”
Spitzer	IRAC1	3.550 [μm]	0.75 [μm]	1.66	Fazio et al. (2004)
	IRAC2	4.493 [μm]	1.01 [μm]	1.72	”
IRAM 30m CO (2-1)	HERA	ν = 230.54 [GHz]		13	Leroy et al. (2009)
VLA HI		ν = 1420.40 [MHz]		5.57×6.80	Walter et al. (2008)

6.1.4 Multi-wavelength photometric data

Photometry in different bands was collected to obtain a reliable estimate of the stellar mass surface density by performing pixel-by-pixel spectral energy distribution (SED) fitting. We collected observations from *GALEX* (Galaxy Evolution Explorer), 2MASS (Two Micron All Sky Survey) and the *Spitzer Space Telescope* IRAC camera. In the optical band, we make use of the photometry from SDSS DR 7. Table 6.1 summarises the basic properties of the dataset used and the relevant references.

6.1.5 Stellar mass surface density

Stellar mass surface densities are estimated by performing SED fitting in each pixel on the multi-wavelength photometric data from UV to near IR, using the software package CIGALE (Code Investigating GAlaxy Emission, Burgarella et al. 2005; Noll et al. 2009).

In detail, we followed the procedure outlined below (similar to Boquien et al. 2012).

1. The different observations were smoothed to the lowest resolution of the photometric dataset (GALEX NUV), using the kernels from Aniano et al. (2011).

2. The maps were then regridded on the same pixel scale as the IFS mosaic.

3. For each pixel, the flux and the flux error in each band was extracted. Errors are computed by taking into account the uncertainty in absolute calibration of the different instruments. Fluxes and errors are used as input for the software package CIGALE.

4. CIGALE creates far-UV to far-IR SEDs consisting of dust-attenuated complex stellar population models. In this analysis we used Maraston (2005) templates (with a Kroupa IMF) to build a grid of stellar models with a range in metallicity (from 0.5 to 2 solar). The star formation history is parametrised by an exponentially decreasing SFR, and an old stellar population with and a grid of younger stellar population bursts. Extinction is fitted using a Calzetti-like attenuation curve.

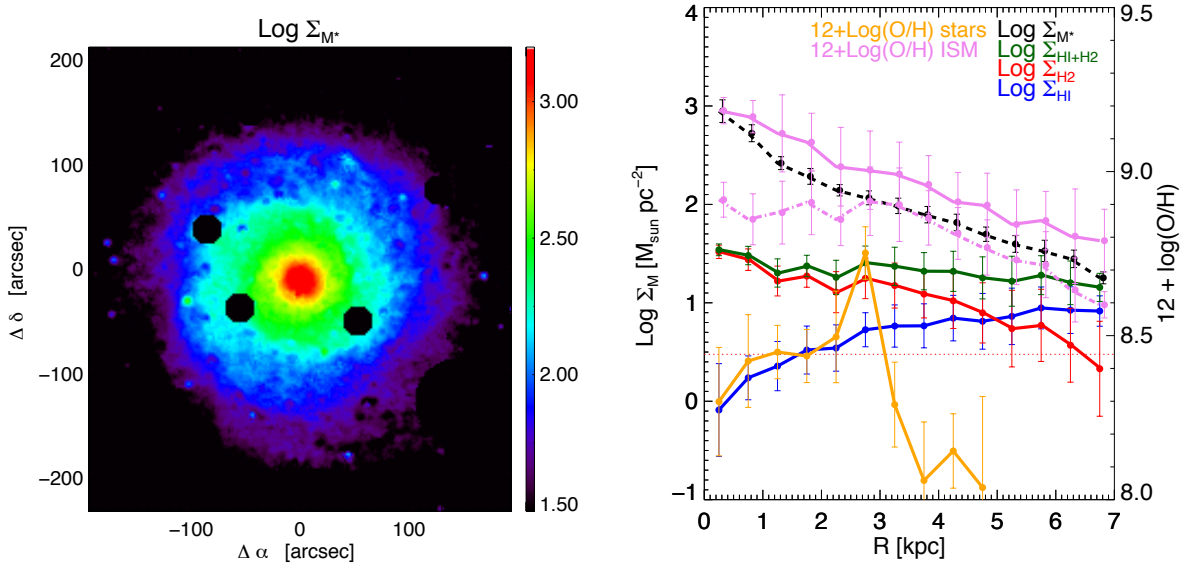

Figure 6.3: *Left*: Stellar mass surface density map, created from the spatially resolved SED fitting. Foreground stars have been masked. *Right*: Radial dependence of various physical quantities across the disk of NGC 628 (in radial bins; error bars represent the scatter in each radial bin). Atomic gas surface density (blue) shows a dip in the central region, while the molecular gas surface density (red) is peaked at the centre and quickly decreases outwards. The horizontal red dashed line corresponds to the sensitivity limit of the CO observations. The total gas content (green) is nearly flat across the whole disk up to 3 R_e (1 R_e = 2.4 kpc). A clear radial gradient is observed in both stellar mass surface density (black, short dashes) and gas metallicity (violet). The latter is shown both for the M08 (solid violet) and PP04 (dot-dashed violet) metallicity calibrations. The stellar metallicity gradient from Sánchez-Blázquez et al. (2014) is shown in orange. Note that the metallicities of gas and stars are plotted with respect to the alternative y-axis on the right in units of 12 + log(O/H).

The optimal galaxy parameters are derived by CIGALE using a Bayesian-like analysis. A map of stellar mass surface density is then created (Fig. 6.3, left panel).

The formal errors computed by CIGALE (which take into account the uncertainty in the data, but not the systematics of the method) are of the order of 0.1 dex. As a further check, we compared the stellar mass estimated by CIGALE with the stellar mass estimate obtained using the procedure in Bell et al. (2003) and using the u-r colour to estimate the mass-to-light ratio. The stellar mass densities obtained with the Bell formulation are consistent with the ones obtained with CIGALE, with a small systematic difference of less than 0.1 dex at very large radii (R > 8 kpc). The total mass of NGC 628 out to 3 R_e computed by CIGALE is $\log(M_\star/M_\odot) = 9.8$.

6.1.6 Stellar metallicity

To take into account the metals locked in stars we make use of the recent study of Sánchez-Blázquez et al. (2014), who present the mass-weighted stellar metallicity gradient for NGC 628 by performing full spectral fitting using the software package STECKMAP on the PINGS IFS data. Despite the increased level of sophistication of the spectral fitting algorithms in recent years (Heavens et al., 2000; Panter et al., 2004; Fernandes et al., 2005; Gallazzi et al., 2006; Sánchez-Blázquez et al., 2011; Cid Fernandes et al., 2014; Wilkinson et al., 2015; McDermid et al., 2015), stellar metallicity remains the hardest quantity to estimate in stellar population studies. The difficulty is due to the non-linear effect of a

limited set of metallicity values generally available in spectral libraries (since most stellar libraries rely on observations in the solar neighbourhood, super-solar metallicity stars are not well represented) and the well-known age-metallicity degeneracy (e.g. Worthey et al., 1994), which acts in the direction of confusing old, metal poor systems with young metal rich ones. While the ability of spectral fitting codes to reliably derive input parameters increases as a function of S/N, it has been shown (see for example Cid Fernandes et al. 2014; Wilkinson et al. 2015) that even for high S/N spectra, stellar metallicity calculated with different sets of simple stellar populations can differ by more than 0.2 dex. It is beyond the scope of this work to perform a new full spectral fitting study of the PINGS data for NGC 628 and further evaluate these systematic uncertainties. We note, however, that our simple approach of propagating of the errors in the stellar metallicities presented in Sánchez-Blázquez et al. (2014) (median error $\sim$ 0.15 dex) does not take a these systematic uncertainties into account.

Taking into account the necessary correction factor due to the fact that Sánchez-Blázquez et al. (2014) adopt a different distance for NGC 628, we can obtain a stellar metallicity gradient out to 5 kpc. We put the gas phase and stellar metallicity on the same abundance scale by using the solar metallicity of Asplund et al. (2009) and assuming solar abundance ratios. We do not attempt to correct for possible non-solar abundance ratios (e.g. α-enhancement) in the bulge, since in any case the correction will only affect our innermost radial bin and will not have a significant effect on the subsequent analysis of integrated properties.

6.1.7 Gas mass surface density

The HI mass is calculated from the HI surface brightness, assuming that HI is everywhere optically thin.

To convert from CO luminosity to H_2 mass we adopt a constant CO to H_2 (α_{CO}) conversion factor given by

$$\alpha_{\rm CO} = 4.35 \frac{\rm M_\odot\ pc^{-2}}{\rm K\ km\ s^{-1}}. \tag{6.1}$$

This value of the conversion factor is appropriate for the Milky Way (Solomon et al., 1987; Strong & Mattox, 1996; Abdo et al., 2010; Bolatto et al., 2013).

A number of studies, based on determinations of α_{CO} via different methods (Wilson, 1995; Bolatto et al., 2008; Leroy et al., 2011; Schruba et al., 2012; McQuinn et al., 2012; Bolatto et al., 2013), have gathered a consistent body of evidence for an increase in α_{CO} in low-metallicity environments. Despite these efforts, a robust parametrisation of the dependence between α_{CO} and metallicity is still lacking. We therefore consider two alternative parametrisations of α_{CO}.

1. An α_{CO} linearly dependent on metallicity, using the parametrisation by Schruba et al. (2012), which is based on dwarf galaxies by inverting the star-formation law. For consistency we use the same metallicity calibrators as used in Schruba et al. (2012) (average of the P05 and KK04 calibration) for calculating α_{CO}.

2. The radial gradient in α_{CO} inferred by Blanc et al. (2013b) for NGC 628 by inverting the star formation law.

The effects of changing the conversion factor on the analysis presented in this paper are small and are discussed below in Sec. 6.1.8. We also note that recent work from Sandstrom et al. (2013), using

far-IR dust modelling to infer the molecular gas mass, obtained a flat α_{CO} gradient for NGC 628, with α_{CO} very close to the adopted Milky Way value.

As the conversion factors are calibrated for the CO (1-0) line, while the HERACLES observations map the CO (2-1) transition, we assume a constant ratio of 0.7 between the two CO luminosities (Leroy et al., 2012). To calculate the total gas mass we multiply the HI component by 1.36 to account for helium and add the molecular gas mass computed using the conversion factor above, which already takes helium into account.

6.1.8 Radial gradients

The metallicity gradient

In Fig. 6.3 we show the derived metallicity gradient for NGC 628 using the M08 and PP04 calibrations (violet solid and dashed lines). The PP04 gas metallicity gradient presents a flattening in the inner 2.5 kpc ($\approx$ 1 R_e, violet dot-dashed line), already reported in previous work (Rosales-Ortega et al., 2011). The M08 metallicity gradient, on the other hand, reaches in the central regions metallicities higher than expected from the profiles measured in galaxies of comparable mass in MaNGA (compare with Fig. 5.4).

We measure a metallicity gradient of -0.053 dex kpc^{-1} (or -0.13 dex R_e^{-1}) using the M08 calibration and -0.033 dex kpc^{-1} (or -0.08 dex R_e^{-1}) using the PP04 calibration. These results are consistent with the results of extensive investigation by Rosales-Ortega et al. (2011), who obtain slopes for the metallicity gradient of NGC 628 in the range -0.03 to -0.06 dex kpc^{-1}, depending on the calibration and the method used to select star-forming regions. More recently Berg et al. (2015) measured T_e-derived metallicity in a sample of 62 HII regions in NGC 628 and obtain a gradient of -0.044 dex kpc^{-1}. Overall the gradient observed in NGC 628 is steeper than the median gradient expected for a typical galaxy of comparable stellar mass. Using the MaNGA sample, the median metallicity gradient for a galaxy in the mass range $\log(M_\star/M_\odot) = 9.75 - 10.0$ is -0.025 dex kpc^{-1} and the associated scatter is 0.017 dex kpc^{-1}, making the Berg et al. (2015) metallicity gradient measurement marginally consistent with the scatter.

The gas mass and effective yield gradients

The HI disc is much more extended than the FoV of the IFS data and presents clumpy substructure (seen in Fig. 6.1). The HI surface density profile is characterised by a central dip and and an increase towards larger radii. The maximum in HI surface density coincides roughly with the edge of the IFS field of view ($\approx$ 3 R_e), hence in our subsequent analysis, which is limited to the radial extent of the IFS observations, we neglect about 40% of the mass of the HI disc. We will discuss the importance of this extended HI disc in Sec. 6.4.

The molecular gas profile is centrally concentrated and its surface density decreases with radius. The sensitivity limit of the HERACLES data is shown as a horizontal dotted line in Fig. 6.3. The combination of the atomic and molecular gas profile generates a total gas surface density profile (green line in Fig. 6.3) which is remarkably constant over the whole field of view of the IFS data. This implies that the gas fraction ($f_{gas} = M_{gas}/(M_\star + M_{gas})$) increases outwards roughly log-linearly with radius.

Fig. 6.4 shows the radial gradient of the effective yield (Eq. 1.14, Sec. 1.3.2) in NGC 628, clearly demonstrating that y_{eff} increases with radius. Importantly, the observed effective yield is always lower

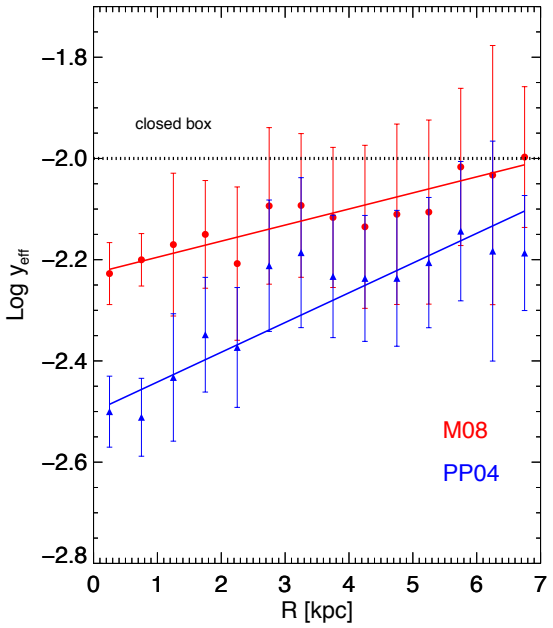

Figure 6.4: The radial variation of the effective yield in NGC 628. The value expected for the closed box case, $y/(1-R) = 0.010$, is indicated as a black dotted line. The red circles and blue triangles represent respectively the results obtained with the Maiolino et al. (2008) and Pettini & Pagel (2004) calibrations and the solid coloured lines represent the best linear fit to the data.

than y=p/(1-R)=0.010, implying that the region of the disc of NGC 628 sampled in this work have not been evolving as a closed box. The information provided by the effective yield is, however, highly degenerate. More specifically, both enriched gas outflows or pristine (or low-metallicity) gas inflows will lead to the observed effective yield to be lower than the closed box value (Edmunds, 1990).

The effect of changing α_{CO}

In Fig. 6.5, left panel, we plot the molecular gas radial gradients obtained with different α_{CO} parametrisations (red) together with the resulting total gas content (green). We note that introducing a metallicity-dependent α_{CO} (or equivalently a positive α_{CO} gradient as in Blanc et al. 2013b) decreases the total gas content in the central regions and increases the gas content in the outskirts. Both these factors contribute to strengthening our results, since central regions acquire lower effective yields and outer regions higher effective yields. We also note that the effect of changing α_{CO} on the total gas content is everywhere less than 0.2 dex, since in the outer regions, where the different α_{CO} give rise to larger discrepancies, the cold ISM is dominated by HI. In Fig. 6.5, right panel, we show that changing between the considered parametrisations of α_{CO} causes a slight steepening of the effective yield gradient, but does not affect any of our conclusions.

6.2 The chemical evolution model

In this section we present the analytical framework that we will use to study the metallicity evolution in resolved regions of NGC 628. We make use of simple relations obtained by invoking the instantaneous recycling approximation and perfect instantaneous mixing (Sec. 1.3.1). This framework has been proven successful in modelling the chemical evolution of oxygen (Zahid et al., 2012; Dayal et al., 2013; Peeples et al., 2014; Peng & Maiolino, 2014), which is predominantly produced by short-lived

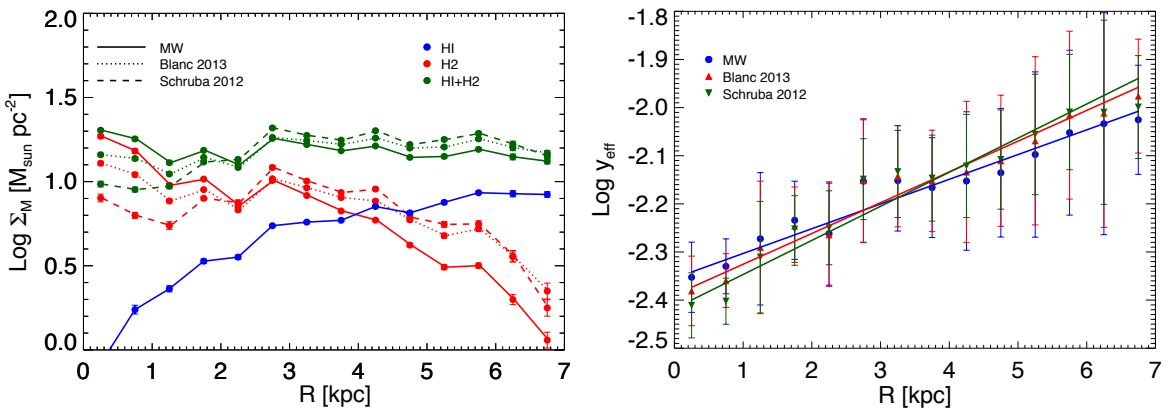

Figure 6.5: Radial gradients in atomic gas surface density (blue), molecular gas surface density (red) and total gas surface density (dark green) in NGC 628 obtained changing the CO $\rightarrow$ H_2 (α_{CO}) conversion factor. The solid lines represent the result for a Milky Way conversion factor, dotted lines are obtained using the radial gradient in α_{CO} inferred by Blanc et al. (2013b) for NGC 628, while the dashed lines represent the results obtained using a metallicity-dependent conversion factor from Schruba et al. (2012).

massive stars dying as core-collapse supernovae. We note in passing that the chemical abundances of other common elements (like nitrogen or iron) require a more detailed model, taking into account stellar lifetimes, the Type Ia supernovae delay time distribution and variation of the nucleosynthetic yields with metallicity, which is not be implemented in this chapter. However, since oxygen is the most abundant metal by mass, it is a good tracer for the total metal content.

When a numerical value for the average yield is required, we make use of the results in Vincenzo et al. (2016b), based on the compilation of stellar yields in Romano et al. (2010), which have been shown to successfully reproduce the oxygen abundance in the Milky Way. We adopt a KTG IMF (Kroupa et al., 1993), $M_{long-lived} = 1\ M_{\odot}$ and therefore get a fiducial average yield of $p = p_O = 0.007$ for oxygen and $R = 0.30$ (Vincenzo et al., 2016b). The same results can be applied to the *total* content of metals, by replacing the numerical value of the average yield with $p = p_Z(tot) = 0.013$.

6.2.1 Analytical solution for constant inflow models

Peng & Maiolino (2014) present solutions for the constitutive equations of chemical evolution (Eq. 1.8-1.11) under the following assumptions:

1. Constant inflow rate, Φ.
2. A linear star formation relation, $SFR = \varepsilon\ M_{gas}$, with constant ε.
3. Outflow rate proportional to the SFR through a constant loading factor λ: $\Psi = \lambda\ SFR$.

We further assume that the yield per stellar generation p (Eq. 1.7) and return factor R (Eq. 1.6) are constant with time and that the inflow is of primordial gas (with zero metallicity). Under these assumptions analytical solutions can be obtained with an explicit time dependence. As discussed in Peng & Maiolino (2014) and in Sec. 1.3.3, the equilibrium timescale,

$$\tau \equiv \frac{1}{\varepsilon\ (1 - R + \lambda)}, \tag{6.2}$$

Table 6.2: Exact analytical time-dependent solution of the Peng & Maiolino (2014) models with constant inflow rate for different galaxy properties. The equilibrium timescale τ is defined in Eq. 6.2.

Galaxy property	Exact solution	t << τ	t >> τ
M_g	$\Phi\ \tau\ (1 - e^{-t/\tau})$	$\Phi\ t$	$\Phi\ \tau$
$SFR = \varepsilon\ M_g$	$\varepsilon\ \Phi\ \tau\ (1 - e^{-t/\tau})$	$\varepsilon\ \Phi\ t$	$\varepsilon\ \Phi\ \tau$
$M_\star$	$\Phi\ \tau^2\ \varepsilon\ (1 - R)\ (t/\tau - (1 - e^{-t/\tau}))$	$\Phi\ \varepsilon\ (1 - R)\ t^2/2$	$\Phi\ \varepsilon\ (1 - R)\ \tau\ t$
$f_{gas} \equiv \frac{M_g}{M_g + M_\star}$	$\left[1 + \varepsilon\ \tau\ (1 - R)\ \left(\frac{t}{\tau}\ \frac{1}{1-e^{-t/\tau}} - 1\right)\right]^{-1}$	$(1 + \varepsilon\ (1 - R)\ t/2)^{-1}$	$(1 + \varepsilon\ (1 - R)\ t)^{-1}$
$Z_g \equiv M_{Z_g}/M_g$	$p\ \varepsilon\ \tau\left(1 - \frac{t/\tau\ e^{-t/\tau}}{1-e^{-t/\tau}}\right)$	$p\ \varepsilon\ t/2$	$p\ \varepsilon\ \tau$
M_Z	$p\ \varepsilon\ \Phi\ \tau^2\left[(1 - \epsilon\ \lambda\ t)(t/\tau - (1 - e^{-t/\tau})) - \varepsilon\ \lambda\ t((t/\tau + 1)e^{-t/\tau} - 1)\right]$	$p\ \varepsilon\ \Phi\ t^2/2$	$p\ \varepsilon\ \Phi\ (1 - \varepsilon\ \lambda\ t)\ \tau\ t$
$M_Z/M_\star$	$\frac{p}{1-R}\left[1 - \varepsilon\ \lambda\ \tau\left(1 + \frac{((1+t/\tau)\ e^{-t/\tau}-1)}{t/\tau+e^{-t/\tau}-1}\right)\right]$	$\frac{p}{1-R}$	$\frac{p}{1-R}(1 - \varepsilon\ \lambda\ \tau)$

is the natural timescale driving the chemical evolution of the system. For t >> τ physical properties of galaxies tend to their equilibrium values. As discussed in Peng & Maiolino (2014), low-mass dwarf galaxies and chemically un-evolved systems will not satisfy the equilibrium condition and need to be studied in the t < τ regime.

In Table 6.2 we summarise the analytical solutions for a number of galaxy properties. We note that, apart from the assumptions stated above, the solutions are mathematically exact.[3] We also remark that, as expected, the only timescale responsible for the chemical evolution of the system is the equilibrium timescale defined above (Eq. 6.2).

The limits of the solutions for the equilibrium case (t >> τ) have a simple physical interpretation. Star formation exactly balances out the inflow and outflow rates, the gas mass (and hence the SFR) stays constant and the stellar mass grows linearly with time. In this regime the gas phase metallicity plateaus at a constant value given by Eq. 1.16.

6.2.2 Metal mass budget

Following Eq. 1.11, the total mass of oxygen *produced* is given by

$$\mathrm{M_{Z_{prod}}} = \mathrm{y\ M_\star}. \tag{6.3}$$

This corresponds to the total mass of oxygen actually present in the galaxy in the case of no outflows (Eq. 1.11 with $\Psi = 0$). In the presence of outflows, the resulting total amount of metals is given by the equation

$$\mathrm{M_{Z(tot)}} = \mathrm{y\ M_\star} - \lambda \int \mathrm{Z_g(t)\ SFR(t)\ dt}. \tag{6.4}$$

Using the solution of the constant inflow model presented in the last subsection, the equilibrium value of the $\mathrm{M_Z/M_\star}$ ratio is $\frac{p}{1-R}(1 - \varepsilon\ \lambda\ \tau)$, lower than the expected value $\mathrm{M_Z/M_\star} = \mathrm{y} = \frac{\mathrm{p}}{1-\mathrm{R}}$ in absence of outflows (i.e. for $\lambda = 0$).

[3]The solution for the gas phase metallicity (Z_g) presented here differs from the one in Peng & Maiolino (2014), who solve for the metallicity evolution making further approximations to simplify the algebra.

The gas fraction f_{gas} is the best property to quantify the degree of chemical evolution of the system: systems with high gas fraction have not reached equilibrium and are chemically un-evolved, while systems with low gas fraction are in equilibrium and chemically evolved.

Considering the analytical solution in Table 6.2, it can be demonstrated that the relation between $M_Z/M_\star$ and f_{gas} depends only on the value of the outflow loading factor, and does not depend on the assumed inflow rate and star formation efficiency. In other words the position of a point in the f_{gas} vs $M_Z/M_\star$ plane depends only on λ. To prove this it is sufficient to observe that both f_{gas} and $M_Z/M_\star$ are only a function of λ and t/τ. Therefore, eliminating t/τ, it would be possible to write a relation between f_{gas} and $M_Z/M_\star$ which depends only on λ. Unfortunately the complex nature of the solutions does not allow such relation to be written in closed form. Physically this statement can be interpreted as stating that the metal deficit (i.e. $M_Z/M_\star$) depends only on how evolved the system is (i.e. its f_{gas}) and the strength of its outflows (i.e. λ). As shown in Sec. 6.5.1, this simple result is *not* valid anymore if we assume that the inflow rate is proportional to the SFR.

Finally we note that exactly the same argument can be applied to the relation between f_{gas} and Z_g, which can therefore be shown to depend only on the outflow loading factor and not on the inflow rate and the star formation efficiency.

6.3 Applying the chemical evolution model to NGC 628

6.3.1 Accounting for the missing metals

The aim of this section is to compute the total mass of oxygen present in NGC 628 as a function of radius and compare it with the total mass of oxygen expected to have been produced by its stellar component. In theory, this comparison provides a direct (model-independent) measurement of the mass of metals lost by each region in the galaxy via metal-enriched outflows.

Both simulations (Marinacci et al., 2014) and observations (Shull et al., 2012; Tumlinson et al., 2013) argue that a large quantity of baryons and metals might reside in the hot haloes around galaxies. For the purposes of chemical evolution, however, this gas is irrelevant, since we assume it does not form stars, at least as long as it remains in the hot phase. In this work, therefore, we consider this gaseous component as effectively external to the galaxy and the metals present in it as 'lost'.

The total observed mass of oxygen is given by the sum of the mass of oxygen in the ISM ($M_{Zg} = Z_g M_g$) and the mass of oxygen locked in stars ($M_{Z\star} = Z_\star M_\star$), i.e.

$$M_{Z(obs,tot)} = M_{Zg} + M_{Z\star} = Z_g M_g + Z_\star M_\star. \tag{6.5}$$

In Fig. 6.6 (left panel) we show the total observed mass of oxygen per unit area in stars (orange), in the ISM (violet), in ISM+stars (red) and the mass of metals that must have been produced by the observed stellar mass using our adopted yield (using Eq. 6.3, blue line) as a function of radius. In the case of the ISM and ISM+stars lines, we show the results obtained with both the M08 (solid) and PP04 (dashed) metallicity calibrations. The error bars represent the error in the mean in each annulus, added in quadrature to the median of the intrinsic error in each of the physical quantities. The intrinsic error budget is dominated by the error on the stellar metallicity, followed by the uncertainty in gas-phase metallicity and stellar mass (for both we get a median error of about 0.1 dex). These errors do not attempt to incorporate systematic effects, which would dominate the uncertainty budget for this study.

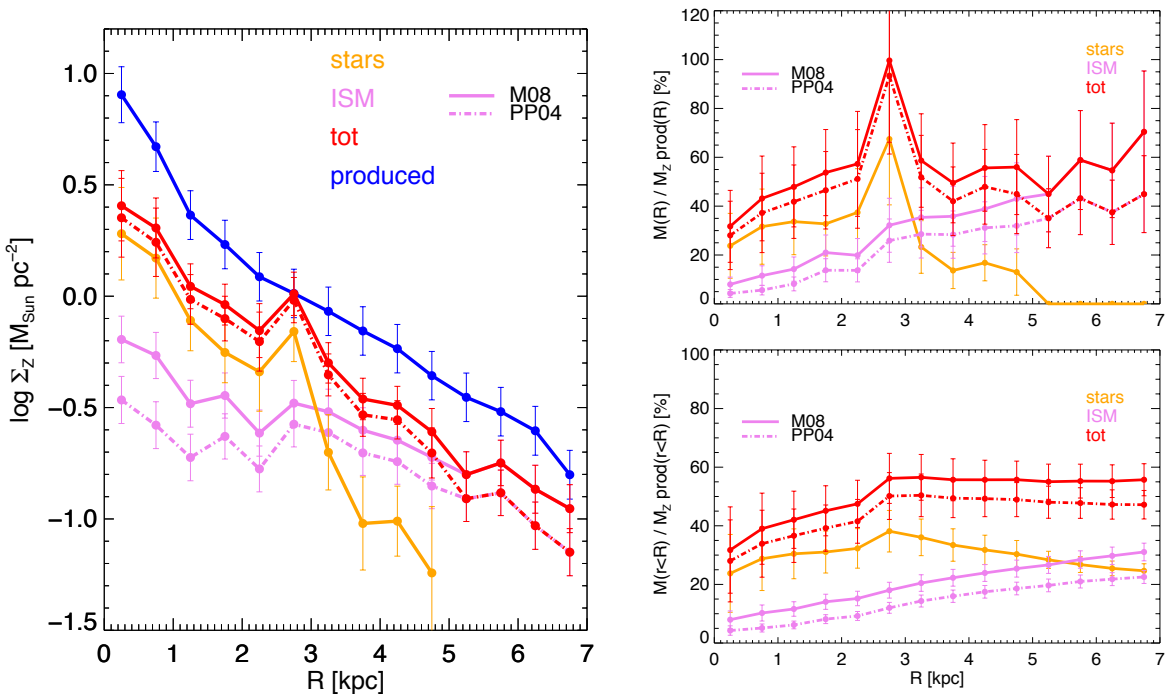

Figure 6.6: *Left*: Oxygen mass per unit area in different galactic components compared with the oxygen mass expected to have been produced by the observed stellar mass surface density, in different radial bins. The orange line shows the oxygen mass locked in stars, calculated adopting the stellar metallicity gradient from Sánchez-Blázquez et al. (2014). The violet solid line shows the oxygen mass in the ISM obtained by using the M08 calibration, while the violet-dashed line shows the oxygen mass in the ISM obtained by using the PP04 calibration. In red we show the total observed mass of oxygen (ISM + stars). The blue line shows the mass of oxygen produced by the observed stellar surface density assuming our fiducial average yield. *Top Right*: Mass of oxygen in each radial bin as a percentage of the mass of oxygen produced in the same radial bin. The colour-coding is the same as in the left panel. *Bottom Right*: The cumulative mass of oxygen within radius R in the different galactic components, expressed as a percentage of the total mass of oxygen produced within the same radius R. The points shown for the last radial bin correspond to the integrated oxygen budget for NGC 628, demonstrating that the galaxy as a whole has retained only ≈ 50% of the metals it has produced.

Moreover we take the net yield (y) and the return fraction (R) to be known exactly. With these caveats, Fig. 6.6 demonstrates that using the fiducial yield *at all radii more metals have been produced than can be accounted for, considering both the metals in the ISM and in stars*.

In the discussion (Sec. 6.4) we argue that a different choice of IMF (adopting for example Salpeter or Chabrier IMF) only makes the metal deficit worse. We also note that the mass of metals in stars presents a sharp feature between 2.5 and 3 kpc, which is a direct consequence of the sharp feature in the stellar metallicity gradient. Since it is present in only one radial bin, the effect of this feature on the overall metal budget of the galaxy is negligible and will not be discussed further.

In Fig. 6.6, top right panel, we show the mass of oxygen in stars (orange) and ISM (violet) as a function of radius as a percentage of the total mass of oxygen produced in that annulus. The total mass of oxygen in each annulus (ISM + stars, red line) is also shown, and we plot the results using both the M08 (solid line) and PP04 (dot-dashed line) metallicity calibrations.

Fig. 6.6 (top-right) shows that the fraction of metals lost is about 45%-55%, and approximatively constant within the uncertainties for R $>$ 3 kpc. There is also some evidence that the fraction of metals lost in the central region is higher (only ∼30% of the metals have been retained). This feature may trace the effect of massive outflows during the formation of the bulge or the cumulative effect of nuclear activity in the past. Interestingly Fig. 6.6 (top-right) also shows that the fraction of metals

Table 6.3: The total oxygen mass in different galactic components, integrating the radial gradients for NGC 628 out to R = 7.00 kpc.

Metals	Mass [10^7 $M_\odot$]	Mass [% M_Z prod]
Stars	2.6 ± 0.9	25 ± 2%
ISM (M08)	3.2 ± 0.9	31 ± 3%
ISM (PP04)	2.3 ± 0.7	23 ± 2%
Stars + ISM (M08)	5.8 ± 1.7	56 ± 5%
Stars + ISM (PP04)	4.9 ± 1.5	47 ± 5%

retained increases at R > 5 kpc. Gas phase metallicity measurements at even larger radii provided by the Berg et al. (2015) dataset confirm and further extend this trend (see discussion in Sec. 6.4.2).

Fig. 6.6 (lower-right) shows the *cumulative* version of the previous plot. For each radius R, the mass of oxygen in different components *within* radius R is computed as a percentage of the mass of metals produced within the considered radius. This plot can be interpreted as the results that would be obtained for the integrated properties of NGC 628 if all quantities (metallicities, gas masses etc) were measured using an aperture corresponding to a radius R on the sky.

We note that cumulatively the mass of oxygen in the ISM is sub-dominant out to R ≈ 5.5 kpc. At this radius stars and ISM contribute roughly equally to the total oxygen budget. For easy reference, the masses of oxygen in the different components within 7.0 kpc are summarised in Table 6.3. Taking into account the uncertainty associated with the choice of metallicity calibration, we conclude that out to R = 7.0 kpc the bulge and the disc of NGC 628 as a whole have lost ∼ 50% of the oxygen they have produced.

6.3.2 Inferred net outflow loading factor

We argued in Sec. 6.2.2 that the relation between $M_Z/M_\star$ and f_{gas} is *independent* of both the inflow rate and of star formation efficiency and depends only on the outflow loading factor. This is an important conclusion, since it demonstrates that the relation between these two quantities is therefore a non-degenerate tracer of the net effect of outflows (unlike the effective yield).

The red lines in Fig. 6.7 show $M_Z/M_\star$ as a function of f_{gas}, for different values of the outflow loading factor. Coloured symbols in Fig. 6.7 show the $M_Z/M_\star$ and f_{gas} observed in different radial annuli in NGC 628, where the colour coding represents the radial distance from the galaxy centre. Filled symbols are for the M08 calibration, while hollow symbols are for the PP04 calibration. We note that this figure is just an alternative representation of the metal deficit discussed in the previous section (Fig. 6.6). Here we have replaced the radial distance with f_{gas}, but the two quantities are related as discussed in Sec. 6.1.8, since the gas fraction increases monotonically with radius. The metal deficit can be visualised in Fig. 6.6 as the distance between the observational data points and the $\lambda = 0$ (solid red) line, which represents the $M_Z = y\ M_\star$ case.

By using the M08 calibration the observed points are well reproduced with an outflow loading factor $\lambda \approx 1$, with a scatter in the range $0.5 < \lambda < 2$, except for the 'anomalous' point at 3 kpc, which requires a lower loading factor approaching zero. The PP04 calibration requires slightly higher loading factors (except again for the anomalous point at 3 kpc).

We emphasise that, since we use the *total* mass of metals relative to the mass of stars, our analysis provides an estimate of the *average* outflow loading factor during the galaxy lifetime, and not the

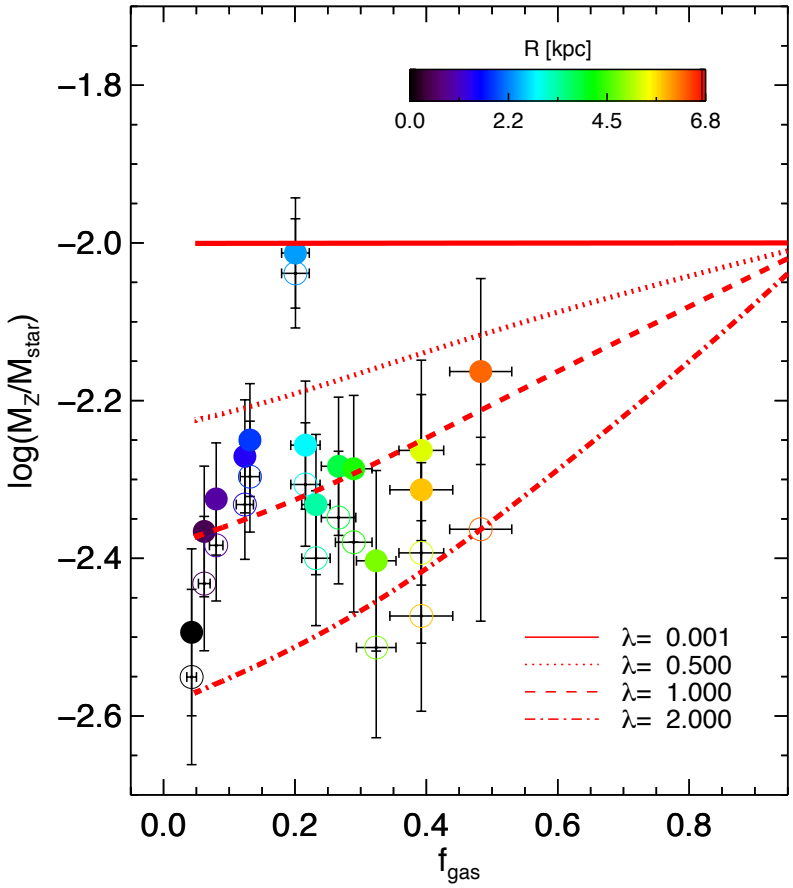

Figure 6.7: Metals-to-stellar mass ratio ($M_Z/M_\star$) versus gas fraction (f_{gas}). Symbols show the values observed in radial annuli in NGC 628, where the colour-coding gives the galactocentric radial distance, as indicated in the colour bar. Solid symbols correspond to the mass of metals in which the ISM metallicity is calculated by using the M08 calibration, while open symbols use the PP04 calibration. The red lines correspond to the prediction of simple chemical evolution models with different values for the average outflow loading factor λ. Note that the model relations are independent of the inflow rate Φ and of the star formation efficiency ε.

current outflow rate in the galaxy. Indeed, within the picture of hierarchical formation of structure, it is possible that this average loading factor is mainly driven by the high efficiency of metal loss at higher redshift, when the physical condition in the galaxy and its sub-components would have been significantly different.

6.3.3 Modelling the gas metallicity

As shown in Sec. 6.2.2, the adopted chemical evolution framework leads to a direct relation between gas metallicity (Z_g) and gas fraction (f_{gas}), that depends only on the outflow loading factor and not on the inflow rate or star formation efficiency. The relation between Z_g and f_{gas} has been studied by several authors, including recently Ascasibar et al. (2014) and Kudritzki et al. (2015), who extend their analysis to resolved scales making use of data from NGC 628.

However, unlike the metals locked in stars, the gas phase metallicity is more subject to recent gas flow events (possible stochastic variations away from the ideal gas regulatory model), hence making it a less reliable tool for inferring the time averaged properties of the system.

Keeping these caveats in mind, the model relations between Z_{gas} and f_{gas} are shown in Fig. 6.8, with the same outflow loading factors as in Fig. 6.7. The data points represent the observed values

in NGC 628 and are colour-coded by radial distance. The two different metallicity calibrations are identified, as in Fig. 6.7, by solid (Maiolino et al., 2008) and hollow (Pettini & Pagel, 2004) circles. The comparison of the models with the data points suggests outflow loading factors consistent with zero, or generally lower than those derived from the $M_Z/M_\star$ vs f_{gas} relation (Fig. 6.7).

We note that the mismatch applies (with about the same magnitude) both to the central regions, where the total mass of metals is dominated by the stellar component, and in the outer regions, where the total mass of metals is dominated by the gaseous component, therefore excluding that the mismatch is simply associated with a different metallicity scales or calibration issues associated with the calculation of one of the two quantities.

As discussed above, a possible solution can be attained assuming that the gas metallicity might not be representative of the average evolutionary processes during the life of the galaxy since it can be subject to recent galactic 'weather'. In particular, a process that may strongly affect the gas metallicity, without significantly affecting the total content of metals, could be recent inflow of enriched gas from the halo. We discuss this option further in Sec. 6.4.

Finally we note that Kudritzki et al. (2015) have inferred a similarly low loading factor (λ = 0.2-0.3) for NGC 628, by fitting the gas phase metallicity gradient and the gas fraction. Since they use T_e-based metallicities, their results should be compared with our analysis using the PP04 calibration. Kudritzki et al. (2015), however, make use of a chemical evolution model where the inflow rate is proportional to the SFR. As discussed in Appendix 6.5.1, this assumption introduces a dependence of the metallicity-gas fraction relation on the inflow rate, which is absent in our model.

6.4 Discussion

In the previous section we have demonstrated that (a) overall $\sim$ 50% of the oxygen produced by NGC 628 out to R = 7.0 kpc is unaccounted for and (b) average outflow loading factors of order unity can explain the observed metal deficit, although there is a tension with the observed gas metallicity. While we cannot exclude that possibility that the tension is due to the unavoidable systematic uncertainties in the determination of gas phase and stellar metallicity and the choice of nucleosynthetic yield/IMF, in this section we discuss possible ways to interpret the discrepancy in light of different physical mechanisms.

6.4.1 Gas flows and disc-halo interaction

The chemical evolution framework used in this work is an intentionally simple prescription. In particular, while the model allows metal rich outflows and pristine gas inflows, and hence some exchange of gas and metals between the different radial bins, it does not treat the case of incoming metal-rich gas or changes in the stellar mass component due to stellar migration.

A number of physical processes, for example, might be responsible for funnelling metal-rich gas into the central galactic regions, including viscous flows generated by gravitational instability or cloud - cloud collisions (Lacey & Fall, 1985; Thon & Meusinger, 1998; Ferguson & Clarke, 2001) or the presence of a bar or other non-axisymmetric perturbation (Minchev & Famaey, 2010; Matteo et al., 2013). The breaks seen in the stellar metallicity, and possibly the central flattening of the gas phase metallicity profile when using the PP04 calibration, combined with the presence of a star formation

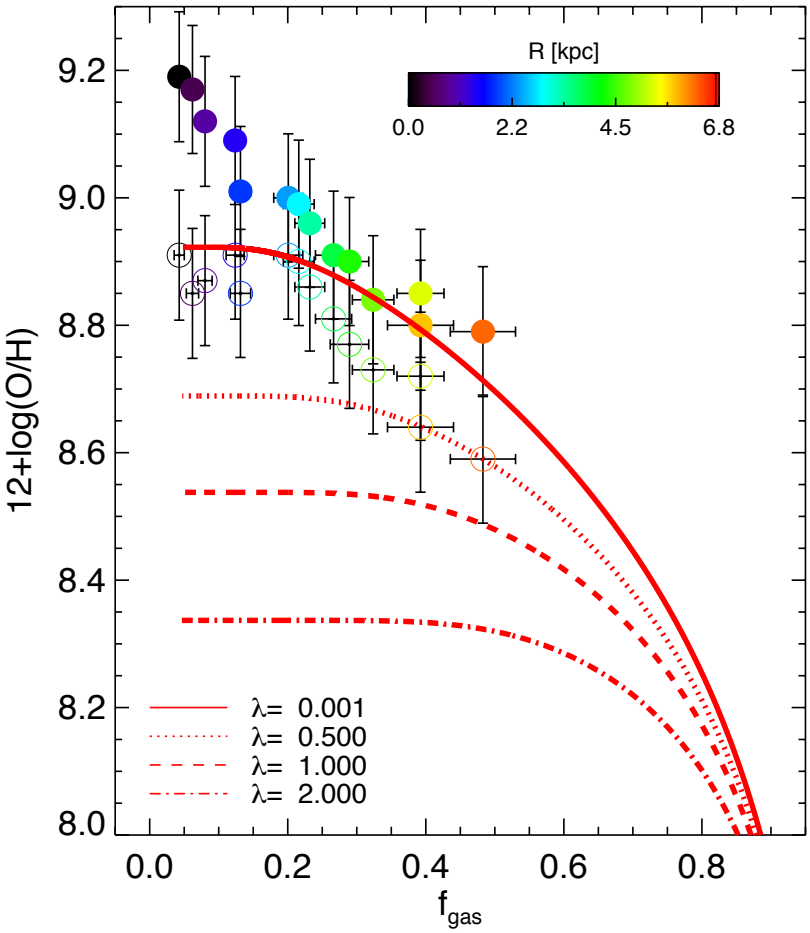

Figure 6.8: Gaseous metallicity 12 + log(O/H) versus gas fraction. Symbols show the values observed in radial annuli in NGC 628, where the colour-coding gives the galactocentric radial distance, as indicated in the colour bar. Solid symbols correspond to the mass of metals in which the ISM metallicity is calculated by using the M08 calibration, while open symbols use the PP04 calibration. The red lines correspond to the prediction of simple chemical evolution models with different values for the average outflow loading factor (λ). Note that the model relations are independent of the inflow rate Φ and of the star formation efficiency ε.

ring just inside the break radius, may indeed support the hypothesis of an oval perturbation playing a role in the evolution of the disc in NGC 628.

More importantly, enriched gas expelled by previous generations of supernovae may fall back onto the disc, generating a galactic fountain. In the literature, however, there is no agreement on the details of the fountain mechanism (Melioli et al., 2008, 2009; Spitoni et al., 2010), the radial distance covered by a galactic fountain, the time needed for the gas to rain back onto the disc and the overall impact of this mechanism on the chemical abundances of the disc itself. In hydrodynamical simulations, if a hot halo is present, metal-enriched gas can fall back towards the galactic centre (Melioli et al., 2009).

The presence of large amounts of metals in the halo of disc (and elliptical) galaxies has been inferred by recent HST-COS observations of absorption systems along the line of sight of background quasars (e.g. Tumlinson et al., 2011; Werk et al., 2014). However, these observations have probed the halo of galaxies at large radii (~100 kpc). In the inner region of the halo the gas metallicity is not known observationally, but simulations expect that the metallicity of the diffuse gas should reach values higher than solar (Marinacci et al., 2014).

We have attempted to model an episode of metal-enriched accretion at late times by modifying the

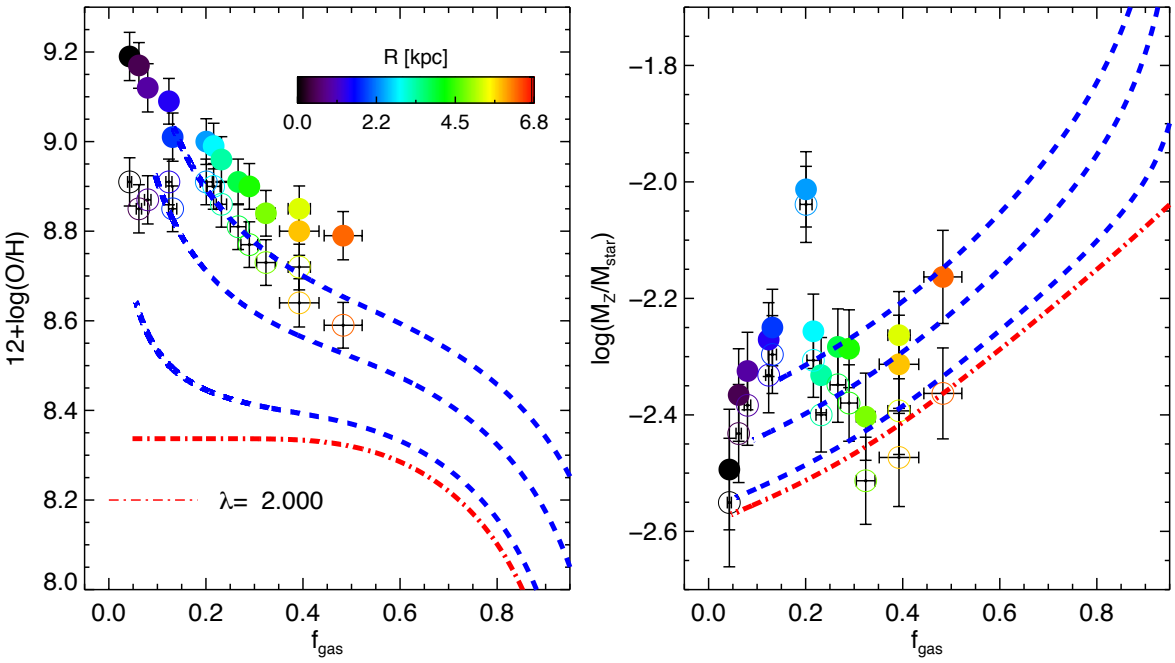

Figure 6.9: Same as Fig. 6.7 and 6.8, but including a late-time inflow of gas-rich material with metallicity 3 $Z_{\odot}$. The red line is the same as in Fig. 6.7 and 6.8 and represents the model with $\lambda = 2$, while the blue lines represent an increasing mass of infalling metal-rich gas. Going upwards in both figures the blue lines represent a infalling metal-rich gas mass that is a fraction of 1%, 5% and 10% of the mass of baryons already present in the disc at a given location.

analytical description of the metallicity evolution discussed above with the introduction of an accreted enriched gas mass, proportional to the mass of baryons already present in the galaxy, and with a given metallicity $Z_{gas-accr}$. The blue lines in Fig. 6.9 shows the effect of such a late enriched accretion by assuming that the accreted gas is 1, 5 and 10% of the mass in baryons already present in the radial bin and that the metallicity of such enriched inflow is $Z_{gas-accr} = 3\ Z_{\odot}$ (which is consistent with the enrichment of the hot gas phase expected by some models, Marinacci et al., 2014). Clearly such a model can now broadly reproduce the trend of the gas metallicities in NGC 628 at several radii. At the same time, Fig. 6.9 illustrates that such a late enriched accretion has little effect on the total content of metals, hence having little effect on the global, average outflow rate that we have inferred from the metal deficit.

In these models we have assumed an outflow loading factor $\lambda = 2.0$, i.e. higher than inferred in the previous section, to better illustrate that late enriched accretion can have a strong effect on the final gas metallicity but little effect on the total content of metals. We note that by starting with a lower loading factor (e.g. $\lambda = 1.0$) the enriched inflow can reproduce the data with a smaller amount of accreted gas ($\sim 3-5\%$).

Both gas flows in the disc and galactic fountains might therefore help resolve the tension between the metal deficit and the outflow loading factor implied from the gas phase metallicity for the central regions of NGC 628 by increasing the metallicity of the central regions beyond what is expected in the absence of these metal rich inflows. There is a fundamental degeneracy in this type of models between the outflow loading factor and the mass (and metallicity) of the enriched inflow, when using the gas phase metallicity alone. Better constrains, however, can be derived if one models, as we do

here, both the stellar and the gas phase metallicity at the same time, because the stellar metallicity is largely independent of gas flows at late times.

Stellar migration (Roškar et al., 2008; Yoachim et al., 2012; Spitoni et al., 2015) might also play a role in alleviating the observed tension. If stars diffuse out of the radial bin in which they are born, we would be making incorrect inferences for the gas fraction and oxygen mass in the bin. We can model this effect naively by considering that the observed stellar mass in each bin should be corrected for the net effect of migration. We experimented with this prescription and found that changes in the stellar mass up to 0.3 dex only generate small changes in $M_Z/M_\star$ for all bins within R = 5 kpc, since the metal budget is dominated by the stellar component and therefore $M_Z/M_\star$ is only weakly dependent on stellar mass. At larger radial distances the oxygen mass budget is dominated by the ISM and the effect of changing the stellar mass content is larger. If a large fraction of the stellar mass currently observed at large radii is the result of stellar migration from the central regions, we would require a lower outflow loading factor in the outer disc, going towards a reduction of the tension between the metal deficit and the observed gas metallicity.

6.4.2 Towards larger galactocentric distances

The behaviour of the metal budget at even larger radii than the ones probed by our investigation constitutes a particularly interesting avenue for future work. Since HI discs extend substantially more than the stellar component, low levels of chemical enrichment in the outer disc might mean that a large fraction of metals have escaped our budget.

Direct measurements of the chemical abundances at large galactocentric radii have been recently obtained for NGC 628 by Berg et al. (2015). Their observations contain 12 HII regions at radii larger than those sampled by the IFS data presented in this work. With the available data, there is no evidence for either a flattening or a break in the metallicity gradient of NGC 628 out to 10 kpc. This observations are interesting in the context of the metal budget, because they confirm the trend that regions at large galactocentric distances have retained a larger fraction of their metals compared to the inner regions of galaxies. In particular, relying on the metallicity gradient reported in Berg et al. (2015), we conclude that the radial bin around 10 kpc has retained ~80-100% of the metals produced in situ.

Intriguingly, previous work has also presented evidence that HII regions at extreme galactocentric distances ($R > R_{24} \approx 3\ R_e$) are more metal rich than expected from in situ star formation (Bresolin et al., 2009, 2012). These observations might be consistent with an extrapolation of the trend discussed above, and in general with the idea that gas rich, relatively un-evolved systems have a smaller metal deficit, or might even have acquired metals through enriched inflows from the central regions (through a galactic fountain). In the context of inside-out disc growth, these outer regions are still in the process of assembly and thus represent an ideal laboratory to study disc formation as it happens.

6.4.3 The effect of the IMF and the nucleosynthetic yield

In this work we have used the Kroupa et al. (1993) IMF, since this is the IMF which fits best the chemical evolution of galaxy discs (Romano et al., 2005, 2010). A different IMF would have an impact on our calculations by implying a different population-averaged net yield, since different elements are produced by stars of different masses. In this section we briefly discuss the implications of adopting different IMFs.

A Salpeter IMF would give a significantly higher metal deficit, implying a loss of about 75% of the metals produced. The inferred average loading factor would be about $\lambda \sim 2-4$. In the case of a Chabrier (2003) IMF the metal deficit is even more severe: more than 85% of the metals should be lost and in the implied average loading factor should be in the range $\lambda > 5$. The Kroupa (2001) IMF gives results very similar to Chabrier (2003). We note that in going from a Kroupa to a Salpeter IMF we correct the stellar mass profile by a factor of 0.26 dex.

Such large loading factors are extreme, especially considering that these are loading factors averaged during the lifetime of the galaxy, and have never been seen in galactic winds studies locally or even in high-z galaxy discs (e.g Steidel et al., 2010; Genzel et al., 2011), which instead infer outflow loading factors more in line with the results obtained by using the Kroupa et al. (1993) IMF, further confirming that this IMF is the most appropriate for modelling galaxy discs.

However, it has been pointed out that the chemical properties of spheroids (including bulges) may be more properly described by a Chabrier (2003) IMF. If we apply the latter IMF only to the central region, we get a large metal deficit ($\sim$ 90%) for the bulge. This would be in line with a similar estimates for the Milky Way, according to which the bulge of our Galaxy has lost about 80% of its metals (Greggio & Renzini, 2011). The Chabrier (2003) applied to the central region would also imply a central outflow loading factor of about $\lambda \sim 5$. Since we are only measuring the time-averaged outflow loading factor, it is not implausible to find that the central regions of galaxies might have experienced stronger outflows, despite the fact that at present time they sit at the bottom of the galaxy's potential well. Indeed outflow rates with such large loading factor are observed in the central region of local and high-z galaxies (Feruglio et al., 2010; Rupke & Veilleux, 2011; Maiolino et al., 2012; Cicone et al., 2014, 2015), and may be explained with the additional boost to the outflow rate associated with quasar-driven winds or with extreme nuclear starbursts in the past, when these feedback processes were likely more violent than in the present Universe.

6.4.4 The oxygen deficit in context

Previous work has estimated the oxygen (or metal) budget in star forming disc galaxies by statistical arguments, making use of scaling relations (between mass and SFR, between gas fraction and stellar mass, and between mass and metallicity) demonstrated to hold in large samples of galaxies observed spectroscopically (Bouché et al., 2007; Zahid et al., 2012; Peeples et al., 2014). These works predict an oxygen deficit ranging from 35% to 90%, with large statistical uncertainties, related both to the intrinsic scatter in the scaling relations used as input for the models and to the difficulty of robustly correcting for aperture effects. Nonetheless it is rewarding to note that our estimate for the metal deficit in NGC 628 falls inside the range of estimates from previous works.

Due to the difficulty of studying the stellar metallicity and thus deriving the total metal content in galaxies, the relation between gas phase metallicity and gas fraction has been widely used as an observationally more accessible tool to investigate the impact of outflows. Recent work (Lilly et al., 2013; Dayal et al., 2013; Ascasibar et al., 2014; Lu et al., 2015) generally agrees on loading factors of order unity for galaxies of stellar mass $\log(M_\star/M_\odot) \sim 10$.

Extending this study to a larger sample of galaxies with resolved gas masses and metallicity information would provide the logical way forward to studying the effect of outflows across the whole galaxy population and uncover trends with galaxy parameters (stellar mass, SFR etc). In particular,

low mass galaxies ($\log(M_\star/M_\odot) < 9$) are predicted to exhibit higher outflow loading factors in order to match their low observed baryon fractions (McGaugh et al., 2010), their metallicity (Lu et al., 2015) and to reconcile the faint-end slopes of the dark matter and galaxy mass functions (Lilly et al., 2013). Some observational evidence for higher outflow rates in dwarf starbursts can be found in the literature (e.g Martin et al., 2002), but more evidence in this mass regime is urgently needed.

While such a program is observationally costly, the synergy between large IFS surveys (CALIFA, SAMI and MaNGA) and radio and sub-mm interferometers (ALMA, NOEMA, JVLA) will greatly increase the availability of matched-resolution datasets to use for this type of study in the near future.

6.4.5 A link between outflows and baryon fraction

The metal deficit is tightly related to the well-known 'missing baryon problem' (e.g. Fukugita et al., 1998; McGaugh et al., 2010; Shull et al., 2012). Within our baryon cycling framework we cannot account for the inventory of cosmic baryons, a large fraction of which are believed to exist in the IGM and circumgalactic medium. However, within the gas regulatory model, outflows modulate the final baryonic mass of the system, while the gas inflow rate can be assumed to be directly proportional to the dark matter halo mass growth rate. Peng & Maiolino (2014) provide a useful parametrisation to relate the halo mass (M_h) and the gas inflow rate (Φ)

$$\Phi = f_b \, f_{gal} \, \frac{dM_h}{dt}, \tag{6.6}$$

where $f_b = 0.155$ (Planck Collaboration et al., 2014) is the cosmic baryon fraction and f_{gal} is the fraction of accreting baryons that penetrates into the inner galaxy disc, which could be a complex function of halo mass and redshift. Relying on results from the hydrodynamical simulations in Dekel et al. (2013), we follow Peng & Maiolino (2014) and assume for simplicity $f_{gal} \sim 0.5$ in this section.

The evolution of the total baryonic content of the system ($M_b = M_g + M_\star$) is the dictated by Eq. 1.8–1.9 so that $dM_b/dt = \Psi - \Phi$. Combining this with Eq. 6.6 we obtain

$$M_b = f_b \, f_{gal} \, M_h - \frac{\lambda}{1-R} \, M_\star. \tag{6.7}$$

Rearranging we finally obtain a relation between gas fraction (f_{gas}), outflow loading factor (λ) and the detected baryon fraction ($f_d \equiv \frac{M_b}{f_b \, M_h}$, as defined in McGaugh et al. 2010),

$$f_d \equiv \frac{M_b}{f_b \, M_h} = f_{gal} \left(1 + \frac{\lambda}{(1-R)(1+f_{gas})} \right)^{-1}. \tag{6.8}$$

Using representative values for NGC 628, $f_{gas} = 0.2$ and $\lambda = 1$ we obtain $f_d \sim 0.23$. This very rough order-of-magnitude calculation leads to a detected baryon fraction that is surprisingly close to the detected baryons fractions measured via the Tully-Fisher relation in McGaugh et al. (2010), who quote $f_d \sim 0.16 - 0.19$ for disc galaxies of stellar mass $\log(M_\star/M_\odot) = 9.9 - 10.1$, comparable to NGC 628.

6.5 Additional material

6.5.1 A comparison with the SFR $\propto$ inflow rate model

To demonstrate the physical difference between the solutions that assume a constant inflow rate and the solutions which assume the inflow rate to the proportional to the SFR at all times, we present a

comparison of their time evolution. The first thing to appreciate is that, if we assume the inflow rate to the proportional to the SFR ($\Phi = \omega$ SFR), Eq. 1.8 only admits the following solution for the gas mass M_g

$$\frac{dM_g}{dt} = (\omega - \lambda - 1 + R)\varepsilon M_g \rightarrow M_g = M_0 e^{-(1-R-\omega+\lambda)\varepsilon t}, \tag{6.9}$$

where M_0 is the initial gas reservoir at t=0. Physical solutions require $1 - R - \omega + \lambda > 0$, and hence imply an exponentially declining SFR. The gas equilibrium timescale (τ') for this model depends on ω and is given by

$$\tau' = \frac{1}{\varepsilon(1 - R + \lambda - \omega)}. \tag{6.10}$$

This timescale tends to the timescale in Eq. 6.2 for small ω. We therefore refer to the model with SFR proportional to the inflow rate as an ω-model. The equilibrium behaviour of the ω-model is very different from the constant inflow regulator. In the ω-model equilibrium can only be reached for SFR $= \varepsilon\ M_g = 0$. Because of its defining assumption, this model implicitly assumes the inflow rate ($\Phi = \omega$ SFR) to be exponentially declining (unless we wish to build a more general model with a different star formation law, i.e. SFR $\neq \varepsilon\ M_g$, which we will not discuss here). In light of the discussion on the cosmological accretion rate in Sec. 1.3.3, this is a much worse parametrisation than the assumption of a constant inflow rate. However, an exponentially declining inflow rate is still a useful model in the context of the overall evolution of galaxies, since it can represent the shutdown of star formation due to a declining inflow rate. This model is therefore similar to the 'strangulation' models used in Peng et al. (2015) to study the build up of the red sequence.

Although the relation between metallicity and gas mass in the ω-model has been widely used in the literature, it is instructive to present here the solutions for the time evolution of this model, which can be found in Table 6.4. We note that, unlike in the constant inflow model, the metallicity in the ω-model does not come to equilibrium on the gas equilibrium timescale defined in Eq. 6.10, but on the dilution timescale $\tau_{dil} \equiv (\varepsilon\,\omega)^{-1} = M_g/\Phi$. Therefore the final relation between metallicity and gas content will depend on combination of the gas equilibrium and the dilution timescales. In particular, by combining the solutions for Z_g and M_g we obtain the well-known relation

$$Z_g = \frac{p}{\omega}\left(1 - \left(\frac{M_g}{M_0}\right)^{\omega/(1-R-\omega+\lambda)}\right), \tag{6.11}$$

and by combing the solution for $M_\star$ and M_g we can eliminate M_0 from the above the re-write the metallicity in the ω-model completely in term of observables.[4]

$$Z_g = \frac{p}{\omega}\left(1 - \left(\frac{M_\star}{M_g}(1 + w) + 1\right)^{-\omega/(1-R-\omega+\lambda)}\right), \tag{6.12}$$

where $w \equiv (\lambda - \omega)/(1 - R)$. As can be explicitly seen from this equation, *the relation between Z_g and gas fraction depends on the inflow rate (through ω), causing the observed degeneracy in the determination of ω and λ when using this model*.

In summary, non-equilibrium models which fix the inflow rate to be proportional to the SFR implicitly assume the inflow rate to be exponentially declining. This is not a good representation of the

[4]Note that there is a +1 missing in the version of Eq. 6.12 which appeared in print in Belfiore et al. (2016). I apologize for this erratum.

Table 6.4: Exact analytical time-dependent solutions of the ideal regulator with inflow rate proportional to the SFR ($\Phi = \omega$ SFR) for different galaxy properties. Note that M_0 below refers to the gas mass at t=0 and τ' is the gas equilibrium timescale defined in Eq. 6.10.

Galaxy property	Exact solution	t = 0	t >> τ'
M_g	$M_0\, e^{-t/\tau'}$	M_0	0
$SFR = \varepsilon\, M_g$	$\varepsilon\, M_0\, e^{-t/\tau'}$	$\varepsilon\, M_0$	0
$M_\star$	$M_0\, \tau'\, \varepsilon\, (1-R)\, (1 - e^{-t/\tau'})$	0	$M_0\, \tau'\, \varepsilon\, (1-R)$
$f_{gas} \equiv \frac{M_g}{M_g + M_\star}$	$\left[1 + \varepsilon\, \tau'\, (1-R)\, (e^{t/\tau'} - 1)\right]^{-1}$	∞	0
$Z_g \equiv M_{Zg}/M_g$	$\frac{p}{\omega}(1 - e^{-\omega\, \varepsilon\, t})$	0	$\frac{p}{\omega}$

cosmological accretion rate for 'main sequence' star forming galaxies, but could constitute a good model for strangulation, as in Peng et al. (2015). Moreover, in this model the relation between the metallicity and the gas fraction depends on both the outflow loading factor and the proportionality factor between inflow rate and SFR (ω), causing a degeneracy between inflows and outflows when interpreting metallicity data.

Chapter 7

Conclusions

Galaxies are not island Universes. The large-scale environment galaxies live in and the balance of heating and cooling processes within their dark matter haloes determine their gas supply. Energetic feedback from supernovae (and possibly supermassive black holes) drives galactic winds, which expel gas from the galaxy disc into the hot halo and the intergalactic medium. Star formation in galaxies appears to be tightly regulated by the cold gas supply. The set of processes responsible for its shutdown, however, have not yet been conclusively identified.

While the early Universe was composed entirely of hydrogen and helium, subsequent generations of stars have been responsible for the production of heavy elements. The current metal abundance and distribution within galaxies reflects both the history of star formation and the role of gas flows. Our theoretical understanding of these processes has significantly increased in the last few decades, with the emergence of new semi-analytical models and hydrodynamical simulations (Somerville & Davé, 2015). These are now capable of following in detail the formation of structure and the assembly of galaxies over cosmological volumes as well as the build-up of the Hubble sequence. These models, however, rely on ad-hoc 'sub-grid' prescriptions for the inclusion of the key processes determining the baryon cycle in galaxies: star formation, outflows and chemical evolution. These sub-grid models require tuning, generally performed by comparing the model universe with observational data.

Since the early 2000s, the general properties of the nearby galaxy population have been investigated by large photometric and spectroscopic surveys, like SDSS. Thanks to these large datasets we have acquired a detailed view of the galaxy stellar mass function, the colour and morphological bimodality of the galaxy population and its relationship with environment, the star formation main sequence and the mass-metallicity relation (Blanton & Moustakas, 2009). These studies, however, have largely considered galaxies as effective 'point sources' because of the lack of spatially-resolved spectral information. With the ever-increasing spatial resolution afforded by numerical models of galaxy evolution, spatially resolved spectroscopic data on a large and representative sample of galaxies in the nearby Universe has the potential of providing new fundamental constraints to directly inform the implementation of feedback and baryon cycling in models.

During the last five years a new generation of IFS surveys of nearby galaxies (CALIFA, Sánchez et al. 2012b, SAMI, Croom et al. 2012, MaNGA, Bundy et al. 2015) has been developed to tackle the challenge of providing spatially resolved spectroscopy for a representative sample of nearby galaxies. These surveys provide a valuable benchmark to compare high-redshift IFS observations, which

will become increasingly common with the next generation of astronomical space- and ground-based facilities (e.g. *JWST*, E-ELT).

7.1 Summary

In this thesis I have focused on two of the key questions that have driven the development of the MaNGA survey: the mapping of star formation and quiescence in galaxies (chapters 3 and 4) and the study of gas phase chemical abundances (chapters 5 and 6). In this section I look back at the aims presented in Sec. 1.5.1 and summarise the main conclusions presented in this thesis.

Where do spatially resolved regions appear on classical BPT diagnostic diagrams, and how applicable are these diagnostics in distinguishing star-forming from quiescent regions? In chapter 3 I have applied classical BPT diagnostics to MaNGA data, and demonstrated the ubiquitous presence of LINER-like emission, both in red-sequence and blue-cloud galaxies. LINER-like ionisation is not only nuclear, but distributed on large (kpc) scales. This observation motivated the relabelling of these regions as 'LIERs' (i.e. dropping the 'N', which stood for 'nuclear', from the historical acronym).

I made use of different lines of evidence to argue against the AGN origin of LIER emission. Instead the analysis in chapter 3 supports the scenario where LIERs are caused by photoionisation from a diffuse ionising background produced by hot evolved (pAGB) stars.

- pAGB stars have been shown to produce the required hard ionising spectrum necessary to excite LIER emission. Stellar evolution models including the pAGB phase demonstrate that the pAGB hypothesis is energetically viable for virtually all LIERs, as the observed EW(Hα) lie in the same range as model predictions (0.5 - 3.0 Å).

- In LIER galaxies not contaminated by star formation, line ratios sensitive to the ionisation parameter ([OIII]λ5007/[OII]λ3727 and partially [OIII]λ5007/Hβ) show flat or very shallow profiles over radial scales of tens of kpc, at odds with the steeper profiles predicted in the AGN scenario.

- The distribution of EW(Hα) in LIERs is flat as a function of galactocentric radius and presents a remarkably small scatter, as expected in the case of nebular lines being excited locally by hot evolved stars associated with the old stellar population. On the other hand, in the AGN scenario, a large scatter is expected in the EW(Hα) distribution, as line and stellar continuum emission would originate from independent sources.

In addition to the above, LIER emission is also found in extra-planar and inter-arm regions of star forming galaxies. This emission can be identified as DIG, an ionised gas component observed in both the Milky Way and other nearby external galaxies. The source of ionisation of the diffuse ionised gas is still unclear, however it is likely that escaping hardened radiation from star forming regions contributes to the ionisation budget. This hypothesis is consistent with the fact that LIER emission in SF galaxies (i.e. DIG) lies close to the star formation-LIER demarcation line in the BPT diagram, implying a softer ionisation field that in true LIER galaxies, and a higher Hα equivalent width, supporting ionisation from a non-local source.

How may we define 'quiescence' using spatially resolved spectroscopic data? How are quiescent regions distributed in galaxies? The realisation that LIER emission is due to old stellar populations, and is not a signature of AGN activity, has led me to reconsider the definition of quiescence in galaxies. In particular, since pAGB stars are the main sources of ionising photons after O- and B-type stars die, LIER and line-less regions both ought to be considered quiescent in terms of absence of current star formation. This inference is reinforced by the fact that LIER emission is strongly correlated with the absence of young stellar populations, as traced by stellar indices like $D_N(4000)$ and $H\delta_A$.

The study of a large sample of galaxies with resolved spectroscopy in chapter 3 reveals that galaxies display remarkably consistent excitation 'morphologies' on kpc scales. To highlight this fact, I proposed a new classification of galaxies based on their emission-line properties.

1. *Line-less galaxies*: No detected line emission (EW(Hα) < 1.0 Å within 1.0 R_e).
2. *Extended LIER galaxies (eLIER)*: galaxies dominated by LIER emission at all radii where emission lines are detected. No evidence for any star forming regions.
3. *Central LIER galaxies (cLIER)*: galaxies where LIER emission is resolved but spatially located in the central regions, while ionisation from star formation dominates at larger galactocentric distances.
4. *Star forming galaxies (SF)*: galaxies dominated by star formation in the central regions and at all radii within the galaxy disc. LIER emission in these galaxies is sometimes observed in edge-on systems at large distances from the disc midplane and/or in inter-arm regions.

Does the presence of a large number of quiescent regions correlate with other fundamental galaxy properties, such as stellar mass, SFR, colour, bulge-to-disc ratio? In chapter 4 I studied the new classification scheme for galaxies (SF, cLIER, eLIER and line-less), which focuses on the increasing importance of quiescent regions, within the context of the evolving galaxy population. To do so, I analysed the integrated colours, SFR, morphology and kinematics of the different classes of galaxies. cLIER galaxies are found to lie between the red sequence and the blue cloud in a number of fundamental galaxy properties:

- Stellar populations: cLIERs span a wide range of stellar ages, with old central LIER regions and outer regions characterised by young stellar populations.
- Colours and SFR: cLIERs lie preferentially in and around the green valley in UV-optical colours, although they appear increasingly consistent with the red sequence using optical colours alone ($u - r$ or $g - r$). In the SFR-$M_\star$ diagram cLIERs lie 0.8 dex below the main sequence of star forming galaxies, albeit with a large scatter.
- Morphology: cLIER galaxies are visually classified as disc galaxies, but have a larger bulge fraction than star forming galaxies of the same mass.
- Kinematics: cLIERs display regular disc-like kinematics in both gas and stars, which are mutually aligned.
- Environment: cLIERs live in slightly denser environments than SF galaxies for $\log(M_\star/M_\odot) = 10.5 - 11.5$, but have the same satellite fraction.

The inside-out quenching pattern in cLIERs is consistent with both gas exhaustion and/or a decrease in the star formation efficiency. In either case, the presence of a bulge is closely connected to the lack of central star formation in these galaxies. The fact that cLIER galaxies generally have larger bulges than their star forming counterparts may imply that they host more massive black holes, thus pointing towards the importance of AGN heating in explaining the intermediate properties of these galaxies. The star forming disc is the likely source of the LIER-emitting gas present in the central regions.

How widespread is line emission on the red sequence and what powers the observed emission? In chapter 4 I compared the properties of red sequence galaxies that host line emission (eLIERs) to those that do not (line-less). Below I highlight some similarities and differences in their fundamental properties.

- Stellar populations: eLIERs host old stellar populations, indistinguishable from those of line-less galaxies.
- Colours and SFR: eLIERs lie on the red sequence in colour-magnitude diagrams, with only a small contamination to the green valley.
- Morphology: eLIER galaxies are visually classified as early-type galaxies and have similar morphologies to those of line-less galaxies of the same stellar mass.
- Kinematics: eLIERs display a variety of gas kinematics, but generally present well-defined rotation/flows on kpc scales. The velocity field of gas and stars are often misaligned ($65 \pm 7\%$ of eLIERs are misaligned by more than $30°$).
- Environment: eLIERs live in less dense environments than line-less galaxies of the same mass. At the high-mass end, line-less galaxies are mostly centrals in high-mass haloes, while at the low-mass end line-less galaxies are mostly satellites.

eLIERs are red sequence galaxies with residual cold gas, acquired mostly via external sources. While this gas does not form stars, it is illuminated by the diffuse ionisation field from hot old stars and shines as a LIER. LIER emission is suppressed in high-density environments, likely because of lack of gas, which has either been consumed due to the shut down of inflows or otherwise heated and/or tidally stripped by the hot halo gas.

How does the metallicity radial gradient change as a function of mass and other fundamental galaxy properties (such as bulge-to-disc ratio, SFR)? In chapter 5 I investigated the gas phase metallicity and nitrogen abundance gradients for a sample of 550 MaNGA galaxies, spanning the stellar mass range $10^9 - 10^{11.5}$ $M_\odot$. I summarise the main findings below.

- The metallicity gradient (measured in the range 0.5 - 2.0 R_e) is flat for low mass galaxies ($M_\star < 10^{9.0}$ $M_\odot$), steepens for more massive galaxies until $M_\star \sim 10^{10.5}$ $M_\odot$ and then flattens slightly for even more massive systems. This behaviour is confirmed when using the disc-only effective radius as a radial scale length, and is robust to the effects of resolution and to the choice of metallicity calibration.

- The most massive galaxies (M$\sim 10^{11}$ $M_{\odot}$) are characterised by a a flattening of the metallicity gradient in the central (R < 1.0 R_e) regions.
- I find a secondary dependance of the metallicity gradient on concentration and sSFR for galaxies of high concentration (C> 2.6) and low sSFR (log(sSFR) < -1.5 Gyr^{-1}), in the sense that galaxies of higher concentration and lower sSFR have flatter gradients than expected from their stellar mass.

Can chemical abundances at large galacotcentric radii (R> 2.0 R_e) provide evidence for direct accretion of pristine gas or metal transport via galactic fountains? Using data from SDSS-IV MaNGA, I demonstrated in chapter 5 that mild flattening of the metallicity gradient is observed for R>2 R_e, especially evident in stacked profiles of galaxies with masses > 10^{10} $M_{\odot}$. Such a flattening at large radii is also observed in stacked profiles of the N/O ratio profile. These finding supports a scenario of wind recycling, in which the outer galactic disc is enriched by metals ejected from the central region.

Moreover, in chapter 6 I make use of IFS and cold gas data for a nearby galaxy (NGC 628) and carry out detailed chemical evolution modelling. Evidence from recent measurements of outlying HII regions in NGC 628 from Berg et al. (2015) (out to 10 kpc) confirms that regions in the outer disc have retained a higher fraction of the metals they have produced with respect to regions at smaller galactocentric radii. In particular, regions at around 10 kpc have retained $\sim$ 80-100 % of the metals produced there. Since some metals must have been lost via outflows, it is likely that the inner disc has been the source of some fraction of the metals observed.

Using the large MaNGA DR13 sample, I find no evidence for the sharp drops in metallicity founds in Moran et al. (2012), and thus no evidence for the direct accretion of pristine gas.

When appropriate knowledge of the gas content of galaxies is available, can the observed gas phase abundance gradient be used to constrain the importance of gas flows (inflows and outflows) over the history of a galaxy? In chapter 6 I have presented a detailed study of the metal content and distribution in the nearby disc galaxy NGC 628. I have mapped the gas phase metallicity by exploiting the largest integral field spectroscopy mosaic available to date. This data was complemented with the stellar metallicity radial profile presented in previous work (Sánchez-Blázquez et al., 2014), the stellar mass surface density distribution, inferred from extensive multi-band photometry, and the observed gas surface density, inferred from HI and CO maps.

By comparing the mass of metals observed in the gaseous and stellar components with the mass of metals produced by stars in the same region I have obtained a spatially resolved metal budget as function of galactocentric radius. Cumulatively, out to a radius of 7 kpc, 45%–50% of the *total* amount of metals produced have been lost by the galaxy. The fraction of metals lost is higher ($\sim$70%) in the central region, which is dominated by the bulge. The fraction of metals lost is also found to decrease for large galactocentric radii.

I have used simple analytical prescriptions ('bathtub' and 'gas regulatory' models), including gas inflow and outflow, to model the data. For models with a constant inflow rate the relation between the metals-to-stellar mass ratio (M_Z/M_{star}) and gas fraction (f_{gas}) is independent of the inflow rate and of the efficiency of star formation, and depends only on the outflow loading factor. I find that an outflow loading factor $\lambda \approx 1$ can explain the data at most radii, though with large scatter ($0.5 < \lambda < 2$).

Can abundance ratios of chemical elements with different nucleosynthetic origin be used to shed light on the star formation and gas flow history of galaxies? In chapter 5 I presented a study of the N/O ratio in a large sample of MaNGA galaxies. The gradient of the N/O abundance ratio shows a steepening as a function of galaxy mass over the whole mass range considered, and is steeper than the O/H profile, as expected from the delayed release of nitrogen into the ISM with respect to oxygen.

The position of resolved galactic regions in the N/O versus O/H plane has been studied, demonstrating that spatially resolved regions follow the expected relation between N/O and O/H. The scatter in this relation is found to depend on galactocentric radius. At fixed O/H, outer regions of massive discs have higher nitrogen abundance N/O than the central region of low mass galaxies. Wind recycling and lower SFE in combination may explain the observed trend.

7.2 Future work

Our understanding of the power source of DIG, which is observed as a low surface brightness diffuse LIER emission in MaNGA star-forming galaxies, is still limited. Making use of the MaNGA data, in Zhang et al. (2017) we have argued that within star forming galaxies, diagnostic line ratio change systematically as a function of Hα surface brightness, even at fixed radius/metallicity. We have modelled these line ratios in terms of both leaky HII regions and hot evolved stars, and conclude that a contribution from hot evolved stars is necessary in order to reproduce the observed line ratios. In the future, a better modelling of the DIG may allow its physical properties (temperature, density, chemical abundances) to be recovered and studied in more detail. A differential study of the ionisation conditions between DIG found in star forming galaxies (where leakage from HII regions may play a role) and LIER emission in eLIERs (which host no star formation) would provide important indications on the relative importance of leaky HII regions and hot evolved stars in powering the diffuse line emission.

The effect of DIG contamination on the chemical abundances measured by an IFS survey like MaNGA on kpc scales remains difficult to quantify. Ad-hoc high-resolution hydrodynamical simulations could be used to gain further insight into this problem. Model galaxies can by processed through an 'observation simulator', in order to produce mock datacubes and other high-level products and quantify the impact of various observational effects, like beam smearing, on the derived properties (Guidi et al., 2016, e.g.). This approach is currently being actively pursued by the MaNGA collaboration.

IFS observations of a small sample of nearby galaxies at higher spatial resolution ($\sim$ 10-100 pc) would allow the study of the inter-arm DIG in more detail by reducing the contamination due to the bright nearby star forming regions. The value of these observations would also be considerable for understanding the effect of spatial resolution in larger datasets like MaNGA. Moreover, a large amount of effort has already been invested by the astronomical community to build a comprehensive multi-wavelength (from the UV to the far-IR) view of nearby galaxies. By choosing targets with comprehensive observations of other phases of the ISM, like atomic and molecular gas and dust, IFS observations would provide the logical next step in our study of the multi-phase ISM, and its role in the star formation process. Suitable datasets will soon be available from the next-generation wide-field IFUs on 8m-class telescopes, like MUSE (Bacon et al., 2010) and KCWI (Martin et al., 2010). Even more ambitious plans to systematically map the ISM of nearby galaxies at $\sim$ pc resolution are currently being developed by the SDSS collaboration for the 2020 horizon.

The relationship between the cold phase of the ISM and star formation has been investigated in detail for nearby galaxies samples on kpc scales (Leroy et al., 2008; Walter et al., 2008; Leroy et al., 2012). These samples, however, have not been selected to be representative of the overall population of star forming galaxies. Moreover, green valley objects have not yet been subject of a similarly thorough investigation. I have demonstrated in this thesis that a large fraction of the galaxies in the green valley are cLIERs: their central regions host old stellar populations and no current star formation. Observations of cold gas in these systems would help to understand whether the absence of star formation is due to low star formation efficiency or to the genuine absence of cold gas. These two scenarios would imply different physical mechanisms as the drivers of the quenching process. Unfortunately, mapping atomic gas via the 21 cm line in a large sample of MaNGA galaxies is a prohibitively expensive enterprise using current-generation radio interferometers like the JVLA. On the other hand, observations of the molecular gas component, probed by the CO(1-0) line, can be accomplished with modest integration times using interferometers like ALMA and NOEMA. We have already obtained matched-resolution ALMA data for three MaNGA galaxies in the green valley (PI: L. Lin), and we plan to expand this observing campaign to larger samples in the future.

With regards to the study of chemical abundances, a robust characterisation of the time evolution of the metallicity gradient, using both models and observations, constitutes a promising avenue for future work. Observationally, the study of metallicity gradients at high redshift will be revolutionised by the spectroscopic abilities of the NIRSPEC instrument on *JWST* (Ferruit et al., 2012). More detailed models, both hydrodynamical simulations and numerical studies focused on chemical evolution, are also urgently needed in order to be able to correctly interpret the wide range of abundance data delivered by current surveys. In particular, the adaptation of the 'bath-tub' equilibrium models to resolved regions in galaxies and the study of metallicity gradients would have interesting implications. In the spirit of 'bath-tub' models, such framework would be useful to interpret the observed correlations between the mass surface density and the surface density of star formation (Cano-Díaz et al., 2016) and metallicity (Barrera-Ballesteros et al., 2016) observed on kpc scales, which mimic the well-known scaling relations (star formation main sequence and mass-metallicity relation) observed for the integrated properties of galaxies.

Finally, the observational study of star formation and chemical abundances in the outer discs of galaxies is crucial to understanding the processes that drive disc assembly and the flow and redistribution of metals in galaxies. The MaNGA survey is designed to cover galaxies to 2.5 R_e but only provides limited statistics for larger radii. I have successfully proposed for MUSE data in order to extend the study of chemical abundances of nearby galaxies to larger radii than those probed by MaNGA. These observations confirm, with higher sensitivity and spatial resolution, the flattening of the metallicity gradient for radii $\sim$ 2.5 R_e. A direct comparison with predictions from high resolution hydrodynamical simulations would be advantageous in order to shed light on the origin of the metals observed at these large radii.

Acknowledgements

I thank Roberto Maiolino for his support, enthusiasm and generosity. In his role as my PhD advisor, Roberto has offered me opportunities and challenges, together with the freedom to pursue my own ideas and interests. I will miss his open-door policy, his phenomenal expertise in every aspect of astrophysics, his contagious enthusiasm for new data and projects and his precious guidance.

It has been a great pleasure to be part of Roberto's ever-evolving group. For all the coffee and lunchtime breaks we have shared, the discussions about science and life and for your friendship, I want to thank Claudia Cicone, Sara Cazzoli, Stefano Carniani, Rebecca Williams, Michele Ginolfi, Andrea Pallottini, Matt Bothwell, Yingjie Peng, Bethan James and Robert Gallagher.

Only one bridge away from the Institute of Astronomy on one side, and the new home of the Cavendish Astrophysics group on the other, it has been a great pleasure to be a student in the Kavli Institute for Cosmology. I have benefited enormously from members of both departments, from their guidance, expertise and friendship. Special thanks to Matt Auger, Max Pettini, Rob Kennicutt, Davide Fiacconi, Sonke Hee, Do Young Kim and Méderic Boquien. I also wish to offer my thanks to the administrators of the Battcock Centre and the Kavli Insitute for Cosmology for their fundamental role in making my experience in our departments such a positive one: Karen, Adeline, Paula and Sandra, thank you for all your help! I thank both departments, the Cavendish Astrophysics and the Institute of Astronomy, for their support. I look forward to a future where current divisions between the two communities, originally separated by the imponderable width of Madingley Road, will finally be just history.

During my time as a PhD student I have had the fortune to meet many colleagues and collaborators from within the wider astronomical community. I wish to thank Giovanni Cresci, Filippo Mannucci and Alessandro Marconi for their visits and their kind invitation to the Astronomical Observatory in Arcetri. I also wish to present a very special thanks to Fiorenzo Vincenzo, and his supervisor Francesca Matteucci, for our long-standing collaboration and friendship.

Looking back at the last three and a half years, I cannot imagine my PhD without my involvement in SDSS. The aspect of my graduate studies which I enjoyed the most was being part of such an open-minded and supportive international collaboration. Through my involvement in MaNGA and SDSS I have met inspiring people, I have seen corners of the world I would not have imagined to explore, I have learnt about spectroscopy, galaxies, how to chair a telecon or a conference session, how to code a pipeline and, I hope, a little bit about how to be a supportive yet critical colleague. I wish to thank the people who have helped me in this journey: Kevin Bundy, Renbin Yan, Anne-Marie Wejmans, Christy Tremonti, Kyle Westfall, Matt Bershady, Eric Emsellem, Michele Cappellari, Daniel Thomas,

Claudia Maraston, David Law, Karen Masters, Brian Cherinka, José Sanchez-Gallego, Kate Rubin, David Wake, Alfonso Aragón-Salamanca, Daniel Goddard, David Wilkinson, Edmund Cheung, Song Huang, Nell Byler, Sebastian Sánchez, Mike Blanton and Jennifer Johnston.

From my first MaNGA meeting in Portsmouth to the successful MaNGA school in Shanghai I have had the pleasure to see the survey grow, develop and flourish. My PhD would not have been possible without the colossal efforts of the MaNGA team to make the survey work and the fundamental contributions of the observing staff at Apache Point Observatory. For this reason, I consider it a duty to include a formal acknowledgement to the institutions that have made such a large enterprise as SDSS possible over the years.

> Funding for SDSS-I-II and SDSS-IV has been provided by the Alfred P. Sloan Foundation and Participating Institutions. Additional funding for SDSS-II comes the National Science Foundation, the U.S. Department of Energy, the National Aeronautics and Space Administration, the Japanese Monbukagakusho, the Max Planck Society, and the Higher Education Funding Council for England. Additional funding towards SDSS-IV has been provided by the U.S. Department of Energy Office of Science. SDSS-IV acknowledges support and resources from the Centre for High-Performance Computing at the University of Utah. The SDSS web site is `www.sdss.org`.
>
> The participating Institution in SDSS-II include the American Museum of Natural History, Astrophysical Institute Potsdam, University of Basel, University of Cambridge, Case Western Reserve University, University of Chicago, Drexel University, Fermilab, the Institute for Advanced Study, the Japan Participation Group, Johns Hopkins University, the Joint Institute for Nuclear Astrophysics, the Kavli Institute for Particle Astrophysics and Cosmology, the Korean Scientist Group, the Chinese Academy of Sciences (LAMOST), Los Alamos National Laboratory, Max-Planck-Institut für Astronomie (MPIA Heidelberg), Max-Planck-Institut für Astrophysik (MPA Garching), New Mexico State University, Ohio State University, University of Pittsburgh, University of Portsmouth, Princeton University, the United States Naval Observatory, and the University of Washington.
>
> SDSS-IV is managed by the Astrophysical Research Consortium for the Participating Institutions of the SDSS Collaboration including the Brazilian Participation Group, the Carnegie Institution for Science, Carnegie Mellon University, the Chilean Participation Group, the French Participation Group, Harvard-Smithsonian Center for Astrophysics, Instituto de Astrofísica de Canarias, The Johns Hopkins University, Kavli Institute for the Physics and Mathematics of the Universe (IPMU) / University of Tokyo, Lawrence Berkeley National Laboratory, Leibniz Institut für Astrophysik Potsdam (AIP), Max-Planck-Institut für Astronomie (MPIA Heidelberg), Max-Planck-Institut für Astrophysik (MPA Garching), Max-Planck-Institut für Extraterrestrische Physik (MPE), National Astronomical Observatory of China, New Mexico State University, New York University, University of Notre Dame, Observatário Nacional / MCTI, The Ohio State University, Pennsylvania State University, Shanghai Astronomical Observatory, United Kingdom Participation Group, Universidad Nacional Autónoma de México, University of Arizona, University of Colorado Boulder, University of Oxford, University of Portsmouth, University of Utah, University of Virginia, University of Washington, University of Wisconsin, Vanderbilt University, and Yale University.

I especially wish to thank Kevin Bundy, Mike Blanton, Jennifer Johnston and Karen Masters for leading MaNGA and SDSS in such a professional and successful manner and for doing so much to make SDSS an inclusive collaboration.

I wish to offer a further acknowledgement to Kevin Bundy for inviting me to the spectral fitting workshop at Tokyo IMPU and for the invitation to a special tofu-based dinner. I also acknowledge Sebastian Sánchez for his invitation to visit UNAM in Mexico City in the near future. I hope I will be able to take advantage of this kind invite once I am done with writing my thesis!

My PhD has not only been a journey into astronomy, but also, and perhaps more importantly, one of professional and personal change. The transition from undergraduate to graduate studies has also lead me to see the world, with its complexity and interdependencies, under a new light and has encouraged me reflect on my role as a scientist within our society.

I am writing this section the day after having listened to two strongly antithetic speeches. One was given by the now 45th president of the United States at his inauguration ceremony, and the other one by Chris Dobson, Master of St. John's College, at the annual dinner dedicated to Johnian graduate students. Needless to say, I very much subscribe to the vision of the world outlined in the second. My experience as graduate student has lead me to believe in the academic endeavour as a force to unite nations, cross borders and build bridges through the sharing of ideas.

I wish to acknowledge my host country, the UK, its research councils and tax payers for funding my PhD, and its people for providing me with such an exceptional place to live and work for the last seven and a half years. I thank the University of Cambridge and St. John's College for having nourished me, physically and intellectually, for a grand total of 23 Full Terms. A special thanks to the fellows of my College who helped me learn and grow since my undergraduate year: Paul Wood, Dr. Hughes, Ms. Tomaselli, Mete Atatüre and Pat Boyde.

Over the years, I have had the fortune to meet many people who have transformed this lovely town on the shores of the Cam into a very special place. Olga Vinnichenko, Germaine Liu, Jasmine Wall, Alison Joseph, Maddy Lawrence-Jones, Svetlana Smirnova, Amar Shah, Jenny Green, Aleksander Makal, Wojtek and Tomek Cymes, Ada Mao, Kotryna Bloznelyte: Cambridge would not been the same without you!

Cambridge is a place for storytelling, as one can infer from listening to the punters of the river Cam or to the ghost stories, told annually in the Senior Combination Room of my College. My favourite Cambridge story, however, is that of two freshers, meeting in a pub during Fresher's Week, seven and a half years ago. Thank you, meine liebste Ricarda, for being part of the story of my life ever since. I look forward to writing many more chapters by your side.

I want to conclude with a heartfelt thanks to my family, my brothers and my parents. Grazie per avere sempre creduto in me.

Bibliography

Abazajian K. N., et al., 2009, ApJS, 182, 543
Abdo A. A., et al., 2010, ApJ, 710, 133
Alatalo K., et al., 2016, ApJS, 224, 38
Albareti F. D., et al., 2016, arXiv:1608.02013v1
Allen M., Groves B., Dopita M., Sutherland R., Kewley L., 2008, ApJs, 178, 20
Alloin D., Collin-Souffrin S., Joly M., Vigroux L., 1979, A&A, 78, 200
Alonso-Herrero A., García-Marín M., Rodríguez Zaurín J., Monreal-Ibero A., Colina L., Arribas S., 2010, A&A, 522, A7
Andrews B. H., Martini P., 2013, ApJ, 765, 140
Aniano G., Draine B. T., Gordon K. D., Sandstrom K., 2011, PASP, 123, 1218
Annibali F., Bressan A., Rampazzo R., Zeilinger W. W., Vega O., Panuzzo P., 2010, A&A, 519, A40
Armillotta L., Fraternali F., Marinacci F., 2016, MNRAS, 462, 4157
Arnaud K. A., et al., 1994, ApJ, 436, L67
Asari N. V., Cid Fernandes R., Stasińska G., Torres-Papaqui J. P., Mateus A., Sodre L., Schoenell W., Gomes J. M., 2007, MNRAS, 381, 263
Asari N. V., Stasinska G., Morisset C., Cid Fernandes R., 2016, MNRAS, 460, 1739
Ascasibar Y., Gavilán M., Pinto N., Casado J., Rosales F., Díaz a. I., 2014, MNRAS, 448, 2126
Asplund M., Grevesse N., Sauval a. J., Scott P., 2009, ARA&A, 47, 481
Bacon R., et al., 2010, Proc. SPIE, 7735, 773508
Baldry I. K., Glazebrook K., Brinkmann J., Ivezic Z., Lupton R. H., Nichol R. C., Szalay A. S., 2004, ApJ, 600, 681
Baldry I. K., Balogh M. L., Bower R. G., Glazebrook K., Nichol R. C., Bamford S. P., Budavari T., 2006, MNRAS, 373, 469
Baldwin J. A., Phillips M. M., Terlevich R., 1981, PASP, 93, 5
Balogh M. L., Morris S. L., Yee H. K. C., Carlberg R. G., Ellingson E., 1999, ApJ, 527, 54
Balogh M. L., Baldry I. K., Nichol R. C., Miller C., R B., Glazebrook K., 2004, ApJ, 615, L101
Bamford S. P., et al., 2009, MNRAS, 393, 1324
Barrera-Ballesteros J. K., et al., 2016, MNRAS, 463, 2513
Beers T. C., Flynn K., Gebhardt K., 1990, AJ, 100, 32
Behroozi P. S., Conroy C., Wechsler R. H., 2010, ApJ, 717, 379
Belfiore F., et al., 2015, MNRAS, 449, 867
Belfiore F., Maiolino R., Bothwell M., 2016, MNRAS, 455, 1218
Bell E. F., de Jong R. S., 2000, MNRAS, 312, 497
Bell E. F., McIntosh D. H., Katz N., Weinberg M. D., 2003, ApJS, 149, 289
Bell E. F., et al., 2004, ApJ, 608, 752
Bell E. F., et al., 2005, ApJ, 625, 23
Bell E. F., et al., 2012, ApJ, 753, 167
Belley J., Roy J.-R., 1992, ApJS, 78, 61
Benson A. J., Frenk C. S., Lacey C. G., Baugh C. M., Cole S., 2002, MNRAS, 333, 177
Berg D. A., et al., 2012, ApJ, 754, 98
Berg D. A., Skillman E. D., Croxall K. V., Pogge R. W., Moustakas J., Johnson-Groh M., 2015, ApJ, 806, 16

Bernardi M., et al., 2003, AJ, 125, 1882
Bershady M. A., Verheijen M. A. W., Swaters R. A., Andersen D. R., Westfall K. B., Martinsson T., 2010, ApJ, 716, 198
Bertola F., Corsini E. M., Vega Beltran J. C., Pizzella A., Sarzi M., Cappellari M., J. G. Funes S., 1999, ApJ, 519, L127
Bigiel F., Leroy A., Walter F., Brinks E., de Blok W. J. G., Madore B., Thornley M. D., 2008, AJ, 136, 2846
Bigiel F., Walter F., Blitz L., Brinks E., de Blok W. J. G., Madore B., 2010, AJ, 140, 1194
Binette L., Magris C. G., Stasińska G., Bruzual A. G., 1994, A&A, 292, 13
Binette L., Matadamas R., Hägele G. F., Nicholls D. C., Magris G. C., 2012, A&A, 547, A29
Binney J., 1977, ApJ, 215, 483
Birnboim Y., Dekel A., 2003, MNRAS, 345, 349
Blanc G. A., Heiderman A., Gebhardt K., Evans N. J., Adams J., 2009, ApJ, 704, 842
Blanc G. A., et al., 2013a, AJ, 145, 138
Blanc G. A., et al., 2013b, ApJ, 764, 117
Blanc G. A., Kewley L., Vogt F. P. A., Dopita M. A., 2015, ApJ, 798, 99
Bland-Hawthorn J., et al., 2010, Proc. SPIE, 7735, 773541
Blanton M. R., Moustakas J., 2009, ARA&A, 47, 159
Blanton M. R., Roweis S., 2007, AJ, 133, 734
Blanton M. R., et al., 2003a, ApJ, 592, 819
Blanton M. R., et al., 2003b, ApJ, 594, 186
Blanton M. R., et al., 2005a, AJ, 129, 2562
Blanton M. R., Eisenstein D., Hogg D. W., Schlegel D. J., Brinkmann J., 2005b, ApJ, 629, 143
Blanton M. R., Kazin E., Muna D., Weaver B. A., Price-Whelan A., 2011, AJ, 142, 31
Bluck A. F. L., Mendel J. T., Ellison S. L., Moreno J., Simard L., Patton D. R., Starkenburg E., 2014, MNRAS, 441, 599
Boissier S., Prantzos N., 1999, MNRAS, 307, 857
Bolatto A. D., Leroy A. K., Rosolowsky E., Walter F., Blitz L., 2008, ApJ, 686, 948
Bolatto A. D., Wolfire M., Leroy A. K., 2013, ARA&A, 51, 207
Boquien M., et al., 2012, A&A, 539, A145
Boselli A., Cortese L., Boquien M., 2014, A&A, 564, A65
Bothwell M. S., Maiolino R., Kennicutt R. C., Cresci G., Mannucci F., Marconi A., Cicone C., 2013, MNRAS, 433, 1425
Bothwell M. S., Maiolino R., Peng Y., Cicone C., Griffith H., Wagg J., 2015, MNRAS, 455, 1156
Bothwell M. S., Maiolino R., Cicone C., Peng Y., Wagg J., 2016, A&A, 595, A48
Bouché N., Lehnert M. D., Aguirre A., Peroux C., Bergeron J., 2007, MNRAS, 378, 525
Bouché N., et al., 2010, ApJ, 718, 1001
Bovy J., Rix H.-W., 2013, ApJ, 779, 115
Bregman J. N., Miller E. D., Seitzer P., Cowley C. R., Miller M. J., 2013, ApJ, 766, 57
Bresolin F., Schaerer D., González Delgado R. M., Stasinska G., 2005, A&A, 441, 981
Bresolin F., Ryan-Weber E., Kennicutt R. C., Goddard Q., 2009, ApJ, 695, 580
Bresolin F., Kennicutt R. C., Ryan-Weber E., 2012, ApJ, 750, 122
Brinchmann J., Charlot S., White S. D. M., Tremonti C., Kauffmann G., Heckman T., Brinkmann J., 2004, MNRAS, 351, 1151
Bromm V., Larson R., 2004, ARA&A, 42, 79
Brook C. B., Stinson G., Gibson B. K., Roškar R., Wadsley J., Quinn T., 2012, MNRAS, 419, 771
Brown T., Ferguson H., Stanford S., Deharveng J.-M., 1998, ApJ, 504, 113
Brown T. M., Smith E., Ferguson H. C., Sweigart A. V., Kimble R. A., Bowers C. W., 2008, ApJ, 682, 319
Bruzual G., Charlot S., 1993, ApJ, 405, 538
Bruzual G., Charlot S., 2003, MNRAS, 344, 1000
Bryant J. J., O'Byrne J. W., Bland-Hawthorn J., Leon-Saval S. G., 2011, MNRAS, 415, 2173
Bundy K., et al., 2006, ApJ, 651, 120
Bundy K., et al., 2010, ApJS, 719, 1969
Bundy K., et al., 2015, ApJ, 798, 7
Burgarella D., Buat V., Iglesias-Páramo J., 2005, MNRAS, 360, 1413
Buzzoni A., Arnaboldi M., Corradi R. L. M., 2006, MNRAS, 368, 877
Byler N., Dalcanton J. J., Conroy C., Johnson B. D., 2016, ArXiv:1611.08305v1
Calzetti D., 2001, PASP, 113, 1449

Calzetti D., Kinney A. L., Storchi-Bergmann T., 1994, ApJ, 429, 582
Calzetti D., Armus L., Bohlin R. C., Kinney A. L., Koornneef J., Storchi-Bergmann T., 2000, ApJ, 533, 682
Cano-Díaz M., et al., 2016, ApJ, 821, L26
Cappellari M., 2016, ARA&A, 54, 1
Cappellari M., Copin Y., 2003, MNRAS, 342, 345
Cappellari M., Emsellem E., 2004, PASP, 116, 138
Cappellari M., et al., 2011a, MNRAS, 413, 813
Cappellari M., et al., 2011b, MNRAS, 416, 1680
Cappellari M., et al., 2013, MNRAS, 432, 1862
Cardelli J. A., Clayton G. C., Mathis J. S., 1989, ApJ, 345, 245
Carniani S., et al., 2015, A&A, 580, A102
Cecil G., et al., 2000, ApJ, 536, 675
Chabrier G., 2003, PASP, 115, 763
Cheung E., et al., 2012, ApJ, 760, 131
Cheung E., et al., 2013, ApJ, 779, 162
Cheung E., et al., 2016, Nature, 533, 504
Chiappini C., Matteucci F., Romano D., 2001, ApJ, 20, 41
Chiosi C., 1980, A&A, 83, 206
Choi E., Naab T., Ostriker J. P., Johansson P. H., Moster B. P., 2014, MNRAS, 442, 440
Christensen C. R., Davé R., Governato F., Pontzen A., Brooks A., Munshi F., Quinn T., Wadsley J., 2016, ApJ, 824, 57
Chung A., van Gorkom J. H., Kenney J. D. P., Crowl H., Vollmer B., 2009, AJ, 138, 1741
Ciardullo R., Rubin V., Jacoby G., Ford H., Kent Ford W., 1988, AJ, 95, 438
Cicone C., et al., 2014, A&A, 562, A21
Cicone C., et al., 2015, A&A, 574, A14
Cid Fernandes R., Stasińska G., Schlickmann M. S., Mateus A., Asari V. N., Schoenell W., Sodré L., 2010, MNRAS, 403, 1036
Cid Fernandes R., Stasińska G., Mateus A., Vale Asari N., 2011, MNRAS, 413, 1687
Cid Fernandes R., et al., 2014, A&A, 561, A130
Ciotti L., Ostriker J. P., 2007, ApJ, 665, 1038
Ciotti L., et al., 1991, ApJ, 376, 380
Coccato L., Gerhard O., Arnaboldi M., Ventimiglia G., 2011, A&A, 138, 8
Colavitti E., Cescutti G., Matteucci F., Murante G., 2009, A&A, 496, 429
Colless M., et al., 2001, MNRAS, 328, 1039
Conroy C., 2013, ARA&A, 51, 393
Conroy C., Gunn J. E., White M., 2009, ApJ, 699, 486
Cortese L., Catinella B., Boissier S., Boselli A., Heinis S., 2011, MNRAS, 415, 1797
Cox D. P., 2005, ARA&A, 43, 337
Croom S. M., et al., 2012, MNRAS, 421, 872
Curti M., Cresci G., Mannucci F., Marconi A., Maiolino R., Esposito S., 2017, MNRAS, 465, 1384
Daddi E., et al., 2007, ApJ, 670, 156
Danforth C. W., Shull J. M., 2005, ApJ, 624, 555
Davé R., Finlator K., Oppenheimer B. D., 2011, MNRAS, 421, 98
Davies R. L., Kewley L. J., Ho I.-T., Dopita M. A., 2014, MNRAS, 444, 3961
Davis T. A., Bureau M., 2016, MNRAS, 457, 272
Davis T. A., et al., 2011, MNRAS, 417, 882
Davis T. A., et al., 2014, MNRAS, 444, 3427
Dawson K. S., et al., 2013, AJ, 145, 10
Dayal P., Ferrara A., Dunlop J. S., 2013, MNRAS, 430, 2891
De Lucia G., Fontanot F., Wilman D., Monaco P., 2011, MNRAS, 414, 1439
Dehnen W., 1993, MNRAS, 265, 250
Dekel A., Silk J., 1986, ApJ, 303, 39
Dekel A., Zolotov A., Tweed D., Cacciato M., Ceverino D., Primack J. R., 2013, MNRAS, 435, 999
Diaz A. I., Castellanos M., Terlevich E., Luisa Garcia-Vargas M., 2000, MNRAS, 318, 462

Dopita M. A., Sutherland R. S., 1995, ApJ, p. 468
Dopita M. A., Groves B. A., Sutherland R. S., Binette L., Cecil G., 2002, ApJ, 572, 753
Dopita M. A., Sutherland R. S., Nicholls D. C., Kewley L. J., Vogt F. P. A., 2013, ApJS, 208, 10
Dopita M. A., et al., 2015, ApJ, 801, 42
Draine B. T. T., 2003, ARA&A, 41, 241
Draine B. T. T., 2011, The physics of the insterstellar and intergalactic medium. Princeton University Press
Dressler a., 1980, ApJ, 236, 351
Drory N., et al., 2015, AJ, 149, 77
Edmunds M. G., 1990, MNRAS, 246, 678
Edmunds M. G., Pagel B. E. J., 1978, MNRAS, 185, 77
Elmegreen B. G., 1993, ApJ, 411, 170
Elmegreen B. G., 1995, MNRAS, 275, 944
Emsellem E., et al., 2004, MNRAS, 352, 721
Emsellem E., et al., 2007, MNRAS, 379, 401
Emsellem E., et al., 2011, MNRAS, 414, 888
Emsellem E., Renaud F., Bournaud F., Elmegreen B., Combes F., Gabor J., 2014, MNRAS, 446, 2468
Erb D. K., 2008, ApJ, 674, 151
Esteban C., Bresolin F., Peimbert M., García-Rojas J., Peimbert A., Mesa-Delgado A., 2009, ApJ, 700, 654
Etherington J., Thomas D., 2015, MNRAS, 451, 660
Evans N. J., 1999, ARA&A, 37, 311
Faber S. M., et al., 2007, ApJ, 665, 265
Fabian A., 2012, ARA&A, 50, 455
Fan X., et al., 2001, AJ, 122, 2833
Fanali R., Dotti M., Fiacconi D., Haardt F., 2015, MNRAS, 454, 3641
Fazio G. G., et al., 2004, ApJS, 154, 10
Ferguson A. M. N., Clarke C. J., 2001, MNRAS, 325, 781
Ferland G. J., Netzer H., 1983, AJ, 264, 105
Ferland G. J., et al., 2013, Revista Mexicana de Astronomia y Astrofisica, 49, 137
Fernandes R. C., Sodr L., Gomes M., 2005, MNRAS, 358, 363
Ferrara A., Scannapieco E., Bergeron J., 2005, ApJ, 634, L37
Ferruit P., et al., 2012, Proc. SPIE, 8442, 84422O
Feruglio C., Maiolino R., Piconcelli E., Menci N., Aussel H., Lamastra A., Fiore F., 2010, A&A, 518, L155
Field G. B., Goldsmith D. W., Habing H. J., 1969, ApJ, 155, L149
Finlator K., Davé R., 2008, MNRAS, 385, 2181
Fitzpatrick E. L., 1999, PASP, 111, 63
Flores-Fajardo N., Morisset C., Stasińska G., Binette L., 2011, MNRAS, 415, 2182
Fogarty L. M. R., et al., 2012, ApJ, 761, 169
Förster Schreiber N. M., et al., 2009, ApJ, 706, 1364
Franx M., Illingworth G., de Zeeuw T., 1991, ApJ, 383, 112
Fu J., Hou J. L., Yin J., Chang R. X., 2009, ApJ, 696, 668
Fukugita M., Ichikawa T., Gunn J. E., Doi M., Shimasaku K., Schneider D. P., 1996, AJ, 111, 1748
Fukugita M., Hogan C. J., Peebles P. J. E., 1998, ApJ, 503, 518
Fumagalli M., Fossati M., Hau G. K. T., Gavazzi G., Bower R., Sun M., Boselli A., 2014, MNRAS, 445, 4335
Gabor J. M., Davé R., 2012, MNRAS, 427, 1816
Gallazzi A., Charlot S., Brinchmann J., White S. D. M., 2006, MNRAS, 370, 1106
Garcia-Benito R., et al., 2015, A&A, 576, A135
Garnett D. R., 1990, ApJ, 363, 142
Garnett D. R., 1992, AJ, 103, 1330
Garnett D. R., 2002, ApJ, 581, 1019
Garnett D. R., Shields G. A., Skillman E. D., Sagan S. P., Dufour R. J., 1997, ApJ, 489, 63
Geha M., Blanton M. R., Yan R., Tinker J. L., Haven N., 2012, ApJ, 85, 85
Genovali K., et al., 2014, A&A, 566, A37
Genzel R., et al., 2011, ApJ, 733, 101

Gerhard O., Binney J., 1996, MNRAS, 279, 993
Gibson B. K., Pilkington K., Brook C. B., Stinson G. S., Bailin J., 2013, A&A, 554, A47
Giovanelli R., Haynes M. P., Salzer J. J., Wegner G., da Costa L. N., Freudling W., 1994, AJ, 107, 2036
Gnedin N. Y., 2000, ApJ, 542, 535
Goddard D., et al., 2016, MNRAS, 31, 1
Goddard D., et al., 2017, MNRAS, 466, 4731
Goetz M., Koeppen J., 1992, A&A, 262, 455
Gomes J. M., et al., 2015a, ArXiv
Gomes J. M., et al., 2015b, ArXiv
González Delgado R. M., Cerviño M., Martins L. P., Leitherer C., Hauschildt P. H., 2005, MNRAS, 357, 945
González Delgado R. M., Pérez E., Fernandes R. C., Amorim A. L. D., 2015, A&A, 581, A103
Goudfrooij P., 1999, ASP Conference Series, 163, 55
Greene J. E., Janish R., Ma C.-P., McConnell N. J., Blakeslee J. P., Thomas J., Murphy J. D., 2015, ApJ, 807, 11
Greggio L., Renzini A., 2011, Stellar Populations. A User Guide from Low to High Redshift. Wiley-VCH-Verlag
Groves B. A., Dopita M. A., Sutherland R. S., 2004a, ApJS, 153, 9
Groves B. A., Dopita M. A., Sutherland R. S., 2004b, ApJS, 153, 75
Guidi G., Scannapieco C., Walcher J., Gallazzi A., 2016, MNRAS, 462, 2046
Gunn J. E., Gott J. R., 1972, ApJ, 176, 1
Gunn J. E., et al., 2006, AJ, 131, 2332
Guth A. H., 1981, Physical Review D, 23, 347
Haffner L., et al., 2009, Reviews of Modern Physics, 81, 969
Häring N., Rix H.-W., 2004, ApJ, 604, L89
Heavens A., Jimenez R., Lahav O., 2000, MNRAS, 317, 965
Heckman T. M., 1980, A&A, 87, 152
Heckman T. M., 1996, in ASP Conference Series. p. 241
Heckman T. M., Best P. N., 2014, ARA&A, 52, 589
Heckman T. M., Lehnert M. D., Strickland D. K., Armus L., 2000, ApJS, 129, 493
Henry R. B. C., Worthey G., 1999, PASP, 111, 919
Henry R. B. C., Edmunds M. G., Koppen J., 2000, ApJ, 541, 660
Hinshaw G., et al., 2013, ApJs, 208, 19
Ho L. C., 2008, ARA&A, 46, 475
Ho L. C., Filippenko A. V., Sargent W. L. W., 1997, ApJ, 487, 568
Ho I.-T., et al., 2014, MNRAS, 444, 3894
Ho I.-T., Kudritzki R.-P., Kewley L., Zahid H. J., Dopita M. A., Bresolin F., Rupke D. S. N., 2015, MNRAS, 448, 2030
Ho I. T., et al., 2016, MNRAS, 457, 1257
Holincheck A. J., et al., 2016, MNRAS, 459, 720
Hoopes C. G., Walterbos R. A. M., 2003, ApJ, 586, 902
Hopkins P. F., Quataert E., Murray N., 2012, MNRAS, 3521, 3488
Hubble E. P., 1925, Popular Astronomy, 33, 252
Hubble E. P., 1926a, ApJ, 63, 236
Hubble E. P., 1926b, ApJ, 64, 321
Hubble E. P., 1936, Realm of the Nebulae. Yale University Press
Hughes T. M., Cortese L., Boselli A., Gavazzi G., Davies J. I., 2013, A&A, 550, A115
Hunter D. A., Elmegreen B. G., Baker A. L., 1998, ApJ, 493, 595
Husemann B., et al., 2013, A&A, 549, A87
Ibarra-Medel H. J., et al., 2016, MNRAS, 463, 2799
Ilbert O., et al., 2010, ApJ, 709, 644
Ilbert O., et al., 2013, A&A, 556, A55
Izotov Y. I., Stasińska G., Meynet G., Guseva N. G., Thuan T. X., 2006, A&A, 448, 955
James P. a., Percival S. M., 2015, MNRAS, 450, 3503
Jeans J. H., 1902, Philosophical Transactions of the Royal Society of London, 199, 1
Jog C. J., Solomon P. M., 1984, ApJ, 276, 127
Johansson J., Thomas D., Maraston C., 2012, MNRAS, 421, 1908

Jones T., Ellis R. S., Richard J., Jullo E., 2013, ApJ, 765, 48
Juneau S., et al., 2014, ApJ, 788, 88
Jungwiert B., Combes F., Palous J., 2001, A&A, 35, 85
Kamphuis J., Briggs F., 1992, A&A, 253, 335
Karakas A. I., 2010, MNRAS, 403, 1413
Kauffmann G., et al., 2003a, MNRAS, 341, 54
Kauffmann G., et al., 2003b, MNRAS, 341, 33
Kauffmann G., et al., 2003c, MNRAS, 346, 1055
Kehrig C., Papaderos P., Vílchez J. M., Gomes J. M., Masegosa J., Sánchez S. F., 2012, A&A, 540, A11
Kelz A., et al., 2006, PASP, 118, 129
Kennicutt R. C., 1998, ARA&A, 36, 189
Kennicutt R. C., Evans N. J., 2012, ARA&A, 50, 531
Kennicutt R. C., Keel W. C., Blaha C. A., 1989, AJ, 97, 1022
Kennicutt R. C., et al., 2003a, PASP, 115, 928
Kennicutt R. C., Bresolin F., Garnett D. R., 2003b, ApJ, 591, 801
Kereš D., Katz N., Weinberg D. H., DaveÃÅ R., 2005, MNRAS, 363, 2
Kereš D., Katz N., Fardal M., DaveÃÅ R., Weinberg D. H., 2009, MNRAS, 395, 160
Kewley L. J., Dopita M. a., 2002, ApJS, 142, 35
Kewley L. J., Ellison S. L., 2008, ApJ, 681, 1183
Kewley L. J., Dopita M. A., Sutherland R. S., Heisler C. A., Trevena J., 2001, ApJ, 556, 121
Kewley L. J., Groves B., Kauffmann G., Heckman T., 2006, MNRAS, 372, 961
Kewley L. J., Rupke D., Jabran Zahid H., Geller M. J., Barton E. J., 2010, ApJ, 721, L48
Kewley L. J., Maier C., Yabe K., Ohta K., Akiyama M., Dopita M. A., Yuan T., 2013, ApJ, 774, L10
Knapen J. H., 2005, A&A, 429, 141
Kobayashi C., Umeda H., Nomoto K., Tominaga N., Ohkubo T., 2006, ApJ, 653, 1145
Kobulnicky H. A., Kewley L. J., 2004, ApJ, 617, 240
Köppen J., Hensler G., 2005, A&A, 434, 531
Kormendy J., Bender R., 1996, ApJ, 464, L119
Kormendy J., Drory N., Bender R., Cornell M. E., 2010, ApJ, 723, 54
Korn A. J., Maraston C., Thomas D., 2005, A&A, 438, 685
Krajnović D., Cappellari M., De Zeeuw P. T., Copin Y., 2006, MNRAS, 366, 787
Krajnović D., et al., 2013, MNRAS, 432, 1768
Kroupa P., 2001, MNRAS, 322, 231
Kroupa P., Tout C. A., Gilmore G., 1993, MNRAS, 262, 545
Kudritzki R.-P., Ho I.-T., Schruba A., Burkert A., Zahid H. J., Bresolin F., Dima G. I., 2015, MNRAS, 450, 342
Lacey C. G., Fall S. M., 1985, ApJ, 290, 154
Lake G., Norman C., 1983, ApJ, 270, 51
Lara-López M. A., et al., 2010, A&A, 521, L53
Larson R. B., 1976, MNRAS, 176, 31
Law D. R., Steidel C. C., Erb D. K., Larkin J. E., Pettini M., Shapley A. E., Wright S. A., 2009, ApJ, 697, 2057
Law D. R., et al., 2015, AJ, 150, 19
Law D. R., et al., 2016, AJ, 152, 83
Le Borgne J.-F., et al., 2003, A&A, 402, 433
Leavitt H., Pickering E., 1912, Harvard College Observatory Circular, 173, 1
Lemasle B., et al., 2013, A&A, 558, A31
Lequeux J., Peimbert M., Rayo J. F., Serrano A., Torres-Peimbert S., 1979, A&A, 80, 155
Leroy A. K., Walter F., Brinks E., Bigiel F., de Blok W. J. G., Madore B., Thornley M. D., 2008, AJ, 136, 2782
Leroy A. K., et al., 2009, AJ, 137, 4670
Leroy A. K., et al., 2011, ApJ, 737, 12
Leroy A. K., et al., 2012, AJ, 144, 3
Leroy A. K., et al., 2013, AJ, 146, 19
Levesque E. M., Kewley L. J., Larson K. L., 2010, AJ, 139, 712
Li C., et al., 2015, ApJ, 804, 125

Lilly S., Le Fevre O., Hammer F., Crampton D., 1996, ApJ, 460, L1
Lilly S. J., Carollo C. M., Pipino A., Renzini A., Peng Y., 2013, ApJ, 772, 119
Lintott C. J., et al., 2008, MNRAS, 389, 1179
Lipari S., et al., 2004, MNRAS, 355, 641
Liu G., Koda J., Calzetti D., Fukuhara M., Momose R., 2011, ApJ, 735, 63
Longmore S. N., et al., 2013, MNRAS, 429, 987
López-Sánchez Á. R., Dopita M. A., Kewley L. J., Zahid H. J., Nicholls D. C., Scharwächter J., 2012, MNRAS, 426, 2630
Lu Y., Blanc G. A., Benson A., 2015, ApJ, 808, 129
Luck R. E., Gieren W. P., Andrievsky S. M., Kovtyukh V. V., Pont F., Kienzle F., 2003, A&A, 401, 939
Lynden-Bell D., 1969, Nature, 223, 690
Lynden-Bell D., 1975, in , Vol. 19, Vistas in Astronomy. pp 299–316, doi:10.1016/0083-6656(75)90005-7
Maciel W., Quireza C., 1999, A&A, 345, 629
Madau P., Dickinson M., 2014, ARA&A, 52, 415
Madau P., Shull J. M., 1996, ApJ, 457, 551
Madore B. F., 1977, MNRAS, 178, 1
Madsen G. J., Reynolds R. J., Haffner L. M., 2006, ApJ, 652, 401
Magrini L., Sestito P., Randich S., Galli D., 2009, A&A, 494, 95
Maiolino R., et al., 2008, A&A, 488, 463
Maiolino R., et al., 2012, MNRAS, 425, L66
Mannucci F., Cresci G., Maiolino R., Marconi A., Gnerucci A., 2010, MNRAS, 408, 2115
Maraston C., 1998, MNRAS, 300, 872
Maraston C., 2005, MNRAS, 362, 799
Maraston C., Strömbäck G., 2011, MNRAS, 418, 2785
Maraston C., Thomas D., 2000, ApJ, 541, 126
Marcon-Uchida M. M., Matteucci F., Costa R. D. D., 2010, A&A, 520, A35
Marconi A., Hunt L. K., 2003, ApJ, 589, L21
Marinacci F., Pakmor R., Springel V., Simpson C. M., 2014, MNRAS, 442, 3745
Marino R. A., et al., 2013, A&A, 559, A114
Martig M., Bournaud F., Teyssier R., Dekel A., 2009, ApJ, 707, 250
Martig M., et al., 2013, MNRAS, 432, 1914
Martin C. L., 1997, ApJ, 491, 561
Martin C. L., 2005, ApJ, 621, 227
Martin C. L., Kennicutt R. C., 1997, ApJ, 483, 698
Martin C. L., Kennicutt R. C., 2001, ApJ, 555, 301
Martin C. L., Kobulnicky H., Heckman T., 2002, ApJ, 574, 663
Martin C., Moore A., Morrissey P., Matuszewski M., Rahman S., Adkins S., Epps H., 2010, Proc. SPIE, 7735, 77350M
Mast D., et al., 2014, A&A, 561, A129
Masters K. L., et al., 2010, MNRAS, 405, 783
Masters K. L., et al., 2011, MNRAS, 418, 1055
Masters K. L., et al., 2012, MNRAS, 424, 2180
Mathews W. G., 1990, ApJ, 354, 468
Mathis J. S., 1990, ARA&A, 28, 37
Matteo P. D., Haywood M., Combes F., Semelin B., Snaith O. N., 2013, A&A, 553, A102
Matteucci F., 1986, PASP, 98, 973
Matteucci F., 1994, A&A, 288, 57
Matteucci F., 2008, Arxiv:0804.1492v1
Matteucci F., Chiosi C., 1983, A&A, 123, 121
Matteucci F., Francois P., 1989, MNRAS, 239, 885
McConnell N. J., Ma C.-P., 2013, ApJ, 764, 184
McDermid R. M., et al., 2015, MNRAS, 448, 3484
McGaugh S. S., 1991, ApJ, 380, 140
McGaugh S. S., Schombert J. M., de Blok W. J. G., Zagursky M. J., 2010, ApJ, 708, L14
McKee C. F., Ostriker J. P., 1977, ApJ, 218, 148

McKee C. F., Ostriker E. C., 2007, ARA&A, 45, 565
McNamara B., Nulsen P., 2007, ARA&A, 45, 117
McQuinn K. B. W., Skillman E. D., Dalcanton J. J., Dolphin A. E., Cannon J. M., Holtzman J., Weisz D. R., Williams B. F., 2012, ApJ, 751, 127
Melioli C., Brighenti F., D'Ercole A., de Gouveia Dal Pino E. M., 2008, MNRAS, 388, 573
Melioli C., Brighenti F., D'Ercole A., de Gouveia Dal Pino E. M., 2009, MNRAS, 399, 1089
Meynet G., Maeder A., 2002, A&A, 390, 561
Minchev I., Famaey B., 2010, ApJ, 722, 112
Mollá M., Díaz A. I., 2005, MNRAS, 558, 521
Mollá M., Ferrini F., Díaz A. I., 1997, ApJ, 475, 519
Mollá M., Vílchez J. M., Gavilán M., Díaz A. I., 2006, MNRAS, 372, 1069
Monreal-Ibero A., Arribas S., Colina L., 2006, ApJ, 637, 138
Morales-Luis A. B., Sánchez Almeida J., Aguerri J. A. L., Muñoz-Tuñón C., 2011, ApJ, 743, 77
Moran S. M., et al., 2012, ApJ, 745, 66
Morrissey P., et al., 2007, ApJS, 173, 682
Mortlock D. J., et al., 2011, Nature, 474, 616
Moster B. P., Somerville R. S., Maulbetsch C., Van Den Bosch F. C., Macciò A. V., Naab T., Oser L., 2010, ApJ, 710, 903
Mott A., Spitoni E., Matteucci F., 2013, MNRAS, 435, 2918
Moustakas J., Kennicutt R. C., Tremonti C. A., Dale D. A., Smith J.-D. T., Calzetti D., 2010, ApJS, 190, 233
Muñoz-Mateos J. C., Gil de Paz A., Boissier S., Zamorano J., Jarrett T., Gallego J., Madore B. F., 2007, ApJ, 658, 1006
Muratov A. L., et al., 2016, Arxiv:1606.09252v1
Mutch S. J., Croton D. J., Poole G. B., 2011, ApJ, 736, 84
Mutch S. J., Croton D. J., Poole G. B., 2013, MNRAS, 435, 2445
Naab T., Ostriker J. P., 2006, MNRAS, 366, 899
Nagao T., Maiolino R., Marconi A., 2006, A&A, 459, 85
Nair P. B., Abraham R. G., 2010, ApJ, 714, L260
Natta A., Panagia N., 1984, ApJ, 287, 228
Nava A., Casebeer D., Henry R. B. C., Jevremovic D., 2006, ApJ, 645, 1076
Noeske K. G., et al., 2007, ApJ, 660, L43
Noll S., Burgarella D., Giovannoli E., Buat V., Marcillac D., Muñoz-Mateos J. C., 2009, A&A, 507, 1793
Nomoto K., Kobayashi C., Tominaga N., 2013, ARA&A, 51, 457
O'Connell R. W., 1999, ARA&A, 37, 603
O'Donnell J. E., 1994, ApJ, 422, 158
Oey M. S., Kennicutt R. C., 1993, ApJ, 411, 137
Oey M. S., Kennicutt R. C., 1997, MNRAS, 291, 827
Oey M. S., et al., 2007, ApJ, 661, 801
Oh K., Sarzi M., Schawinski K., Yi S. K., 2011, ApJS, 195, 13
Oppenheimer B. D., Davé R., Kereš D., Fardal M., Katz N., Kollmeier J. A., Weinberg D. H., 2010, MNRAS, 406, 2325
Osterbrock D. E., Ferland G. J., 2006, Astrophysics of gaseous nebulae and active galactic nuclei. University Science Books, Mill Valley, CA
Padovani P., Matteucci F., 1993, ApJ, 416, 26
Pagel B. E. J., Edmunds M. G., Blackwell D. E., Chun M. S., Smith G., 1979, MNRAS, 189, 95
Pagel B. E. J., Simonson E. A., Terlevich R. J., Edmunds M. G., 1992, MNRAS, 255, 325
Panter B., Heavens A. F., Jimenez R., 2004, MNRAS, 355, 764
Papaderos P., Gomes J. M., Vílchez J. M., Kehrig C., Lehnert M. D., Ziegler B., Sánchez S. F., Husemann B., 2013, A&A, 555, L1
Pasquali A., Gallazzi A., van den Bosch F. C., 2012, MNRAS, 425, 273
Pastorello N., Sarzi M., Cappellari M., Emsellem E., Mamon G. A., Bacon R., Davies R. L., Tim de Zeeuw P., 2013, MNRAS, 430, 1219
Pastorello N., et al., 2015, MNRAS, 451, 2625
Pedicelli S., et al., 2009, A&A, 504, 81
Peeples M. S., Shankar F., 2011, MNRAS, 417, 2962
Peeples M. S., Werk J. K., Tumlinson J., Oppenheimer B. D., Prochaska J. X., Katz N., Weinberg D. H., 2014, ApJ, 786, 54

Peimbert M., 1967, ApJ, 150, 825
Peña-Guerrero M. A., Peimbert A., Peimbert M., 2012, ApJ, 756, L14
Peng Y.-j., Maiolino R., 2014, MNRAS, 443, 3643
Peng Y.-j., et al., 2010, ApJ, 721, 193
Peng Y.-j., Maiolino R., Cochrane R., 2015, Nature, 521, 192
Pérez-Montero E., Contini T., 2009, MNRAS, 398, 949
Pérez-Montero E., et al., 2016, A&A, 595, A62
Pérez E., et al., 2013, ApJ, 764, L1
Perlmutter S., et al., 1999, ApJ, 517, 565
Pettini M., Pagel B. E. J., 2004, MNRAS, 348, L59
Pettini M., Ellison S. L., Steidel C. C., Bowen D. V., 1999, ApJ, 510, 576
Pezzulli G., Fraternali F., 2016, MNRAS, 455, 2308
Phillips M. M., Jenkins E. B., Dopita M. A., Sadler E. M., Binette L., 1986, AJ, 91, 1062
Pilkington K., et al., 2012a, MNRAS, 425, 969
Pilkington K., et al., 2012b, A&A, 540, A56
Pilyugin L. S., Thuan T. X., 2005, ApJ, 631, 231
Pilyugin L. S., Mattsson L., Vílchez J. M., Cedrés B., 2009, MNRAS, 398, 485
Pilyugin L. S., Vílchez J. M., Thuan T. X., 2010, ApJ, 720, 1738
Pilyugin L. S., Grebel E. K., Zinchenko I. A., 2015, MNRAS, 450, 3254
Planck Collaboration et al., 2014, A&A, 571, A16
Planck Collaboration et al., 2016, A&A, 594, A13
Pogge R. W., Maoz D., Ho L. C., Eracleous M., 2000, ApJ, 532, 323
Poggianti B. M., et al., 2016, AJ, 151, 78
Prantzos N., Boissier S., 2000, MNRAS, 313, 338
Rand R. J., Kulkarni S. R., Hester J. J., 1990, ApJ, 352, L1
Recchi S., Spitoni E., Matteucci F., Lanfranchi G. A., 2008, A&A, 565, 11
Rees M., 1984, ARA&A, 22, 471
Rees M., Ostriker J., 1977, MNRAS, 179, 541
Renzini A., Peng Y.-j., 2015, ApJ, 801, L29
Renzini A., Voli M., 1981, A&A, 94, 175
Reynolds R. J., 1984, In NASA. Goddard Space Flight Center Local Interstellar Medium, 2345, 97
Reynolds R. J., 1991, Proceedings of the International Astronomical Union, 144, 67
Reynolds R. J., Tufte S. L., Kung D. T., McCullough P. R., Heiles C., 1995, ApJ, 448, 715
Rich J. a., Dopita M. a., Kewley L. J., Rupke D. S. N., 2010, ApJ, 721, 505
Rich J. A., Kewley L. J., Dopita M. A., 2011, ApJ, 734, 87
Rich J. A., Torrey P., Kewley L. J., Dopita M. A., Rupke D. S. N., 2012, ApJ, 753, 5
Rich J. A., Kewley L. J., Dopita M. A., 2013, ASP Conference Series, 477, 231
Rich J. A., Kewley L. J., Dopita M. A., 2014, ApJ, 781, L12
Riess A. G., et al., 1998, AJ, 116, 1009
Roberts M. S., Haynes M. P., 1994, ARA&A, 32, 115
Rolleston W., Smartt S., Dufton P., Ryans R., 2000, A&A, 363, 537
Romano D., Chiappini C., Matteucci F., Tosi M., 2005, A&A, 430, 491
Romano D., Karakas A. I., Tosi M., Matteucci F., 2010, A&A, 522, A32
Romeo A. B., Wiegert J., 2011, MNRAS, 416, 1191
Rosales-Ortega F. F., Kennicutt R. C., Sánchez S. F., Díaz a. I., Pasquali A., Johnson B. D., Hao C. N., 2010, MNRAS, 405, 735
Rosales-Ortega F. F., Díaz A. I., Kennicutt R. C., Sánchez S. F., 2011, MNRAS, 415, 2439
Rosales-Ortega F. F., Arribas S., Colina L., 2012, A&A, 539, A73
Rosenfield P., et al., 2012, ApJ, 755, 131
Roškar R., Debattista V. P., Quinn T. R., Stinson G. S., Wadsley J., 2008, ApJ, 684, L79
Rossa J., Dettmar R.-J., 2003, A&A, 406, 505
Rossa J., Dettmar R.-J., Walterbos R. A. M., Norman C. A., 2004, AJ, 128, 674
Rudolph A. L., Fich M., Bell G. R., Norsen T., Simpson J. P., Haas M. R., Erickson E. F., 2006, AJ, 162, 346

Rupke D. S. N., Veilleux S., 2011, ApJ, 729, L27
Rybicki G. B., 1987, in Structure and Dynamics of Elliptical Galaxies. p. 397
Saintonge A., et al., 2011, MNRAS, 415, 61
Saintonge A., et al., 2012, ApJ, 758, 73
Salim S., et al., 2007, ApJS, 173, 267
Salpeter E. E., 1955, ApJ, 121, 161
Sánchez Almeida J., Elmegreen B. G., Muñoz-Tuñón C., Elmegreen D. M., 2014, A&AR, 22, 1
Sánchez-Blázquez P., Ocvirk P., Gibson B. K., Pérez I., Peletier R. F., 2011, MNRAS, 415, 709
Sánchez-Blázquez P., Rosales-Ortega F., Diaz A., Sanchez S. F., 2014, MNRAS, 437, 1534
Sánchez-Menguiano L., et al., 2016, A&A, 587, A70
Sánchez S. F., Rosales-Ortega F., Kennicutt R. C., Johnson B. D., Diaz A. I., Pasquali A., Hao C. N., 2011, MNRAS, 410, 313
Sánchez S. F., et al., 2012a, A&A, 538, A8
Sánchez S. F., et al., 2012b, A&A, 546, 2
Sánchez S. F., et al., 2014, A&A, 563, A49
Sánchez S. F., et al., 2015, A&A, 574, A47
Sancisi R., Fraternali F., Oosterloo T., van der Hulst T., 2008, A&AR, 15, 189
Sandage A., 1961, The Hubble atlas of galaxies
Sanders R., 1981, ApJ, 244, 820
Sandstrom K. M., et al., 2013, ApJ, 777, 5
Sarzi M., Rix H., Shields J. C., Ho L. C., Barth A. J., Rudnick G., Filippenko A. V., Sargent W. L. W., 2005, ApJ, 628, 169
Sarzi M., et al., 2006, MNRAS, 366, 1151
Sarzi M., Allard E. L., Knapen J. H., Mazzuca L. M., 2007, MNRAS, 380, 949
Sarzi M., et al., 2010, MNRAS, 402, 2187
Sarzi M., et al., 2013, MNRAS, 432, 1845
Schawinski K., Thomas D., Sarzi M., Maraston C., Kaviraj S., Joo S. J., Yi S. K., Silk J., 2007, MNRAS, 382, 1415
Schawinski K., et al., 2014, MNRAS, 440, 889
Schaye J., 2004, ApJ, 609, 667
Schechter P., 1976, ApJ, 203, 297
Schiminovich D., et al., 2007, ApJS, 173, 315
Schlegel D. J. D., Finkbeiner D. P. D., Davis M., 1998, ApJ, 500, 525
Schmidt M., 1959, ApJ, 129, 243
Schmidt M., 1963, ApJ, 137, 758
Schönrich R., Binney J., 2009, MNRAS, 396, 203
Schruba A., et al., 2012, AJ, 143, 138
Searle L., Sargent W. L. W., 1972, ApJ, 173, 25
Sérsic J. L., 1963, Boletin de la Asociacion Argentina de Astronomia, 6, 41
Shapley A. E., et al., 2015, ApJ, 801, 88
Sharp R. G., Bland-Hawthorn J., 2010, ApJ, 711, 818
Sharples R., et al., 2006, New Astronomy Reviews, 50, 370
Shields J. C., et al., 2007, ApJ, 654, 125
Shull J. M., Smith B. D., Danforth C. W., 2012, ApJ, 759, 23
Silk J., 1977, ApJ, 211, 638
Silk J., 1997, ApJ, 481, 703
Simard L., Trevor Mendel J., Patton D. R., Ellison S. L., McConnachie A. W., 2011, ApJS, 196, 11
Simmons B. D., et al., 2013, MNRAS, 429, 2199
Singh R., et al., 2013, A&A, 558, A43
Skrutskie M. F., et al., 2006, AJ, 131, 1163
Smartt S. J., Rolleston W. R. J., 1997, ApJ, 481, L47
Smee S. A., et al., 2013, AJ, 146, 32
Smethurst R. J., et al., 2015, MNRAS, 450, 435
Solomon P. M., Rivolo A. R., Barrett J., Yahil A., 1987, ApJ, 319, 730
Somerville R. S., Davé R., 2015, ARA&A, 53, 51

Spitoni E., Matteucci F., 2011, A&A, 531, A72
Spitoni E., Calura F., Matteucci F., Recchi S., 2010, A&A, 514, A73
Spitoni E., Romano D., Matteucci F., Ciotti L., 2015, ApJ, 802, 129
Spitoni E., Vincenzo F., Matteucci F., 2016, Arxiv:1605.05603v1
Springel V., Hernquist L., 2003, MNRAS, 339, 312
Springel V., et al., 2005, Nature, 435, 629
Stanghellini L. S., Renzini A. R., 2000, ApJ, 542, 308
Stanghellini L., Guerrero M. A., Cunha K., Manchado A., Villaver E., 2006, ApJ, 651, 898
Stasińska G., 1990, A&A Supplement Series, 83, 501
Stasińska G., 2005, A&A, 434, 507
Stasińska G., Cid Fernandes R., Mateus A., Sodre L., Asari N. V., 2006, MNRAS, 371, 972
Stasińska G., Asari N. V., Cid Fernandes R., Gomes J. M., Schlickmann M., Mateus A., Schoenell W., Sodré Jr L., 2008, MNRAS, 33, 29
Stasińska G., et al., 2012, EAS Publications Series, 54, 65
Steidel C. C., Erb D. K., Shapley A. E., Pettini M., Reddy N., Bogosavljević M., Rudie G. C., Rakic O., 2010, ApJ, 717, 289
Stott J. P., et al., 2014, MNRAS, 443, 2695
Strateva I., Ivezic Z., Knapp G. R., Narayanan V. K., Strauss M. a., 2001, AJ, 122, 1861
Strauss M. a., Weinberg D. H., Lupton R. H., Narayanan V. K., 2002, AJ, 124, 1810
Strong A. W., Mattox J. R., 1996, A&A, 308, L21
Sutherland R. S., Dopita M. A., 1993, ApJS, 88, 253
Tan J. C., 2000, ApJ, 536, 173
Thomas D., Davies R. L., 2006, MNRAS, 366, 510
Thomas D., Greggio L., Bender R., 1998, MNRAS, 296, 119
Thomas D., Maraston C., Korn A., 2004, MNRAS, 351, L19
Thomas D., Maraston C., Bender R., 2005, Astrophysics and Space Science, 621, 673
Thomas D., Maraston C., Schawinski K., Sarzi M., Silk J., 2010, MNRAS, 404, 1775
Thomas D., Maraston C., Johansson J., 2011, MNRAS, 412, 2183
Thon R., Meusinger H., 1998, A&A, 338, 413
Thurston T. R., Edmunds M. G., Henry R. B. C., 1996, MNRAS, 283, 990
Tinsley B., 1980, Fundamentals of cosmic physics, 5, 287
Tohline J. E., Durisen R. H., 1982, ApJ, 257, 94
Tojeiro R., et al., 2013, MNRAS, 432, 359
Toomre a., 1964, ApJ, 139, 1217
Tremonti C. A., Heckman T. M., Kauffmann G., Brinchmann J., White S. D. M., Seibert M., Peng E. W., Schlegel D. J., 2004, ApJ, 613, 898
Trinchieri G., di Serego Alighieri S., 1991, AJ, 101, 1647
Tumlinson J., et al., 2011, Science, 334, 948
Tumlinson J., et al., 2013, ApJ, 777, 59
Tylenda R., Stasinska G., 1989, A&A, 217, 209
Van de Voort F., Schaye J., Altay G., Theuns T., 2012, MNRAS, 421, 2809
Vazdekis A., Ricciardelli E., Cenarro a. J., Rivero-González J. G., Díaz-García L. a., Falcón-Barroso J., 2012, MNRAS, 424, 157
Veilleux S., Osterbrock D. E., 1987, ApJS, 63, 295
Veilleux S., Cecil G., Bland-Hawthorn J., 2005, ARA&A, 43, 769
Ventura P., Di Criscienzo M., Carini R., D'Antona F., 2013, MNRAS, 431, 3642
Veron-Cetty M. P., Veron P., 2000, A&AR, 10, 81
Vila-Costas M. B., Edmunds M. G., 1992, MNRAS, 259, 121
Vila-Costas M. B., Edmunds M. G., 1993, MNRAS, 265, 199
Vílchez J. M., Esteban A., 1996, MNRAS, 280, 720
Vincenzo F., Belfiore F., Maiolino R., Matteucci F., Ventura P., 2016a, MNRAS, 358, 3466
Vincenzo F., Matteucci F., Belfiore F., Maiolino R., 2016b, MNRAS, 455, 4183
Volonteri M., 2010, A&AR, 18, 279

Wake D. A., van Dokkum P. G., Franx M., 2012, ApJ, 751, L44
Walcher C. J., et al., 2014, A&A, 569, A1
Walter F., Brinks E., Blok W. J. G. D., Bigiel F., Kennicutt R. C., Thornley M. D., Leroy A., 2008, AJ, 136, 2563
Walterbos R. A. M., Braun R., 1994, ApJ, 431, 156
Wang J., et al., 2011, MNRAS, 413, 1373
Weidemann V., 2000, A&A, 363, 647
Weijmans A.-M., et al., 2014, MNRAS, 444, 3340
Weinberg D. H., Andrews B. H., Freudenburg J., 2016, ArXiv:1604.07435v1
Werk J. K., Putman M. E., Meurer G. R., Thilker D. A., Allen R. J., Bland-Hawthorn J., Kravtsov A., Freeman K., 2010, ApJ, 715, 656
Werk J. K., Putman M. E., Meurer G. R., Santiago-Figueroa N., 2011, ApJ, 735, 71
Werk J. K., et al., 2014, ApJ, 792, 8
Wetzel A. R., Tinker J. L., Conroy C., van den Bosch F. C., 2013, MNRAS, 432, 336
White S. D. M., Frenk C. S., 1991, ApJ, 379, 52
White S. D. M., Rees M. J., 1978, MNRAS, 183, 341
Wiersma R. P. C., Schaye J., Theuns T., 2011, MNRAS, 415, 353
Wilkinson D. M., et al., 2015, MNRAS, 449, 328
Willett K. W., et al., 2013, MNRAS, 435, 2835
Williams B. F., Dalcanton J. J., Dolphin A. E., Holtzman J., Sarajedini A., 2009, ApJ, 695, L15
Wilson C. D., 1995, ApJ, 448
Wisnioski E., et al., 2015, ApJ, 799, 209
Wolf C., et al., 2009, MNRAS, 393, 1302
Woosley S. E., Weaver T. A., 1995, ApJS, 101, 181
Worthey G., Ottaviani D. L., 1997, ApJS, 111, 377
Worthey G., Faber S. M., Gonzalez J. J., Burstein D., 1994, ApJS, 94, 687
Wu Y.-Z., Zhang S.-N., 2013, MNRAS, 436, 934
Wuyts E., et al., 2016, ApJ, 827, 74
Wyder T. K., et al., 2007, ApJs, 173, 293
Yan R., Blanton M. R., 2012, ApJ, 747, 61
Yan R., et al., 2016a, AJ, 151, 8
Yan R., et al., 2016b, AJ, 152, 197
Yang X., Mo H. J., Van der Bosch F. C., Jing Y. P., 2005, MNRAS, 356, 1293
Yang X., Mo H. J., van den Bosch F. C., Pasquali A., Li C., Barden M., 2007, ApJ, 671, 153
Yates R. M., Kauffmann G., 2014, MNRAS, 439, 3817
Yoachim P., Roškar R., Debattista V. P., 2012, ApJ, 752, 97
Yong D., Carney B. W., Friel E. D., 2012, AJ, 144, 95
York D. G., et al., 2000, AJ, 120, 1579
Yuan T.-T., Kewley L. J., Rich J., 2013, ApJ, 767, 106
Zahid H. J., Dima G. I., Kewley L. J., Erb D. K., Davé R., 2012, ApJ, 757, 54
Zaritsky D., Kennicutt R. C., Huchra J. P., 1994, ApJ, 420, 87
Zhang K., et al., 2017, MNRAS, 466, 3217
Zuckerman B., Palmer P., 1974, ARA&A, 12, 279
de Jong R. S., Lacey C. G., 2000, ApJ, 545, 781
de Vaucouleurs G., 1948, Annales d'Astrophysique, 11, 247
de Vaucouleurs G., de Vaucouleurs A., Corwin Jr. H. G., Buta R. J., Paturel G., Fouqué P., 1991, Third Reference Catalogue of Bright Galaxies.
de Zeeuw P. T., et al., 2002, MNRAS, 329, 513
van Den Hoek B., Groenewegen M., 1997, A&A Supplement Series, 123, 305
van Dokkum P. G., Conroy C., 2010, Nature, 468, 940
van Dokkum P. G., Franx M., Fabricant D., Kelson D. D., Illingworth G. D., 1999, ApJ, 520, L95
van Zee L., Salzer J. J., Haynes M. P., O'Donoghue A. A., Balonek T. J., 1998, AJ, 116, 2805
van de Voort F., Schaye J., Booth C. M., Haas M. R., Dalla Vecchia C., 2011, MNRAS, 414, 2458
van de Voort F., Davis T. A., Kereš D., Quataert E., Faucher-Giguéré C. A., Hopkins P. F., 2015, MNRAS, 451, 3269

van den Bergh S., 1976, ApJ, 206, 883

Appendix

List of publications

1. *Galaxy gas flows inferred from a detailed, spatially resolved metal budget*, F. Belfiore, R. Maiolino & M. Bothwell, 2016, MNRAS, 455, 1218.

2. *P-MaNGA Galaxies: emission-lines properties - gas ionization and chemical abundances from prototype observations*, F. Belfiore, R. Maiolino, K. Bundy et al., 2015, MNRAS, 449, 867.

3. *SDSS IV MaNGA - Spatially resolved diagnostic diagrams: A proof that many galaxies are LIERs*, F. Belfiore, R. Maiolino, C. Maraston, et al., 2016, MNRAS, 461, 3111.

4. *SDSS IV MaNGA - The spatially resolved transition from star formation to quiescence*, F. Belfiore, R. Maiolino, C. Maraston et al., 2017, MNRAS, 446, 2570.

5. *SDSS IV MaNGA - The shape of the gas metallicity and nitrogen abundance gradients in the local Universe*, F. Belfiore, R. Maiolino, C. Tremonti et al., 2017, MNRAS, 469, 151.

6. *Nitrogen and oxygen abundances in the Local Universe*, F. Vincenzo, F. Belfiore, R. Maiolino, F. Matteucci, P. Ventura, 2016, MNRAS, 358, 3466.

7. *Modern yields per stellar generation: the effect of the IMF*, F. Vincenzo, F. Matteucci, F. Belfiore, R. Maiolino, 2016, MNRAS, 455, 4183.

8. *Overview of the SDSS-IV MaNGA Survey: Mapping Nearby Galaxies at Apache Point Observatory*, K. Bundy, M. Bershady, D. Law, [...], F. Belfiore et al., ApJ, 2015, 798, 7.

9. *SDSS-IV MaNGA IFS Galaxy Survey - Survey Design, Execution, and Initial Data Quality*, R. Yan, K. Bundy, D. Law, [...], F. Belfiore et al., AJ, 2016, 152, 197.

10. *The Thirteenth Data Release of the Sloan Digital Sky Survey: First Spectroscopic Data from the SDSS-IV Survey MApping Nearby Galaxies at Apache Point Observatory*, F. Albareti, [...], F. Belfiore et al., arXiv:1608.02013, submitted to ApJS.

11. *P-MaNGA: full spectral fitting and stellar population maps from prototype observations*, D. Wilkinson, C. Maraston, D. Thomas, [...], F. Belfiore et al., MNRAS, 2015, 449, 328.

12. *SDSS-IV MaNGA: The Impact of Diffuse Ionized Gas on Emission-line Ratios, Interpretation of Diagnostic Diagrams, and Gas Metallicity Measurements*, K. Zhang, R. Yan, K. Bundy, [...], F. Belfiore et al., MNRAS, 2017, 466, 3217.

13. *Suppressing star formation in quiescent galaxies with supermassive black hole winds*, E. Cheung, K. Bundy, M. Cappellari, [...], F. Belfiore et al., 2016, Nature, 533, 504.

14. *Molecular gas on large circumgalactic scales at z=3.47*, M. Ginolfi, R. Maiolino, T. Nagao, [...], F. Belfiore et al., MNRAS, 2017, 468, 3468.